

# CORRELATION EFFECTS IN LAYERED HETEROSTRUCTURES

ON THE IMPACT OF LONG-RANGE AND DYNAMICALLY SCREENED  
COULOMB INTERACTIONS TO NORMAL AND SUPERCONDUCTING STATES  
IN ONE-LOOP THEORIES AND BEYOND



Institute for Molecules  
and Materials

YANN IN 'T VELD

RADBOUD  
UNIVERSITY  
PRESS

Radboud  
Dissertation  
Series



**CORRELATION EFFECTS IN LAYERED  
HETEROSTRUCTURES**

ON THE IMPACT OF LONG-RANGE AND DYNAMICALLY SCREENED  
COULOMB INTERACTIONS TO NORMAL AND SUPERCONDUCTING STATES  
IN ONE-LOOP THEORIES AND BEYOND

**Author:** Yann in 't Veld

**Title:** Correlation Effects in Layered Heterostructures: On the Impact of Long-Range and Dynamically Screened Coulomb Interactions to Normal and Superconducting States in One-Loop Theories and Beyond

**Radboud Dissertations Series**

SSN: 2950-2772 (Online); 2950-2780 (Print)

Published by RADBOUD UNIVERSITY PRESS  
Postbus 9100, 6500 HA Nijmegen, The Netherlands  
[www.radbouduniversitypress.nl](http://www.radbouduniversitypress.nl)

Design: ClassicThesis | André Miede and Ivo Pletikosić

Cover: Proefschrift AIO | Guntra Laivacuma

Printing: DPN Rikken/Pumbo

ISBN: 9789465150918

DOI: 10.54195/9789465150918

Free download at: <https://doi.org/9789465150918>

© 2025 Yann in 't Veld

**RADBOUD  
UNIVERSITY  
PRESS**

This is an Open Access book published under the terms of Creative Commons Attribution-Noncommercial-NoDerivatives International license (CC BY-NC-ND 4.0). This license allows reusers to copy and distribute the material in any medium or format in unadapted form only, for noncommercial purposes only, and only so long as attribution is given to the creator, see <http://creativecommons.org/licenses/by-nc-nd/4.0/>.

# CORRELATION EFFECTS IN LAYERED HETEROSTRUCTURES

ON THE IMPACT OF LONG-RANGE AND DYNAMICALLY SCREENED  
COULOMB INTERACTIONS TO NORMAL AND SUPERCONDUCTING STATES  
IN ONE-LOOP THEORIES AND BEYOND

PROEFSCHRIFT

ter verkrijging van de graad van doctor  
aan de Radboud Universiteit Nijmegen  
op gezag van de rector magnificus prof. dr. J. M. Sanders,  
volgens besluit van het college voor promoties  
in het openbaar te verdedigen op

maandag 23 juni 2025  
om 10:30 uur precies

door

YANN IN 'T VELD

geboren op 21 april 1997  
te Nijmegen

PROMOTOR

prof. dr. M. I. Katsnelson

COPROMOTOR

dr. M. K. Rösner

MANUSCRIPTCOMMISSIE

prof. dr. U. Zeitler

prof. dr. J. van Wezel (Universiteit van Amsterdam)

dr. E. G. C. P. van Loon (Lunds Universitet, Zweden)

Voor mijn familie





# CONTENTS

---

1	Introduction	1
2	Brief Review of Quantum Many Body Theory	5
2.1	The Hamiltonian	6
2.2	Hedin's Equations	8
2.2.1	The Green's Function	8
2.2.2	Hedin's Perturbation Theory	11
2.3	$G_0W_0$ Theory	16
2.3.1	Random Phase Approximation	17
2.3.2	Normal State Renormalization	21
2.3.3	GW + Cumulant Theory	22
2.4	2D Coulomb Interactions	27
2.4.1	2D Coulomb Matrix Elements in a Local Basis	27
2.4.2	cRPA and Static Environmental Screening	28
2.5	Superconductivity	32
2.5.1	BCS Theory	32
2.5.2	One-Loop Theory	34
2.5.3	Eliashberg Theory	37
2.6	Discrete Lehman Representation	40
3	Brief Overview of Relevant Materials	43
3.1	Graphene	43
3.2	Transition Metal Dichalcogenides	46
4	Interlayer Plasmon Polarons in $WS_2$ /Graphene Heterostructures	49
4.1	Introduction	49
4.2	Electronic Structure of Doped $WS_2$ and Graphene/ $WS_2$	50
4.3	Doping-Dependence of Shake-Off Bands	52
4.4	Many-Body Analysis of Electron-Plasmon Interactions	54
4.5	Discussion	58
4.A	Density Functional Theory Calculations	59
4.B	Analytical $G_0W_0 + C$ Expressions	61

5	Crossover between Phonon- and Plasmon-Mediated Superconductivity	63
5.1	Introduction . . . . .	63
5.2	Formalism . . . . .	64
5.3	Transition Temperature . . . . .	67
5.4	Normal-State . . . . .	69
5.5	Anomalous Self-Energy . . . . .	70
5.6	Experimental Verification . . . . .	71
5.7	Conclusions . . . . .	74
5.A	Non-Local Electron-Phonon Interaction . . . . .	76
5.B	Non-Local Background Screening . . . . .	76
5.C	Doping Dependence . . . . .	78
6	Enhanced Superconductivity from Dynamical Environmental Screening	81
6.1	Introduction . . . . .	81
6.2	Model . . . . .	83
6.3	Computational Details . . . . .	85
6.4	Interlayer Plasmon Modes . . . . .	85
6.5	Normal-State . . . . .	88
6.6	Effect of Interlayer Coupling to Superconductivity . . . . .	88
6.7	Qualitative Modelling of Plasmon Mediated Superconductivity . . . . .	91
6.8	Optimizing Superconductivity . . . . .	93
6.9	Conclusions . . . . .	95
7	Beyond One-Loop Superconductivity Theory	99
7.1	Introduction . . . . .	99
7.2	Second-Order Diagrams . . . . .	100
7.3	The Perturbative Formalism . . . . .	105
7.4	The Model . . . . .	107
7.5	Preliminary Results: Electron-Phonon Coupling . . . . .	108
7.6	Preliminary Results: Local Coulomb Interactions . . . . .	110
7.7	Conclusions & Outlook . . . . .	113
8	Conclusions & Outlook	115
	Popular Summary	117
	Populaire Samenvatting	119
	Bibliography	121
	Research Data Management	149
	Publications	151
	Acknowledgments	153
	Curriculum Vitae	155

## INTRODUCTION

---

In 2004, Novoselov and Geim exfoliated, for the first time, atomically thin monolayers of graphite, called graphene. [1,2] Together with the work of many others, this initiated a new, rapidly growing field on two-dimensional (2D) materials, which now includes various other materials, such as hexagonal Boron Nitride (hBN), transition metal dichalcogenides (TMDCs) and many more. [3,4] Already on their own, various 2D materials host exciting properties, ranging from exceptionally high electron mobilities to large tensile strengths. Moreover, collective many-body excitations have striking new features in 2D, such as quadratically dispersing acoustic phonon modes [5], excitons with enormous binding energies [6–8] or low-energy plasmon modes which couple strongly to electrons [5,9].

Arguably even more intriguing is the ability to stack arbitrary combinations of 2D materials into multilayered heterostructures. [10] This is possible even with significant lattice mismatch, because the van-der-Waals force that keeps the layers together is relatively weak, thus giving rise to an almost endless variety of novel artificial materials that can be created. [11] This freedom is now being exploited to design novel devices and has already yielded transistors, photo-detectors and more. [12,13]

The versatility and tunability of layered materials is furthermore extraordinarily interesting for the study of correlation effects, which are induced by many-body interactions and may cause electrons to behave unlike the effective non-interacting (quasi-)particles of a Fermi liquid. This gives rise to some of the more unintuitive and less-well understood phenomena in solid-state physics, such as unconventional superconductivity, quantum magnetism or Mott insulating behaviour. Moreover, these phenomena can be especially pronounced in layered materials, because the reduced internal screening compared to three-dimensional (3D) bulk materials may lead to relatively strong electron-electron interactions. At the same time, layered materials are sensitive to external stimuli, such as environmental screening, doping or applied fields [10,14], which makes their properties relatively easy to tune. The combination of these features thus paves the way for a microscopic control over correlated phenomena.

However, in order to gain full control over correlated layered materials, we require a fundamental understanding of the physics that governs their properties. In this thesis, we place particular focus on layered superconductors, which host many phenomena that are not yet well understood. This includes, for example, the superconducting critical temperature in doped semi-conducting TMDCs, which

has been observed to enhance as the number of material layers is increased. [15–17] Other examples include the drastic increase of the critical temperature of monolayer FeSe when grown on top of a SrTiO<sub>3</sub> substrate [18, 19] or the emergence of superconductivity in twisted bilayer graphene and twisted bilayer WSe<sub>2</sub> at specific ‘magic’ twist angles [20–22]. Moreover, most high- $T_c$  superconductors have a layered structure, which is believed to be crucial for the emergence of their peculiar superconducting state. [23] So far, a universal theory which explains such ‘unconventional’ layered superconductors does not exist.

The theoretical description of layered materials is however complicated by the reduced screening. It causes the long-range nature of the Coulomb interaction to be less suppressed when compared to 3D bulk materials. Therefore, a theory that is capable of describing Coulomb-induced effects in layered materials cannot rely on local approximations commonly used for 3D systems. To resolve this, there are well-established ‘one-loop’ theories which can explicitly take into account non-locality, such as the GW approximation [24, 25] or (extensions to) Eliashberg theory [26–28]. However, in 2D it is unknown to what extent so-called ‘vertex corrections’ to those theories are required. In this thesis, we will address these complications and propose methods to resolve them.

Overall, the aim of this thesis is to gain a deeper theoretical understanding of the effect of the long-range 2D Coulomb interaction, as well as screening to it, on the normal and superconducting states of layered materials. To this end, we will develop and apply methods that go beyond state-of-the-art, in order to analyze the importance of non-locality and vertex corrections to one-loop theories in 2D systems.

We start in chapter 2 by reviewing the prerequisite quantum many-body theory used throughout the thesis. Here we furthermore discuss the recently developed discrete Lehman representation (DLR), which is a considerable advancement that allows for calculations at significantly lower temperatures than previously possible. In chapter 3 we briefly introduce two material classes, graphene and TMDCs, which we studied in collaboration with our experimental colleagues. These materials will furthermore serve as an inspiration for generic models used throughout this thesis. After these introductory chapters, we proceed by presenting our results. In chapter 4 we consider a doped heterostructure of graphene and WS<sub>2</sub>. In this system, angle-resolved photoemission spectroscopy (ARPES) measurements show a cascade of replica bands below the conduction band minimum, which cannot be explained by considering isolated monolayers alone. In order to explain this phenomenon, we study the effect of dynamical interlayer screening to normal state properties. Based on our results, we are able to give a qualitative description of the normal state of such heterostructures which is in agreement with the experimental findings.

In the chapters that follow, we shift our focus to the superconducting state. In chapter 5, we first consider a generic 2D monolayer in a static dielectric screening

environment. By consistently taking into account the non-local 2D Coulomb interaction and the electron-phonon interaction, we reveal a screening-induced crossover to an unconventional superconducting state mediated by dynamical charge fluctuations called ‘plasmons’. We furthermore discuss the properties of this plasmonic superconducting state and list some of its experimentally observable signatures.

In chapter 6 we extend the methods of the previous chapter to bilayer systems, to study the effect of dynamic interlayer screening to the superconducting state. In this way, we are able to make general qualitative predictions for the trends of critical temperatures of plasmon-mediated layered superconductors.

Finally, in chapter 7, we propose a new formalism which can quantify the importance of vertex corrections for the superconducting state. Using this formalism, we aim to verify the validity of one-loop theories in 2D materials. We will show preliminary results for local interaction models, which serve as a proof of concept for the method.



BRIEF REVIEW OF QUANTUM MANY BODY THEORY

---

The following chapter summarizes the theoretical methods and frameworks used throughout this thesis. While all text in this chapter has been written by me, the attentive reader might find overlap of information and/or structure with other works from which inspiration has been drawn. References to those works will be highlighted whenever applicable.

The structure of this chapter is as follows. In section 2.1 we will first briefly discuss the quantum many-body Hamiltonian, which forms the basis for all the physics in this thesis. In section 2.2, we discuss a general framework for describing properties of this Hamiltonian in the form of Hedin's equations. These equations are in principle exact, but unfeasible to solve for a general condensed matter system. Therefore, in section 2.3, we describe the common  $G_0W_0$  approximation to Hedin's equations, as well as the cumulant extension to it. An important ingredient for the  $G_0W_0$  theory is the unscreened (bare) Coulomb interaction, which we discuss in detail in section 2.4. In section 2.5, we discuss natural extensions of the  $G_0W_0$  theory into the superconducting state, focusing on a one-loop theory for superconductivity as well as the closely related Eliashberg theory. Finally, we discuss the discrete Lehman representation in section 2.6, which is a significant numerical advancement that allows us to perform (superconductivity) calculations at lower temperatures than before.

In the following chapter and throughout the thesis, we will use units within which the reduced Planck constant  $\hbar = 1$ , the Boltzmann constant  $k_B = 1$  and the vacuum permittivity  $\varepsilon_0 = 1/(4\pi)$ .

## 2.1 THE HAMILTONIAN

Our ultimate aim is to describe physical observables that are governed by the time-independent Schrödinger equation

$$H\Psi = E\Psi. \quad (2.1)$$

In this thesis we consider crystalline materials, consisting of negatively charged electrons and positively charged ionic cores distributed on a periodic lattice. One of the most general formulations for the Hamiltonian operator of such a system is the following Fröhlich-like Hamiltonian, written in second quantization as

$$\begin{aligned} H = & \sum_{\mathbf{k}} \sum_{ab} \sum_{\sigma} h_{ab}^{(0)}(\mathbf{k}) c_{\mathbf{k}a\sigma}^{\dagger} c_{\mathbf{k}b\sigma} \\ & + \frac{1}{2} \sum_{\mathbf{k}\mathbf{k}'\mathbf{q}} \sum_{abcd} \sum_{\sigma\sigma'} V_{abcd}(\mathbf{k}, \mathbf{k}', \mathbf{q}) c_{\mathbf{k}+\mathbf{q}a\sigma}^{\dagger} c_{\mathbf{k}'-\mathbf{q}c\sigma'}^{\dagger} c_{\mathbf{k}'d\sigma'} c_{\mathbf{k}b\sigma} \\ & + \sum_{\mathbf{q}\nu} \omega_{\nu}(\mathbf{q}) \left( b_{\mathbf{q}\nu}^{\dagger} b_{\mathbf{q}\nu} + \frac{1}{2} \right) \\ & + \sum_{\mathbf{k}\mathbf{q}} \sum_{ab\sigma\nu} g_{ab}^{\nu}(\mathbf{k}, \mathbf{q}) \left( b_{\mathbf{q}\nu} + b_{-\mathbf{q}\nu}^{\dagger} \right) c_{\mathbf{k}+\mathbf{q}a\sigma}^{\dagger} c_{\mathbf{k}b\sigma} \\ & - \mu \sum_{\mathbf{k}a\sigma} c_{\mathbf{k}a\sigma}^{\dagger} c_{\mathbf{k}a\sigma}. \end{aligned} \quad (2.2)$$

Here  $c_{\mathbf{k}a\sigma}^{\dagger}$  and  $c_{\mathbf{k}a\sigma}$  are the usual fermionic creation and annihilation operators, respectively, for an electron in the state with crystal momentum  $\mathbf{k}$ , orbital  $a$  and spin  $\sigma$ . Similarly,  $b_{\mathbf{q}\nu}^{\dagger}$  and  $b_{\mathbf{q}\nu}$  are the respective bosonic creation and annihilation operators of a phonon in a state with momentum  $\mathbf{q}$  and branch  $\nu$ . In the following we will briefly discuss each term in the Hamiltonian.

The first term is the kinetic non-interacting single-electron term. The matrix elements  $h_{ab}^{(0)}(\mathbf{k})$  describe the non-interacting quasi-particle states resulting from the static ionic potential. Most generally,  $h^{(0)}$  can also depend on spin indices, for example to describe spin-orbit coupling, but in this thesis we will focus on materials where such terms are small such that we can neglect them.  $h^{(0)}$  can be described by a tight-binding model, which is either derived from or inspired by ab-initio downfolding methods. [29–31] For free electrons, the matrix elements would be given by  $h_{ab}^{(0)}(\mathbf{k}) \approx \frac{\hbar^2 k^2}{2m_e} \delta_{ab}$ , with  $m_e$  the electron mass.

The second term of the Hamiltonian captures the electron-electron repulsion resulting from the Coulomb interaction. The effect of this term on the electronic properties is the main focus of this thesis. The matrix elements  $V_{abcd}(\mathbf{k}, \mathbf{k}', \mathbf{q})$  will



be discussed in further detail in section 2.4.

The third and fourth term capture the dynamics of the ionic lattice and its coupling to the electrons, respectively. The phonon dispersion  $\omega_\nu(\mathbf{q})$  captures the energy of the eigenmodes, enumerated by  $\nu$ . The electron-phonon coupling  $g_{ab}^\nu(\mathbf{k}, \mathbf{q})$  describes the scattering strength of an electron from state  $(\mathbf{k}, b)$  to state  $(\mathbf{k} + \mathbf{q}, a)$ , under the emission or absorption of a phonon with momentum  $\mathbf{q}$  and mode  $\nu$ .

The final term is the chemical potential term. This term is strictly spoken not part of the Hamiltonian, but it appears whenever one calculates the density operator  $e^{-\beta(H-\mu N)}/Z$  in the grand canonical ensemble, with  $\mu$  the chemical potential,  $N$  the number operator and  $Z$  the partition function. Since we are generally interested in expectation values of operators, we will absorb the chemical potential term into the Hamiltonian for simplicity.

## 2.2 HEDIN'S EQUATIONS

The following section introduces the Green's function as well as the general many-body framework we will use throughout the thesis. In writing this section, information and derivations have been gathered from a variety of sources. Most influential have been the GW review article by F. Aryasetiawan and O. Gunnarsson [25] and the lecture notes of the Jülich autumn school on correlated electrons [31–33]. The introduction of the Green's function and many-body perturbation theory can also be found in many textbooks, such as Mahan [34], Bruus and Flensberg [35] or Coleman [36].

### 2.2.1 The Green's Function

Obtaining the full eigenspectrum and the corresponding eigenvectors of Eq. 2.2 would, in principle, allow for the evaluation of any physical observable. However, due to the enormous amount of particles in a solid state system (on the order of Avogadro's number  $N_A \approx 6 \times 10^{23}$  particles\*), it is impossible to obtain or even store that information numerically. Fortunately, it turns out that in order to describe properties of a many-body quantum system, knowledge of the single-particle Green's function is often enough. For brevity, we discuss the Green's function immediately in imaginary time, as this makes the finite temperature derivations more straightforward. For the interested reader, all derivations in this section are also discussed in real time and in more detail in common textbooks. [34–36]

We define the single-particle fermionic Green's function as

$$G_{ab}(\mathbf{k}, \tau_a - \tau_b) = - \left\langle \mathcal{T} c_{\mathbf{k}a}(\tau_a) c_{\mathbf{k}b}^\dagger(\tau_b) \right\rangle = \begin{cases} - \langle c_{\mathbf{k}a}(\tau_a) c_{\mathbf{k}b}^\dagger(\tau_b) \rangle & \text{when } \tau_a > \tau_b \\ \langle c_{\mathbf{k}b}^\dagger(\tau_b) c_{\mathbf{k}a}(\tau_a) \rangle & \text{when } \tau_b > \tau_a \end{cases}, \quad (2.3)$$

with  $c_{\mathbf{k}a}^{(\dagger)}(\tau) = e^{\tau H} c_{\mathbf{k}a}^{(\dagger)} e^{-\tau H}$  the annihilation (creation) operator at imaginary time  $\tau$  in the Heisenberg picture.  $\mathcal{T}$  denotes the time-ordering operator. Green's functions are also commonly referred to as propagators, because it contains information on the likelihood of an electron that is created at time  $\tau_b$  in state  $(\mathbf{k}, b)$ , to propagate and be in state  $(\mathbf{k}, a)$  at a later time  $\tau_a > \tau_b$ . Similarly, it describes the propagation of holes when  $\tau_b > \tau_a$ .

Instead of working directly with time variables, it is often more convenient to Fourier transform the Green's function to the frequency domain. Since we are

---

\* By exploiting lattice symmetries one can already significantly reduce the number of particles that need to be taken into account. Nonetheless, exact methods are currently restricted to relatively small system sizes.

working here with imaginary time Green's functions, with a periodic time variable  $\tau$  with a periodicity given by the inverse temperature  $\beta = 1/(k_B T)$ , the frequency axis will consist of discrete Matsubara frequencies. The Fourier transform for fermionic Green's functions is therefore given by

$$G_{ab}(\mathbf{k}, i\omega_n) = \int_0^\beta d\tau G_{ab}(\mathbf{k}, \tau) e^{i\omega_n \tau}, \quad (2.4)$$

with  $i\omega_n = (2n + 1)\pi/\beta$  a fermionic Matsubara frequency and  $n$  being an integer. Analytical continuation to the real-frequency retarded (advanced) Green's function  $G_{ab}^R(\mathbf{k}, \omega)$  ( $G_{ab}^A(\mathbf{k}, \omega)$ ) can be done from here by substituting  $i\omega_n \rightarrow \omega + i\delta$ , where  $\delta$  is an infinitesimally small constant with positive (negative) sign. For completeness, the fermionic Fourier transform back to imaginary time is given by

$$G_{ab}(\mathbf{k}, \tau) = \frac{1}{\beta} \sum_n G_{ab}(\mathbf{k}, i\omega_n) e^{-i\omega_n \tau}. \quad (2.5)$$

The single-particle phononic Green's function  $D$  is defined in a similar way as the fermionic one

$$D_\nu(\mathbf{q}, \tau_a - \tau_b) = - \left\langle \mathcal{T} \left( b_{\mathbf{q}\nu}(\tau_a) + b_{-\mathbf{q}\nu}^\dagger(\tau_a) \right) \left( b_{-\mathbf{q}\nu}(\tau_b) + b_{\mathbf{q}\nu}^\dagger(\tau_b) \right) \right\rangle. \quad (2.6)$$

Similar to the fermionic Green's function, it describes the propagation of a phonon with momentum  $\mathbf{q}$  and mode  $\nu$  which is emitted at time  $\tau_b$  and absorbed at time  $\tau_a$  (or, equivalently, a phonon with inverse momentum  $-\mathbf{q}$  being absorbed at time  $\tau_b$  and re-emitted at time  $\tau_a$ ). The bosonic Fourier transforms have the same expressions as the fermionic ones, except that the Matsubara frequencies are now given by  $i\nu_m = 2m\pi/\beta$ , with  $m$  being an integer. Here and in the following we will use the convention of using the character  $\omega$  with subscript  $n$  for fermionic Matsubara frequencies and the character  $\nu$  with subscript  $m$  for bosonic ones.

**THE SPECTRAL FUNCTION** To gain some more physical intuition to the Green's function, it is helpful to write it in the spectral representation. We do this by inserting the completeness relation  $1 = \sum_j |j\rangle\langle j|$  in Eq. 2.3 and subsequently Fourier transforming to Matsubara frequency, yielding

$$\begin{aligned} G_{ab}(\mathbf{k}, i\omega_n) &= \frac{1}{Z} \sum_{ij} \frac{\langle i | c_{\mathbf{k}a} | j \rangle \langle j | c_{\mathbf{k}b}^\dagger | i \rangle}{i\omega_n + E_i - E_j} e^{-\beta(E_i + E_j)} \\ &= \int_{-\infty}^{\infty} d\omega \frac{A_{ab}(\mathbf{k}, \omega)}{i\omega_n - \omega}, \end{aligned} \quad (2.7)$$

where  $E_i$  are eigenvalues of the Hamiltonian and  $|i\rangle$  the corresponding eigenstates.  $Z$  is the partition function. In the second line we defined the spectral function as

$$\begin{aligned} A_{ab}(\mathbf{k}, \omega) &= -\frac{1}{\pi} \text{Im} (G_{ab}^R(\mathbf{k}, \omega)) \\ &= \frac{1}{Z} \sum_{ij} \delta(\omega + E_i - E_j) e^{-\beta(E_i + E_j)} \langle i | c_{\mathbf{k}a} | j \rangle \langle j | c_{\mathbf{k}b}^\dagger | i \rangle. \end{aligned} \quad (2.8)$$

From Eq. 2.7 we understand that the Green's function is given by an integral over poles. The spectral function  $A_{ab}(\mathbf{k}, \omega)$  determines the position of these poles and the intensity they have. Whenever the frequency  $\omega$  is equal to the difference between two eigenenergies  $E_i - E_j$  the spectral function peaks, such that the Green's function has poles whenever an excitation at frequency  $\omega$  is possible. This reflects that the Green's function can also intuitively be understood to describe a photoemission process. In fact, using an experimental technique called angle-resolved photoemission spectroscopy (ARPES) one can directly probe the spectral function for occupied states with both momentum and frequency resolution. [37] Besides providing the single-particle excitation spectrum, the spectral function can also be used to evaluate the electron density as

$$\begin{aligned} n &= \frac{1}{\beta} \sum_{\mathbf{k}, n} \sum_a G_{aa}(\mathbf{k}, i\omega_n) \\ &= \int_{-\infty}^{\infty} d\omega \sum_{\mathbf{k}} \sum_a A_{aa}(\mathbf{k}, \omega) n_F(\omega), \end{aligned} \quad (2.9)$$

with  $n_F(\omega) = 1/(e^{\beta\omega} + 1)$  the Fermi-Dirac distribution function. Comparing this expression to the expression for the density of a free electron gas, we learn that the trace of the momentum-summed spectral function can be understood as a density of states (DOS)

$$N(\omega) = \sum_{\mathbf{k}} \sum_a A_{aa}(\mathbf{k}, \omega). \quad (2.10)$$

We have shown that if we can calculate the single-particle Green's function for a given system, we can predict single-particle spectral properties and electron densities. In principle, any other expectation value of a single-particle operator can be obtained as well. [24, 25] One of the strengths of the Green's function formalism is the ability to obtain this information without having to diagonalize the full Hamiltonian.

**THE BARE GREEN'S FUNCTION** The Green's function of a non-interacting system  $H_0 = \sum_{\mathbf{k}ab} (h_{ab}^{(0)}(\mathbf{k}) - \mu\delta_{ab}) c_{\mathbf{k}a}^\dagger c_{\mathbf{k}b}$  we call the bare Green's function  $G_{ab}^{(0)}(\mathbf{k}, i\omega_n)$ . Since we can derive exact expressions for this Green's function, it is a good starting

$$G_{ab}^{(0)}(\mathbf{k}, i\omega_n) = \begin{array}{c} \xrightarrow{\hspace{1.5cm}} \\ b \quad \mathbf{k}, i\omega_n \quad a \end{array} \quad G_{ab}(\mathbf{k}, i\omega_n) = \begin{array}{c} \xrightarrow{\hspace{1.5cm}} \\ b \quad \mathbf{k}, i\omega_n \quad a \end{array}$$

Figure 2.1: Feynman diagrams corresponding to the bare (left) and dressed (right) single-particle Green's functions, propagating from orbital  $b$  to orbital  $a$  with crystal momentum  $\mathbf{k}$  and Matsubara frequency  $i\omega_n$ .

point for the perturbation theory we will discuss in the next section. To this end, we derive from the usual fermionic commutation relations that

$$c_{\mathbf{k}a}(\tau) = \sum_b \left[ e^{-\tau(\hat{h}^{(0)}(\mathbf{k}) - \hat{\mathcal{I}}\mu)} \right]_{ab} c_{\mathbf{k}b} \quad \text{and} \quad c_{\mathbf{k}a}^\dagger(\tau) = \sum_b \left[ e^{\tau(\hat{h}^{(0)}(\mathbf{k}) - \hat{\mathcal{I}}\mu)} \right]_{ab} c_{\mathbf{k}b}^\dagger,$$

where the time dependence is treated in the Heisenberg picture. Here and in the following we denote matrices in the orbital basis with a hat, where  $\hat{\mathcal{I}}$  is the identity matrix. Substituting these expressions into the definition of the Green's function and remembering that for a non-interacting Hamiltonian  $\langle c_{\mathbf{k}a}^\dagger c_{\mathbf{k}b} \rangle = n_F \left( \hat{h}^{(0)}(\mathbf{k}) - \hat{\mathcal{I}}\mu \right)_{ab}$  we find for the bare Green's function (written as a matrix in the orbital basis)

$$\hat{G}^{(0)}(\mathbf{k}, \tau) = e^{-\tau(\hat{h}^{(0)}(\mathbf{k}) - \hat{\mathcal{I}}\mu)} \left( n_F \left( \hat{h}^{(0)}(\mathbf{k}) - \hat{\mathcal{I}}\mu \right) - \hat{\mathcal{I}}\Theta(\tau) \right). \quad (2.11)$$

Performing the Fourier transform yields

$$\hat{G}^{(0)}(\mathbf{k}, i\omega_n) = \left( \hat{\mathcal{I}}(i\omega_n + \mu) - \hat{h}^{(0)}(\mathbf{k}) \right)^{-1}. \quad (2.12)$$

In terms of Feynman diagrams, the bare electronic Green's function is denoted by a single straight line, as shown in Fig. 2.1.

In a similar way as for electrons, we can derive that the bare phonon Green's function is given by

$$D_\nu^{(0)}(\mathbf{q}, i\nu_m) = \frac{1}{i\nu_m - \omega_\nu(\mathbf{q})} - \frac{1}{i\nu_m + \omega_\nu(\mathbf{q})} = \frac{2\omega_\nu(\mathbf{q})}{(i\nu_m)^2 - \omega_\nu(\mathbf{q})^2}. \quad (2.13)$$

### 2.2.2 Hedin's Perturbation Theory

When including interaction terms to our Hamiltonian, i.e.  $H = H_0 + V$ , it is no longer straightforward to find an analytic expression for the Green's function. A common way to treat this problem is in perturbation theory, where we expand

Figure 2.2: Feynman diagrams corresponding to the bare (left) and dressed (right) interactions of an electron at orbital  $b$  scattered to site  $a$  and an electron at orbital  $d$  scattered to orbital  $c$ , with momentum transfer  $\mathbf{q}$  and energy transfer  $i\nu_m$ . The gray Green's function lines are considered amputated and do not enter the expressions.

in terms of the interaction  $V$ . The resulting Green's function we call the dressed Green's function  $G_{ab}(\mathbf{k}, i\omega_n)$ , depicted diagrammatically by the double line shown in Fig. 2.1.

A full derivation of Hedin's many-body perturbation theory would be too lengthy to cover here. For a more detailed discussion we refer the reader to the review article by Aryasetiawan and Gunnarsson [25] or to the 2011 Jülich lecture notes by Held [31]. Common textbooks [34–36] also cover many-body perturbation theory. In most Green's function based perturbation theories, a central quantity is the self-energy  $\Sigma_{ab}(\mathbf{k}, i\omega_n)$ . It is the quantity which connects the bare Green's function  $G_{ab}^{(0)}(\mathbf{k}, i\omega_n)$  to the dressed one  $G_{ab}(\mathbf{k}, i\omega_n)$  in the so-called Dyson equation

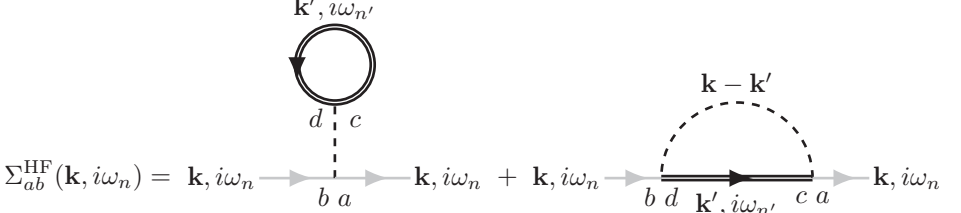
$$\begin{aligned} G_{ab}(\mathbf{k}, i\omega_n) &= G_{ab}^{(0)}(\mathbf{k}, i\omega_n) + \sum_{cd} G_{cb}^{(0)}(\mathbf{k}, i\omega_n) \Sigma_{dc}(\mathbf{k}, i\omega_n) G_{ad}(\mathbf{k}, i\omega_n) \\ &= \left( \hat{\mathcal{I}}(i\omega_n + \mu) - \hat{h}^{(0)}(\mathbf{k}) - \hat{\Sigma}(\mathbf{k}, i\omega_n) \right)_{ab}^{-1} \end{aligned} \quad (2.14)$$

The equivalent expression in terms of Feynman diagrams is

The self-energy is the sum of all irreducible single-particle diagrams, i.e., all diagrams that do not fall apart when one Green's function line is cut.

We now transferred the problem from calculating the Green's function  $G$  to calculating the self-energy  $\Sigma$ . The way of approximating the self-energy therefore becomes the cornerstone of diagrammatic quantum many-body theories in condensed matter physics. The most straightforward approximation is to simply apply perturbation theory in terms of the bare interaction  $V$  (denoted diagrammatically by a dashed

line, as shown in Fig. 2.2). Truncating after first order in  $V$  yields the Hartree-Fock self-energy

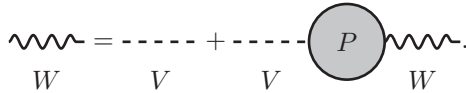


$$\begin{aligned} \Sigma_{ab}^{\text{HF}}(\mathbf{k}, i\omega_n) &= \text{diagram 1} + \text{diagram 2} \\ &= \frac{1}{\beta} \sum_{\mathbf{k}', n'} \sum_{cd} V_{abcd}(\mathbf{q} = 0) G_{dc}(\mathbf{k}', i\omega_{n'}) \\ &\quad - \frac{1}{\beta} \sum_{\mathbf{k}', n'} \sum_{cd} V_{acdb}(\mathbf{k} - \mathbf{k}') G_{cd}(\mathbf{k}', i\omega_{n'}) \end{aligned} \quad (2.15)$$

where the gray Green's function lines are considered amputated and do not enter the corresponding mathematical expressions. The first term is the Hartree contribution. It is essentially a mean-field term, which captures the response of an electron to the total density of all other electrons. The second term is the Fock contribution, which takes into account non-local exchange. While the Hartree-Fock approximation works relatively well for atoms, it breaks down for solids due to missing contributions from screening and/or correlations. [25] In these cases, the perturbation series converges prohibitively slow or even diverges. A solution was proposed by Lars Hedin, in his pioneering work in 1965. [24] He devised a perturbation series in the screened interaction  $W$ , instead of the bare interaction  $V$ . Screening reduces the strength of the interaction in solids, such that a perturbation series in  $W$  might converge where the previous method could not. Similar to the Green's function, the screened interaction is given by a Dyson equation

$$W_{abcd}(\mathbf{q}, i\nu_m) = V_{abcd}(\mathbf{q}) + \sum_{efgh} V_{abef}(\mathbf{q}) P_{fegh}(\mathbf{q}, i\nu_m) W_{hgcd}(\mathbf{q}, i\nu_m), \quad (2.16)$$

with the corresponding diagrammatic expression



$$W = V + V \circlearrowleft P \circlearrowright W$$

Here we used a wavy line to denote the screened interaction, as defined in Fig 2.2. The function  $P$  is the polarization, which can here be understood as a bosonic

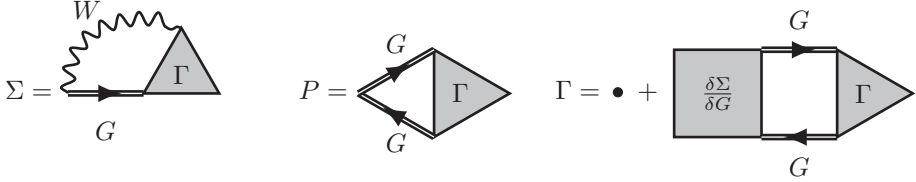


Figure 2.3: Feynman diagrams corresponding to the self-energy  $\Sigma$  (left), polarization  $P$  (middle) and vertex  $\Gamma$  (right). Orbital, momentum and frequency indices have been omitted for simplicity.

self-energy. Both the self-energy and the polarization are defined by Hedin using the vertex  $\Gamma$  as [24, 25, 31]

$$\begin{aligned} \Sigma_{ab}(\mathbf{k}, i\omega_n) = & -\frac{1}{\beta} \sum_{n'\mathbf{k}'} \sum_{cdkl} G_{cd}(\mathbf{k}, i\omega_{n'}) W_{lkdb}(\mathbf{k} - \mathbf{k}', i\omega_n - i\omega_{n'}) \\ & \times \Gamma_{cakl}(\mathbf{k}, i\omega_n, \mathbf{k}', i\omega_{n'}) \end{aligned} \quad (2.17)$$

$$\begin{aligned} P_{abcd}(\mathbf{q}, i\nu_m) = & \frac{1}{\beta} \sum_{n\mathbf{k}} \sum_{kl} G_{ka}(\mathbf{k}, i\omega_n) G_{bl}(\mathbf{k} + \mathbf{q}, i\omega_n + i\nu_m) \\ & \times \Gamma_{klcd}(\mathbf{k} + \mathbf{q}, i\omega_n + i\nu_m, \mathbf{k}, i\omega_n). \end{aligned} \quad (2.18)$$

Finally, the loop is closed by defining the vertex as

$$\begin{aligned} \Gamma_{abcd}(\mathbf{k}, i\omega_n, \mathbf{k}', i\omega_{n'}) = & \delta_{ac}\delta_{bd} \\ & + \sum_{ijkl} \left( \frac{\delta\Sigma}{\delta G} \right)_{bajk}(\mathbf{k}, i\omega_n, \mathbf{k}', i\omega_{n'}) G_{ij}(\mathbf{k}', i\omega_{n'}) G_{kl}(\mathbf{k}, i\omega_n) \\ & \times \Gamma_{ilcd}(\mathbf{k}, i\omega_n, \mathbf{k}', i\omega_{n'}), \end{aligned} \quad (2.19)$$

where  $\delta\Sigma/\delta G$  denotes a functional derivative. The corresponding diagrams are shown in Fig. 2.3.

Eqs. 2.16-2.19, together with Eq. 2.14, form a closed set of equations known as Hedin's equations. [24, 25, 31] They have to be solved self-consistently, by choosing some starting point and iterating through the equations until convergence is reached, as illustrated in Fig. 2.4. This procedure would, in principle, yield the exact many-body single-particle Green's function of a given Hamiltonian. However, in practice it takes an unfeasible amount of computation power to actually perform these calculations, such that further approximations discussed in the next section are necessary.

While in the original formulation of Hedin's equations the interaction  $V$  is assumed to be a Coulomb interaction, one can include phonons in this scheme by integrating



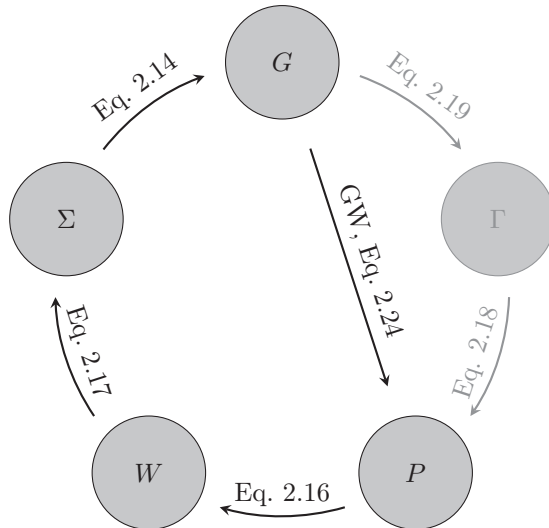


Figure 2.4: The self-consistency cycle for solving Hedin's equations. The diagonal line denoted by GW illustrates the self-consistency cycle of the GW approximation, in which the vertex  $\Gamma$  is approximated by unity.

them out. This procedure leads to the following substitution for all bare interactions in Hedin's equations [34, 35]

$$V_{abcd}(\mathbf{q}) \rightarrow V_{abcd}^C(\mathbf{q}) + V_{abcd}^{ph}(\mathbf{q}, i\nu_m), \quad (2.20)$$

where  $V_{abcd}^C(\mathbf{q})$  is the bare Coulomb interaction and  $V_{abcd}^{ph}(\mathbf{q}, i\nu_m)$  is an effective electron-electron interaction mediated by phonons given by [32, 33]

$$V_{abcd}^{ph}(\mathbf{q}, i\nu_m) = \sum_{\nu} g_{ab}^{\nu}(\mathbf{q}) g_{cd}^{\nu}(\mathbf{q}) D_{\nu}(\mathbf{q}, i\nu_m). \quad (2.21)$$

In this way, we treat the electron-phonon and the Coulomb interactions on equal footing, such that we take the mutual screening of the phonons by the Coulomb interaction and vice versa into account.

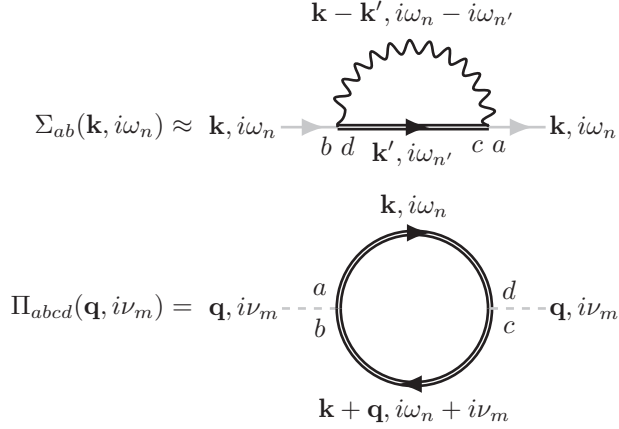


Figure 2.5: Feynman diagrams corresponding to the GW self-energy  $\Sigma$  (top) and polarization  $\Pi$  (bottom). The gray Green's function and interaction lines are considered amputated.

### 2.3 $G_0W_0$ THEORY

One of the most common ways to make Hedin's equations more feasible to solve is by employing the GW approximation (GWA). [24, 25, 31, 38] It is obtained by approximating the vertex  $\Gamma$  by unity

$$\Gamma_{abcd}(\mathbf{k}, i\omega_n, \mathbf{k}', i\omega_{n'}) \approx \delta_{ac}\delta_{bd}. \quad (2.22)$$

As a consequence, the self-energy  $\Sigma$  and the polarization  $P$  simplify to

$$\Sigma_{ab}(\mathbf{k}, i\omega_n) \approx -\frac{1}{\beta} \sum_{\mathbf{k}, n'} \sum_{cd} W_{acdb}(\mathbf{k} - \mathbf{k}', i\omega_n - i\omega_{n'}) G_{cd}(\mathbf{k}', i\omega_{n'}) \quad (2.23)$$

$$P_{abcd}(\mathbf{q}, i\nu_m) \approx \Pi_{abcd}(\mathbf{q}, i\nu_m) = \frac{1}{\beta} \sum_{\mathbf{k}, i\omega_n} G_{da}(\mathbf{k}, i\omega_n) G_{bc}(\mathbf{k} + \mathbf{q}, i\omega_n + i\nu_m), \quad (2.24)$$

with the corresponding diagrams shown in Fig. 2.5. As a consequence of this approximation, Hedin's self-consistency cycle is simplified by skipping the vertex function, as illustrated in Fig. 2.4.

The GWA can be interpreted as an extension to the Hartree-Fock approximation, where instead of the bare interaction  $V$  the screened interaction  $W$  is used. GW calculations are commonly performed in a one-shot, or  $G_0W_0$ , approximation. In this framework one starts from  $G = G^{(0)}$  and subsequently performs the GW

self-consistency cycle only once, i.e., without reaching a self-consistent solution. Surprisingly, it turns out that ab-initio  $G_0W_0$  results are generally much closer to experiments than self-consistent ab-initio GW results, especially for semiconductors and insulators. [39, 40] While there is not yet a consensus on why this is the case, there are strong hints that it is due to an error cancellation of missing vertex corrections and missing terms from self-consistency. [41–43] A drawback of the  $G_0W_0$  approximation is that it is non-conserving, such that the total electron number is not conserved before and after the calculations. [41, 44] To correct for this, we include a chemical potential shift in the dressed Green’s function, such that it has the same electron-density as the bare Green’s function (i.e., the bare and dressed Green’s functions will have different chemical potentials).

Arguably the largest success of the  $G_0W_0$  approximation has been in the ab-initio description of band gaps of semi-conductors. Density functional theory (DFT) calculations using the local density approximation (LDA) consistently underestimate band gaps for semiconductors such as Si, GaAs, Ge and more [25, 45–47]. Including Hartree-Fock (HF) corrections leads to an overestimation of the band gap. [46] Since screening heavily reduces the strength of the bare interaction,  $G_0W_0$  predicts band gaps which are in between those of the LDA and the HF, thus yielding results much closer to experimental results. [39, 40] However, as any approximation, the GWA has limited validity. It breaks down for sufficiently strong interactions, such that it cannot describe strongly correlated electron physics, such as Mott-insulating states. In those cases different approximations, such as dynamical mean field theory (DMFT) [48, 49], should be used instead. Another scenario where the GWA fails is for dilute metals. For the three-dimensional electron gas the GWA is known to fail when the electron gas parameter  $r_s = m^*e^2/(\epsilon\sqrt{\pi n}) \gtrsim 1$  [9, 34, 43, 50, 51], but in two dimensions its exact limits are not known. Some indications that a theory beyond the GWA should be used are the presence of a sharp plasmon-induced shakeoff feature below the conduction band, or the experimental observation of multiple shakeoff features. [52, 53] In such cases, extensions to the GWA that include vertex corrections should be used. One example of such a method is the GW+cumulant approach, which will be discussed in Sect. 2.3.3. In the preceding sections we will discuss each step of a  $G_0W_0$  calculation in detail.

### 2.3.1 *Random Phase Approximation*

The first step in  $G_0W_0$  theory is to evaluate the polarization function  $\Pi^{(0)}$ . It turns out to correspond to the polarization function obtained from the random phase approximation (RPA), which was derived independently from the  $G_0W_0$  approximation. [54–58] It can be derived by substituting the exact expression of

the bare Green's function (Eq. 2.12) into the GW expression of the polarization (Eq. 2.24) and subsequently evaluating the Matsubara sums. The result is the well-known Lindhard function [54]

$$\begin{aligned}\Pi_{abcd}^{(0)}(\mathbf{q}, i\nu_m) &= g \frac{1}{\beta} \sum_{\mathbf{k}, i\omega_n} G_{da}^{(0)}(\mathbf{k}, i\omega_n) G_{bc}^{(0)}(\mathbf{k} + \mathbf{q}, i\omega_n + i\nu_m) \\ &= g \sum_{\mathbf{k}} \sum_{ij} \frac{n_F(\xi_{\mathbf{k},i}) - n_F(\xi_{\mathbf{k}+\mathbf{q},j})}{i\nu_m + \xi_{\mathbf{k},i} - \xi_{\mathbf{k}+\mathbf{q},j}} T_{ai}(\mathbf{k}) T_{id}^\dagger(\mathbf{k}) T_{cj}(\mathbf{k} + \mathbf{q}) T_{jb}^\dagger(\mathbf{k} + \mathbf{q}),\end{aligned}\quad (2.25)$$

where the factor  $g$  in front is the (spin, valley, etc.) degeneracy factor.  $\xi_{\mathbf{k},i}$  is the bare electron dispersion in the band basis, obtained from the unitary transformation

$$\xi_{\mathbf{k},i} = \sum_{ab} T_{ia}^\dagger(\mathbf{k}) h_{ab}(\mathbf{k}) T_{bi}(\mathbf{k}) - \mu, \quad (2.26)$$

where  $a$  and  $b$  are orbital indices and  $i$  is a band index. The Lindhard function is a linear response function of the electron density to some perturbation. The poles of  $\Pi^{(0)}$  are at the energy difference between two single-electron states and the Fermi-Dirac distribution functions in the numerator ensure that one of those states is occupied and the other is unoccupied. In other words, the Lindhard function describes the excitation of electrons across the Fermi surface, creating electron-hole pairs. There is a continuum of points in the frequency-momentum space where electron-hole pairs can be excited, which we call the electron-hole continuum. [9, 34] The bare Coulomb interaction  $V$  is screened by these virtual electron-hole excitations, which results in the screened Coulomb interaction  $W$  given by Eq. 2.16. For simplicity, we commonly approximate the Coulomb interaction using the density-density approximation  $V_{abcd}(\mathbf{q}) \approx V_{ac}(\mathbf{q}) \delta_{ab} \delta_{cd}$ . In this case  $V$  and  $W$  are matrices, such that the Dyson equation for  $W$  simplifies to a matrix equation

$$\begin{aligned}\hat{W}(\mathbf{q}, i\nu_m) &= \hat{V}(\mathbf{q}) + \hat{V}(\mathbf{q}) \hat{\Pi}^{(0)}(\mathbf{q}, i\nu_m) \hat{W}(\mathbf{q}, i\nu_m) \\ &= \left( \hat{\mathcal{I}} - \hat{V}(\mathbf{q}) \hat{\Pi}^{(0)}(\mathbf{q}, i\nu_m) \right)^{-1} \hat{V}(\mathbf{q}).\end{aligned}\quad (2.27)$$

An alternative way to derive this expression is using the linear response formalism, in which the screened Coulomb interaction is given by the sum of the bare potential and the induced potential  $W(\mathbf{q}, i\nu_m) = V(\mathbf{q}) + V_{\text{ind}}(\mathbf{q}, i\nu_m)$ . The induced potential is written in linear response theory as  $V_{\text{ind}}(\mathbf{q}, i\nu_m) \approx W(\mathbf{q}, i\nu_m) \delta n(\mathbf{q}, i\nu_m) \approx W(\mathbf{q}, i\nu_m) \Pi^{(0)}(\mathbf{q}, i\nu_m) V(\mathbf{q})$ . Substituting the two expressions yields again Eq. 2.27. [9, 34]

**PLASMONS** The screened Coulomb interaction  $W$  is frequency dependent and has poles whenever the dielectric function  $\hat{\epsilon}(\mathbf{q}, i\nu_m) = \hat{\mathcal{I}} - \hat{V}(\mathbf{q}) \hat{\Pi}^{(0)}(\mathbf{q}, i\nu_m)$  vanishes.

These poles describe the excitation of a quantized, coherent oscillation of the electron density. [9, 34] Since those oscillations are the quantum mechanical counterpart of classical plasma oscillations, the corresponding bosonic quasi-particles are called plasmons. A plasmon has a relatively long lifetime as long as its dispersion  $\omega_{\mathbf{q}}$  lies outside the electron-hole continuum. Once the plasmon dispersion merges with the electron-hole continuum, the collective excitation will decay into single electron-hole pairs and is therefore damped by a process we call Landau damping. The shape and energy of the plasmon dispersion has important consequences, especially for optical properties. For example, many metals have their characteristic color because the plasmon dispersion lies in the visible spectrum, allowing them to absorb certain wavelengths of light. Plasmons can also couple to electrons, creating new excitations that are called plasmon polarons. These states have been observed in bulk materials using ARPES measurements [52, 59] and more recently also in two-dimensional in doped semi-conductors. [60, 61] Even more, while it has not yet been verified experimentally, the coupling between electrons and plasmons has also been predicted to be able to mediate superconductivity. [62–72] The effects of electron-plasmon coupling on the normal and superconducting states will be discussed in detail in chapters 5 and 6.

Experimentally, the most effective way to measure plasmons (and other bosonic excitations) is using electron energy loss spectroscopy (EELS). [73] The basic idea behind EELS is to radiate the sample with a beam of electrons within a narrow and known range of kinetic energies. When these electrons interact with the material some will scatter inelastically, losing some energy in the process. By measuring this energy loss one can infer the excitation energies that exist within the material.

**PLASMON-POLE APPROXIMATION** Calculating the screened interaction  $W$  in the RPA is computationally expensive. The plasmon pole approximation (PPA) aims to simplify the RPA by casting  $W$  in the form of a bare phononic propagator. [25, 74] In this way we gain a more intuitive understanding of the strength of the electron-plasmon coupling. We furthermore obtain an analytic expression for the pole-structure of  $W$ , which will allow us to perform some Matsubara summations analytically. We start by writing the screened Coulomb interaction in the spectral representation

$$W_{abcd}(\mathbf{q}, i\nu_m) = V_{abcd}(\mathbf{q}) + \int_0^\infty d\omega B_{abcd}(\mathbf{q}, \omega) \frac{2\omega}{(i\nu_m)^2 - \omega^2}, \quad (2.28)$$

where the first term is the repulsive bare Coulomb interaction and the second term is the effective plasmon induced attractive electron-electron interaction.  $B_{abcd}(\mathbf{q}, \omega) = -\text{Im}(W_{abcd}^R(\mathbf{q}, \omega) - V_{abcd}(\mathbf{q})) / \pi$  is the spectral function of the screened interaction. In the PPA we assume that the spectral function is completely governed by the plasmon excitations, i.e., we neglect spectral weight coming from electron-hole

excitations. Therefore, we approximate (assuming a single orbital system for simplicity) [25]

$$B(\mathbf{q}, \omega) \approx |a_{\mathbf{q}}|^2 (\delta(\omega - \omega_{\mathbf{q}}) - \delta(\omega + \omega_{\mathbf{q}})), \quad (2.29)$$

where  $|a_{\mathbf{q}}|$  is the electron-plasmon coupling and  $\omega_{\mathbf{q}}$  is the plasmon dispersion. As a consequence, the second term of the screened Coulomb interaction has the form of a bare phonon propagator

$$W(\mathbf{q}, i\nu_m) \approx V(\mathbf{q}) + |a_{\mathbf{q}}|^2 \frac{2\omega_{\mathbf{q}}}{(i\nu_m)^2 - \omega_{\mathbf{q}}^2}. \quad (2.30)$$

The dispersion  $\omega_{\mathbf{q}}$  can be determined from the roots of the real part of the dielectric function. For the 2D free electron gas we can find it analytically, by writing the RPA polarization at  $\omega > k_F q$  as [75]

$$\text{Re} \left( \Pi^{(0)}(\mathbf{q}, \omega) \right) \approx gN_0 \left( \frac{\omega}{\sqrt{\omega^2 - (qv_F)^2}} - 1 \right), \quad (2.31)$$

with  $N_0$  the DOS at the Fermi energy and  $v_F = \sqrt{2E_F/m^*}$  the Fermi velocity. Substituting this expression into the dielectric function and finding its roots yields [68]

$$\omega_{\mathbf{q}} = qv_F \sqrt{1 + \frac{(gN_0V(\mathbf{q}))^2}{1 + 2gN_0V(\mathbf{q})}}. \quad (2.32)$$

The electron-plasmon coupling can then be found without further approximations from Eq. 2.30 as

$$|a_{\mathbf{q}}|^2 = \frac{1}{2}\omega_{\mathbf{q}} (V(\mathbf{q}) - W_{\mathbf{q}}(\omega = 0)). \quad (2.33)$$

Substituting the bare Coulomb interaction of the 2D free electron gas  $V(\mathbf{q}) = 2\pi e^2/(A\varepsilon q)$  as well as its DOS  $N_0 = Am^*/(2\pi)$ , and expanding around  $\mathbf{q} = 0$  gives

$$\omega_{\mathbf{q}} \approx \sqrt{\frac{2\pi g e^2 n}{\varepsilon m^*}} q \propto \sqrt{q} \quad (2.34)$$

$$|a_{\mathbf{q}}|^2 \approx \frac{1}{2}\omega_{\mathbf{q}} V(\mathbf{q}) \propto \frac{1}{\sqrt{q}}, \quad (2.35)$$

where  $n = E_F N_0/A$  is the electron density. We find that in the long-wavelength limit the plasmon dispersion has a square-root dependence on  $\mathbf{q}$  and that the electron-plasmon coupling has an inverse square-root dependence on  $\mathbf{q}$ . These are characteristic features of the 2D free electron gas plasmon mode. In contrast, in the 3D free electron gas the plasmon dispersion will tend towards the classical plasma frequency  $\omega_{\mathbf{q} \rightarrow 0} \rightarrow \omega_{pl}$  in the long-wavelength limit. [9] Furthermore, because the square-root structure of 2D plasmons is derived in the small  $\mathbf{q}$  limit, most 2D

materials which can be approximated by a Fermi liquid around the Fermi energy will have a plasmon dispersion of this form. [9] Even weakly doped graphene, which has a linearly dispersing electron dispersion around the Fermi level, has a plasmon dispersion which is proportional to  $\sqrt{q}$ . [5]

### 2.3.2 Normal State Renormalization

Once we have calculated the screened interaction  $W$ , we can evaluate the  $G_0W_0$  self-energy by simply substituting  $G^{(0)}$  for  $G$  in Eq. 2.23

$$\Sigma_{ab}(\mathbf{k}, i\omega_n) = -\frac{1}{\beta} \sum_{\mathbf{k}', n'} \sum_{cd} W_{acdb}(\mathbf{k} - \mathbf{k}', i\omega_n - i\omega_{n'}) G_{cd}^{(0)}(\mathbf{k}', i\omega_{n'}). \quad (2.36)$$

The dressed Green's function in  $G_0W_0$  is finally obtained using the Dyson equation (Eq. 2.14). A more physically intuitive picture arises when we substitute the spectral representation of  $W$  (Eq. 2.28). In this case we can perform the Matsubara sum analytically, yielding in the density-density approximation

$$\begin{aligned} \Sigma_{ab}(\mathbf{k}, i\omega_n) = & - \sum_{\mathbf{k}'} \sum_i T_{ai}(\mathbf{k}') T_{ib}^\dagger(\mathbf{k}') V_{aabb}(\mathbf{k} - \mathbf{k}') n_F(\xi_{\mathbf{k}', i}) \\ & + \sum_{\mathbf{k}'} \sum_i \int_{-\infty}^{\infty} d\omega T_{ai}(\mathbf{k}') T_{ib}^\dagger(\mathbf{k}') B_{aabb}(\mathbf{k} - \mathbf{k}', \omega) \frac{n_B(\omega) + n_F(\xi_{\mathbf{k}', i})}{i\omega_n + \omega - \xi_{\mathbf{k}', i}}. \end{aligned} \quad (2.37)$$

The electron dispersion in the band basis  $\xi_{\mathbf{k}, i}$  and the corresponding transformation matrices  $\hat{T}$  are defined in Eq. 2.26. In the (single-orbital) PPA the  $G_0W_0$  self-energy simplifies further to

$$\begin{aligned} \Sigma(\mathbf{k}, i\omega_n) = & - \sum_{\mathbf{k}'} V(\mathbf{k} - \mathbf{k}') n_F(\xi_{\mathbf{k}'}) \\ & + \sum_{\mathbf{q}} |a_{\mathbf{q}}|^2 \left( \frac{n_B(\omega_{\mathbf{q}}) + n_F(\xi_{\mathbf{k}-\mathbf{q}})}{i\omega_n + \omega_{\mathbf{q}} - \xi_{\mathbf{k}-\mathbf{q}}} + \frac{n_B(\omega_{\mathbf{q}}) + 1 - n_F(\xi_{\mathbf{k}-\mathbf{q}})}{i\omega_n - \omega_{\mathbf{q}} - \xi_{\mathbf{k}-\mathbf{q}}} \right). \end{aligned} \quad (2.38)$$

This expression will be useful for analyzing the  $G_0W_0$  results and for analytical derivations based on the  $G_0W_0$  approximation.

The first term of the  $G_0W_0$  self-energy is simply the Fock self-energy, which together with the Hartree potential forms the Hartree-Fock approximation. It captures the redistribution of electrons due to the static mean field of all other electrons. As such, it is frequency independent and only causes shifts in the occupied non-interacting electron states.

The second term captures the retardation effects induced by screening. It can be understood as the effect of the plasmons on the normal state. Due to its frequency

dependence, it can cause an additional pole to appear in the dressed Green's function, which induces an additional 'shakeoff band' in the spectral function below the conduction band minimum. This new state reflects the excitation of a quasi-particle consisting of a coupled electron-plasmon mode, which is often called a plasmaron in the literature. [76–79] Plasmarons were originally thought to have been observed in graphene [76, 77, 80–83], but after further works that investigated the effect of vertex corrections, it is now understood that the plasmaron is actually an artifact of the  $G_0W_0$  approximation. [78, 79] Instead, the shakeoff bands observed in graphene, as well as in other two-dimensional materials [61], originate from incoherent plasmon polaron excitations, consisting of electrons dressed by a cloud of plasmon excitations. [52, 53, 61, 78, 79, 84, 85]

The plasmon polaron shakeoff bands can be described correctly by the  $G_0W_0$  approximation in the limit of a dense electron gas with weak electron-plasmon coupling. However, as the electron density is reduced and/or the electron-plasmon coupling is enhanced, one at some point requires a theory that includes vertex corrections. The exact regime of validity of  $G_0W_0$  is not known, but some signatures that vertex corrections are important are that the energy splitting  $\Delta E$  of the shakeoff band is overestimated compared to experiments, or when multiple shakeoff bands are observed below the conduction band minimum. [52, 78, 84] One theory which can include vertex corrections is the GW+cumulant approach, which we will discuss in the next section.

### 2.3.3 *GW + Cumulant Theory*

As mentioned in the previous section, the GWA is known to work well for the corrections to the electron quasi-particle bands beyond the LDA, but it generally fails in the description of shakeoff bands. While  $G_0W_0$  can yield a single shakeoff band, this shakeoff band often has an overestimated binding energy and intensity. [38, 52, 53, 84] Furthermore, experimentally one observes a whole cascade of shakeoff bands, each separated by the binding energy  $\Delta E$ . These can be interpreted as electrons dressed by multiple boson modes at once, yielding excitations at energies  $n \times \Delta E$  below the conduction band minimum, where  $n$  is the number of coupled boson modes.

To go beyond the GWA one needs to include vertex corrections. There are various methods which achieve this, including, but not limited to, the GWT methods [41], local field effects in the Kukkonen and Overhauser (KO) approximation [86, 87] and excitonic corrections using the Bethe-Salpeter Equation (BSE) [88] or T-matrix approaches [89]. The method of interest in this section, however, is the GW+cumulant approach. [52, 53, 84] This method was shown to accurately reproduce shakeoff bands, with binding energies and intensities comparable to those measured in experiments, for a variety of materials including elemental Na and



Al [52], silicon [85, 90, 91] as well as various 2D materials such as graphene [90] and monolayer TMDCs [61]. The GW+cumulant method is based on an exponential cumulant expansion of the Green's function, which is motivated by the spectrum of 3D core-electrons coupled to bosonic modes, in which case the electronic spectral function can be evaluated analytically and has an exponential form. [92, 93] In fact, for 3D core-electrons the GW+cumulant method is exact. [38] It was furthermore shown that an exponential form of the Green's function implies that there are dynamical vertex correction terms included in the self-energy. [78] There is, however, no formal proof for the correctness of the ansatz in the cumulant expansion.

One of the main benefits of the GW+cumulant method is that it is rather lightweight, such that it can be done after a G<sub>0</sub>W<sub>0</sub> calculation without much additional computational complexity. We further note that the cumulant method is not restricted to Coulomb induced shakeoff bands. It can also be used in combination with the Fan-Migdal self-energy or with the Fröhlich self-energy to describe phonon-induced Fröhlich polarons. [94] In this section we will derive the main equations of the retarded GW+cumulant formalism by Kas *et al.* [84] To this end, we will closely follow Refs. [52] and [84], which is why the derivations are done in real time and real frequencies.

Unlike the many-body perturbation theory we discussed at the beginning of this chapter, the cumulant expansion is a perturbative theory directly in the Green's function itself. It is given by the following exponential ansatz for the real-time Green's function

$$\begin{aligned} G(\mathbf{k}, t) &= G^{(0)}(\mathbf{k}, t)e^{C(\mathbf{k}, t)} \\ &= G^{(0)}(\mathbf{k}, t) + G^{(0)}(\mathbf{k}, t)C(\mathbf{k}, t) + \frac{1}{2}G^{(0)}(\mathbf{k}, t)C(\mathbf{k}, t)^2 + \mathcal{O}(C^3), \end{aligned} \quad (2.39)$$

where  $C(\mathbf{k}, t)$  is the cumulant function which we aim to find. We compare the cumulant expansion to the usual self-energy expansion

$$\begin{aligned} G(\mathbf{k}, t) &= G^{(0)}(\mathbf{k}, t) \\ &+ \mathcal{FT} \left( G^{(0)}(\mathbf{k}, \omega) \Sigma(\mathbf{k}, \omega) G^{(0)}(\mathbf{k}, \omega) \right) \\ &+ \mathcal{FT} \left( G^{(0)}(\mathbf{k}, \omega) \Sigma(\mathbf{k}, \omega) G^{(0)}(\mathbf{k}, \omega) \Sigma(\mathbf{k}, \omega) G^{(0)}(\mathbf{k}, \omega) \right) \\ &+ \mathcal{O}(\Sigma^3), \end{aligned} \quad (2.40)$$

where we used Fourier transforms (denoted by  $\mathcal{FT}$ ) to avoid convolutions on the time axis. Since up to first order in the interaction the G<sub>0</sub>W<sub>0</sub> self-energy is exact (barring the Hartree term), we require the two expansions to be equivalent up to first order. This leads to the requirement

$$G^{(0)}(\mathbf{k}, t)C(\mathbf{k}, t) = \mathcal{FT} \left( G^{(0)}(\mathbf{k}, \omega) \Sigma(\mathbf{k}, \omega) G^{(0)}(\mathbf{k}, \omega) \right), \quad (2.41)$$

from which we find an expression for the cumulant function by inverting the bare Green's function

$$C(\mathbf{k}, t) = ie^{-i(-\epsilon_{\mathbf{k}} + \mu + i\delta)t} \int_{-\infty}^{\infty} \frac{d\omega}{2\pi} e^{-i\omega t} G^{(0)}(\mathbf{k}, \omega) \Sigma(\mathbf{k}, \omega) G^{(0)}(\mathbf{k}, \omega), \quad (2.42)$$

where we assumed  $t > 0$ . We then split the self-energy into its static and dynamic parts, i.e.  $\Sigma(\mathbf{k}, \omega) = \Sigma^{\text{stat}}(\mathbf{k}) + \Sigma^{\text{dyn}}(\mathbf{k}, \omega)$ , which allows us to split the cumulant as well  $C(\mathbf{k}, t) = C^{\text{stat}}(\mathbf{k}, t) + C^{\text{dyn}}(\mathbf{k}, t)$ . The cumulant from the static part of the self-energy can be evaluated using contour integration as

$$C^{\text{stat}}(\mathbf{k}, t) = i\Sigma^{\text{stat}}(\mathbf{k}) \int_{-\infty}^{\infty} \frac{d\omega}{2\pi} \frac{e^{-i(\omega - \epsilon_{\mathbf{k}} + \mu + i\delta)t}}{(\omega - \epsilon_{\mathbf{k}} + \mu + i\delta)^2} = -i\Sigma^{\text{stat}}(\mathbf{k})t, \quad (2.43)$$

yielding exactly the Fock contribution of  $G_0W_0$  theory. The dynamic part can be simplified by writing the self-energy in the spectral representation

$$\Sigma^{\text{dyn}}(\mathbf{k}, \omega) = \int_{-\infty}^{\infty} d\omega' \frac{\beta_{\mathbf{k}}(\omega' - \epsilon_{\mathbf{k}} + \mu)}{\omega - \omega' + i\delta}, \quad (2.44)$$

where we defined

$$\beta_{\mathbf{k}}(\omega) = \frac{1}{\pi} |\text{Im}(\Sigma^{\text{dyn}}(\mathbf{k}, \omega + \epsilon_{\mathbf{k}} - \mu))|. \quad (2.45)$$

Substituting this into Eq. 2.42 and shifting the integration variables  $\omega^{(i)} \rightarrow \omega^{(i)} + \epsilon_{\mathbf{k}} - \mu$  yields

$$C^{\text{dyn}}(\mathbf{k}, t) = i \int_{-\infty}^{\infty} \frac{d\omega}{2\pi} \int_{-\infty}^{\infty} d\omega' e^{-i(\omega + i\delta)t} \frac{1}{(\omega + i\delta)^2} \frac{\beta_{\mathbf{k}}(\omega')}{\omega - \omega' + i\delta}. \quad (2.46)$$

For clarity we extract the  $\omega$  integral

$$I(\omega', t) = \int_{-\infty}^{\infty} d\omega e^{-i(\omega + i\delta)t} \frac{1}{(\omega + i\delta)^2} \frac{1}{\omega - \omega' + i\delta}, \quad (2.47)$$

which is evaluated using contour integration techniques. We identify two poles: a simple pole at  $\omega_1 = \omega' - i\delta$  and a second-order pole at  $\omega_2 = -i\delta$ . The respective residues are

$$R_1 = \lim_{\omega \rightarrow \omega_1} (\omega - \omega_1) f(\omega) = \frac{1}{(\omega')^2} e^{-i\omega't}$$

$$R_2 = \lim_{\omega \rightarrow \omega_2} \frac{d}{d\omega} (\omega - \omega_2)^2 f(\omega) = i \frac{t}{\omega'} - \frac{1}{(\omega')^2},$$

where  $f(\omega)$  is the integrant. From the residue theorem we find the integral as

$$I(\omega', t) = -2\pi i (R_1 + R_2) = -\frac{2\pi i}{(\omega')^2} \left( e^{-i\omega't} + i\omega't - 1 \right), \quad (2.48)$$

where the additional negative sign comes from the inversion of the integration boundaries due to the poles being on the negative side of the imaginary axis. Substituting this integral back into Eq. 2.46 and relabeling  $\omega'$  as  $\omega$  yields the result from Ref. [84]

$$C^{\text{dyn}}(\mathbf{k}, t) = \int_{-\infty}^{\infty} d\omega \frac{\beta_{\mathbf{k}}(\omega)}{\omega^2} (e^{-i\omega t} + i\omega t - 1). \quad (2.49)$$

Numerically, the  $\omega = 0$  term in the integral has to be handled carefully due to cancelling singularities. By expanding the exponential function around  $\omega = 0$  we find that the integrand at this point is  $-t^2\beta_{\mathbf{k}}(\omega = 0)/2$ . The dressed Green function in the cumulant approximation is finally found by substituting  $C(\mathbf{k}, t)$  back into Eq. 2.39

$$G(\mathbf{k}, t) = -i\Theta(t > 0)e^{i(-\varepsilon_{\mathbf{k}} + \mu - \Sigma_{\mathbf{k}}^{\text{stat}} + i\delta)t} e^{C_{\mathbf{k}}^{\text{dyn}}(t)}. \quad (2.50)$$

We can get some physical intuition by separating the parts of  $C^{\text{dyn}}(\mathbf{k}, t)$  which do and do not oscillate in time. To that end we define

$$O_{\mathbf{k}}(t) = \int_{-\infty}^{\infty} d\omega \frac{\beta_{\mathbf{k}}(\omega)}{\omega^2} e^{-i\omega t}, \quad (2.51)$$

$$\Delta_{\mathbf{k}} = \int_{-\infty}^{\infty} d\omega \frac{\beta_{\mathbf{k}}(\omega)}{\omega} = -\text{Re} \left( \Sigma_{\mathbf{k}}^{\text{dyn}}(\varepsilon_{\mathbf{k}} - \mu) \right), \quad (2.52)$$

$$a_{\mathbf{k}} = \int_{-\infty}^{\infty} d\omega \frac{\beta_{\mathbf{k}}(\omega)}{\omega^2}, \quad (2.53)$$

$$Z_{\mathbf{k}} = e^{-a_{\mathbf{k}}}, \quad (2.54)$$

such that

$$C^{\text{dyn}}(\mathbf{k}, t) = O_{\mathbf{k}}(t) + i\Delta_{\mathbf{k}}t - a_{\mathbf{k}}. \quad (2.55)$$

Substituting this expression into Eq. 2.50 to obtain the cumulant Green's function yields

$$G(\mathbf{k}, t) = -iZ_{\mathbf{k}}\Theta(t > 0)e^{i(-\varepsilon_{\mathbf{k}} + \mu - \Sigma^{\text{stat}}(\mathbf{k}) + \Delta_{\mathbf{k}} + i\delta)t} e^{O_{\mathbf{k}}(t)}. \quad (2.56)$$

From this we learn that  $\Delta_{\mathbf{k}}$  shifts the quasiparticle dispersion, that  $Z_{\mathbf{k}}$  is the renormalization constant and that  $O_{\mathbf{k}}(t)$  is the oscillating part which induces the shakeoff bands.

To illustrate the appearance of shakeoff bands, we consider the extreme forward scattering limit, i.e.  $|a_{\mathbf{q}}|^2 \approx |a|^2\delta(\mathbf{q})$ , of the G<sub>0</sub>W<sub>0</sub> self-energy in the PPA (Eq. 2.38). We also take the limit of zero temperature and only consider occupied states, such that the dynamic part of the self-energy is given by

$$\Sigma^{\text{dyn}}(\mathbf{k}, \omega) = \frac{|a|^2}{\omega + i\delta + \omega_p - \varepsilon_{\mathbf{k}} + \mu}. \quad (2.57)$$

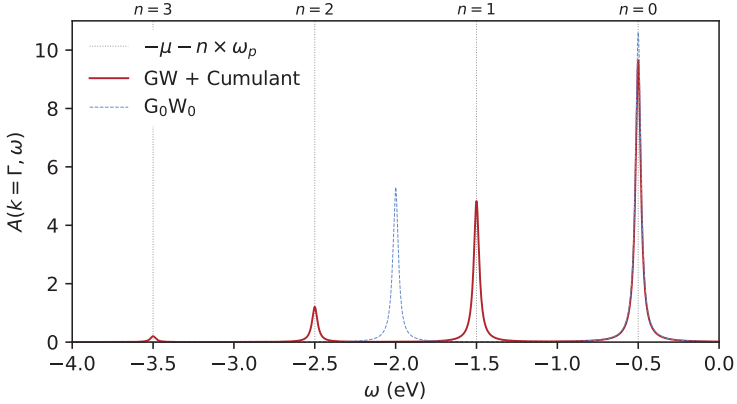


Figure 2.6: A representative example of the dressed spectral function  $A(\mathbf{k}, \omega)$  of a free-electron gas, evaluated at  $\mathbf{k} = \Gamma$  using the extreme forward scattering self-energy given by Eq. 2.57. The solid red line denotes the GW+cumulant approximation, the dashed blue line represents the  $G_0W_0$  approximation and the vertical dotted lines denote  $\omega = -\mu - n \times \omega_p$ , for  $n = 0 \dots 3$ . These data were obtained for  $m^* = 0.5m_e$ ,  $\mu = 0.5 \text{ eV}$ ,  $|a|^2 = 0.5 \text{ eV}^2$  and  $\omega_p = 1 \text{ eV}$ . Delta functions are represented using Lorentzian broadening, with  $\delta = 0.02 \text{ eV}$ .

Here  $\omega_p$  is some effective plasmon frequency. The oscillating part is now trivially given by  $O(t) = |a|^2 \exp(i\omega_p t) / \omega_p^2$ . Expanding Eq. 2.56 in terms of  $O(t)$  and Fourier transforming leads to the following spectral function [52]

$$A(\mathbf{k}, \omega) = Z \sum_{n=0}^{\infty} \frac{1}{n!} \left( \frac{|a|^2}{\omega_p^2} \right)^n \delta(\omega - \varepsilon_{\mathbf{k}} + \mu - \Sigma^{\text{stat}}(\mathbf{k}) + \Delta + n\omega_p), \quad (2.58)$$

where  $\Delta = -|a|^2 / \omega_p$  and  $Z = \exp(-|a|^2 / \omega_p^2)$ . We show  $A(\mathbf{k} = \Gamma, \omega)$  in Fig. 2.6, together with the corresponding result in the  $G_0W_0$  approximation (obtained by substituting Eq. 2.57 into the Dyson equation). The  $n = 0$  term simply yields the quasi-particle peak also predicted by  $G_0W_0$  theory. Higher orders of  $n$  give a cascade of shakeoff features which appear at energies in multiples of  $\omega_p$  below the conduction band minimum. Each of these peaks represents a plasmon polaron excitation, consisting of a single electron dressed by a cloud of  $n$  plasmon states. Peaks further away from the conduction band minimum are suppressed by the factor  $1/n!$ , indicating the reduced probability of exciting plasmon polarons with multiple plasmon modes. On the other hand, the  $G_0W_0$  approximation predicts only a single shakeoff feature, which is furthermore located in between multiples  $\omega_p$  below the conduction band minimum.

## 2.4 2D COULOMB INTERACTIONS

In the previous sections we discussed theories that describe how Coulomb interactions affect the normal state. In this section we will discuss the starting point for such calculations, namely the Coulomb matrix elements  $V_{abcd}(\mathbf{k}, \mathbf{k}', \mathbf{q})$  and the basis they are defined in. For the non-interacting electronic term of the Hamiltonian, the most natural basis is the Bloch basis, because we immediately have access to the band energies  $\xi_{\mathbf{k},i}$ . When including electron-electron terms, however, it is more intuitive to use a local basis, as used for example to define the (extended) Hubbard model. A particularly convenient local basis are Wannier functions, which are highly localized atomic-like orbitals. [29, 30, 95–97] They are especially popular in the ab-initio downfolding community, because the Wannier basis allows to define an effective low-energy tight-binding model which reproduces a subset of non-interacting bands around the Fermi energy. From there, downfolding methods are used to define effective (interacting) models within this low-energy subspace, such that computationally demanding computations can be performed on a significantly smaller low-energy subspace only.

In this section we will first derive the Coulomb matrix elements in a local basis. Then, we will briefly describe the constrained random phase approximation (cRPA), which is a downfolding method used to obtain effective Coulomb matrix elements in the low-energy subspace. [30] Finally, we will discuss the Wannier function continuum electrostatics (WFCE) approach [98], which is a method for augmenting 2D Coulomb matrix elements to include screening effects from the surrounding materials. For a more in-depth discussion on downfolding methods or on the cRPA, we refer the reader to Refs. [29, 30, 97].

### 2.4.1 2D Coulomb Matrix Elements in a Local Basis

The most general form of the Coulomb matrix elements in a local orbital basis is

$$V_{abcd}(\mathbf{k}, \mathbf{k}', \mathbf{q}) = \langle \phi_{a\mathbf{k}+\mathbf{q}}(\mathbf{r}) | \langle \phi_{c\mathbf{k}'-\mathbf{q}}(\mathbf{r}') | V(\mathbf{r}, \mathbf{r}') | \phi_{d\mathbf{k}'}(\mathbf{r}') \rangle | \phi_{b\mathbf{k}}(\mathbf{r}) \rangle, \quad (2.59)$$

with  $V(\mathbf{r}, \mathbf{r}') = e^2/|\mathbf{r} - \mathbf{r}'|$  the bare Coulomb potential. The Bloch states are defined by

$$\phi_{a\mathbf{k}}(\mathbf{r}) = \sum_{\mathbf{R}} e^{i\mathbf{k}\mathbf{R}} w_a(\mathbf{R}, \mathbf{r}). \quad (2.60)$$

Here the new basis function  $w_a(\mathbf{R}, \mathbf{r})$  is an atomic-like wave function, which we assume to be localized within the unit cell  $\mathbf{R}$ . For material realistic calculations these basis functions are often taken to be maximally localized Wannier functions [29, 95, 96], but for model calculations we might assume a completely local delta-

function instead. In either case, we assume that  $w_a(\mathbf{R}, \mathbf{r})$  has negligible overlap with the basis functions outside its unit-cell, such that

$$\begin{aligned}\phi_{a\mathbf{k}+\mathbf{q}}^*(\mathbf{r})\phi_{b\mathbf{k}}(\mathbf{r}) &= \sum_{\mathbf{R}, \mathbf{R}'} w_a^*(\mathbf{R}, \mathbf{r})w_b(\mathbf{R}', \mathbf{r})e^{i\mathbf{k}(\mathbf{R}'-\mathbf{R})}e^{-i\mathbf{q}\mathbf{R}} \\ &\approx \sum_{\mathbf{R}} w_a^*(\mathbf{R}, \mathbf{r})w_b(\mathbf{R}, \mathbf{r})e^{-i\mathbf{q}\mathbf{R}},\end{aligned}\quad (2.61)$$

which no longer depends on the momentum  $\mathbf{k}$ . Consequently, also the Coulomb matrix elements lose the dependence on the individual momenta  $\mathbf{k}$  and  $\mathbf{k}'$

$$V_{abcd}(\mathbf{q}) \approx \sum_{\mathbf{R}} \langle w_a(\mathbf{R}, \mathbf{r}) | \langle w_c(\mathbf{0}, \mathbf{r}') | V(\mathbf{r}, \mathbf{r}') | w_d(\mathbf{0}, \mathbf{r}') \rangle | w_b(\mathbf{R}, \mathbf{r}) \rangle e^{-i\mathbf{q}\mathbf{R}}. \quad (2.62)$$

Finally, we employ the density-density approximation, in which we assume the terms with  $a = b$  and  $c = d$  dominate in the Coulomb interaction and neglect all other elements. This approximation is justified when the overlap of the basis functions between different orbitals is small. We arrive at

$$V_{aabb}(\mathbf{q}) \approx \sum_{\mathbf{R}} \int d\mathbf{r} \int d\mathbf{r}' |w_a(\mathbf{R}, \mathbf{r})|^2 |w_b(\mathbf{0}, \mathbf{r}')|^2 V(\mathbf{r}, \mathbf{r}') e^{-i\mathbf{q}\mathbf{R}}. \quad (2.63)$$

For model calculations, we might assume the basis functions  $w_a(\mathbf{R}, \mathbf{r})$  to be completely localized, such that  $|w_a(\mathbf{R}, \mathbf{r})|^2 \approx \delta(\mathbf{R} + \boldsymbol{\tau}_a - \mathbf{r})$ , with  $\boldsymbol{\tau}_a$  the location of orbital  $a$  within the unit cell. In this case

$$\begin{aligned}V_{aabb}(\mathbf{q}) &\approx \sum_{\mathbf{R}} \int d\mathbf{r} \int d\mathbf{r}' \delta(\mathbf{R} + \boldsymbol{\tau}_a - \mathbf{r}) \delta(\boldsymbol{\tau}_b - \mathbf{r}') V(\mathbf{r}, \mathbf{r}') e^{-i\mathbf{q}\mathbf{R}} \\ &= \sum_{\mathbf{R}} V(\mathbf{R} + \boldsymbol{\tau}_a, \boldsymbol{\tau}_b) e^{-i\mathbf{q}\mathbf{R}} \\ &= \sum_{\mathbf{R}} \frac{e^2}{|\mathbf{R} + \boldsymbol{\tau}_a - \boldsymbol{\tau}_b|} e^{-i\mathbf{q}\mathbf{R}},\end{aligned}\quad (2.64)$$

we end with the Fourier transform of the bare Coulomb potential. Evaluating this integral in 2D yields

$$V_{aabb}^{2D}(\mathbf{q}) \approx \frac{2\pi e^2}{Aq} e^{-i\mathbf{q}\boldsymbol{\tau}_{ab}} e^{-qd_{ab}}, \quad (2.65)$$

with  $\boldsymbol{\tau}_{ab}$  the in-plane vector connecting orbital  $a$  and  $b$  within the unit-cell, and  $d_{ab}$  the out-of-plane distance between orbital  $a$  and  $b$ . For the integration we approximated  $\sum_{\mathbf{R}} \approx 1/A \int d\mathbf{R}$ , where  $A$  is the unit-cell area.

#### 2.4.2 cRPA and Static Environmental Screening

The cRPA is a downfolding method used to construct the effective Coulomb interaction within a low-energy subset of bands. It takes into account the screening

from all the bands that are being integrated out in the downfolding procedure. To start the discussion, we separate the non-interacting band structure into a low-energy target space and a high-energy rest space. Correspondingly, the RPA polarization can be separated by splitting the sum over band indices in Eq. 2.25, such that

$$\Pi^{(0)}(\mathbf{q}, i\nu_m) = \Pi_{\text{target}}^{(0)}(\mathbf{q}, i\nu_m) + \Pi_{\text{rest}}^{(0)}(\mathbf{q}, i\nu_m), \quad (2.66)$$

where  $\Pi_{\text{target}}^{(0)}(\mathbf{q}, i\nu_m)$  includes only transitions within bands in the target space and all other transitions are captured in  $\Pi_{\text{rest}}^{(0)}(\mathbf{q}, i\nu_m)$ . The transitions in  $\Pi_{\text{rest}}^{(0)}$  have energies much larger than the Fermi energy, such that we might neglect the dynamics of the rest-space polarization, i.e.,  $\Pi_{\text{rest}}^{(0)}(\mathbf{q}, i\nu_m) \approx \Pi_{\text{rest}}^{(0)}(\mathbf{q})$ . The screened Coulomb interaction (in the density-density approximation for simplicity) can now be rewritten as [30]

$$\begin{aligned} \hat{W}(\mathbf{q}, i\nu_m) &\approx \left( \hat{\mathcal{I}} - \hat{V}(\mathbf{q})(\hat{\Pi}_{\text{target}}^{(0)}(\mathbf{q}, i\nu_m) + \hat{\Pi}_{\text{rest}}^{(0)}(\mathbf{q})) \right)^{-1} \hat{V}(\mathbf{q}) \\ &= \left( \hat{\mathcal{I}} - \hat{U}(\mathbf{q})\hat{\Pi}_{\text{target}}^{(0)}(\mathbf{q}, i\nu_m) \right)^{-1} \hat{U}(\mathbf{q}). \end{aligned} \quad (2.67)$$

The resulting expression is of the same form as  $W$  in the full RPA except that we use an effective bare ‘background screened’ Coulomb interaction  $U$ , which includes screening from the rest space. It is given by

$$\hat{U}(\mathbf{q}) = \left( \hat{\mathcal{I}} - \hat{V}(\mathbf{q})\hat{\Pi}_{\text{rest}}^{(0)}(\mathbf{q}) \right)^{-1} \hat{V}(\mathbf{q}) = \hat{\varepsilon}_{\text{back}}(\mathbf{q})^{-1} \hat{V}(\mathbf{q}). \quad (2.68)$$

In principle, one can obtain  $\hat{U}(\mathbf{q})$  from the full (DFT) band structure on a given momentum-mesh. However, in order to perform converged dynamic and non-local  $G_0W_0$  calculations in 2D, one often needs a prohibitively large momentum resolution to capture the long-wavelength behaviour of the 2D Coulomb interaction and plasmon dispersion. Furthermore, to consider environmental screening in this framework, one needs to explicitly take the environmental materials into account in the microscopic model. To remedy this, Rösner *et al.* proposed the Wannier function continuum electrostatics (WFCE) approach. [98] It is based on the realization that in the macroscopic long-wavelength limit, the dielectric function  $\varepsilon_{\text{back}}(\mathbf{q})$  can be expressed using classical electrostatics. The resulting equations can be fitted to a single bulk cRPA calculation in order to obtain the ab-initio parameters of the (analytic) electrostatic screening model. In this way, the Coulomb interaction  $U(\mathbf{q})$  can be determined for arbitrary momentum points  $\mathbf{q}$ , without having to perform computationally expensive cRPA calculations. In addition, the macroscopic dielectric function allows us to tune the effect of environmental screening, without having to perform additional cRPA calculations. Therefore, the WFCE formalism is ideal for model calculations incorporating the

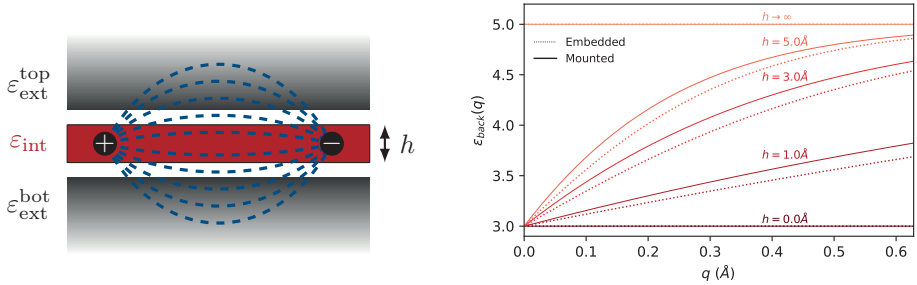


Figure 2.7: (Left) Schematic image of the slab configuration for the electrostatic screening model. The red box illustrates the thin slab with dielectric constant  $\epsilon_{\text{int}}$  and the black boxes illustrate the half-infinite substrates with dielectric constants  $\epsilon_{\text{ext}}^{\text{top}}$  and  $\epsilon_{\text{ext}}^{\text{bot}}$ . The blue dashed lines illustrate electric field lines between two charged particles (black dots). (Right) The background dielectric function  $\epsilon_{\text{back}}(\mathbf{q})$  for a variety of  $h$ , at  $\epsilon_{\text{int}} = 5$ . We consider a material which is mounted on a substrate with  $\epsilon_{\text{ext}}^{\text{bot}} = 5$  and vacuum above  $\epsilon_{\text{ext}}^{\text{top}} = 1$  (solid lines), and a material embedded from the top and bottom in a dielectric material with  $\epsilon_{\text{ext}} = (\epsilon_{\text{ext}}^{\text{top}} + \epsilon_{\text{ext}}^{\text{bot}})/2 = 3$  (dotted lines).

effect of screening from the environment, as well as screening from bands in the rest space.

For the electrostatic screening model, let us consider a slab of thickness  $h$  with internal dielectric constant  $\epsilon_{\text{int}}$  encapsulated from the top and bottom by half-infinite semi-conductors with respective dielectric constants  $\epsilon_{\text{ext}}^{\text{top}}$  and  $\epsilon_{\text{ext}}^{\text{bot}}$ , as illustrated in the left panel of Fig. 2.7. By solving the Poisson equation for such a system we find [98,99]

$$\epsilon_{\text{back}}(\mathbf{q}) = \epsilon_{\text{int}} \frac{1 - \beta_{\text{top}}\beta_{\text{bot}}e^{-2qh}}{1 + (\beta_{\text{top}} + \beta_{\text{bot}})e^{-qh} + \beta_{\text{top}}\beta_{\text{bot}}e^{-2qh}}, \quad (2.69)$$

where

$$\beta_{\text{top/bot}} = \frac{\epsilon_{\text{int}} - \epsilon_{\text{ext}}^{\text{top/bot}}}{\epsilon_{\text{int}} + \epsilon_{\text{ext}}^{\text{top/bot}}}. \quad (2.70)$$

$\epsilon_{\text{back}}(\mathbf{q})$  as a function of  $q$  is shown in the right panel of Fig. 2.7 for a variety of material thicknesses  $h$  (solid lines). In the long wavelength limit  $\epsilon_{\text{back}}(\mathbf{q} \rightarrow 0) = (\epsilon_{\text{ext}}^{\text{top}} + \epsilon_{\text{ext}}^{\text{bot}})/2$  the dielectric function yields the average dielectric constant of the environment, whereas for the short wavelength limit  $\epsilon_{\text{back}}(\mathbf{q} \rightarrow \infty) = \epsilon_{\text{int}}$  it gives the internal screening of the slab. For intermediate  $\mathbf{q}$ , the dielectric function interpolates between these two limits. For simplicity, one might approximately describe the dielectric environment with a single scalar  $\epsilon_{\text{ext}} \approx (\epsilon_{\text{ext}}^{\text{top}} + \epsilon_{\text{ext}}^{\text{bot}})/2$ , such that

$$\epsilon_{\text{back}}(\mathbf{q}) \approx \epsilon_{\text{int}} \frac{1 - \tilde{\epsilon}^2 e^{-2qh}}{1 + 2\tilde{\epsilon} e^{-qh} + \tilde{\epsilon}^2 e^{-2qh}}, \quad (2.71)$$



where  $\tilde{\epsilon} = (\epsilon_{\text{int}} - \epsilon_{\text{ext}})/(\epsilon_{\text{int}} + \epsilon_{\text{ext}})$ . This approximation is exact when  $\epsilon_{\text{ext}}^{\text{top}} = \epsilon_{\text{ext}}^{\text{bot}}$  and otherwise yields results which are qualitatively similar to the full expression, as shown by the dotted lines in the right panel of Fig. 2.7.

The classical expressions above are scalar functions, whereas the density-density Coulomb interaction is matrix valued. To remedy this, the WFCE argues that the electrostatic dielectric function above mainly alters the leading eigenvalue of the Coulomb interaction, whereas the subleading eigenvalues are approximately unchanged from those of the corresponding layered bulk material. [98] This can be understood by analyzing the eigenvectors of the diagonalization procedure, which show that the eigenvalues of the bare Coulomb interaction correspond to energies of effective generalized charge density waves. The charge density wave corresponding to the leading eigenvalue has the longest wavelength, such that it will be most sensitive to the dielectric environment. In this way, the WFCE can be used to obtain the effective Coulomb interaction in a 2D material from bulk calculations. Since this part of the WFCE is not explicitly used in this thesis we will not discuss it here, but further information can be found in the original work by M. Rösner *et al.* [98] Suffice to say, the WFCE has been shown to accurately describe two-dimensional Coulomb interactions from first principles in a variety of material systems. [98, 100–104]

## 2.5 SUPERCONDUCTIVITY

In 1950, Fröhlich derived an effective electron-electron interaction mediated by phonons by performing perturbation theory in the electron-phonon coupling strength. He found an expression of the form [33, 36, 105, 106]

$$V^{\text{ph,eff}}(\mathbf{k}, \mathbf{k}', \mathbf{q}) \approx g_{\mathbf{k},\mathbf{q}} g_{\mathbf{k}',-\mathbf{q}} \frac{2\omega_{\mathbf{q}}}{(\varepsilon_{\mathbf{k}'} - \varepsilon_{\mathbf{k}'-\mathbf{q}})^2 - \omega_{\mathbf{q}}^2}. \quad (2.72)$$

Importantly, this interaction can be negative and thus attractive when  $\varepsilon_{\mathbf{k}'} - \varepsilon_{\mathbf{k}'-\mathbf{q}} < \omega_{\mathbf{q}}$ . It was Bardeen, Schrieffer and Cooper, with their famous BCS theory, who first realized that this attraction between electrons could lead to the formation of bound electron pairs, which we now call Cooper pairs. [107] These Cooper pairs are bosonic quasi-particles, which means that they can condense into a single collective ground state. At low enough temperatures, scattering processes or energy fluctuations are not strong enough to overcome the binding energy  $\Delta$  of the Cooper pairs, such that there are no processes which can alter their kinetic energy. As a consequence, Cooper pairs can flow without resistance in this regime, which gives rise to the superconducting state.

### 2.5.1 BCS Theory

The BCS theory gives a microscopic understanding of superconductivity by treating the effective electron-electron interaction in the mean-field approximation. [107] In a conventional superconductor without an applied field, we can assume that the Cooper pairs have a vanishing total momentum. For simplicity we can therefore consider the following Hamiltonian, which captures the interaction between two electrons of opposite momentum

$$H = \sum_{\mathbf{k},\sigma} \varepsilon_{\mathbf{k}} c_{\mathbf{k}\sigma}^{\dagger} c_{\mathbf{k}\sigma} + \sum_{\mathbf{k},\mathbf{k}'} V^{\text{eff}}(\mathbf{k}, \mathbf{k}') c_{\mathbf{k}\uparrow}^{\dagger} c_{-\mathbf{k}\downarrow}^{\dagger} c_{-\mathbf{k}'\downarrow} c_{\mathbf{k}'\uparrow}, \quad (2.73)$$

where  $V^{\text{eff}}(\mathbf{k}, \mathbf{k}') = V^{\text{ph,eff}}(\mathbf{k}, -\mathbf{k}, \mathbf{k} - \mathbf{k}')$ . Defining a set of operators for the creation and annihilation of Cooper pairs

$$A_{\mathbf{k}}^{\dagger} = c_{\mathbf{k}\uparrow}^{\dagger} c_{-\mathbf{k}\downarrow}^{\dagger} \quad \text{and} \quad A_{\mathbf{k}} = c_{-\mathbf{k}\downarrow} c_{\mathbf{k}\uparrow}, \quad (2.74)$$

we can apply the usual mean-field approximation  $A_{\mathbf{k}}^{\dagger} A_{\mathbf{k}'} \approx A_{\mathbf{k}}^{\dagger} \langle A_{\mathbf{k}'} \rangle - \langle A_{\mathbf{k}}^{\dagger} \rangle A_{\mathbf{k}'} + \langle A_{\mathbf{k}}^{\dagger} \rangle \langle A_{\mathbf{k}'} \rangle$ . Substituting this back into the Hamiltonian above and neglecting any constant energy shifts we find the mean-field BCS Hamiltonian

$$H = \sum_{\mathbf{k},\sigma} \varepsilon_{\mathbf{k}} c_{\mathbf{k}\sigma}^{\dagger} c_{\mathbf{k}\sigma} + \sum_{\mathbf{k}} \left( \Delta_{\mathbf{k}} c_{\mathbf{k}\uparrow}^{\dagger} c_{-\mathbf{k}\downarrow}^{\dagger} + \Delta_{\mathbf{k}}^* c_{-\mathbf{k}\downarrow} c_{\mathbf{k}\uparrow} \right), \quad (2.75)$$

with the gap-function

$$\Delta_{\mathbf{k}} = \sum_{\mathbf{k}'} V^{\text{eff}}(\mathbf{k}, \mathbf{k}') \langle c_{-\mathbf{k}'\downarrow} c_{\mathbf{k}'\uparrow} \rangle. \quad (2.76)$$

The eigenvalues of the BCS Hamiltonian are given by  $E_{\mathbf{k}} = \pm \sqrt{\varepsilon_{\mathbf{k}}^2 + |\Delta_{\mathbf{k}}|^2}$ , from which we learn that a superconducting energy gap  $\Delta_{\mathbf{k}}$  opens around the Fermi energy. Using the eigenvectors of the BCS Hamiltonian we find a self-consistent expression for the gap-function

$$\Delta_{\mathbf{k}} = - \sum_{\mathbf{k}'} V^{\text{eff}}(\mathbf{k}, \mathbf{k}') \frac{\tanh(\beta E_{\mathbf{k}'}/2)}{2E_{\mathbf{k}'}} \Delta_{\mathbf{k}'}, \quad (2.77)$$

which is known as the BCS gap-equation. At temperatures  $T$  above the superconducting transition temperature  $T_c$ , the gap-equation only has the trivial solution  $\Delta_{\mathbf{k}} = 0$ . When  $T < T_c$  there are additional non-trivial solutions, such that the gap-function  $\Delta_{\mathbf{k}}$  can be understood as the order parameter of the superconducting phase.

A common approximation is to simplify the effective phonon-mediated interaction by a step function. It should be a negative constant  $-\lambda_{\text{BCS}}/N_0$  in the region where  $V^{\text{ph, eff}}$  is attractive and zero elsewhere

$$N_0 V^{\text{eff}}(\mathbf{k}, \mathbf{k}') \approx -\lambda_{\text{BCS}} \Theta(|\varepsilon_{\mathbf{k}}| < \omega_D) \Theta(|\varepsilon_{\mathbf{k}'}| < \omega_D), \quad (2.78)$$

where  $\omega_D$  is an effective phonon frequency,  $N_0$  is the DOS at the Fermi energy and  $\lambda_{\text{BCS}} = 2N_0 g^2 / \omega_D$  is the dimensionless phonon mediated coupling strength. Within this simple model the superconducting critical temperature and superconducting gap at  $T = 0$  K are readily found to be

$$k_B T_c \approx 1.13 \omega_D e^{-1/\lambda_{\text{BCS}}} \quad (2.79)$$

$$\Delta_{T=0} \approx 2 \omega_D e^{-1/\lambda_{\text{BCS}}}. \quad (2.80)$$

BCS theory, and its strong-coupling extension Eliashberg theory, have been used to describe a plethora of conventional superconductors. [108–114] Materials for which these theories break down are called unconventional superconductors, for example signified by a weak isotope effect or by the BCS ratio  $k_B T_c / \Delta_{T=0} \approx 0.57$  being violated. There is as-of-yet no general theory which can describe unconventional superconductivity, but a common suggestion for its origin is that it is not phonons, but other bosons that mediate the Cooper pairing. [115] For example, in many iron-based unconventional superconductors, spin fluctuations have been proposed as a promising candidate for the coupling. [116–118] In this thesis the focus is on the 2D Coulomb interaction, which gives rise to the non-local and dynamic screened Coulomb interaction  $W$  described in Sect. 2.3. As we have shown with

the PPA, the interaction can be split into a high-frequency repulsive term  $V(\mathbf{q}) = W(\mathbf{q}, i\nu_m \rightarrow \infty)$ , and an attractive low-frequency term  $\Delta W(\mathbf{q}, i\nu_m) = W(\mathbf{q}, i\nu_m) - V(\mathbf{q})$  induced by plasmons. The similarity of the attractive term to the conventional phonon-mediated electron-electron interaction, as well as the strong electron-plasmon coupling in the long-wavelength limit, hints at the possibility of plasmon-mediated superconductivity. [63–66, 68–72, 119–121] However, a complication in the description of 2D plasmons is the inherently non-local nature of the 2D plasmon mode due to its gapless  $\sqrt{q}$  dispersion in the long-wavelength limit. As a consequence, a theory which can capture both the non-locality and the dynamic nature of the Coulomb interaction is required to describe plasmon mediated superconductivity. We therefore need a theory that goes beyond the mean-field BCS theory.

### 2.5.2 One-Loop Theory

In the one-loop theory of superconductivity we essentially perform a GW calculation in the superconducting state. In this way we go beyond the mean-field approximation of BCS, allowing the treatment of a both non-local and dynamic interaction. Even more, the framework allows for a consistent treatment of multiple interactions, properly taking account their mutual screening in the RPA. We start the derivation by defining the spinors

$$\psi_{\mathbf{k}a}(\tau) = \begin{pmatrix} c_{\mathbf{k}a\uparrow}(\tau) \\ c_{-\mathbf{k}a\downarrow}^\dagger(\tau) \end{pmatrix}, \psi_{\mathbf{k}a}^\dagger(\tau) = \begin{pmatrix} c_{\mathbf{k}a\uparrow}^\dagger(\tau) & c_{-\mathbf{k}a\downarrow}(\tau) \end{pmatrix}, \quad (2.81)$$

which allow us to use the usual definition of the two-particle Green's function in the Nambu-Gor'kov formalism [122, 123]

$$\begin{aligned} \mathbf{G}_{ab}(\mathbf{k}, \tau) &= -\langle \mathcal{T} \psi_{\mathbf{k}a}(\tau) \psi_{\mathbf{k}b}^\dagger(0) \rangle \\ &= \begin{pmatrix} -\langle \mathcal{T} c_{\mathbf{k}a\uparrow}(\tau) c_{\mathbf{k}b\uparrow}^\dagger(0) \rangle & -\langle \mathcal{T} c_{\mathbf{k}a\uparrow}(\tau) c_{-\mathbf{k}b\downarrow}(0) \rangle \\ -\langle \mathcal{T} c_{-\mathbf{k}a\downarrow}^\dagger(\tau) c_{\mathbf{k}b\uparrow}^\dagger(0) \rangle & -\langle \mathcal{T} c_{-\mathbf{k}a\downarrow}^\dagger(\tau) c_{-\mathbf{k}b\downarrow}(0) \rangle \end{pmatrix} \\ &= \begin{pmatrix} G_{ab}(\mathbf{k}, \tau) & F_{ab}(\mathbf{k}, \tau) \\ F_{ab}^\dagger(\mathbf{k}, \tau) & -G_{ba}(-\mathbf{k}, -\tau) \end{pmatrix}, \end{aligned} \quad (2.82)$$

where we used a bold notation for matrices in the Nambu-Gor'kov basis and we assumed that the diagonal spin-up and spin-down Green's functions are equivalent. The off-diagonal elements are the anomalous propagators, defined as

$$F_{ab}(\mathbf{k}, \tau) = -\langle \mathcal{T} c_{\mathbf{k}a\uparrow}(\tau) c_{-\mathbf{k}b\downarrow}(0) \rangle. \quad (2.83)$$

Similarly, we define the bare Green's function and self-energy matrices in the Nambu-Gor'kov basis respectively as

$$\mathbf{G}_{ab}^{(0)}(\mathbf{k}, i\omega_n) = \begin{pmatrix} G_{ab}^{(0)}(\mathbf{k}, i\omega_n) & 0 \\ 0 & -G_{ba}^{(0)}(-\mathbf{k}, -i\omega_n) \end{pmatrix} \quad (2.84)$$

$$\Sigma_{ab}(\mathbf{k}, i\omega_n) = \begin{pmatrix} \Sigma_{ab}(\mathbf{k}, i\omega_n) & \phi_{ab}(\mathbf{k}, i\omega_n) \\ \phi_{ab}^*(\mathbf{k}, i\omega_n) & -\Sigma_{ba}(-\mathbf{k}, -i\omega_n) \end{pmatrix}, \quad (2.85)$$

such that we can write down the Dyson equation

$$\begin{aligned} \mathbf{G}_{ab}(\mathbf{k}, i\omega_n) &= \mathbf{G}_{ab}^{(0)}(\mathbf{k}, i\omega_n) + \sum_{cd} \mathbf{G}_{cb}^{(0)}(\mathbf{k}, i\omega_n) \Sigma_{dc}(\mathbf{k}, i\omega_n) \mathbf{G}_{ad}(\mathbf{k}, i\omega_n) \\ &= \left( \hat{\mathbf{G}}^{(0)}(\mathbf{k}, i\omega_n)^{-1} - \hat{\Sigma}(\mathbf{k}, i\omega_n) \right)_{ab}^{-1}. \end{aligned} \quad (2.86)$$

Performing the block-inversion in the Nambu-Gor'kov space yields expressions for the normal and anomalous propagators

$$G_{ab}(\mathbf{k}, i\omega_n) = \sum_c \hat{\Theta}(\mathbf{k}, i\omega_n)_{cb}^{-1} G_{ac}^{(e)}(\mathbf{k}, i\omega_n) \quad (2.87)$$

$$F_{ab}(\mathbf{k}, i\omega_n) = - \sum_{cde} \hat{\Theta}(\mathbf{k}, i\omega_n)_{cb}^{-1} G_{dc}^{(e)}(\mathbf{k}, i\omega_n) \phi_{ed}(\mathbf{k}, i\omega_n) G_{ea}^{(e)}(-\mathbf{k}, -i\omega_n), \quad (2.88)$$

where the denominator is given by

$$\Theta_{ab}(\mathbf{k}, i\omega_n) = \delta_{ab} + \sum_{cde} G_{cb}^{(e)}(\mathbf{k}, i\omega_n) \phi_{dc}(\mathbf{k}, i\omega_n) G_{de}^{(e)}(-\mathbf{k}, -i\omega_n) \phi_{ea}^*(\mathbf{k}, i\omega_n). \quad (2.89)$$

We defined  $G^{(e)}(\mathbf{k}, i\omega_n)$  as the dressed normal-state electronic Green's function

$$G_{ab}^{(e)}(\mathbf{k}, i\omega_n) = \left( \hat{\mathcal{I}}(i\omega_n + \mu) - \hat{h}^{(0)}(\mathbf{k}) - \hat{\Sigma}(\mathbf{k}, i\omega_n) \right)_{ab}^{-1}. \quad (2.90)$$

In the one-loop approximation we write the Nambu-Gor'kov self-energy in a GW-like form [26, 27, 33, 112, 124–126]

$$\Sigma_{ab}(\mathbf{k}, i\omega_n) = -\frac{1}{\beta} \sum_{\mathbf{k}', n'} \sum_{cd} \tau_3 \mathbf{G}_{cd}(\mathbf{k}', i\omega_{n'}) \tau_3 W_{acdb}(\mathbf{k} - \mathbf{k}', i\omega_n - i\omega_{n'}), \quad (2.91)$$

where  $\tau_3$  is the third Pauli matrix. In the community of electron-phonon interactions, this approximation of the self-energy is also known as the Fan-Migdal self-energy. [126] In the case of neglected Coulomb interactions, it is justified by Migdal's theorem, which states that vertex corrections are of the order  $(m_e/M)^{1/2} \propto \omega_e/E_F$  [26], where  $m_e/M$  is the ratio of the electron and ionic masses and  $\omega_e/E_F$  is the ratio of the characteristic phonon energy and the Fermi energy. Therefore,

in systems where  $\omega_e \gg E_F$  the one-loop self-energy approximation breaks down. When including Coulomb contributions, the one-loop self-energy has a less well-defined limit of applicability. Therefore, in chapter 7, we will introduce a formalism for quantifying the importance of corrections beyond the one-loop approximation in the presence of Coulomb interactions. For now, we assume that the one-loop self-energy holds as long as  $r_s > 1$ , similar to the GWA discussed in section 2.3. Performing the matrix products yields the usual GW self-energy (Eq. 2.23) for the diagonal components of  $\Sigma$  and

$$\phi_{ab}(\mathbf{k}, i\omega_n) = \frac{1}{\beta} \sum_{\mathbf{k}', n'} \sum_{cd} W_{acdb}(\mathbf{k} - \mathbf{k}', i\omega_n - i\omega_{n'}) F_{cd}(\mathbf{k}', i\omega_{n'}) \quad (2.92)$$

for the off-diagonal anomalous components. Substituting Eq. 2.88 finally gives the gap-equation for the one-loop superconductivity theory. Similar to the BCS theory, we only find non-trivial solutions of the gap-equation when  $T < T_c$ , such that  $\phi$  can be understood as the order parameter of the superconducting phase. Notably, when the interaction  $W$  has no frequency dependence, the BCS gap-equation (Eq. 2.77) with  $V^{\text{eff}}(\mathbf{k}, \mathbf{k}') = W(\mathbf{k} - \mathbf{k}')$  is recovered.

**LINEARIZATION** Solving the one-loop gap-equation is a rather involving calculation, since one needs to self-consistently solve a non-linear equation. Linearizing in the anomalous self-energy leads to a significant reduction of the computational cost, since it recasts the gap-equation into a leading eigenvalue problem. To this end, we assume that calculations are performed close to the superconducting phase transition. In this case, the anomalous self-energy (i.e., the order parameter) is small, such that we can neglect terms of  $\mathcal{O}(\phi^2)$  in the Dyson equation, yielding  $\Theta_{ab}(\mathbf{k}, i\omega_n) = \delta_{ab}$ , such that

$$G_{ab}(\mathbf{k}, i\omega_n) \approx G_{ab}^{(e)}(\mathbf{k}, i\omega_n) \quad (2.93)$$

$$F_{ab}(\mathbf{k}, i\omega_n) \approx - \sum_{cd} G_{cb}^{(e)}(\mathbf{k}, i\omega_n) \phi_{dc}(\mathbf{k}, i\omega_n) G_{da}^{(e)}(-\mathbf{k}, -i\omega_n). \quad (2.94)$$

Substituting the linearized  $F$  into Eq. 2.92 finally gives the linearized gap-equation for the one-loop superconductivity theory

$$\begin{aligned} \lambda(T) \phi_{ab}(\mathbf{k}, i\omega_n) = & -\frac{1}{\beta} \sum_{\mathbf{k}', n'} \sum_{cdef} W_{acdb}(\mathbf{k} - \mathbf{k}', i\omega_n - i\omega_{n'}) \\ & \times G_{ed}^{(e)}(\mathbf{k}', i\omega_{n'}) \phi_{fe}(\mathbf{k}', i\omega_{n'}) G_{fc}^{(e)}(-\mathbf{k}', -i\omega_{n'}). \end{aligned} \quad (2.95)$$

Here we introduced the factor  $\lambda(T)$  on the left-hand side. In this way, we have cast the linearized gap-equation into the form an an eigenvalue problem, with  $\phi$  being the eigenvector and  $\lambda(T)$  the leading eigenvalue. The temperature at which  $\lambda(T) = 1$  is the superconducting critical temperature  $T_c$ .

### 2.5.3 Eliashberg Theory

The one-loop theory described above is closely related to the well known Eliashberg theory for phonon-mediated superconductivity. [27, 28, 33, 125] Here, we will discuss the theory in the context of the one-loop theory discussed above, deriving only the relevant elements and highlighting the difference between the two theories. For a more complete discussion of Eliashberg theory we refer the reader to the Jülich lecture notes by Heid [33], the review article by Marsiglio [127] or the master thesis by Berges [128].

Eliashberg theory was developed for phonon-mediated superconductors and therefore heavily simplifies the Coulomb interaction. First of all, it neglects dynamic screening to the Coulomb interaction, as well as the mutual screening between the electron-phonon and electron-electron interactions. Second of all, the (bare) Coulomb potential is approximated by a local parameter  $\mu^C$ , which is usually defined by a projection of  $V(\mathbf{q})$  onto the Fermi surface. [109, 111, 129] Using these simplifications, the electron-electron interaction can be written as

$$N_0 W(\mathbf{q}, i\nu_m) \approx -\lambda^{\text{ph}}(\mathbf{q}, i\nu_m) + \mu^C, \quad (2.96)$$

with  $-\lambda^{\text{ph}}(\mathbf{q}, i\nu_m)$  the attractive phonon-induced electron-electron interaction. The DOS at the Fermi energy  $N_0$  was added to make the interaction dimensionless and we omitted the orbital indices for simplicity. In Eliashberg theory we furthermore assume that the bare electron dispersion  $\varepsilon_{\mathbf{k}}$  effectively includes the Coulomb induced normal-state renormalization, such that we can neglect the Coulomb contributions to the normal-state self-energy. Using those simplifications we can express Eliashberg theory as a set of three coupled equations known as the Eliashberg equations [112, 124, 128]

$$\phi(\mathbf{k}, i\omega_n) = \frac{1}{\beta N_0} \sum_{\mathbf{k}', n'} \frac{\lambda^{\text{ph}}(\mathbf{k} - \mathbf{k}', i\omega_n - i\omega_{n'}) - \mu^C}{\Theta(\mathbf{k}', i\omega_{n'})} \phi(\mathbf{k}', i\omega_{n'}) \quad (2.97)$$

$$Z(\mathbf{k}, i\omega_n) = 1 + \frac{1}{\beta N_0} \frac{1}{\omega_n} \sum_{\mathbf{k}', n'} \frac{\omega_{n'} \lambda^{\text{ph}}(\mathbf{k} - \mathbf{k}', i\omega_n - i\omega_{n'})}{\Theta(\mathbf{k}', i\omega_{n'})} Z(\mathbf{k}', i\omega_{n'}) \quad (2.98)$$

$$\chi(\mathbf{k}, i\omega_n) = -\frac{1}{\beta N_0} \sum_{\mathbf{k}', n'} \frac{\lambda^{\text{ph}}(\mathbf{k} - \mathbf{k}', i\omega_n - i\omega_{n'})}{\Theta(\mathbf{k}', i\omega_{n'})} (\varepsilon_{\mathbf{k}'} - \mu + \chi(\mathbf{k}', i\omega_{n'})), \quad (2.99)$$

where  $\Theta(\mathbf{k}, i\omega_n) = (\omega_n Z(\mathbf{k}, i\omega_n))^2 + (\varepsilon_{\mathbf{k}} - \mu + \chi(\mathbf{k}, i\omega_n))^2 + |\phi(\mathbf{k}, i\omega_n)|^2$ . The new quantities  $Z$  and  $\chi$  can be interpreted as the mass-renormalization factor and the chemical potential shift, respectively. Together they capture the phonon-induced normal-state renormalization coming from the one-loop self-energy, which can be expressed as  $\Sigma(\mathbf{k}, i\omega_n) = i\omega_n(1 - Z(\mathbf{k}, i\omega_n)) + \chi(\mathbf{k}, i\omega_n)$ .

While the Eliashberg equations are nowadays routinely solved numerically [130], this was not always doable in the past. Therefore, considerable work has been put into finding exact solutions to the Eliashberg equations under certain approximations. [108, 131–133] Now, we will use a few of those approximations and use them to derive an analytic BCS-like expression for  $T_c$ . The first approximation is to again linearize the gap-equation by neglecting terms of  $\mathcal{O}(\phi^2)$ . The second is to assume a constant DOS (i.e.,  $N(\varepsilon) \approx N_0$ ) in order to simplify the momentum sums. Lastly, we assume similarly to the BCS theory that the phonon-mediated electron-electron interaction is local and can be written as a step-function

$$\lambda^{\text{ph}}(i\omega_n - i\omega_{n'}) \approx \lambda_{\text{BCS}} \Theta(|\omega_n| < \omega_D) \Theta(|\omega_{n'}| < \omega_D). \quad (2.100)$$

With these approximations we find that the normal state renormalization simplifies heavily to  $Z \approx 1 + \lambda_{\text{BCS}}$  and  $\chi \approx 0$ . The gap-equation becomes

$$\phi(i\omega_n) = \frac{1}{\beta N_0} \sum_{\mathbf{k}', n'} \frac{\lambda^{\text{ph}}(i\omega_n - i\omega_{n'}) - \mu^C}{(\omega_{n'} Z)^2 + (\varepsilon_{\mathbf{k}} - \mu)^2} \phi(i\omega_{n'}). \quad (2.101)$$

From this expression it is clear that the superconducting state depends on two distinct energy scales. The low-energy physics  $|\omega_n| < \omega_D$  is dominated by the electron-phonon interaction  $\lambda_{\text{BCS}}$ , whereas the high energy physics  $|\omega_n| > \omega_D$  is dominated by Coulomb repulsion  $\mu^C$ . As a consequence, one needs a large amount of Matsubara frequencies to converge both regimes of the gap-equation. One can improve the convergence by introducing the Tolmachev-Morel-Anderson (TMA) pseudo-potential [109, 134]

$$\mu^* = \frac{\mu^C}{1 + \mu^C \log\left(\frac{E_B}{\omega_D}\right)}, \quad (2.102)$$

with  $E_B$  the bandwidth. It is derived by integrating out the high-energy physics, such that we are left with an effective gap-equation  $\phi$  for the low-energy physics

$$\phi = \frac{\lambda_{\text{BCS}} - \mu^*}{Z} \frac{\pi}{\beta} \sum_{|\omega_{n'}| < \omega_D} \frac{\phi}{|\omega_{n'}|}. \quad (2.103)$$

Analytically solving this gap-equation gives an expression for the critical temperature [108]

$$k_B T_c = 1.13 \omega_D \exp\left(-\frac{Z}{\lambda_{\text{BCS}} - \mu^*}\right). \quad (2.104)$$

This expression is reminiscent of the BCS result in Eq. 2.79, but includes additional effects. The critical temperature is still exponentially dependent on the coupling  $\lambda_{\text{BCS}}$ , but the coupling is effectively reduced by a constant  $\mu^*$ . Intuitively, this



reflects the competition between the phonon-mediated attraction and the Coulomb induced repulsion between electrons in a Cooper pair. Furthermore, the exponent is multiplied by a factor  $Z \approx 1 + \lambda_{\text{BCS}} > 1$ , which reduces the  $T_c$  due to the renormalization of the normal state.

## 2.6 DISCRETE LEHMAN REPRESENTATION

Phase transitions to correlated phases often occur at temperatures as low as a few Kelvin. Superconductivity, as discussed in the previous section, is one example of such a phase and of particular interest in this thesis. However, performing calculations at such low temperatures is challenging, due to the increasingly large Matsubara frequency point density as the temperature is reduced. To illustrate this, let us introduce a high-frequency cutoff energy  $\omega_c$  to the frequency axis, which is the most straightforward way to represent the Matsubara axis numerically. Since the Matsubara frequencies are given by odd or even multiples of  $2\pi/\beta$  for fermionic or bosonic quantities, respectively, we can determine the number of required Matsubara points for a given bosonic Matsubara mesh as

$$N_\omega = \text{round}(\beta\omega_c/\pi) \propto \mathcal{O}(\beta\omega_c), \quad (2.105)$$

and similarly for a fermionic mesh. We find that the amount of Matsubara points scales linearly with  $\beta$ . As a consequence, performing numerical Matsubara summations at lower temperatures quickly becomes prohibitively computationally expensive and/or numerical representations of Green's functions quickly become too memory intensive.

To circumvent this problem, significant effort has been put into finding more efficient ways to represent quantities on the Matsubara axis. Some examples include representing the Green's function by an orthogonal polynomial expansion, such as Chebyshev [135] or Legendre [136, 137] polynomials. These methods can improve the scaling to  $N_\omega = \mathcal{O}(\sqrt{\beta})$ . Other examples include power grid methods [138, 139], in which the imaginary time axis is discretized non-uniformly, with a higher point density around  $\tau = 0$  and  $\beta$ . Such methods can already improve the scaling to  $N_\omega = \mathcal{O}(\log(\beta))$ . Recently, a variety of methods have been proposed which exploit the physical structure of the Green's function to find even more compact representations. In this thesis the discrete Lehman representation (DLR) [140, 141] has been used such that we will focus on that, but related methods such as the intermediate representation (IR) [142–145] and the minimax isometry method [146] exist and have been used effectively. [147–151]

Any fermionic single-particle Green's function  $G$  can be expressed by a spectral representation Eq. 2.7, here Fourier transformed to the imaginary time axis

$$G(\tau) = \int_{-\infty}^{\infty} d\omega K(\tau, \omega) A(\omega), \quad (2.106)$$

with  $A(\omega)$  the spectral function and  $K(\tau, \omega) = -e^{-\omega\tau}/(1 + e^{-\beta\omega})$  the fermionic kernel. This expression yields a well-defined way to obtain the imaginary-time Green's function  $G(\tau)$  from the retarded real-time Green's function  $G(t)$ . However, the opposite procedure of obtaining  $G(t)$  from  $G(\tau)$ , known as analytic continuation,

is an infamously ill-defined problem. This is a consequence of the low rank of the fermionic kernel  $K$ . It is however exactly this property which can be exploited to find a compact representation of  $G$ . Numerically, we discretize the  $\tau$  and  $\omega$  axes and introduce a real-frequency cutoff energy  $\omega_c$ , such that we can write the spectral representation as a matrix-vector product

$$G_{\tau_i} = \sum_j \hat{K}_{\tau_i, \omega_j} A_{\omega_j}, \quad (2.107)$$

with the fermionic kernel  $\hat{K}_{\tau_i, \omega_i} = -e^{-\omega_i \tau_i} / (1 + e^{-\beta \omega_i})$ .

Shinaoka *et al.* [142] realized that, due to the low rank of  $\hat{K}$ , it is possible to construct an efficient orthogonal basis (the IR basis) for the Green's function by performing a singular value decomposition (SVD) of  $\hat{K}$ . While this procedure gives the mathematically optimal compression of the kernel  $\hat{K}$ , the resulting basis functions are complicated and known only numerically. The DLR, on the other hand, uses the interpolative decomposition (ID) instead of a SVD. The resulting basis is slightly less compact than the IR, but has the advantage that its basis functions are given by analytical exponentials

$$G_{\tau_i} \approx \sum_{k=1}^r \frac{e^{-\omega_k \tau_i}}{1 + e^{-\beta \omega_k}} g_k. \quad (2.108)$$

Here  $\omega_k$  is a subset of  $r$  optimal real-frequencies which has to be determined numerically, and  $g_k$  is the compressed representation of the Green's function  $G_{\tau_i}$ . The real-frequencies  $\omega_k$  have been chosen in such a way that we only need to know  $G_{\tau_i}$  on a subset of  $r$  imaginary time points in order to obtain  $g_k$ . These points, denoted by  $\tau_k$ , are called the interpolation nodes. Equivalently, one can obtain  $g_k$  by evaluating the Matsubara Green's function  $G(i\omega_n)$  on a subset of Matsubara frequency interpolation nodes  $i\omega_{n_k}$ . Therefore, a common procedure when using the DLR is the following: first evaluate the Green's function only on the interpolation nodes  $\tau_k$  or  $i\omega_{n_k}$ , then invert Eq. 2.108 (or a similar expression for the Matsubara axis) to obtain  $g_k$ , and finally interpolate the Green's function for any imaginary time point or Matsubara frequency by evaluating

$$G(\tau) \approx \sum_{k=1}^r \frac{e^{-\omega_k \tau}}{1 + e^{-\beta \omega_k}} g_k \quad (2.109)$$

$$G(i\omega_n) \approx \sum_{k=1}^r \frac{1}{i\omega_n - \omega_k} g_k. \quad (2.110)$$

The problem, then, is to determine the optimal subset of real-frequencies  $\omega_k$  and interpolation nodes  $\tau_k$  and  $i\omega_{n_k}$ . The procedure is rather mathematical such that we will not discuss it here, but it can be found in the original work. [140] It turns

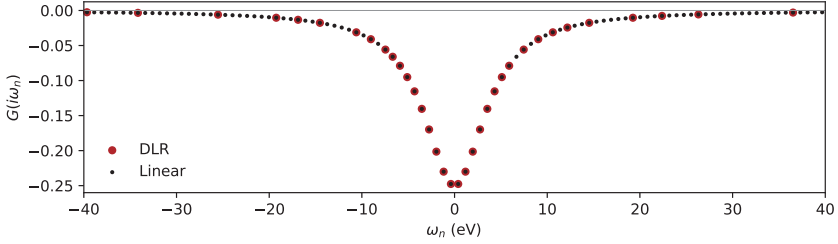


Figure 2.8: Comparison of the full Matsubara frequency point density and the point density in the DLR, for a fermionic Green's function  $G(i\omega_n) = (i\omega_n - 4 \text{ eV})^{-1}$ . The black dots denote the full Matsubara axis, whereas the red dots denote the DLR interpolation nodes  $i\omega_{n_k}$ . This data has been obtained for  $\beta = 8 \text{ eV}^{-1}$ ,  $\omega_c = 100 \text{ eV}$  and  $\epsilon = 10^{-10}$ .

out that the optimal sets do not depend on the Green's function itself, only on the properties of the mesh. As a consequence, the algorithm for finding the optimal subsets has to be done only once and may be pre-computed. Furthermore, the size of the optimal subsets scale as  $r \propto \mathcal{O}(\log(\beta\omega_c)\log(1/\epsilon))$ , where  $\epsilon$  is the accuracy with which the DLR reproduces the original Green's function. In other words, for a given accuracy  $\epsilon$  and high-energy cutoff  $\omega_c$ , the DLR allows to represent the full imaginary time axis using  $\mathcal{O}(\log(\beta))$  elements. This is possible because the interpolation nodes are logarithmically distributed around the  $i\omega_{n=0}$  point ( $\tau = 0$  and  $\tau = \beta$  points) of the Matsubara (imaginary time) axis, as shown in Fig. 2.8.

DLR implementations are publicly available for Fortran (libdlr) [152], Julia (NumericalEFT) [153] and c++ (cppdlr) [154], with most of them also having Python interfaces. In this thesis we will be using the cppdlr library, since it is integrated in the TRIQS framework. [155]

## BRIEF OVERVIEW OF RELEVANT MATERIALS

---

In this chapter we will highlight two specific 2D material classes which are of particular interest for this thesis: graphene and transition metal dichalcogenides (TMDCs). These materials are often combined together, forming van-der-Waals heterostructures. [10–12] As we will explore in chapter 4, such layered systems can give rise to exciting new physics.

### 3.1 GRAPHENE

Graphene is famously the first 2D material ever fabricated. It is a zero-overlap semimetal, where the low-energy electron dispersion is given by two linearly dispersing bands that cross at the Fermi energy. This unusual band structure makes graphene stand out among the class of 2D materials, leading to various intriguing phenomena including Klein tunneling [5, 156, 157] or the half-integer quantum Hall effect [3, 5, 158, 159]. The atomic lattice of graphene consists of carbon atoms bound in a hexagonal pattern, shown in Fig. 3.1. This strong carbon-carbon bond makes graphene one of the strongest materials, while at the same time being flexible and having exceptionally high electrical and thermal conductivities. [1, 3] Due to these particular properties graphene is still extensively studied today, especially in combination with other materials, for example in 2D heterostructures.

The unit cell vectors of graphene are

$$\mathbf{a}_1 = \frac{a}{2} \begin{pmatrix} 3 \\ \sqrt{3} \end{pmatrix} \quad \text{and} \quad \mathbf{a}_2 = \frac{a}{2} \begin{pmatrix} 3 \\ -\sqrt{3} \end{pmatrix}, \quad (3.1)$$

where  $a \approx 1.42 \text{ \AA}$  is the distance between two carbon atoms. [5] The corresponding reciprocal lattice vectors are

$$\mathbf{b}_1 = \frac{2\pi}{3a} \begin{pmatrix} 1 \\ \sqrt{3} \end{pmatrix} \quad \text{and} \quad \mathbf{b}_2 = \frac{2\pi}{3a} \begin{pmatrix} 1 \\ -\sqrt{3} \end{pmatrix}. \quad (3.2)$$

The electron configuration of carbon is  $1s^2 2s^2 2p^2$ . In graphene, the 2s orbitals hybridize with the  $2p_x$  and  $2p_y$  orbitals, forming in-plane  $\sigma$ -bonds between the carbon atoms in the hexagon. The remaining  $2p_z$  orbitals form out-of-plane  $\pi$ -states, which are strongly delocalized across the system. These  $\pi$ -states dictate the low-energy physics of graphene and are captured well in a tight-binding model

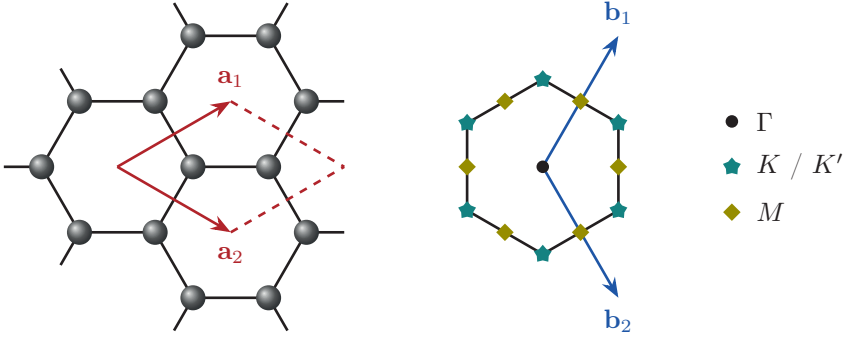


Figure 3.1: (Left) Schematic image of the graphene real-space lattice. The black spheres denote carbon atoms and the red arrows indicate the unit cell vectors  $\mathbf{a}_1$  and  $\mathbf{a}_2$ . (Right) The first Brillouin zone of graphene. The blue arrows indicate the reciprocal lattice vectors  $\mathbf{b}_1$  and  $\mathbf{b}_2$ . The various symbols indicate the high-symmetry points.

with only nearest-neighbour hopping  $t \approx -2.97$  eV. [5, 160] Diagonalizing it and expanding around the high-symmetry points (indicated also in Fig. 3.1)

$$K = \begin{pmatrix} 2\pi/(3a) \\ -2\pi/(3\sqrt{3}a) \end{pmatrix} \quad \text{and} \quad K' = \begin{pmatrix} 2\pi/(3a) \\ 2\pi/(3\sqrt{3}a) \end{pmatrix} \quad (3.3)$$

yields the well-known linear Dirac dispersion

$$\varepsilon_{\mathbf{k}} = \pm v_F |\mathbf{q}| + \mathcal{O}(\mathbf{q}^2), \quad (3.4)$$

with  $\mathbf{q} = \mathbf{k} - K^{(\prime)}$  the momentum relative to the  $K$  ( $K'$ ) point and  $v_F = 3a|t|/2$  the graphene Fermi velocity. To compare, we show in Fig. 3.2 a full DFT band structure of graphene. One can recognize in red the linear dispersion around the Fermi energy at the  $K$  point. The  $K'$  point is equivalent to the  $K$  point by symmetry of the lattice, such that there are two Dirac cones at the Fermi surface. This gives graphene an additional degeneracy on top of the spin degeneracy, often called the valley degeneracy. The DFT band-structure also includes the higher-energy bands from the  $\sigma$ -states in yellow. These bands will not directly affect the low-energy physics, but they will screen the Coulomb interaction. For doped graphene systems, we furthermore introduce a chemical potential shift  $\mu$ . This shift changes the electron density by  $n = k_F^2/\pi$ , with  $k_F = \mu/v_F$  the Fermi wave vector.

Equipped with the low-energy Dirac model, we can now evaluate the polarization in the RPA using Eq. 2.25. The expression is rather lengthy, but can be found, for example, in Refs. [5, 162–164]. In the small  $\mathbf{q}$  and static screening limit, the polarization is given by

$$\Pi^{(0)}(\mathbf{q} \rightarrow 0, \omega = 0) \approx -\frac{g_s g_v \mu}{2\pi v_F^2} A = -g_s g_v N_0, \quad (3.5)$$

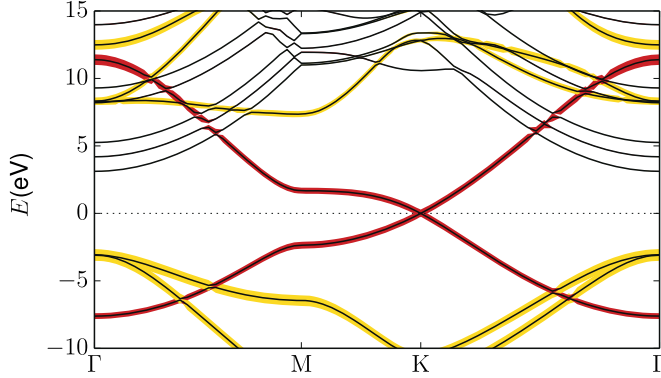


Figure 3.2: The DFT band structure of graphene, reproduced from the Ph.D. thesis of M. Rösner with permission. [161] The yellow lines are bands from the  $\sigma$ -states and the red lines are bands from the  $\pi$ -states.

where  $g_s = 2$  and  $g_v = 2$  are the spin and valley degeneracy factors, respectively. We find that the static polarization in the long-wavelength limit reproduces the Thomas-Fermi limit, i.e., it does not depend on  $\mathbf{q}$  and is proportional to the DOS at the Fermi energy  $N_0$ . If we consider dynamical screening at small  $\mathbf{q}$  and for  $\omega \gg v_F q$  we find that

$$\Pi^{(0)}(\mathbf{q} \rightarrow 0, \omega) \approx \frac{g_s g_v \mu q^2}{4\pi\omega^2} A. \quad (3.6)$$

Substituting this expression into Eq. 2.27 and using Eq. 2.68 for the bare Coulomb interaction we can evaluate screened Coulomb interaction  $W$ . From its poles we then evaluate the graphene plasmon dispersion, which yields

$$\omega_{\mathbf{q}} \approx \sqrt{\frac{g_s g_v e^2 \mu}{2\varepsilon_{\text{back}}(\mathbf{q})}} q = \sqrt{\frac{g_s g_v e^2 v_F \sqrt{\pi n}}{2\varepsilon_{\text{back}}(\mathbf{q})}} q. \quad (3.7)$$

As expected for two-dimensional systems, we find a plasmon mode with a  $\sqrt{q}$  dispersion for small  $\mathbf{q}$ . Similar to the 2D electron gas discussed in Sect. 2.3.1, the graphene plasmon is extremely sensitive to doping and environmental screening. However, unlike the electron gas, the graphene plasmon is proportional to  $n^{1/4}$  instead of  $\sqrt{n}$ .

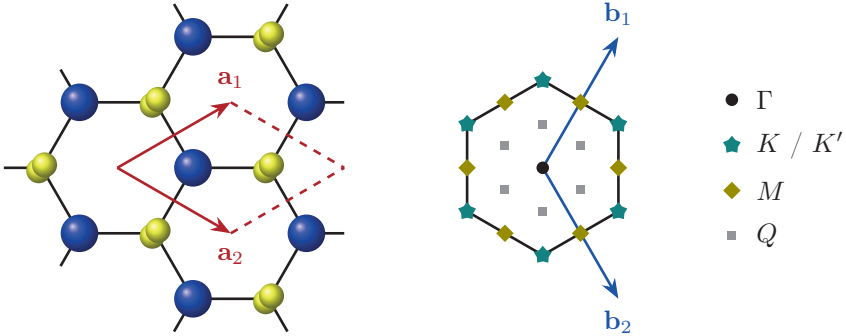


Figure 3.3: (Left) Schematic image of the real-space lattice of a TMDC monolayer in the 2H phase. The larger blue spheres denote transition metal atoms and the smaller yellow spheres denote chalcogen atoms above and below the plane. The red arrows indicate the unit cell vectors  $\mathbf{a}_1$  and  $\mathbf{a}_2$ . (Right) The corresponding first Brillouin zone. The blue arrows indicate the reciprocal lattice vectors  $\mathbf{b}_1$  and  $\mathbf{b}_2$ . The various symbols indicate the high-symmetry points, as well as the  $Q$  point.

### 3.2 TRANSITION METAL DICHALCOGENIDES

Following graphene, the TMDCs were among the second set of materials to have been exfoliated to atomically thin layers. [3] While the class of TMDCs also includes metals, we will focus here on the semi-conducting TMDCs, which includes materials such as  $\text{MoS}_2$ ,  $\text{WS}_2$  and more. [165] Interestingly, the band-gap of these materials changes from indirect in the bulk to direct in the monolayer limit. This property makes them very promising for the design of atomically thin transistors [12, 13, 165–168] or optical devices [169–172]. TMDCs furthermore have a rich phase diagram, with a variety of correlated phases. Of particular interest in this thesis is superconductivity, which has been observed in doped monolayers of  $\text{MoS}_2$  [173] and  $\text{WS}_2$  [174], as well as in multilayered structures. [15–17]

Here we will focus on direct band-gap semi-conducting monolayer TMDCs in the 2H phase, with a particular focus on  $\text{MoS}_2$  and  $\text{WS}_2$ . Similar to graphene, these TMDCs have a hexagonal lattice. Unlike graphene however, the three corners of the hexagon are occupied by a transition metal atom and the other three corners by two chalcogen atoms above and below the 2D plane, as shown in the left panel of Fig. 3.3. The lattice vectors are

$$\mathbf{a}_1 = \frac{a}{2} \begin{pmatrix} \sqrt{3} \\ 1 \end{pmatrix} \quad \text{and} \quad \mathbf{a}_2 = \frac{a}{2} \begin{pmatrix} \sqrt{3} \\ -1 \end{pmatrix}, \quad (3.8)$$



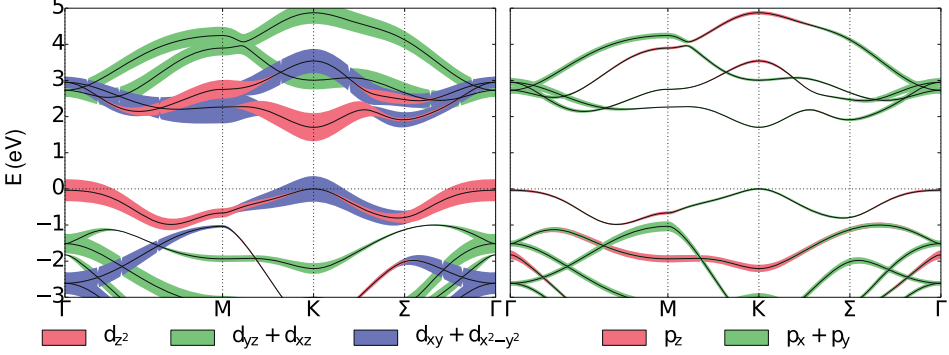


Figure 3.4: The DFT band structure of the 2H phase of two-dimensional MoS<sub>2</sub>. In the left and right panels the linewidths represent the contributions from the Mo d-orbitals and from the S p-orbitals, respectively. This figure has been reproduced from the Ph.D. thesis of M. Rösner with permission. [161]

where now  $a$  is the distance between two neighbouring transition metal atoms. Both MoS<sub>2</sub> and WS<sub>2</sub> have  $a \approx 3.16 \text{ \AA}$ . [175] The corresponding first Brillouin zone is shown in the right panel of Fig. 3.3, with reciprocal lattice vectors given by

$$\mathbf{b}_1 = \frac{2\pi}{3a} \begin{pmatrix} \sqrt{3} \\ 3 \end{pmatrix} \quad \text{and} \quad \mathbf{b}_2 = \frac{2\pi}{3a} \begin{pmatrix} \sqrt{3} \\ -3 \end{pmatrix}. \quad (3.9)$$

Most of the monolayer semi-conducting TMDCs have qualitatively similar band structures around the Fermi energy, with quantitative differences in the size of the band gap, the strength of the spin-orbit coupling and the location of the Fermi energy. As a representative example, we show in Fig. 3.4 the DFT band structure of monolayer MoS<sub>2</sub>. We see that the valence and conduction bands of monolayer MoS<sub>2</sub> have mostly d-orbital character coming from the transition metal atoms. [176] The respective maxima and minima both lie at the  $K$  and  $K'$  points, such that it is a direct band gap semi-conductor. The size of the band-gap is 1.58 eV, when evaluated in DFT using the PBE exchange-correlation functional. [165, 177–179]  $G_0W_0$  corrections enhance the gap to 2.53 eV, which is significantly closer to experimental observations. [180]

We furthermore note that for both MoS<sub>2</sub> and WS<sub>2</sub>, the bottom of the conduction band has a relatively weak spin-orbit splitting of around 30 meV, such that it can be approximated well using an effective free-electron model when including spin and valley degeneracy factors  $g_s = 2$  and  $g_v = 2$ , respectively. The corresponding effective masses are  $m^* \approx 0.43m_e$  and  $m^* \approx 0.37m_e$ , for MoS<sub>2</sub> and WS<sub>2</sub>, respectively. [177, 178] As a consequence, the low-energy plasmon mode of weakly

electron-doped MoS<sub>2</sub> or WS<sub>2</sub> can be approximated well by that of the 2D free electron gas (discussed in Sect. 2.3.1). Here, we write it in terms of the chemical potential  $\mu$  for consistency with chapter 4, such that in the long-wavelength limit

$$\omega_{\mathbf{q}} \approx \sqrt{\frac{g_s g_v e^2 \mu}{\varepsilon_{\text{back}}(\mathbf{q})}} q. \quad (3.10)$$

For cases where the effective-mass approximation breaks down, there are downfolded three-band models which have been shown to accurately describe the low-energy physics of MoS<sub>2</sub> and WS<sub>2</sub> (as well as other semi-conducting TMDCs). [101, 181] This is for example the case upon sufficiently strong electron doping, when the band minimum between the  $K$  and  $\Gamma$  points shifts below the Fermi energy. The Brillouin zone point of this band minimum is often denoted by  $Q$  or  $\Sigma$ , as also indicated in Fig. 3.3 (though it is not a high-symmetry point).

## INTERLAYER PLASMON POLARONS IN WS<sub>2</sub>/GRAPHENE HETEROSTRUCTURES

---

This chapter is based on the following publication:

S. Ulstrup, Y. in 't Veld, J. A. Miwa, A. J. H. Jones, K. M. McCreary, J. T. Robinson, B. T. Jonker, S. Singh, R. J. Koch, E. Rotenberg, A. Bostwick, C. Jozwiak, M. Rösner and J. Katoch, *Observation of Interlayer Plasmon Polaron in Graphene/WS<sub>2</sub> Heterostructures*, Nature Comm. **15**, 3845 (2024)

The  $G_0W_0 + \text{cumulant}$  calculations and the corresponding analysis was done by me. Fig. 4.3 has also been made by me. Sects. 4.4 and 4.B have been written by me, with revisions from M. Rösner. All other text was initially written by S. Ulstrup and J. Katoch, with revisions from me and M. Rösner and further input from all other authors.

Other contributions are as follows. K. M. McCreary, B. T. Jonker, J. T. Robinson, S. Singh and J. Katoch contributed to synthesizing or assembling the heterostructures. The angle-resolved photoemission spectroscopy measurements were performed and/or analyzed by S. Ulstrup, J. A. Miwa, R. J. Koch, E. Rotenberg, A. Bostwick, C. Jozwiak, J. Katoch and A. J. H. Jones. M. Rösner performed the density functional theory calculations and the corresponding analysis.

The text in this chapter is mostly equivalent to the original work, with minor edits by me to improve cohesion with the rest of the thesis.

### 4.1 INTRODUCTION

Sophisticated heterostructure designs involving two-dimensional (2D) crystals with pre-defined lattice mismatch and interlayer twist angle have emerged as promising platforms for tailoring potential energy surfaces and excitations in solid state quantum simulators [182, 183]. While these systems leverage fine-control of complex lattice structures and quantum states, the close proximity of materials may further induce additional interlayer correlation effects [184]. For example, in heterostructures composed of graphene and semiconducting transition metal dichalcogenides (TMDCs), superlattice bands are generated concomitant with screening-induced band shifts that dictate quasiparticle band alignments and gaps [185–188]. Intriguingly, recent experiments on twisted bilayer graphene interfaced with single-layer (SL) WSe<sub>2</sub> point towards even richer interactions, as the presence of SL WSe<sub>2</sub>

stabilises superconductivity below the magic twist angle of bilayer graphene [189]. In SL WS<sub>2</sub> contacted with the topological insulator Bi<sub>2</sub>Se<sub>3</sub>, interlayer exciton-phonon bound states have been detected [190]. Such observations point to the importance of interlayer collective excitations involving bosonic modes. These may lead to the formation of polaronic quasiparticles that dramatically impact charge transport, surface reactivity, thermoelectric and optical properties, as observed in a variety of crystals and interfaces composed of polar materials [191–195]. Similarly, when oscillations of the charge density couple to conduction electrons the more elusive plasmon polaron emerges [85], which has been detected in electron-doped semiconductors [59, 61, 196] and graphene [76].

We endeavour to determine how the electronic excitation spectrum of a representative semiconducting SL TMDC is affected by a doped graphene overlayer, as is present in a variety of device architectures [197–202]. To this end, we focus on SL WS<sub>2</sub> as this material exhibits a direct band gap at the  $\bar{K}$ -point of the Brillouin zone (BZ) and a large spin-orbit coupling (SOC) induced splitting of the valence bands, allowing to simultaneously resolve energy- and momentum-dependent electronic excitations around the valence and conduction band extrema using high-resolution angle-resolved photoemission spectroscopy (ARPES) [203, 204]. The heterostructures are supported on 10-30 nm thick hBN, which serves two purposes: (i) it replicates the heterostructures that are typically used in transport and optical measurements, and (ii) provides an atomically flat and inert interface that preserves the salient dispersion of SL WS<sub>2</sub>, since hybridization is strongly suppressed due to the large band gap of hBN [203]. The entire stack is placed on degenerately-doped TiO<sub>2</sub> in order to prevent charging during photoemission. The quasiparticle band structure from the heterostructure is spatially-resolved using micro-focused angle-resolved photoemission spectroscopy (microARPES) during *in situ* electron doping by depositing potassium atoms on the surface. In order to determine the effect of the graphene overlayer, we measure two types of heterostructures - one with graphene and one without. A schematic of our doped heterostructures is presented in Fig. 4.1(a). Spectra are collected along the  $\bar{\Gamma}$ - $\bar{Q}$ - $\bar{K}$  direction of the SL WS<sub>2</sub> BZ, as sketched in Fig. 4.1(b).

## 4.2 ELECTRONIC STRUCTURE OF DOPED WS<sub>2</sub> AND GRAPHENE/WS<sub>2</sub>

Figure 4.1(c) presents ARPES spectra of the effect of strong electron-doping on bare WS<sub>2</sub> with potassium atoms deposited directly on the surface. Before doping, the expected band structure of SL WS<sub>2</sub> is observed with a local valence band maximum (VBM) at  $\bar{\Gamma}$  and a global VBM at  $\bar{K}$ , a total gap larger than 2 eV and a SOC splitting of 430 meV in the VBM [205] (see left panel of Fig. 4.1(c)). At an estimated highest electron density of  $(3.0 \pm 0.2) \cdot 10^{13} \text{ cm}^{-2}$ , induced by the adsorbed potassium atoms, the conduction band minimum (CBM) is populated and

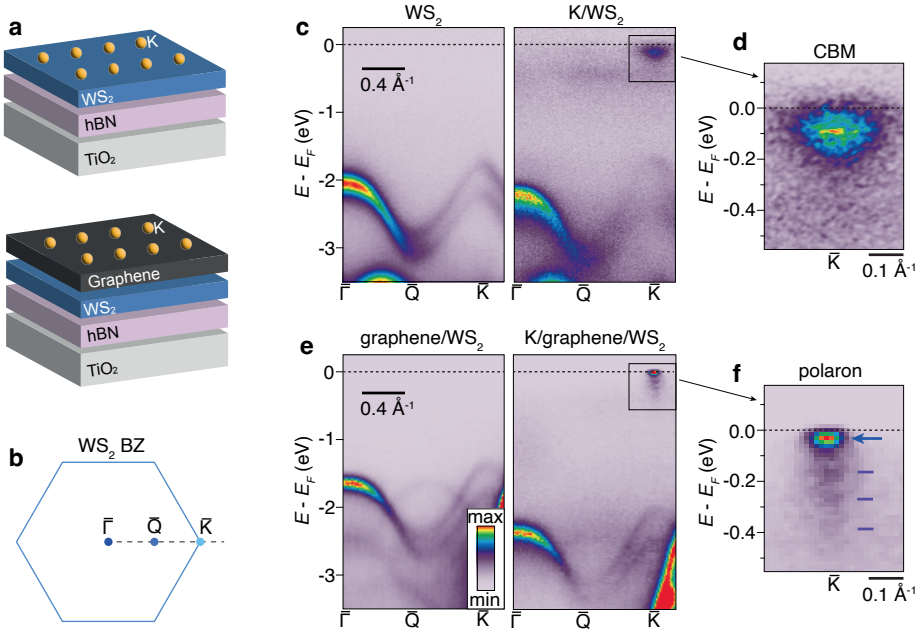


Figure 4.1: Quasiparticle bands of electron-doped WS<sub>2</sub> heterostructures. **a**, Layout of systems with doping achieved by deposition of potassium atoms. **b**, Brillouin zone (BZ) of SL WS<sub>2</sub> with ARPES measurement direction marked by a dashed line. **c**, ARPES spectra of bare (left panel) and potassium doped WS<sub>2</sub> (right panel) supported on hBN. The achieved electron density in the strongly doped case is estimated to be  $(3.0 \pm 0.2) \cdot 10^{13} \text{ cm}^{-2}$ . **d**, Close-up of the CBM region marked in (c). **e-f**, Corresponding ARPES spectra for WS<sub>2</sub> with graphene on top. The achieved electron density in the potassium-dosed graphene layer is  $(4.8 \pm 0.1) \cdot 10^{13} \text{ cm}^{-2}$ . The close-up of the CBM region of WS<sub>2</sub> in (f) reveals the formation of a polaron via a sharp quasiparticle peak, which is demarcated by a blue arrow, and several shake-off replicas marked by purple ticks.

the shape of the VBM is strongly renormalized, as observed in the right panel of Fig. 4.1(c) and previously reported [203]. The direct band gap at  $\bar{K}$  is furthermore reduced to  $(1.64 \pm 0.02) \text{ eV}$  (Supplementary Fig. 1 of the original work [60]), indicating enhanced internal screening. A detailed view of the CBM region in Fig. 4.1(d), reveals the CBM to be relatively broad with an energy distribution curve (EDC) linewidth of  $(0.17 \pm 0.02) \text{ eV}$  and a momentum distribution curve (MDC) width of  $(0.29 \pm 0.02) \text{ \AA}^{-1}$  (Supplementary Fig. 2 of the original work [60]). These spectra are contrasted with the situation where a graphene layer is placed on top of WS<sub>2</sub> in Fig. 4.1(e). In the undoped case shown in the left panel of Fig.

4.1(e), the bands exhibit the same general features as seen in the left panel of Fig. 4.1(c), although they are noticeably sharper and shifted towards the Fermi energy due to the additional screening of the Coulomb interaction by the graphene [186]. Furthermore, a replica of the WS<sub>2</sub> local VBM around  $\bar{\Gamma}$  is noticeable close to Q due to the superlattice formed between graphene and WS<sub>2</sub> [187]. Upon doping graphene to an electron density of about  $(4.8 \pm 0.1) \cdot 10^{13} \text{ cm}^{-2}$ , the SL WS<sub>2</sub> valence band shifts down in energy and the shape of the VBM does not renormalize as in the case of bare WS<sub>2</sub> (see right panel of Fig. 4.1(e) and Supplementary Fig. 1 of the original work [60]). The strongly doped graphene is accompanied by a relatively small occupation in the WS<sub>2</sub> CBM (see ARPES spectra of doped WS<sub>2</sub> and graphene in Supplementary Fig. 3 of the original work [60]). The total gap is now  $(2.04 \pm 0.02) \text{ eV}$  (Supplementary Fig. 1 of the original work [60]), indicating that the non-local Coulomb interaction in WS<sub>2</sub> is not fully suppressed. However, the CBM region looks dramatically different, as seen by comparing Figs. 4.1(f) and 4.1(d). In the situation with a doped graphene overlayer, a sharp quasiparticle peak occurs. The peak is accompanied by a series of replica bands towards lower kinetic energy, that are conventionally called shake-off bands. The EDC and MDC linewidths of the main quasiparticle peak are reduced by a factor of 3-4, compared to bare K/WS<sub>2</sub> (Supplementary Fig. 2 of the original work [60]). The feature bears resemblance to a Fröhlich polaron that is observable in ARPES when the conducting electrons couple strongly to phonons [191, 192, 195, 206].

Density functional theory (DFT) calculations for the K/graphene/WS<sub>2</sub> heterostructure (see Appendix 4.A) confirm the experimental results which show that the graphene Dirac bands do not strongly hybridize with the WS<sub>2</sub> CBM at  $\bar{K}$ , in line with previous reports [207, 208]. As a result, there is only a vanishingly small charge transfer from the strongly K doped graphene layer to the WS<sub>2</sub> layer. This explains the experimental observation of strongly doped graphene, accompanied by the small  $\bar{K}$  valley occupation in WS<sub>2</sub>. This also explains the absence of VBM renormalization in WS<sub>2</sub> covered by graphene, as this only occurs at carrier concentrations larger than  $(2.0 \pm 0.2) \cdot 10^{13} \text{ cm}^{-2}$  in WS<sub>2</sub> [203]. These DFT calculations, however, do not reproduce the still significant band gap or the shake-off bands, pointing towards the important role played here by many-body interactions, that are beyond the scope of DFT calculations.

### 4.3 DOPING-DEPENDENCE OF SHAKE-OFF BANDS

In order to understand the origin of the shake-off bands in the dispersion at  $\bar{K}$  in the graphene/WS<sub>2</sub> heterostructure, we tune the charge carrier density by sequentially increasing the amount of adsorbed potassium on graphene. After each dosing step we measure both the WS<sub>2</sub> conduction band region and the graphene Dirac cone to correlate the evolution of the shake-off bands spectral line shapes with the filling

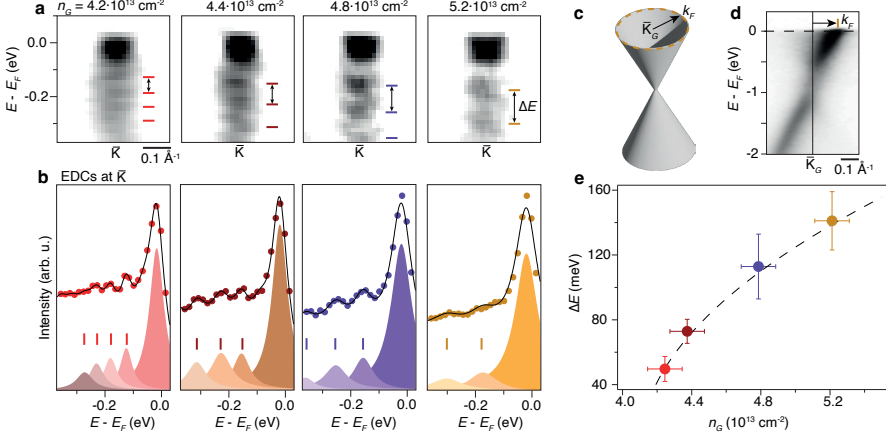


Figure 4.2: Doping-dependence of shake-off bands. **a**, Second-derivative ARPES intensity in the CBM region of potassium doped graphene/WS<sub>2</sub> at the given electron density in graphene ( $n_G$ ). The error bars on the  $n_G$  values are  $\pm 0.1 \cdot 10^{13} \text{ cm}^{-2}$ . Ticks demarcate shake-off bands and the double-headed arrows indicate their energy separation ( $\Delta E$ ). **b**, Energy distribution curves (EDCs) with fits (black curves) to Lorentzian components on a linear background. Peak components are shown with fitted positions marked by colored ticks. **c**, Sketch of graphene Dirac cone and Fermi surface (dashed circle) with radius  $k_F$  measured simultaneously by ARPES at each doping step. **d**, ARPES spectrum of potassium doped graphene on WS<sub>2</sub> with  $k_F$  indicated by an arrow. The spectrum is for the maximum achieved doping of graphene of  $(5.2 \pm 0.1) \cdot 10^{13} \text{ cm}^{-2}$ . **e**, Increase of shake-off energy separation with graphene doping extracted from the analysis. The dashed line is a fit to a function proportional to  $\sqrt{n_G}$ .

of the Dirac cone. Second derivative plots of the ARPES intensity are shown in Fig. 4.2(a) to highlight the relatively faint shake-off bands compared to the intense quasiparticle peak for a range of doping where the graphene carrier concentration is varied over a range of  $(1.0 \pm 0.1) \cdot 10^{13} \text{ cm}^{-2}$ . Corresponding EDCs with fits to Lorentzian components are shown in Fig. 4.2(b). The graphene wave vector  $k_F$ , illustrated with the Dirac cone in Fig. 4.2(c), is extracted from ARPES cuts through the center of the graphene Dirac cone at  $\bar{K}_G$ , as shown for doped graphene on WS<sub>2</sub> in Fig. 4.2(d). The Fermi momentum is then obtained from an MDC fit at  $E_F$  and given as the difference in  $k$  between the MDC peak position and  $\bar{K}_G$ . Note that  $\bar{K}_G$  is determined by mapping the  $(E, k_x, k_y)$ -dependent ARPES intensity around the Dirac cone. One of the Dirac cone branches is suppressed in Fig. 4.2(d) because of strong photoemission matrix element effects along this particular cut, which is taken along the so-called dark corridor [209]. The EDC analysis of the shake-off bands as a function of graphene doping reveals the energy

separation between shake-off bands increases from  $(50 \pm 8)$  meV to  $(141 \pm 18)$  meV and that the increase is proportional to  $\sqrt{n_G}$ , as shown in Fig. 4.2(e), while the WS<sub>2</sub> CBM binding energy, and thus doping level, approximately stays constant. Note that a minimum carrier density in graphene of  $n_0 = (4.1 \pm 0.1) \cdot 10^{13} \text{ cm}^{-2}$  is required for the WS<sub>2</sub> CBM to become occupied and thereby make the shake-off bands observable. The EDC fits in Fig. 4.2(b) demonstrate that the shake-off band intensity relative to the main quasiparticle peak diminishes with doping in line with our theoretical analysis below. Combined with the diminishing intensity of shake-offs towards higher binding energies, this reduces the number of shake-off bands we can observe with increasing doping.

These observations provide further clues on the origin of the shake-off bands. An internal coupling between WS<sub>2</sub> conducting electrons and phonons can be ruled out, because the energy separation of the shake-off bands at high doping exceeds the WS<sub>2</sub> phonon bandwidth of 55 meV [210]. Given the significant doping of graphene, there are, however, two other bosonic excitations that could be responsible for the shake-off bands in WS<sub>2</sub>: phonons and plasmons in graphene. In doped graphene there are indeed phonons with energies between 150 and 200 meV with significant electron-phonon coupling. These phonon energies change, however, only by up to 20 meV upon tuning the electron doping [211, 212] and can thus be ruled out as the origin for the observed shake-offs. In stark contrast, plasmons in 2D materials are known to be significantly affected by the doping level of the system. Indeed, significant plasmon excitations have been observed in graphene in the regime of doping we are considering [76]. Taken together with the significant doping dependence of the energy separation between shake-off bands, this suggests that the observed feature is an interlayer plasmon polaron with unusually sharp line shapes and well-defined shake-offs occurring at moderate low WS<sub>2</sub> doping levels, unlike the previously observed plasmonic polarons in electron-doped bulk materials [59, 85, 196] and in internally doped SL MoS<sub>2</sub> [61].

#### 4.4 MANY-BODY ANALYSIS OF ELECTRON-PLASMON INTERACTIONS

To theoretically substantiate this interpretation, we use a generic model consisting of a single layer with a parabolic electronic spectrum, mimicking the occupied WS<sub>2</sub>  $\bar{K}$ -valley by setting the effective mass to  $m^* = 0.3m_e$  and the chemical potential to  $\mu_{\text{WS}_2} = 0.02 \text{ eV}$  ( $n_{\text{WS}_2} \approx 0.5 \cdot 10^{13} \text{ cm}^{-2}$ ). As justified by our DFT calculations, we assume that the WS<sub>2</sub> and graphene layers are electronically decoupled, such that the only coupling between them is the long-range Coulomb interaction. Based on this, we apply the plasmon-pole approximation (PPA) for the screened Coulomb interaction  $W_q(\omega)$ , which we subsequently use within the  $G_0W_0$  and retarded  $G_0W_0$  + cumulant ( $G_0W_0 + C$ ) [84] frameworks to calculate the interacting spectral



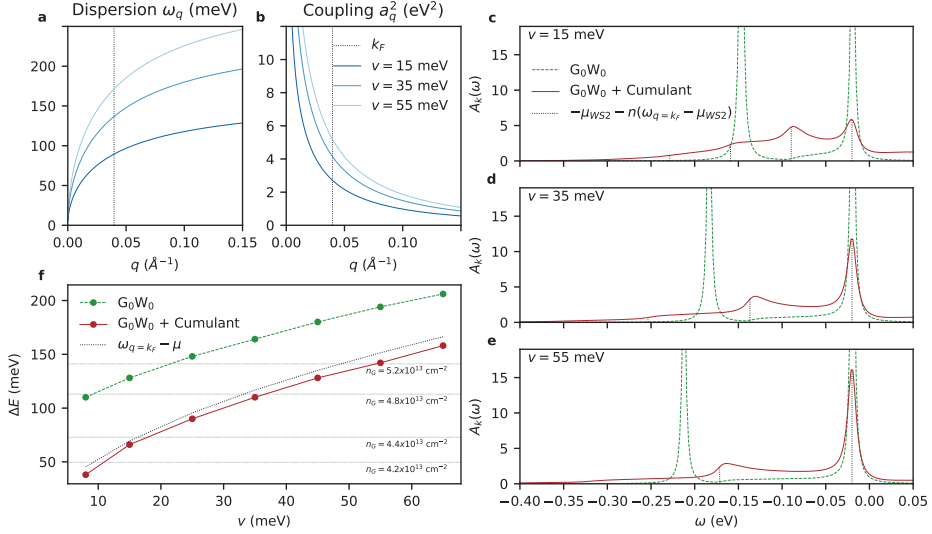


Figure 4.3: Theoretical results. **a-b**, The plasmon dispersion  $\omega_q$  and electron-plasmon coupling  $a_q^2$ , respectively, for various  $v$ . The vertical dotted line denotes  $q = k_F$ . **c-e**, EDCs of the WS<sub>2</sub> normal state spectral function in  $G_0W_0$  theory (green dashed) and  $G_0W_0 + C$  theory (red solid) at  $\bar{K}$  for a variety of  $v$ . The vertical dotted black lines denote  $\omega = -\mu_{WS_2} - n(\omega_{q=k_F} - \mu_{WS_2})$ , for  $n = 0$  to 4. **f**, Energy splitting  $\Delta E$  between the WS<sub>2</sub> CBM and the first shakeoff band as a function of  $v$ , in  $G_0W_0$  theory (green dashed) and  $G_0W_0 + C$  theory (red solid). The black dotted line denotes  $\omega_{q=k_F} - \mu_{WS_2}$ , and the gray horizontal lines denote the experimentally measured  $\Delta E$ .

function within the effective WS<sub>2</sub>  $\bar{K}$ -valley. All theoretical methods are discussed in detail in Sect. 2.3.

For the plasmon pole model, we assume a 2D plasmon dispersion of the form  $\omega_q = \sqrt{4e^2 v q / \varepsilon_{\text{back}}(q)}$ , as depicted in Fig. 4.3(a). Here the environmental screening is taken into account using the long-wavelength limit of the non-local background dielectric function  $\varepsilon_{\text{back}}(q)$  (Eq. 2.71), given by  $\varepsilon_{\text{back}}(q) = \varepsilon_{\text{ext}} + qh(\varepsilon_{\text{int}}^2 - \varepsilon_{\text{ext}}^2) / (2\varepsilon_{\text{ext}})$  [99], where  $\varepsilon_{\text{ext}} = 3.0$  and  $\varepsilon_{\text{int}} = 8.57$  are the dielectric constants of the substrate and the WS<sub>2</sub> layer, respectively, and  $h \approx 3.0 \text{ \AA}$  an effective dielectric thickness of the WS<sub>2</sub> layer. In the plasmon dispersion,  $v$  is a tunable parameter which would correspond to a chemical potential in an isolated two-dimensional free electron gas, that here controls the energy scale of the plasmon. The electron-plasmon coupling  $a_q^2$  is given by the usual long-wavelength PPA expression  $a_q^2 = \omega_q U_q / 2$ , with  $U_q = 2\pi e^2 / (A \varepsilon_q q)$  the background screened Coulomb interaction in the WS<sub>2</sub> layer and  $A = 8.79 \text{ \AA}^2$  the WS<sub>2</sub> unit-cell area. In Fig. 4.3(b) we show  $a_q^2$  for a

variety of plasmon energy scales  $v$ . Note that the electron-plasmon coupling and the plasmon dispersion are related, such that  $a_q^2$  increases as  $v$  increases.

In Figs. 4.3(c-e) we show EDCs of the dressed spectral function  $A_k(\omega)$  within the effective WS<sub>2</sub>  $\bar{K}$ -valley, for various plasmon energy scales  $v$ . Within both  $G_0W_0$  and  $G_0W_0 + C$  theories, we identify the expected CBM quasiparticle peak at  $\omega = -0.02$  eV and a plasmon polaron shakeoff peak with reduced intensity at lower energies. Within  $G_0W_0 + C$  this is extended to a whole series of partially pronounced plasmon polaron shakeoff peaks, which reduce in intensity for peaks further from the CBM. As  $v$  is enhanced, the separation between shakeoff bands  $\Delta E$  increases and the shakeoff peak intensity decreases. These results are reminiscent of polarons formed by dispersionless bosons, where the energy separation between shakeoff bands is given by the boson frequency  $\omega_b$  [52]. This suggests that, even though the 2D plasmon is a highly dispersive mode, there exists an effective plasmon frequency which dictates the energy separation  $\Delta E$ . Since WS<sub>2</sub> is only weakly doped we can evaluate the spectral function of the first shakeoff band in  $G_0W_0 + C$  theory analytically (see Appendix 4.B) and understand that the shakeoff bands appear in multiples of  $\omega_{q=k_F} - \mu_{WS_2}$  below the CBM (indicated by vertical black lines in Figs. 4.3(c-e)), with  $k_F \approx 0.04 \text{ \AA}^{-1}$  the WS<sub>2</sub> Fermi wavevector. To confirm this prediction, we plot in Fig. 4.3(f) the energy splitting  $\Delta E$  in  $G_0W_0 + C$  theory (red line) as a function of the plasmon energy scale  $v$ , which follows the analytically predicted  $\Delta E = \omega_{q=k_F} - \mu_{WS_2}$  (dotted line). From the analytical derivations we also understand that the intensity of the first shakeoff peak is proportional to

$$A_{k=\bar{K}}(\omega = -\omega_{q=k_F}) \propto \frac{a_{q=k_F}^2}{(\omega_{q=k_F} - \mu_{WS_2})^2} \frac{v_F}{|v_{pl} - v_F|}, \quad (4.1)$$

with  $v_{pl} = \partial\omega_q/\partial q|_{q=k_F}$  the plasmon group velocity at  $q = k_F$  and  $v_F$  the WS<sub>2</sub> Fermi velocity. Due to the low WS<sub>2</sub> occupation, both  $\mu_{WS_2} < \omega_{q=k_F}$  and  $v_F < v_{pl}$ , which explains the reduced intensity of the shakeoff peaks upon enhancing the plasmon energy scale  $v$ . Finally, the analytic  $G_0W_0 + C$  expressions explain that the non-zero intensity between the shakeoff peaks and the CBM is a consequence of the gapless dispersion of the 2D plasmon mode.

Comparing  $G_0W_0$  and  $G_0W_0 + C$  theory, we show in Figs. 4.3(c-e) that the EDCs predicted by  $G_0W_0$  theory (green lines) capture only a single shakeoff band, whereas  $G_0W_0 + C$  theory (red lines) predicts an infinite series of shakeoff bands. Furthermore, Fig. 4.3(f) shows that  $\Delta E$  predicted by  $G_0W_0$  theory overestimates  $\Delta E$  from  $G_0W_0 + C$  theory by more than 50 meV for all plasmon energy scales  $v$  considered. These discrepancies are consistent with earlier works [52, 61, 84, 85, 213] and are a clear sign that correlations beyond  $G_0W_0$  theory (i.e., vertex corrections) are playing a significant role here.

From the analysis above, we understand that in order to observe an enhancement of  $\Delta E$  on the order of 100 meV upon K-adsorption, the plasmon energy at  $q = k_F$

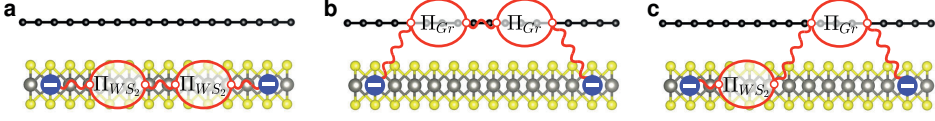


Figure 4.4: Illustrations of the Coulomb interaction in WS<sub>2</sub> and its screening channels in graphene/WS<sub>2</sub> heterostructures. Wavy lines and “bubbles” represent bare Coulomb interactions and polarization processes, respectively. **a**, Coulomb interaction and screening from WS<sub>2</sub> only. **b**, Coulomb interaction between electrons in WS<sub>2</sub> screened by graphene polarization processes only, which couple graphene plasmons to the WS<sub>2</sub> Coulomb interaction. **c**, Illustration of mixed screening channels from WS<sub>2</sub> and graphene. Interlayer polarization effects are suppressed due to the vanishingly small hybridization between the WS<sub>2</sub> K valley and graphene’s Dirac cone.

should increase by the same amount. Additionally, the group velocity of the plasmon should be of similar magnitude to the WS<sub>2</sub> Fermi velocity to increase the shakeoff intensity. These restrictions allow us to investigate the origin of the relevant plasmon mode. To this end, we depict in Fig. 4.4 the three possible screening channels to the Coulomb interaction within the WS<sub>2</sub> layer, which could be responsible for the relevant plasmonic mode. Fig. 4.4(a) describes screening processes from within the WS<sub>2</sub> layer, which induces a plasmon mode that is spatially restricted to the WS<sub>2</sub> layer. Due to the quadratic dispersion of the WS<sub>2</sub> CBM, this plasmon mode behaves as  $\omega_q^{\text{WS}_2} = \sqrt{4e^2\mu_{\text{WS}_2}q/\epsilon_q}$  in the long wavelength limit [9]. There are therefore two ways in which the energy of this mode can be tuned: doping of the WS<sub>2</sub> layer and external screening to it. As for doping, from the ARPES data we learn that the WS<sub>2</sub> CBM does not exhibit an observable shift over the range of K-doping where the polaron effect emerges. Additionally, no shifts in the valence bands are observed, such that we can conclude that the WS<sub>2</sub> occupation is not significantly altered over this doping range. We can therefore exclude that WS<sub>2</sub> doping significantly changes the WS<sub>2</sub> plasmon energy. As for screening, static screening from the graphene layer can change the energy scale of the WS<sub>2</sub> plasmon and is sensitive to the doping of graphene. However, within a Thomas-Fermi screening model, we understand that as the doping of graphene is increased, the screening increases, such that the WS<sub>2</sub> plasmon energy decreases with enhanced K-doping. This is opposite to the trend which is observed experimentally, thereby excluding this mechanism. We conclude that the WS<sub>2</sub> plasmon energy is not significantly enhanced upon K-doping, which means it cannot cause changes of the shakeoff energy splitting on the order of 100 meV.

Fig. 4.4(b) describes a dynamical screening process from the graphene layer, which induces a graphene-like plasmon mode which is coupled to the WS<sub>2</sub> layer via long-range Coulomb interaction. The experimental data as well as the DFT results

show that the graphene layer is readily doped by K-adsorption, such that this plasmon mode, which behaves as  $\omega_q^G = \sqrt{2e^2\mu_G q/\varepsilon_q}$  in the long wavelength limit [5], significantly increases in energy. While the trends in this scenario are correct, the graphene plasmon energy scale of  $\omega_{q=k_F}^G \approx 460$  meV at the measured graphene occupation of  $n_G = 4.8 \cdot 10^{13} \text{ cm}^{-2}$  yields an energy separation  $\Delta E$  which is too large compared to the measured values. In addition, the group velocity of the graphene plasmon  $v_{q=k_F}^{pl,G}$  is approximately 4 times larger than the WS<sub>2</sub>  $v_F$ , such that the intensity of the resulting shakeoff peak is reduced. However, hybridization with another boson mode, such as a phonon mode in graphene, could flatten the plasmon dispersion and lower its energy at  $q = k_F$  to a more suitable regime, such that it could induce the observed plasmon polaron bands in the WS<sub>2</sub> layer.

Finally, Fig. 4.4(c) describes interlayer screening processes, which induces interlayer plasmon modes. These can be interpreted as hybridized graphene and WS<sub>2</sub> plasmon modes. Such modes live on energy scales in between those of decoupled intralayer graphene and WS<sub>2</sub> modes, while at the same time being sensitive to the graphene occupation. These hybridized interlayer plasmon modes can explain all relevant experimental observations without the need of taking further bosonic excitations into account.

Based on this, we conclude that the shakeoff bands observed in K-doped graphene/WS<sub>2</sub> heterostructures are signatures of interlayer plasmon polarons, which are formed by WS<sub>2</sub> electrons coupling either to renormalized graphene plasmon modes, or to interlayer hybridized plasmon modes as a result of the inter-layer Coulomb interaction in the heterostructure.

#### 4.5 DISCUSSION

Taking only the WS<sub>2</sub> layer in the passive screening and/or doping background of K-doped graphene into account cannot explain the experimentally observed K-tunable formation of a series of shakeoff bands within the WS<sub>2</sub>  $\bar{K}$  valley. Our results thus clearly underline the relevance of the full heterostructure, and especially the interlayer Coulomb coupling, in facilitating the formation of plasmon polaron bands in the WS<sub>2</sub> layer. The graphene layer acts as a buffer to weaken the doping of the WS<sub>2</sub> layer, as well as providing an interlayer plasmon mode, which couples strongly to the WS<sub>2</sub> electrons and leads to the formation of plasmon polarons. The sensitivity of these interlayer plasmon modes to the graphene occupation leads to a high degree of tunability in the positions of the plasmon polaron shakeoff bands. The missing higher order shake-off bands in the  $G_0W_0$  approximation are further evidence for the need of vertex corrections [52, 61, 78], which we incorporated here within the  $G_0W_0 + C$  approach.

The impact of these findings could be far-reaching, as interfaces between graphene and TMDCs have been exploited in various ways: to induce large spin-orbital

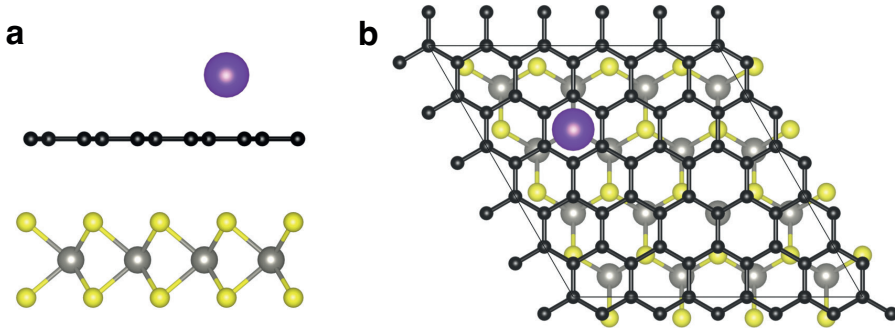


Figure 4.5: DFT heterostructure model. **a-b**, View from the (a) side and (b) top of the utilized  $4 \times 4$   $\text{WS}_2$  /  $5 \times 5$  graphene supercell with K doping.

proximity effects [214], for the stabilization of superconductivity below magic angle twists in bilayer graphene interfaced with  $\text{WSe}_2$  [189], or for charge carrier control of Wigner crystallization and realizations of discrete Mott states in dual-gated TMDC heterobilayers contacted with graphite [182, 183]. Our observation of interlayer polaronic quasiparticles induced by interlayer Coulomb coupling and upon adding charge to a contacting graphene layer will thus be important to consider in the interpretation and modelling of device measurements. Further experiments will be required to evaluate their impact on the optoelectronic properties and band engineering of heterostructures as well as their utility for ultrathin photonics and plasmonic devices.

## METHODS

Detailed discussion on the fabrication of the heterostructures, as well as on the micro-focused angle-resolved photoemission spectroscopy can be found in the original work. [60] Here, we will only discuss the methods relevant for the theoretical discussions.

### 4.A DENSITY FUNCTIONAL THEORY CALCULATIONS

To study the hybridization and the possible charge transfer between the graphene and  $\text{WS}_2$  layers, we performed density functional theory (DFT) calculations using a  $4 \times 4$   $\text{WS}_2$  /  $5 \times 5$  graphene supercell with K doping, as indicated in Fig. 4.5. The supercell height has been fixed to about  $26 \text{ \AA}$  to suppress unwanted wavefunction overlap between adjacent supercells. The  $\text{WS}_2$  lattice constant has been fixed to its

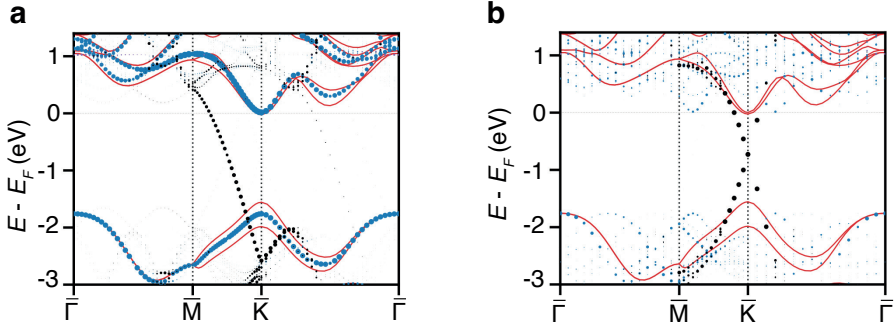


Figure 4.6: DFT electronic structure. **a-b**, Band structure of WS<sub>2</sub> with SOC (red line) plotted together with the unfolded band structure without SOC (dots) in the (a) WS<sub>2</sub> and (b) graphene primitive BZs. Blue and black dots represent W and C weights.

experimental value of 3.184 Å while the graphene lattice constant has been strained by about 3% to 2.547 Å to obtain a commensurable heterostructure. The graphene-WS<sub>2</sub> interlayer separation has been set to previously reported 3.44 Å [215] and the K-graphene distance has been optimized in DFT yielding 2.642 Å in the out-of-plane direction. All calculations were performed within the Vienna Ab initio Simulation Package (VASP) [216, 217] utilizing the projector-augmented wave (PAW) [218, 219] formalism within the PBE [220] generalized-gradient approximation (GGA) using  $12 \times 12 \times 1$   $k$  point grids and an energy cut-off of 400 eV.

In Fig. 4.6 we show the resulting unfolded band structure (without SOC effects) together with the pristine WS<sub>2</sub> band structure (including SOC effects) following the approach from Ref. [221] as implemented in [222]. From this we can clearly see that in the heterostructure new states in the gap of WS<sub>2</sub> arise, which we identify as graphene bands. Due to unfolding (matrix element) effects, the second linear band forming graphene's Dirac cone is not visible. Upon unfolding to the primitive graphene structure, the Dirac point becomes visible (right panel) showing a graphene Fermi energy of about 0.6 eV in good agreement with the experimentally achieved range. In the upmost valence states around the  $\bar{K}$ -point, we see that the graphene and WS<sub>2</sub> bands hybridize similar to reported band structures on undoped graphene/WS<sub>2</sub> [208, 215]. In the conduction band region, we however see that graphene states are far from the  $\bar{K}$ -valley, such that hybridization between graphene  $p_z$  and W  $d_{z^2}$  orbitals (which are dominating the  $\bar{K}$ -valley) is almost completely suppressed. As a result, there is negligible charge transfer from graphene to WS<sub>2</sub>, so that primarily graphene is doped by potassium. This is fully in line with our experimental results.

4.B ANALYTICAL  $G_0W_0 + C$  EXPRESSIONS

For the  $G_0W_0 + C$  calculations we use the formalism proposed by Kas *et al.* [84], discussed in detail in Sect. 2.3.3. Numerical calculations are performed using the full  $G_0W_0$  self-energy in the PPA (defined by Eq. 2.38), but for the analytical analysis we are mainly interested in the occupied states. Therefore, we will neglect the last term of Eq. 2.38, such that the dynamic part of the  $G_0W_0$  self-energy is approximated by

$$\Sigma_{\mathbf{k}}^{\text{dyn}}(\omega) \approx \sum_{\mathbf{q}} a_{\mathbf{q}}^2 \frac{n_B(\omega_{\mathbf{q}}) + n_F(\varepsilon_{\mathbf{k}+\mathbf{q}} - \mu)}{\omega - \varepsilon_{\mathbf{k}+\mathbf{q}} + \mu + \omega_{\mathbf{q}} + i\delta}, \quad (4.2)$$

where  $\varepsilon_{\mathbf{k}} = k^2/(2m^*)$  is the electron dispersion. We will furthermore focus on the effective K-valley of the  $\text{WS}_2$  layer by setting  $\mathbf{k} = 0$  and we will assume zero temperature for simplicity. Taking the limit  $\delta \rightarrow 0$  we find for the spectral function of the self-energy (defined by Eq. 2.44)

$$\beta_{\mathbf{k}=0}(\omega) = \sum_{\mathbf{q}} a_{\mathbf{q}}^2 \Theta(\mu - \varepsilon_{\mathbf{q}}) \delta(\omega - \varepsilon_{\mathbf{q}} + \omega_{\mathbf{q}}), \quad (4.3)$$

with  $\Theta(x)$  the Heaviside step function. Substituting  $\beta_{\mathbf{k}=0}(\omega)$  into the three terms of the cumulant function gives

$$O_{\mathbf{k}=0}(t) = \sum_{\mathbf{q}} a_{\mathbf{q}}^2 \frac{e^{-i(\varepsilon_{\mathbf{q}} - \omega_{\mathbf{q}})t}}{(\varepsilon_{\mathbf{q}} - \omega_{\mathbf{q}})^2} \Theta(\mu - \varepsilon_{\mathbf{q}}), \quad (4.4)$$

$$\Delta_{\mathbf{k}=0} = \sum_{\mathbf{q}} a_{\mathbf{q}}^2 \frac{1}{\varepsilon_{\mathbf{q}} - \omega_{\mathbf{q}}} \Theta(\mu - \varepsilon_{\mathbf{q}}), \quad (4.5)$$

$$a_{\mathbf{k}=0} = \sum_{\mathbf{q}} a_{\mathbf{q}}^2 \frac{1}{(\varepsilon_{\mathbf{q}} - \omega_{\mathbf{q}})^2} \Theta(\mu - \varepsilon_{\mathbf{q}}). \quad (4.6)$$

To obtain a Green's function for each shakeoff band separately, we expand in Eq. 2.56  $\exp(O_{\mathbf{k}}(t)) = \sum_n O_{\mathbf{k}}^n(t)/n!$ , such that each term in the expansion corresponds to the  $n$ -th shakeoff band. Fourier transforming and subsequently evaluating the spectral function  $A_{\mathbf{k}=0}(\omega) = \lim_{\delta \rightarrow 0} -\text{Im}(G_{\mathbf{k}=0}(\omega))/\pi$  gives

$$\begin{aligned} A_{\mathbf{k}=0}(\omega) &= Z_{\mathbf{k}=0} \delta(\omega + E_{\text{CBM}}) \\ &+ Z_{\mathbf{k}=0} \sum_{\mathbf{q}} a_{\mathbf{q}}^2 \frac{1}{(\varepsilon_{\mathbf{q}} - \omega_{\mathbf{q}})^2} \Theta(\mu - \varepsilon_{\mathbf{q}}) \delta(\omega + E_{\text{CBM}} - \varepsilon_{\mathbf{q}} + \omega_{\mathbf{q}}) \\ &+ \mathcal{O}(O^2), \end{aligned} \quad (4.7)$$

where  $E_{\text{CBM}}$  is the energy of the CBM. For all parameter regimes considered,  $\omega_{\mathbf{q}} - \varepsilon_{\mathbf{q}}$  is a monotonically increasing function of the norm  $q$  in the range  $0 < q < k_F$ .

As a consequence, the step-function restricts the shakeoff band induced by a dispersive 2D plasmon mode to the energy range between  $\omega = -E_{\text{CBM}}$  and  $\omega = -E_{\text{CBM}} + \mu - \omega_{q=k_F}$ , where we used that  $\omega_{q=0} = 0$  for 2D plasmons, leading to the maximal energy splitting  $\Delta E = \omega_{q=k_F} - \mu$ . In contrast, a dispersionless boson mode with energy  $\omega_b$  has a smaller allowed energy range  $-E_{\text{CBM}} - \omega_b < \omega < -E_{\text{CBM}} + \mu - \omega_b$ , which leads to a shakeoff feature which is completely detached from the CBM.

At each  $\omega$ , the spectral intensity of the first occupied shakeoff band can be evaluated by approximating  $\sum_{\mathbf{q}} f(q) \approx \frac{A}{2\pi} \int q f(q) dq$ , with  $A$  the unit-cell area, and using the property  $\delta(g(x)) = \sum_i \delta(x - x_i)/|g'(x_i)|$  with  $x_i$  the solutions of  $g(x_i) = 0$ . This finally yields

$$A_{\mathbf{k}=0}^{(1)}(\omega) = Z_{\mathbf{k}=0} \frac{A}{2\pi} \frac{a_{q(\omega)}^2}{(\varepsilon_{q(\omega)} - \omega_{q(\omega)})^2} \frac{q(\omega)}{\left| \frac{\partial \omega_q}{\partial q} - \frac{\partial \varepsilon_q}{\partial q} \right|_{q=q(\omega)}} \Theta(0 < q(\omega) < k_F). \quad (4.8)$$

with  $q(\omega)$  the solution of  $\omega + E_{\text{CBM}} = \varepsilon_{q(\omega)} - \omega_{q(\omega)}$ . Evaluating this function at the lower edge of the allowed frequency range (i.e., at  $q(\omega) = k_F$ ) yields Eq. 4.1 of the main text.



## CROSSOVER BETWEEN PHONON- AND PLASMON-MEDIATED SUPERCONDUCTIVITY

---

This chapter is based on the following publication:

Y. in 't Veld, M. I. Katsnelson, A. J. Millis and M. Rösner, *Screening Induced Crossover between Phonon- and Plasmon-Mediated Pairing in Layered Superconductors*, *2D Materials* **10**, 045031 (2023)

All calculations and derivations in this chapter have been done by me. The figures have also been made by me. The text in the original work was written by all collaborators equally. The text in this chapter is mostly equivalent to the original work, with minor edits by me to improve cohesion with the rest of the thesis.

### 5.1 INTRODUCTION

Superconductivity in ultra-thin two-dimensional (2D) films is of long-standing scientific importance and has undergone a recent revival of interest. Experimental studies of atomically thin elemental superconductors [223–225], superconducting 2D electron gases formed in layered oxide heterostructures [226, 227], as well as 2D van-der-Waals materials such as transition metal dichalcogenides [15, 16, 228–232], FeSe [18, 19, 67, 119, 233], and various forms of multilayer graphene [212, 234–236] have produced results that challenge the conventional understanding of superconductivity. Most recently, the ability to tune properties by gate voltages and novel heterostructuring including “moiré” systems [20, 101, 102, 237–240] has further increased the interest in 2D superconductivity and rendered layered superconductors a promising platform for many-body material design.

The origin of superconductivity observed in atomically thin 2D materials remains debated. In some materials unconventional coupling mechanisms from charge [63–66, 68–72, 106, 119–121, 228, 241] or spin [116–118] fluctuations as well as their combined effect [242] have been proposed, while for other compounds conventional electron-phonon coupling has been suggested as the origin of pairing [243–248]. Even the conventional theory of 2D superconductivity is challenging since in ultra-thin systems the reduced electronic screening yields gapless  $\sqrt{q}$ -like plasmon excitations with diverging electron-plasmon coupling in the long-wavelength limit [61, 249, 250], implying Coulomb interactions with enhanced long-range character in space and strong retardation in frequency [61, 249, 250]. These particular plasmonic

properties have a non-trivial influence on superconductivity that is qualitatively different from phonon mediated mechanisms. Additionally, the low-energetic gapless plasmon allows for efficient hybridization between plasmons and longitudinal optical phonons [251]. Thus, in contrast to conventional 3D superconductors, in which plasmons have large gaps, a fully momentum-dependent and dynamical theory is required to accurately describe 2D superconductors in the presence of electron-phonon and electron-electron interactions. [27, 28, 65, 66, 70, 121, 129, 241] Furthermore, even for 3D materials the commonly used Tolmachev-Morel-Anderson pseudopotential  $\mu^*$  approximation for the Coulomb interaction [109, 134] has been called into question [252], further highlighting the need for a consistent treatment of both interactions.

Here, we present a first step towards addressing these fundamental theoretical issues at hand of a generic monolayer model. Focusing on *s*-wave superconductivity we present a consistent theory including both electron-electron and electron-phonon interactions on the same one-loop theoretical level. We study the interplay of electron-phonon, electron-plasmon, and phonon-plasmon interactions effects on normal-state as well as superconducting properties as a function of the external screening and find that conventional electron-phonon mediated superconductors can be driven to an unconventional plasmon-mediated regime when the overall screening is small.

## 5.2 FORMALISM

We use a non-local 2D background-screened Coulomb interaction

$$U(\mathbf{q}) = \frac{2\pi e^2}{A\varepsilon_{\text{back}}(\mathbf{q})q}, \quad (5.1)$$

with  $\varepsilon_{\text{back}}(\mathbf{q})$  being the background dielectric function of capping and substrate layers set a distance  $h$  from the two dimensional electron gas (here taken to be atomically thin), given by Eq. 2.71.  $\varepsilon_{\text{back}}(\mathbf{q})$  interpolates as a function of the effective material thickness  $h$  between the external dielectric screening  $\varepsilon_{\text{ext}}$  (from the substrate and encapsulating materials) in the long-wavelength limit and the internal interband screening  $\varepsilon_{\text{int}}$  in the short-wavelength limit with  $\varepsilon_{\text{back}}(\mathbf{q}) \rightarrow \varepsilon_{\text{ext}}$  for  $h \rightarrow 0$ , as shown in Sect. 2.4.2. This model has been shown to adequately describe non-metallic screening channels in ab initio calculations for Coulomb [98, 100–104] and electron-phonon [253] interactions in various layered materials. With a small extension, the model can also describe asymmetric dielectric environments, where the dielectric environment above ( $\varepsilon_{\text{ext}}^{\text{top}}$ ) and below ( $\varepsilon_{\text{ext}}^{\text{bot}}$ ) the 2D material differ. However, as we have shown in Sect. 2.4.2, for the purposes of this paper we may to sufficient accuracy approximate such a situation by averaging  $\varepsilon_{\text{ext}} \approx (\varepsilon_{\text{ext}}^{\text{top}} + \varepsilon_{\text{ext}}^{\text{bot}})/2$ .

The Coulomb interaction  $U(\mathbf{q})$  may thus be tuned in experiments by varying the substrate on which the sample is mounted and the materials that encapsulate it. For simplicity we consider dispersionless longitudinal (LO) and transverse (TO) optical phonons with the same phonon frequency  $\omega_e$  and momentum-independent electron-phonon coupling  $g^2$  (for most of the calculation in this paper set to 0.3 eV and 0.3 eV<sup>2</sup>, respectively), such that the bare phonon-mediated electron-electron interactions read  $v_{ph}^{LO/TO}(i\nu_m) = g^2 2\omega_e / [(i\nu_m)^2 - \omega_e^2]$  (see Appendix 5.A for non-local electron-phonon coupling models). While this phonon frequency is set for computational reasons to a value higher than physical phonon frequencies in most materials, it is still much less than the Fermi energy or zone boundary plasmon frequency. Thus, this value does not affect our qualitative conclusions. We use the random phase approximation (RPA) to compute the mutual screening of electrons and longitudinal phonon modes (the transverse mode is unaffected by the Coulomb interaction) from the metallic states. The longitudinal interaction then reads

$$I_L(\mathbf{q}, i\nu_m) = \frac{U(\mathbf{q}) + v_{ph}^{LO}(i\nu_m)}{1 - [U(\mathbf{q}) + v_{ph}^{LO}(i\nu_m)]\Pi^{(0)}(\mathbf{q}, i\nu_m)}, \quad (5.2)$$

with  $\Pi^{(0)}(\mathbf{q}, i\nu_m)$  the RPA polarization given by Eq. 2.25. The full interaction is given by  $I_0(\mathbf{q}, i\nu_m) = I_L(\mathbf{q}, i\nu_m) + v_{ph}^{TO}(i\nu_m)$  and hosts frequency and momentum dependent screened electron-phonon [254–256] and electron-electron interactions including their hybridization. We evaluate the electron dispersion within a nearest-neighbour square-lattice tight binding model with a hopping of  $t = 1.5$  eV ( $m^* \approx 0.1 m_e$ ) and a chemical potential yielding approximately quarter filling. The electron gas parameter  $r_s = m^* e^2 / (\varepsilon_{\text{ext}} \sqrt{\pi n}) < 1$  for all values of  $\varepsilon_{\text{ext}}$  considered, justifying the RPA [34, 50]. To study the effects of plasmons we will compare to results obtained with the statically screened

$$I_L^{\text{stat}}(\mathbf{q}, i\nu_m) = \frac{U(\mathbf{q}) + v_{ph}^{LO}(i\nu_m)}{1 - [U(\mathbf{q}) + v_{ph}^{LO}(i\nu_m)]\Pi^{(0)}(\mathbf{q}, i\nu_m = 0)} \quad (5.3)$$

and the non-mutually screened

$$I_L^{C+ph}(\mathbf{q}, i\nu_m) = \frac{U(\mathbf{q})}{1 - U(\mathbf{q})\Pi^{(0)}(\mathbf{q}, i\nu_m)} + \frac{v_{ph}^{LO}(i\nu_m)}{1 - v_{ph}^{LO}(i\nu_m)\Pi^{(0)}(\mathbf{q}, i\nu_m)} \quad (5.4)$$

longitudinal interactions.

The spectral functions of the longitudinal interaction  $A_L(\mathbf{q}, \omega) = -\text{Im}(I_L(\mathbf{q}, \omega))$ , together with their local spectra  $A_L(\omega) = \sum_{\mathbf{q} \neq 0} A_L(\mathbf{q}, \omega)$ , are shown in Fig. 5.1 for a variety of  $\varepsilon_{\text{ext}}$  (for  $h = 0$ ). For clarity we present only the longitudinal part. For  $\varepsilon_{\text{ext}} = 1$  we find the  $\sqrt{q}$ -like 2D plasmon dispersion. In this regime the bare Coulomb interaction strongly screens the electron-phonon interaction, causing the

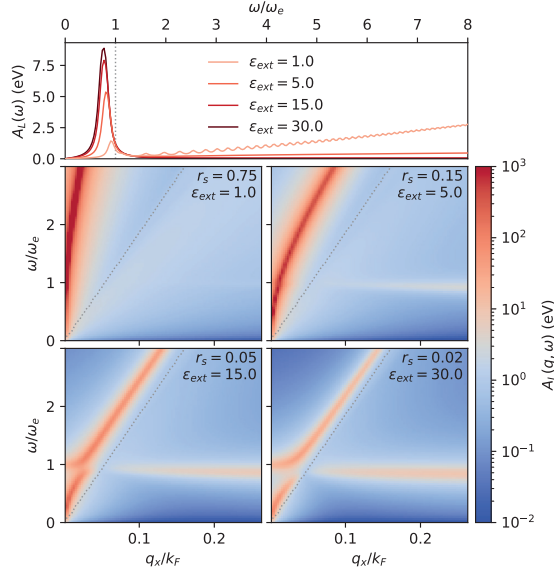


Figure 5.1: Momentum-integrated longitudinal interaction spectral function  $A_L(\omega) = \sum_{\mathbf{q} \neq 0} A_L(\mathbf{q}, \omega)$  (top panel) and momentum-resolved longitudinal spectral function  $A_L(\mathbf{q}, \omega)$  (bottom panels) of the mutually screened longitudinal interaction  $I_L(\mathbf{q}, \omega)$ , calculated using Eq. 5.2 on the real frequency axis for various  $\varepsilon_{\text{ext}}$  in the  $\hbar = 0$  limit. The dotted gray line in the bottom panels traces the upper frequency boundary of the electron-hole continuum.

latter to be negligible. As a result,  $A_L(\omega)$  is governed by the plasmon spectrum. As  $\varepsilon_{\text{ext}}$  is increased, the electron-phonon interaction is screened less, and the phonon dispersion starts to appear at large  $q$ . The effective phonon frequency is reduced in comparison to the bare  $\omega_e$  as a result of screening. This is also visible in  $A_L(\omega)$ , showing phonon peaks always below  $\omega_e$ , which gain intensity as  $\varepsilon_{\text{ext}}$  decreases. In addition we find that as  $\varepsilon_{\text{ext}}$  is increased the resulting softening of the plasmon allows for the phonons and plasmons to hybridize at a  $q$  value which for the parameters used here is around  $q \approx 0.05k_F$ , with  $k_F$  the Fermi wave vector. This non-trivial momentum and frequency structure of the interaction necessitates a consistent theory that retains both the full frequency and momentum structure of the normal and anomalous self-energies to describe superconductivity in 2D materials.

We treat both the normal and anomalous self-energies in a one-loop approximation. The linearized equation for the anomalous self-energy  $\phi(k, i\omega_n)$  is an eigenvalue equation given by Eq. 2.95, where instead of  $W(\mathbf{q}, i\nu_m)$  we use  $I_0(\mathbf{q}, i\nu_m)$ . The leading eigenvalue  $\lambda(T)$  is defined such that at the transition temperature  $T_c$ ,

$\lambda(T_c) = 1$ . The dressed normal-state Green's function  $G_e(k, i\omega_n)$  is obtained from Eq. 2.14, with the normal-state self-energy given by Eq. 2.36. The  $k = k'$  terms in the momentum sums are excluded to account for the counteracting positive charge background. The gap equation was solved using an iterative solver implemented in the TRIQS [155] and TPRF [257] packages using  $180 \times 180$   $k$  and  $q$  grids and a Matsubara cut-off of  $\omega_c = 30$  eV.

### 5.3 TRANSITION TEMPERATURE

Resolving low  $T_c$  is challenging due to the number of required Matsubara frequencies. Instead we analyze  $\lambda$  at a fixed temperature  $T = 98$  K (the reference  $T_c$  for  $\varepsilon_{\text{ext}} \rightarrow \infty$ ) which serves as a proxy for the dependence of  $T_c$  on parameters.

The solid-blue curve in Fig. 5.2(a) shows  $\lambda$  of as a function of the strength of the Coulomb interaction controlled by the background dielectric constant  $\varepsilon_{\text{ext}}$  in the  $\hbar = 0$  limit. As  $\varepsilon_{\text{ext}} \rightarrow \infty$  the Coulomb interaction is suppressed and the eigenvalue tends to the value  $\lambda = 1$  found for  $T = 98$  K in the phonon-only model. Decreasing  $\varepsilon_{\text{ext}}$  from  $\infty$  initially decreases  $\lambda$  consistent with the conventional expectation that the Coulomb repulsion formally counteracts the phonon-mediated attraction. However, a minimum in  $\lambda$  at  $\varepsilon_{\text{ext}} \approx 3$  is evident, and for smaller  $\varepsilon_{\text{ext}}$  the leading eigenvalue again increases, signalling a different behavior in the Coulomb-dominated small  $\varepsilon_{\text{ext}}$  regime.

In Fig. 5.2(a) we compare the full  $\lambda$  to that from the statically screened interaction  $I_0^{\text{stat}}(\mathbf{q}, i\nu_m)$  (orange-dotted line), and the dynamical interaction without mutual screening between the electron-electron and electron-phonon interactions  $I_0^{C+ph}(\mathbf{q}, i\nu_m)$  (green-dashed line). In the weak Coulomb regime  $\varepsilon_{\text{ext}} \gtrsim 7$  we see that dynamic screening has a negligible effect on superconductivity (orange and blue lines coincide) but the static Coulomb interaction is important (difference from black line). In this regime the plasmon is strongly Landau-damped over most of the relevant momentum range, rendering the electron-phonon interaction the dominant pairing interaction. The superconducting state can qualitatively be understood within the Tolmachev-Morel-Anderson pseudopotential  $\mu^*$  approximation [109, 134], such  $T_C \propto e^{-1/\lambda^*}$ , with the effective pairing strength  $1/\lambda^* = (1 + \lambda_{ph})/(\lambda_{ph} - \mu^*)$  [131–133]. As  $\varepsilon_{\text{ext}}$  is decreased the Coulomb repulsion parameterized by  $\mu^*$  increases in strength, leading to a lower  $T_c$  and thus a lower  $\lambda$ . Furthermore, we find in this regime that  $\lambda$  is overestimated when the cross-coupling of the longitudinal phonon and the plasmon is neglected (difference between green and orange/blue lines). This effect can be understood as an effective decrease of  $\lambda_{ph}$ , due to the static Coulomb interaction screening the electron-phonon interaction [129, 241, 258].

In the  $\varepsilon_{\text{ext}} < 3$  regime we see that the static screening approximation (orange line) predicts a strongly suppressed  $\lambda$  compared to the full model (blue line). This is

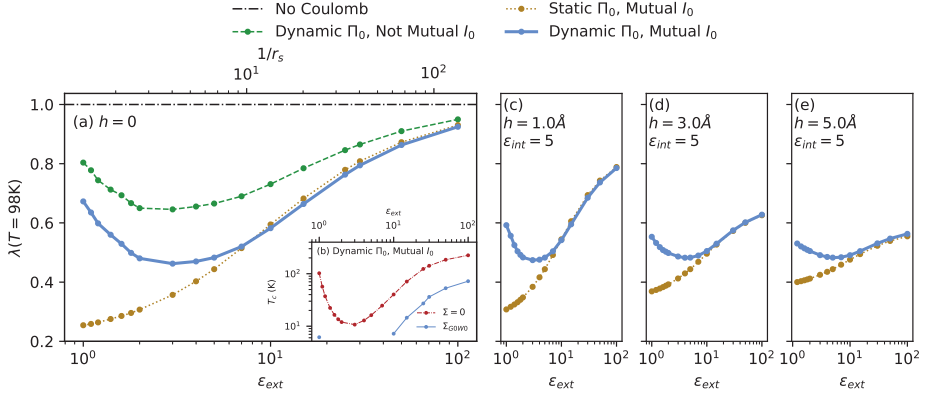


Figure 5.2: (a) Leading eigenvalue  $\lambda$  of Eq. 2.95 at temperature  $T = T_c^{\varepsilon \rightarrow \infty} = 98$  K as a function of the external background screening parameter  $\varepsilon_{\text{ext}}$  at  $h = 0$  (lower axis) and the inverse gas parameter  $1/r_s = (m^* e^2 / (\varepsilon_{\text{ext}} \sqrt{\pi n}))^{-1}$  (upper axis), for a variety of different models for the total interaction. (Black-dashed) Neglecting the Coulomb interaction, i.e.,  $I_0(\mathbf{q}, i\nu_m)$  where  $U(\mathbf{q}) = 0$ . (Green-dashed) Neglecting mutual screening  $I_0^{C+ph}(\mathbf{q}, i\nu_m)$ . (Yellow-dotted) Statically mutually screened  $I_0^{\text{stat}}(\mathbf{q}, i\nu_m)$ . (Blue-solid) Fully dynamically and mutually screened  $I_0(\mathbf{q}, i\nu_m)$ . (b) The critical temperatures for the full dynamic and mutually screened model obtained by solving the linearized gap equation including (blue) and excluding (red) normal-state renormalization. (c)-(e) The leading eigenvalue  $\lambda$  at  $T = 98$  K as a function of external screening  $\varepsilon_{\text{ext}}$ , for a variety of effective material thicknesses  $h$  at  $\varepsilon_{\text{int}} = 5$ .

due to the static Coulomb interaction which strongly screens the electron-phonon interaction, rendering conventional phonon pairing negligible. From this we can conclude that in this regime the dominant pairing channel is the electron-plasmon interaction. This is in line with the spectral functions shown in Fig. 5.1, where the phonon mode is negligible compared to the plasmon mode at  $\varepsilon_{\text{ext}} = 1$ . Mutual screening between the different bosons again decreases  $\lambda$  (difference between green and blue curves), which we still understand as resulting from the strong screening of the electron-phonon interactions in this limit.

The minimum around  $\varepsilon_{\text{ext}} \approx 3$  arises from the crossover between the two different pairing regimes, which vanish in opposite limits. Here, the electron-plasmon coupling is too weak and the static Coulomb repulsion too strong to induce any strong pairing.

In the inset of Fig. 5.2(a) we compare the actual  $T_c$  of the full model to  $T_c$  calculated from Eq. 2.95 without the normal-state self energy. For the full model, the computational complexities restrict us to  $T_c$  only over part of the  $\varepsilon_{\text{ext}}$  range, but in the model without normal-state self-energy the entire curve can be traced

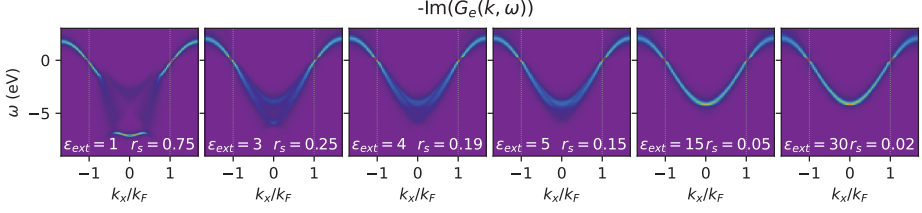


Figure 5.3: Spectral function of the dressed normal-state Green’s function  $-\text{Im}(G_e(k, i\omega_n))$  calculated on the real frequency axis for various  $\varepsilon_{\text{ext}}$ , at  $h = 0$ .

out. These curves confirm that the  $\varepsilon_{\text{ext}}$  dependence of  $\lambda$  is a good proxy for  $T_c$ , such that  $T_c$  as a function of  $\varepsilon_{\text{ext}}$  will show the same trends as  $\lambda$ . We further see, in agreement with results previously obtained in the 3D plasmon-only model [70, 252], that normal-state self-energy effects drastically reduce  $T_c$ , which is in 2D, however, strongly tuned by the screening  $\varepsilon_{\text{ext}}$ .

In Figs. 5.2(c)-(e) we further show  $\lambda$  for various  $\varepsilon_{\text{ext}}$ , at fixed internal screening  $\varepsilon_{\text{int}} = 5$  (graphene has  $\varepsilon_{\text{int}} \approx 2$  and transition metal dichalcogenides have  $\varepsilon_{\text{int}} \approx 10$ ) [98, 102] for various finite material thicknesses  $h$ . We again find the same qualitative behaviour with distinct plasmon and phonon mediated regimes at small and large  $\varepsilon_{\text{ext}}$ , respectively. As the material thickness  $h$  increases the superconducting state becomes less susceptible to the external screening, while the internal screening  $\varepsilon_{\text{int}}$  becomes more and more dominant (see Appendix 5.B for details).

#### 5.4 NORMAL-STATE

In Fig. 5.3 we show the spectral function of  $G_e(k, \omega)$  for  $h = 0$ . For  $\varepsilon_{\text{ext}} = 30$  and  $\varepsilon_{\text{ext}} = 15$  we find the conventional electron-phonon coupling induced mass enhancement, accompanied by an increase of the spectral weight at the bottom of the quasi-particle band. Both of these features are characteristic for phononic normal-state renormalizations. [126] This is in line with the decrease of  $T_c$  by a factor of about 3 for  $\varepsilon \geq 7$ , as shown in the inset of Fig. 5.2, which is well approximated by the ratio of  $T_c$  with and without normal-state contributions

$$T_c(\Sigma)/T_c(\Sigma = 0) \approx e^{\frac{1}{\lambda_{ph}} - \frac{1+\lambda_{ph}}{\lambda_{ph}}} = e^{-1} \approx 1/2.72.$$

As  $\varepsilon_{\text{ext}}$  is decreased below 5, spectral weight of occupied states around  $k = 0$  is shifted away from the main quasi-particle band into a plasmonic side band at lower energies. Eventually, at  $\varepsilon_{\text{ext}} = 1$ , due to the strong static Coulomb interaction, most of the spectral weight has shifted into the shake-off band, rendering the latter strongly coherent and the initial quasi-particle band incoherent. These results are

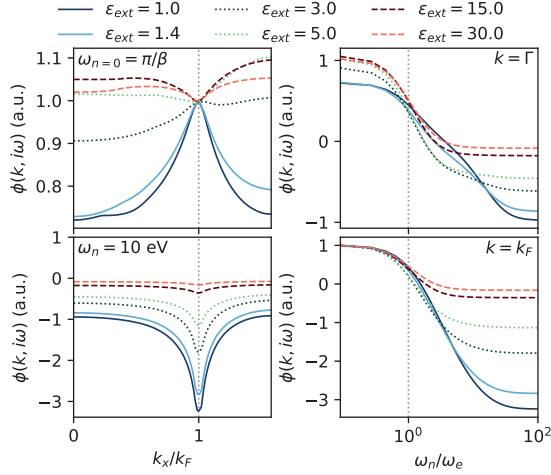


Figure 5.4: Eigenvector  $\phi(k, i\omega_n)$  corresponding to the leading eigenvalue of Eq. 2.95 at temperature  $T = T_c^{\epsilon \rightarrow \infty} = 98$  K, as a function of  $k_x$  (left panels) and as a function of Matsubara frequency  $\omega_n$  (right panels), for  $\epsilon_{\text{ext}}$  in the plasmonic (blue solid), phononic (red dashed) and intermediate (green dotted) regimes. In all cases  $\phi(k = k_F, i\omega_{n=0}) = 1$ .

reminiscent of plasmonic polarons, which were observed in various 2D materials using angle-resolved photoemission spectroscopy (ARPES) measurements. [61, 76] At  $\epsilon_{\text{ext}} = 1$ ,  $T_c$  is reduced by a factor of 18 by the normal-state self-energy, as visible in the inset of Fig. 5.2. This significant  $T_c$  reduction is caused by the strong spectral weight transfer described by  $G_e(k, \omega) \approx Z_k G_0(k, \omega)$ , where  $Z_k^{-1} = 1 - \partial_\omega \Sigma(k, \omega)|_{\omega=\xi_k}$  is a measure for the amount of spectral weight transfer. This approximation is justified in the low  $\epsilon_{\text{ext}}$  regime, as here the dynamic and non-local Coulomb interactions do not significantly change the effective mass. [241] Within this approximation it is clear that the anomalous self-energy of Eq. 2.36 is scaled by a factor  $Z_k^2 < 1$ , yielding a strongly reduced  $T_c$ . [70, 252]

## 5.5 ANOMALOUS SELF-ENERGY

The distinct phonon and plasmon mediated regimes are also clearly visible in the eigenvectors  $\phi(k, i\omega_n)$ , shown in Fig. 5.4. In the phonon-mediated regime ( $\epsilon_{\text{ext}} > 3$ ),  $\phi(k, i\omega_n)$  shows the conventional characteristics of electron-phonon mediated superconductivity affected by static Coulomb repulsion; we find a strong peak around  $i\omega_{n=0}$  with a width on the order of the phonon frequency  $\omega_e$  accompanied by a negative high-frequency tail. In momentum space  $\phi(k, i\omega_n)$  is only



weakly structured as a result of the momentum-independent bare electron-phonon interaction  $v_{ph}(i\nu_m)$  in our model. Approximating the Coulomb interaction with a constant Tolmachev-Morel-Anderson pseudopotential  $\mu^*$  might thus be reasonable for phonon mediated superconductivity in this regime.

In the plasmon-mediated regime ( $\varepsilon_{\text{ext}} < 3$ ),  $\phi(k, i\omega_n)$  also shows a peak around  $i\omega_{n=0}$ , but with an enhanced width, which increases with decreasing  $\varepsilon_{\text{ext}}$ . The high-frequency negative tail is furthermore strongly enhanced. In momentum space,  $\phi(k, i\omega_n)$  has a strong momentum dependence around  $k_F$ , which is qualitatively changing with Matsubara frequency. While  $\phi(k, i\omega_n)$  shows a maximum at  $i\omega_{n=0}$ , it turns into a minimum at large  $i\omega_n$ , which we identify as a clear signature of plasmonic superconductivity in 2D. In the plasmon-dominated limit at  $\varepsilon_{\text{ext}} = 1$ , we interpret this behaviour as a result of the interplay between the static bare and dynamic screened Coulomb interaction  $W(\mathbf{q}, \omega) = U(\mathbf{q}) + \Delta W(\mathbf{q}, \omega)$ , which, respectively, yield a repulsive static  $\phi_C(\mathbf{q})$  and attractive dynamic  $\phi_{\Delta W}(\mathbf{q}, \omega)$  in analogy to the conventional electron-phonon pairing mechanism under the influence of static Coulomb repulsion. Here, however, the dynamic  $\phi_{\Delta W}(\mathbf{q}, \omega)$  is controlled by the rather large plasmon energies, which does not allow for a separation of energies anymore. As a result there is no logarithmic renormalization of the repulsive term from  $U(\mathbf{q})$ . This explains the strong negative tail in frequency space. Since the attractive  $\phi_{\Delta W}(\mathbf{q}, \omega)$  is driven by the plasmon frequencies the pairing frequency is enhanced. Finally, as the attraction is induced by the electron-plasmon coupling, which strongly favours pairing at small momentum transfer  $q$ , we find a pronounced momentum structure. The plasmon-mediated regime is very sensitive to the precise value of  $\varepsilon_{\text{ext}}$ , which is in line with the Coulomb-based interpretation.

In the intermediate regime around  $\varepsilon_{\text{ext}} \approx 3$  we find a pronounced negative tail in the frequency domain, which cannot be compensated by the weak momentum structure. This again shows the interplay between the weak electron-plasmon coupling and strong static Coulomb repulsion, which explains the suppressed superconducting state here.

## 5.6 EXPERIMENTAL VERIFICATION

Our theory predicts plasmonic effects to superconductivity to be dominant at low external screening  $\varepsilon_{\text{ext}} \lesssim 3$ . Therefore, using substrates with dielectric constants in this range, such as very thin hBN or SiO<sub>2</sub> [259–261] and especially suspended monolayers (i.e.,  $\varepsilon_{\text{ext}} = 1$ ), are promising options for finding plasmon mediated superconductivity, while a substrate such as SrTiO<sub>3</sub>, with a large dielectric constant of  $\varepsilon_{\text{ext}} > 100$  below room temperature [262], will most likely screen out any plasmonic effects. In addition, we argue in Appendix 5.B that thin materials ( $h \lesssim 3 \text{ \AA}$ ) with low internal screening, are likely especially good candidates to

observe the distinct plasmon and phonon regimes, since these materials are most sensitive to the external dielectric environment  $\varepsilon_{\text{ext}}$ .

The most promising method would be measuring the critical temperature as a function of external screening. Especially the observation of an enhanced  $T_c$  upon reduced external screening is a clear sign of plasmon mediated superconductivity, as this is in direct contradiction to predictions from conventional electron-phonon mediated superconductivity. In the conventional Tolmachev-Morel-Anderson Coulomb pseudopotential  $\mu^*$  approximation, reduced external screening would reduce  $T_c$  due to enhanced static Coulomb repulsion. Therefore, if plasmonic effects play a role, fitting the  $\mu^*$  parameter using the experimentally measured  $T_c$  will result in unexpected trends as a function of  $\varepsilon_{\text{ext}}$ , even in the intermediate regime where  $T_c$  is not yet increasing with  $\varepsilon_{\text{ext}}$ . This might be realized with spatially varying the screening environment [263, 264] of the layered superconductor by partially covering it, such that the external dielectric environment changes between the covered and non-covered parts of the superconductor.

A second hint towards plasmonic superconductivity is an unusual  $T_c$  behavior as a function of doping. In conventional superconductors one expects  $T_c$  to scale exponentially with the density of states at the Fermi level  $N_0$ , since  $\lambda_{ph} \propto N_0$ . In the two dimensional case considered here the main density of states feature is a van Hove singularity. Decreasing the density away from it would be expected to lead to a dramatic decrease in  $T_c$ . However, as we show in Appendix 5.C, in the plasmon mediated regime  $T_c$  is less affected by  $N_0$  and might even increase at small doping because decreasing the density also increases the relative importance of the electron-electron interaction.

Thirdly, the observation of plasmonic renormalization effects in the normal state signifies a strong electron-plasmon coupling, and thus hints towards plasmonic effects in the superconducting state as well. In our results, plasmon mediated superconductivity is always accompanied by plasmonic shake-off bands and spectral weight transfer away from the Fermi energy. These effects could be observed by, for example, ARPES measurements.

Finally, the isotope effect may also be modified in the plasmonic regime, as it involves both the ionic mass (phonon frequency) dependence of the electron-phonon coupling via  $\lambda_{ph} = g^2/\omega_e$  and the interplay of the phonon and plasmon frequency scales. Note also that in realistic materials additional complications arise [265–268]. A full treatment is therefore beyond the scope of this paper. To nevertheless obtain an estimate, we present in Fig. 5.5(a) the leading eigenvalue  $\lambda$  as a function of  $\varepsilon_{\text{ext}}$  for different phonon frequencies  $\omega_e$  with  $\lambda_{ph} \propto g^2/\omega_e$  held fixed, for the fully dynamically (solid lines) and statically (dotted lines) screened interactions. We see that at large  $\varepsilon_{\text{ext}} \gtrsim 7$  (phonon regime) there is a substantial dependence of  $\lambda$  on the phonon frequency, while at smaller  $\varepsilon_{\text{ext}}$  the leading eigenvalue becomes almost independent of the phonon frequency.

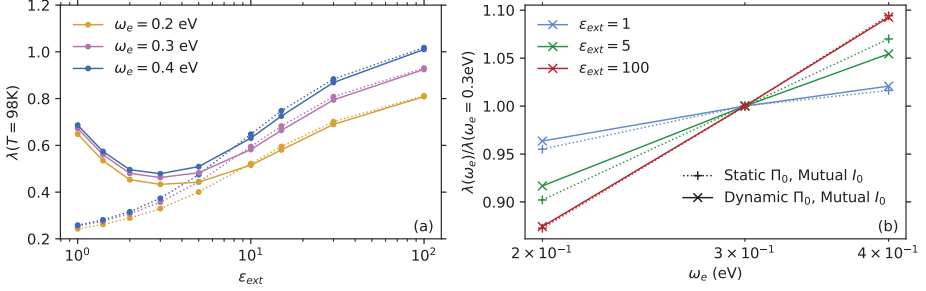


Figure 5.5: Isotope effect analysis of the leading eigenvalue  $\lambda$  at  $T = 98\text{K}$  and  $h = 0$ . (a)  $\lambda$  as a function of  $\epsilon_{\text{ext}}$ , for various  $\omega_e$ . (b)  $\lambda/\lambda(\omega_e = 0.3\text{eV})$  as a function of  $\omega_e$ , for various  $\epsilon_{\text{ext}}$ . In all plots, we kept  $\lambda_{ph}$  constant by changing  $g^2$  accordingly for each  $\omega_e$ . Solid (dotted) lines signify calculations using fully dynamically and mutually screened  $I_0(\mathbf{q}, i\nu_m)$  (statically mutually screened  $I_0^{\text{stat}}(\mathbf{q}, i\nu_m)$ ).

To understand the implications of this result, note that in the conventional theory of electron-phonon-coupled superconductivity one may approximate the eigenvalue Eq. 2.95 as

$$\lambda(T, \omega_e) = C(\lambda_{ph} - \mu^*) \ln \frac{\omega_e}{T}, \quad (5.5)$$

where the constant  $C$  includes factors arising from the normal state self energy and from angular and frequency integrations. At  $\epsilon_{\text{ext}} = 100$ ,  $\mu^* \approx 0$  such that Eq. 5.5 may be recast as

$$\frac{\lambda(T, \omega_e)}{\lambda(T, \omega_e = 0.3\text{eV})} = 1 + \frac{\ln \frac{\omega_e}{0.3\text{eV}}}{\ln \frac{0.3\text{eV}}{T}}. \quad (5.6)$$

Fig 5.5(b) plots this ratio against  $\ln \omega_e$ . For  $\epsilon_{\text{ext}} = 100$  the agreement between the calculated data and the simple formula is excellent. As  $\epsilon_{\text{ext}}$  is decreased, we find in Fig 5.5(a) a decrease in the dependence of  $\lambda$  on  $\omega_e$ , which is reflected in panel (b) as a decrease in the slope of the ratio. In the statically screened interaction case (dotted lines) we may understand this decrease in slope as arising from the dependence of  $\mu^*$  on  $\omega_e$  (in the strong coulomb limit,  $\mu^* \propto -1/\ln \omega_e$ ). Thus in the instantaneous interaction picture a weaker isotope effect is a signature of the importance of  $\mu^*$  and goes along with a *low*  $T_c$ . A weak isotope effect accompanied by a *high*  $T_c$  therefore indicates plasmonic pairing. However this analysis requires independent assessments of  $\lambda_{ph}$  and  $\mu^*$  in the conventional picture and may not be definitive in any given experimental system.

## 5.7 CONCLUSIONS

We have shown that superconductivity in layered materials, when consistently influenced by electron-phonon, electron-plasmon, and phonon-plasmon interactions, can develop three distinct regimes, which can be tuned by the overall strength of Coulomb interactions. For strong Coulomb interactions (small screening) we find a plasmon mediated regime, for (strongly) reduced Coulomb interactions we find that phonon mediation becomes prominent, while for intermediate Coulomb interaction the static repulsion is too strong and the plasmonic pairing too weak such that superconductivity is suppressed. These regimes have clear individual footprints in the gap functions and also show distinctively different impacts on the normal-state self-energy renormalizations. We can expect to find these phases for materials with a small internal background screening  $\varepsilon_{int}$ . The external, e.g., substrate-screening, tunability will be most prominent if the effective height  $h$  of the material is small. Our results furthermore show that two-dimensional superconductivity mediated by plasmons is possible within the RPA when the background screening is weak, such that the plasmon dispersion is well separated from the electron-hole continuum. Note that in all cases considered here  $r_s < 1$  holds (different to Takada's [63, 64] seminal results). In this regime the electron-phonon pairing is mostly suppressed due screening. While above we focused on the sensitive role of the screening  $\varepsilon_{ext}$ , we show in Appendix 5.C that the plasmonic regime also survives as a function of doping, with distinctively different characteristics from the phonon-mediated regime. Our results are qualitatively similar to the findings by Wang *et al.* in 3D [252]. However, here we consistently account for the mutual screening between electrons and phonons, find a minimum in  $T_c$  around  $r_s \approx 0.25$ , and have an overall more pronounced structure in  $T_c(r_s)$ , which we find to be strongly influenced by the environmental screening. We attribute these differences between 3D and 2D to the qualitatively different characteristics of plasmonic excitations in 2D.

The pronounced sensitivity to the background screening which drives the crossover between the plasmon- and phonon-mediated regimes is important for the descriptions and measurements of layered superconducting heterostructures. Most experimental data on layered superconductors are obtained from samples mounted on some substrates or encapsulated by other layered materials, which creates a non-local screening environment as described by our background-dielectric function. Our results also show that this background screening channel can be utilized to precisely tune the superconducting state via modifications of the environment. In the limit of strong substrate screening phonons are responsible for Cooper pairing. In this regime our results show that the Coulomb pseudo-potential  $\mu^*$  can be a valid approximation. However, mutual screening should be taken into account and the static but non-local Coulomb interaction must be handled carefully [129, 241, 258].

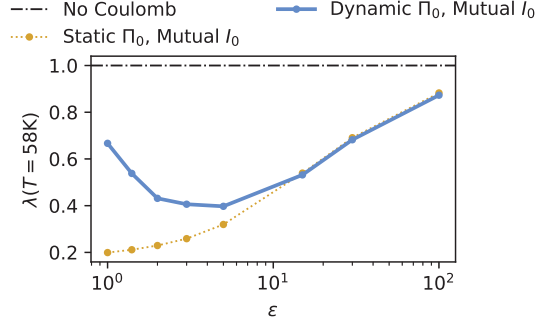


Figure 5.6: Leading eigenvalue  $\lambda$  at temperature  $T = T_c^{\varepsilon \rightarrow \infty} = 58$  K as a function of the local background screening parameter  $\varepsilon$ , using a non-local Fröhlich electron-phonon interaction  $g(q)^2$  with parameters  $h = 2 \text{ \AA}$ ,  $g_F^2 = 0.7 \text{ eV}^2$  and  $\omega_e = 0.3 \text{ eV}$ , for a variety of different models for the total interaction. (Black-dashed) Neglecting the Coulomb interaction, i.e.,  $I_0(q, i\nu_m)$  where  $\nu_C(q) = 0$ . (Yellow-dotted) Statically mutually screened  $I_0^{\text{stat}}(q, i\nu_m)$ . (Blue-solid) Fully dynamically and mutually screened  $I_0(q, i\nu_m)$ .

The intermediate regime around  $\varepsilon_{\text{ext}} = 3$ , in which both electron-plasmon and electron-phonon interactions act simultaneously, is likely especially relevant, since commonly used substrates for 2D materials, such as hBN or SiO<sub>2</sub>, have dielectric constants in this range. [259–261] In this regime, the  $\mu^*$  approximation can cause an underestimation of the critical temperature and would hide plasmonic footprints on the gap function. As discussed in the Appendix 5.C, a signature of this situation could be that fits of  $\mu^*$  to experimental results yield unexpected trends as a function of  $\varepsilon$  or the doping of a system. An alternative potential signature of plasmonic effects on the superconducting state is the observation of plasmonic shake-off bands in the normal state, which our results show accompany the plasmon-mediated and intermediate regimes. In future work it may also be interesting to fully analyze the isotope effect in the plasmon mediated regime and to investigate the difference in coherence length and penetration depth between the two regimes. All these effects could have distinct footprints of plasmon mediated superconductivity, which might help to identify this pairing experimentally.

## 5.A NON-LOCAL ELECTRON-PHONON INTERACTION

In order to understand how non-locality in the bare electron-phonon coupling will affect the results of the main text, we consider the following Fröhlich electron-phonon coupling appropriate for 2D materials [269]

$$g(q)^2 = g_F^2 \operatorname{erfc} \left( \frac{1}{2} h q \right)^2, \quad (5.7)$$

where  $\operatorname{erfc}(x)$  is the complementary error function and  $h$  tunes the non-locality induced by the effective thickness of the material. For  $h = 0$  we recover the local coupling  $g(q)^2 = g_F^2$  model from the main text. The non-local bare electron-phonon interactions are  $v_{ph}^{LO/TO}(q, i\nu_m) = g(q)^2 2\omega_e / [(i\nu_m)^2 - \omega_e^2]$ . In Fig. 5.6 we show the leading eigenvalue  $\lambda$  of the superconducting gap equation at  $T = 58$  K (which is the critical temperature  $T_c$  if Coulomb contributions are neglected), where  $h = 2 \text{ \AA}$  and  $g_F^2 = 0.7 \text{ eV}^2$ . The phonon energy was set to  $\omega_e = 0.3 \text{ eV}$ , as in the main text. We find that non-locality in the bare electron-phonon interaction does not qualitatively change the results discussed in the main text. This can be understood from the structure of the Fröhlich interaction, which strongly suppresses the electron-phonon interaction in the  $q \gtrsim 1/h \approx 1.3k_F$  regime (and thus reduces  $T_c$  by reducing the effective  $\lambda_{ph}$ ), while the interplay between phonon and plasmon branches takes place at much smaller momenta  $q \approx 0.05k_F$  (see the main text). The interplay is thus only weakly affected by the non-locality of the electron-phonon interaction and as a result the qualitative structure of the plasmon- and phonon-mediated regimes is not changed.

## 5.B NON-LOCAL BACKGROUND SCREENING

In Fig. 5.7 we show the superconducting leading eigenvalue  $\lambda$  at  $T = 98$  K as a function of external screening  $\varepsilon_{ext}$ . We compare  $\lambda$  including (blue-solid) and excluding (yellow-dotted) plasmonic contributions to understand the behaviour of the plasmon and phonon mediated regimes upon varying material properties  $h$  and  $\varepsilon_{int}$ . Similar to the conclusions of the main text, we find that plasmonic contributions to superconductivity are strong when the total screening is weak. The effective height  $h$  tunes whether  $\varepsilon_{ext}$  or  $\varepsilon_{int}$  contributes most to the total screening, as discussed in chapter 2. For example, at  $h = 0$  the background screening is completely determined by the external screening at all momenta  $q$ , such that plasmonic enhancement of  $\lambda$  is found only when  $\varepsilon_{ext} \lesssim 10$ . On the other hand, for  $h = 5 \text{ \AA}$  the effect of  $\varepsilon_{ext}$  is rather weak, and we only find plasmonic enhancement for weak internal screening  $\varepsilon_{int} \lesssim 10$ .

From this, we clearly understand that if the overall screening is weak plasmons can enhance superconductivity (as compared to the situation with electron-phonon

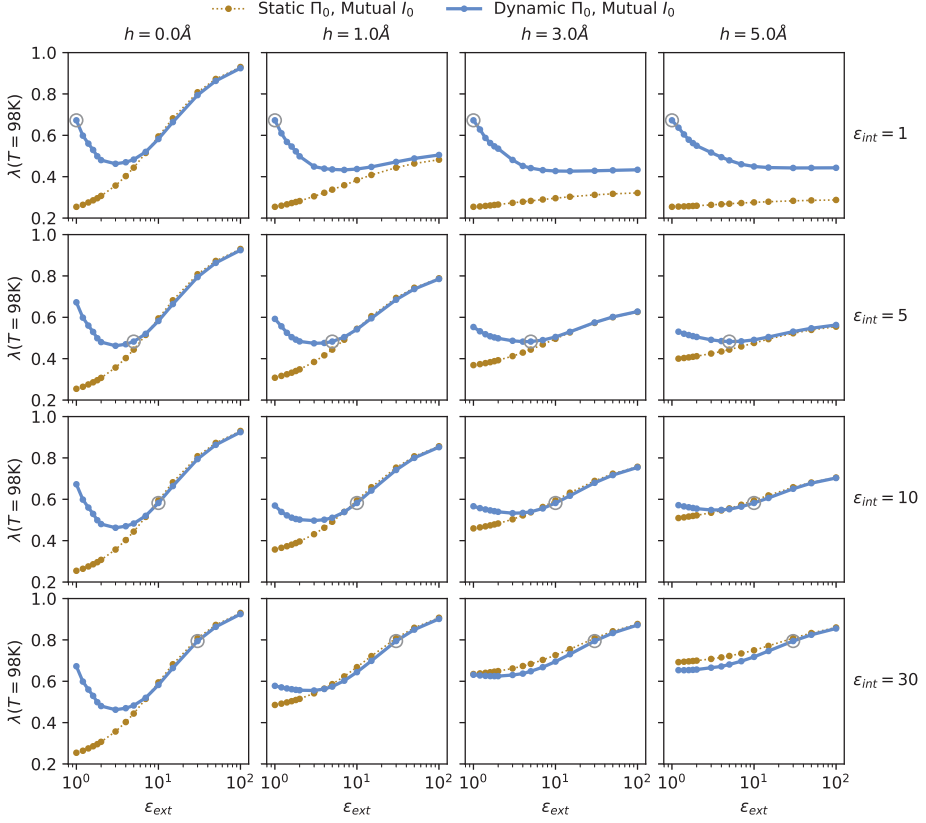


Figure 5.7: The leading eigenvalue  $\lambda$  at  $T = 98 \text{ K}$  including non-local background screening as a function of external screening  $\varepsilon_{ext}$ , for a variety of effective material thicknesses (or setback distance of screening layer from superconducting sheet)  $h$  and internal screening  $\varepsilon_{int}$ . (Yellow-dotted) Statically mutually screened  $I_0^{stat}(q, i\nu_m)$ . (Blue-solid) Fully dynamically and mutually screened  $I_0(q, i\nu_m)$ . The gray circles surround the point where  $\varepsilon_{ext} = \varepsilon_{int}$ .

and statically screened Coulomb interaction only), the interplay between enhanced electron-plasmon and electron-phonon interactions generically suppresses superconductivity as a result of the simultaneously present and equally strong static Coulomb repulsion in this regime, and that for enhanced overall screening the systems behaves as a conventional superconductor under the influence of static Coulomb repulsion.

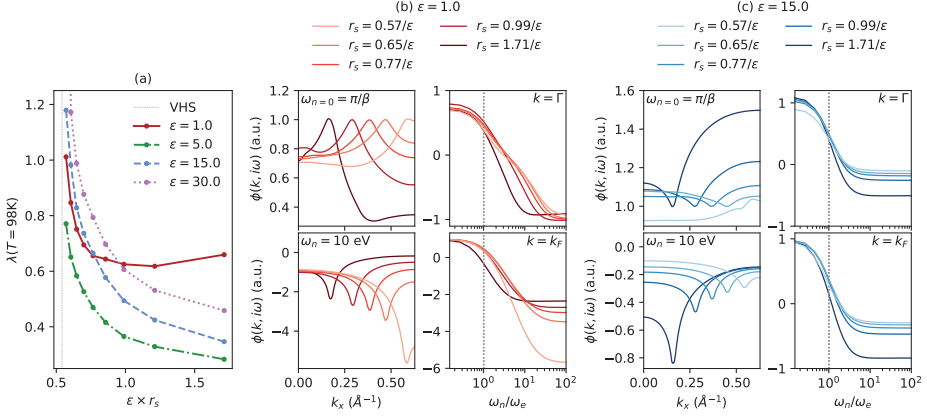


Figure 5.8: (a) The leading eigenvalue  $\lambda$  of Eq. 2.95 at temperature  $T = 98\text{ K}$  for the fully mutual and dynamic model  $I_0(q, i\nu_m)$ , as a function of  $\varepsilon \times r_s$ , while varying the electron occupation, for various  $\varepsilon$  and at  $h \rightarrow 0$ . The dotted gray line indicates the location of the Van Hove singularity. The other panels show the corresponding eigenvectors  $\phi(k, i\omega_n)$  at  $\varepsilon = 1$  (b) and  $\varepsilon = 15$  (c) at temperature  $T = 98\text{ K}$ , as a function of  $k_x$  and as a function of Matsubara frequency  $\omega_n$ , for various electron occupations. In all cases  $\phi(k = k_F, i\omega_{n=0}) = 1$ .

### 5.C DOPING DEPENDENCE

To investigate the dependence of our results on the doping level, we performed additional calculations varying the electron occupation  $n$ . Changing the carrier concentration changes the effective electron-electron interaction strength, parameterized by the electron gas parameter  $r_s = m^*e^2/(\varepsilon\sqrt{\pi n})$ , and also may move the Fermi level nearer or farther from the van Hove singularity. Fig. 5.8(a) shows the leading eigenvalue  $\lambda$  as a function of the electron occupation (here parameterized by  $\varepsilon r_s$ ) for the full dynamically mutually screened model  $I_0(q, i\nu_m)$ . The previously noted non-monotonic variation of  $\lambda$  with interaction strength is observed at all densities. As the doping is increased towards the van Hove singularity (around  $r_s \approx 0.5/\varepsilon$ ), the density of states at the Fermi level increases, and therefore  $T_c$  increases as well due to the enhanced  $\lambda^*$ . At larger  $r_s$  and  $\varepsilon \neq 1$  the systematic decrease in  $\lambda$  arises from the combination of decrease in density of states as the Fermi level is moved away from the van Hove singularity and the increase in effective electron-electron interaction. However for  $\varepsilon = 1$  the theory is in the plasmon mediated regime where the eigenvalue increases as the interaction strength decreases; this competes with the density of states effect leading to the weakly non-monotonic  $r_s$  dependence.



In Fig. 5.8 (b) and (c) we analyze the eigenvectors  $\phi(k, i\omega_n)$  for  $\varepsilon = 1$  (plasmon regime) and  $\varepsilon = 15$  (phonon regime), respectively. The trends of the eigenvector with occupation are rather different in the two regimes. At  $\varepsilon = 15$  the results can be understood using the conventional electron-phonon and static Coulomb interactions. As  $r_s$  is increased away from the Van Hove singularity (doping is reduced), the screening is reduced and thus the Coulomb interaction is enhanced. This is reflected in  $\phi(k, i\omega_n)$  by the enhanced high-frequency tail and by the more pronounced momentum structure at large  $r_s$ . At  $\varepsilon = 1$  we find that the negative high-frequency tail at  $k_F$  is reduced as  $r_s$  increases, which is opposite to what one would expect from the Tolmachev-Morel-Anderson Coulomb pseudopotential approximation  $\mu^*$  [109, 134], showing again the breakdown of this approximation in the weakly screened limit. We also find that, unlike at  $\varepsilon = 15$ , the strong momentum peak of  $\phi(k, i\omega_n)$  at  $\varepsilon = 1$  and  $\omega_n = 10$  eV is reduced as  $r_s$  increases. Simultaneously the momentum structure at  $i\omega_{n=0}$  is enhanced, such that we see a shift of the momentum structure from  $i\omega_n = 10$  eV to  $i\omega_{n=0}$  as  $r_s$  increases at  $\varepsilon = 1$ . A final feature that highlights the distinct phonon and plasmon regimes is the width of the peak of  $\phi(k, i\omega_n)$  along  $\omega_n$ . At  $\varepsilon = 15$  the width is close to the bare phonon frequency  $\omega_e$  for all  $r_s$ , showing that the dominant pairing boson is the phonon at all doping levels. On the other hand, at  $\varepsilon = 1$  the width of  $\phi(k, i\omega_n)$  at  $k = \Gamma$  decreases as  $r_s$  increases. This indicates that the energy of the pairing boson decreases with decreased doping, as expected for the two-dimensional plasmon dispersion.



## ENHANCED SUPERCONDUCTIVITY FROM DYNAMICAL ENVIRONMENTAL SCREENING

---

This chapter is based on work that is currently in preparation for publication and was done in collaboration with M.I. Katsnelson, A.J. Millis, and M. Rösner. All calculations were performed by me, with frequent discussions on the interpretation and further steps from all collaborators. The text in this chapter has been written by me, with input from M. Rösner.

### 6.1 INTRODUCTION

In the previous chapter we have seen that the fundamental interactions that drive correlated physics in layered materials can be tuned via static environmental screening. Such static Coulomb engineering is in fact a very efficient tool for the precise tailoring of many-body properties of 2D materials, including band-gaps [98, 102, 186, 270, 271], exciton binding energies [186, 264] and potentially even Mott insulating phases [272]. In chapter 5 specifically, we have shown that the properties of layered superconductors, such as superconducting gaps or critical temperatures, can also be tuned in this way. [62, 101, 129]

This concept is, however, not restricted to static environmental screening. In fact, dynamical screening from the environment, which can be described by bosonic excitations in surrounding materials, has also been shown to affect correlated material properties. Via this mechanism, substrate bosons can for example change exciton binding energies [273, 274] or induce interlayer plasmon polaron excitations [60], as discussed in detail in chapter 4. The drastic  $T_c$  enhancement of monolayer FeSe when grown on top of SrTiO<sub>3</sub> has furthermore been hypothesized to originate from SrTiO<sub>3</sub> boson modes [19, 275], such as phonons [67, 233, 276–279] or plasmons [119], coupled into the FeSe layer. In layered bulk superconductors, the hybridization of intralayer plasmon modes via dynamical interlayer screening was theoretically predicted to enhance the critical temperature significantly [68, 72] and has also been suggested to be a relevant pairing channel in high- $T_c$  superconductors. [69, 280] Also in twisted bilayer graphene and twisted bilayer WSe<sub>2</sub>, coupled interlayer plasmon modes have been argued to play a role in the superconducting state. [281–283] They have furthermore been suggested to yield a relatively high plasmon-induced critical temperature in a stack consisting of a Dirac semi-metal and a transition metal dichalcogenide. [284]

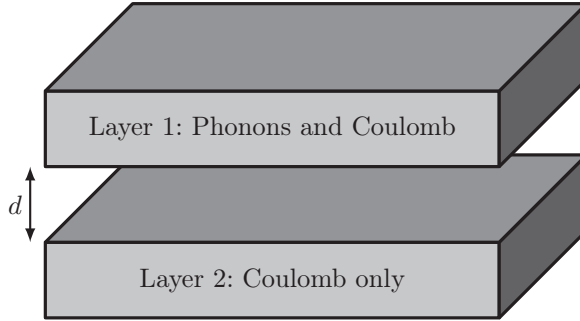


Figure 6.1: Schematic illustration of the heterostructure that we consider. The top layer is the target layer, which hosts superconductivity. The bottom layer is a neighbouring layer which (dynamically) screens the target layer via the long-range Coulomb interaction. Hybridization between the layers is assumed to be negligible.

Taken together, these works show that dynamical environmental screening can affect correlated ground states of 2D materials in non-trivial ways. It is therefore intriguing to study to what extent this mechanism can be exploited to tailor correlated phases in layered materials. More specifically, the tunability of plasmon-induced phases in this way needs to be studied, since plasmonic properties, such as dispersions or electron-plasmon couplings, are particularly sensitive to dynamical environmental screening. [285–290]

To this end, we will show in the following that such ‘boson engineering’ is especially promising for layered plasmon-mediated superconductors [62–64, 71, 284], because it allows to tune the plasmon-induced superconducting pairing at low frequencies, without affecting the high-frequency static Coulomb induced repulsion. In this way, by engineering the 2D plasmon mode via dynamical environmental screening, we are able to find significantly enhanced plasmon-induced superconducting critical temperatures.

As a proof of concept, we will consider the effect of interlayer dynamical screening in a bilayer system, consisting of a superconducting and a metallic layer. We further assume that the layers do not hybridize electronically, for example because they are spatially separated by insulating hexagonal boron nitride (hBN) layers. In this way, we aim to understand how the superconducting state can be tailored solely by exploiting interlayer dynamical screening. Using the formalism of chapter 5, we furthermore consistently take into account the mutual screening between all relevant boson modes.

## 6.2 MODEL

In Fig. 6.1 we show a schematic illustration of the heterostructure we are considering. It consists of two metallic monolayers, which are separated by an interlayer distance  $d$ . Electronic hybridization between the layers is assumed to be negligible and thus neglected. We assume layer 1 hosts superconductivity that is mediated by the combination of phonon and plasmon modes within that layer. Layer 2 acts as a metallic environment which screens layer 1. For simplicity, we neglect the electron-phonon coupling in layer 2, such that it is not superconducting at the temperatures we are considering. Layer 2 does, however, host plasmon modes which can be coupled into the superconducting layer via the interlayer Coulomb interaction.

We define the non-interacting Hamiltonian using the effective-mass approximation, such that it is given in the layer-basis as

$$\hat{h}(\mathbf{k}) = \begin{pmatrix} k^2/(2m_1^*) - E_{F1} & 0 \\ 0 & k^2/(2m_2^*) - E_{F2} \end{pmatrix} \quad (6.1)$$

with  $m_1^*$  and  $m_2^*$  the effective masses in layer 1 and 2, respectively, and  $E_{F1}$  and  $E_{F2}$  the respective Fermi energies. In the layer basis, the diagonal components capture the intralayer contributions, whereas the off-diagonal terms capture interlayer electronic hybridization. Since we aim to study the impact of environmental screening, we will fix the properties of the superconducting layer (layer 1) to  $m_1^* = 0.2m_e$  and  $E_{F1} = 1\text{eV}$ , while the properties of layer 2 will be varied.

For the interaction, we use the same model as in Chap. 5 and Ref. [62] extended to a multilayer system. We will furthermore use the density-density approximation for all interactions, such that they can be described by matrices in the layer basis. Therefore, the total interaction matrix is given by

$$\hat{I}(\mathbf{q}, i\nu_m) = \left[ \hat{\mathcal{I}} - \left( \hat{U}(\mathbf{q}) + \hat{I}_{ph,LO}^{(0)}(\mathbf{q}, i\nu_m) \right) \hat{\Pi}^{(0)}(\mathbf{q}, i\nu_m) \right]^{-1} \left( \hat{U}(\mathbf{q}) + \hat{I}_{ph,LO}^{(0)}(\mathbf{q}, i\nu_m) \right) + \hat{I}_{ph,TO}^{(0)}(i\nu_m), \quad (6.2)$$

with  $\hat{\mathcal{I}}$  the identity matrix. In this formalism, the bare Coulomb interaction  $\hat{U}(\mathbf{q})$  and the electron-electron interaction mediated by the longitudinal optical (LO) phonon mode  $\hat{I}_{ph,LO}^{(0)}(\mathbf{q}, i\nu_m)$  are mutually screened by each other in the random phase approximation (RPA). The transverse optical (TO) phonon mode (and the corresponding electron-electron interaction  $\hat{I}_{ph,TO}^{(0)}(i\nu_m)$ ) is assumed to be unscreened. The RPA polarization tensor is a matrix in the density-density approximation  $\hat{\Pi}^{(0)}(\mathbf{q}, i\nu_m)$ . Since the layers are not hybridized, it is diagonal

$$\hat{\Pi}^{(0)}(\mathbf{q}, i\nu_m) = \begin{pmatrix} \Pi_1^{(0)}(\mathbf{q}, i\nu_m) & 0 \\ 0 & \Pi_2^{(0)}(\mathbf{q}, i\nu_m) \end{pmatrix}, \quad (6.3)$$

with  $\Pi_i^{(0)}(\mathbf{q}, i\nu_m)$  the Lindhard function evaluated for layer  $i$ .

For the phonon modes in layer 1, we assume that both the TO and LO phonon modes have frequency  $\omega_e = 0.3 \text{ eV}$  and electron-phonon coupling  $g_{ph}^2 = 0.3 \text{ eV}^2$ . In order to make numerical computations more feasible, these parameters have values that are high for realistic materials. However, they are still in the regime  $\omega_e < E_F$  where Migdal's theorem is believed to be valid, such that our qualitative conclusions are not affected. In layer 2 we assume that the electron-phonon interaction vanishes, such that the total longitudinal and transverse phonon mediated electron-electron interaction matrices are given by

$$\hat{I}_{ph,LO}^{(0)}(i\nu_m) = \hat{I}_{ph,TO}^{(0)}(i\nu_m) = \begin{pmatrix} g_{ph}^2 D_{ph}(i\nu_m) & 0 \\ 0 & 0 \end{pmatrix}, \quad (6.4)$$

with  $D_{ph}(i\nu_m) = 2\omega_e/((i\nu_m)^2 - \omega_e^2)$  the bare phonon propagator in layer 1. The layers are coupled via the long-range Coulomb interaction in the density-density approximation. The diagonal components of the corresponding matrix have the usual intralayer bare 2D Coulomb interaction  $U_{\mathbf{q}} = 2\pi e^2/(A\varepsilon q)$ , where  $\varepsilon$  captures the electrostatic screening from the environment of the heterostructure. The off-diagonal terms are approximated by a layer-distance dependant exponential form-factor  $\exp(-qd)$ , such that the full bare Coulomb matrix is given by

$$\hat{U}(\mathbf{q}) = U_{\mathbf{q}} \begin{pmatrix} 1 & e^{-qd} \\ e^{-qd} & 1 \end{pmatrix}. \quad (6.5)$$

In this chapter our focus is on the effect of interlayer screening on the superconducting layer. In principle, superconductivity can also be induced in the neighbouring layer via the proximity effect, but here we neglect such effects. We can therefore simplify our theory by integrating out the screening layer, such that we find an effective scalar interaction in layer 1. It is given by  $I_1(\mathbf{q}, i\nu_m) = I_1^L(\mathbf{q}, i\nu_m) + I_1^T(i\nu_m)$ , with the transversal part given by  $I_1^T(i\nu_m) = g_{ph}^2 D_{ph}(i\nu_m)$  and the longitudinal part by

$$I_1^L(\mathbf{q}, i\nu_m) = \frac{\tilde{I}_1^{(0)}(\mathbf{q}, i\nu_m)}{1 - \tilde{I}_1^{(0)}(\mathbf{q}, i\nu_m)\Pi_1^{(0)}(\mathbf{q}, i\nu_m)}. \quad (6.6)$$

Here  $\tilde{I}_1^{(0)}(\mathbf{q}, i\nu_m)$  is the effective bare interaction in layer 1, which is defined as

$$\tilde{I}_1^{(0)}(\mathbf{q}, i\nu_m) = U_{\mathbf{q}} + g_{ph}^2 D_{ph}(i\nu_m) + U_{\mathbf{q}} e^{-qd} \frac{\Pi_2^{(0)}(\mathbf{q}, i\nu_m)}{1 - U_{\mathbf{q}} \Pi_2^{(0)}(\mathbf{q}, i\nu_m)} U_{\mathbf{q}} e^{-qd}. \quad (6.7)$$

The resulting expression for  $I_1^L$  is reminiscent of the full mutually screened interaction of a monolayer in a static dielectric environment as given by Eq. 5.2. [62] The only difference is the last term in Eq. 6.7, which takes into account polarization

processes in layer 2 that are coupled into layer 1 via the interlayer Coulomb interaction. We use  $I_1$  to perform  $G_0W_0$  and linearized one-loop superconductivity calculations within layer 1, following the formalism outlined in Sect. 2.5 and in Ref. [62].

### 6.3 COMPUTATIONAL DETAILS

All calculations were performed using the TRIQS [155] and TPRF [257] codebases, using a linearly discretized momentum mesh of 300x300 points. The Matsubara axis was represented using the recently developed discrete Lehman representation (DLR) [140], which drastically reduces the temperature scaling of the required amount of Matsubara frequencies to  $\mathcal{O}(\log(\beta))$  compared to a full Matsubara mesh which scales as  $\mathcal{O}(\beta)$ . Due to the improved scaling with temperature, we can now resolve the superconducting critical temperatures in the low screening limit. For all calculations, the DLR error tolerance was set to  $\epsilon = 1e - 10$  and the high-energy cutoff to  $\omega_{\max} = 50$  eV. Real-frequency  $G_0W_0$  calculations have been performed on a 100x100 momentum mesh and a linearly spaced frequency mesh with 1000 points between -20 and 20 eV.

### 6.4 INTERLAYER PLASMON MODES

In order to connect to the usual Eliashberg formalism of superconductivity, we write the effective electron-electron interaction in layer 1 in the spectral representation

$$I_1(\mathbf{q}, i\nu_m) = U_{\mathbf{q}} + \frac{1}{N_0} \int_0^\infty d\omega (\lambda_{\mathbf{q}}^L(\omega) + \lambda^T(\omega)) \frac{\omega^2}{(i\nu_m)^2 - \omega^2}, \quad (6.8)$$

where  $N_0$  is the DOS at the Fermi energy and we defined the longitudinal electron-electron coupling as

$$\lambda_{\mathbf{q}}^L(\omega) = \frac{2N_0 B_{\mathbf{q}}^L(\omega)}{\omega}, \quad (6.9)$$

with  $B_{\mathbf{q}}^L(\omega) = -\text{Im}(I_1^L(\mathbf{q}, \omega)) / \pi$ . The transversal electron-electron coupling  $\lambda^T(\omega)$  originates from an unscreened Einstein phonon mode, such that it is described by the usual BCS expression  $\lambda^T(\omega) = 2N_0 g_{ph}^2 / \omega_e \delta(\omega - \omega_e)$ . The longitudinal electron-electron coupling  $\lambda_{\mathbf{q}}^L(\omega)$  originates from the hybridized longitudinal phonon mode and interlayer plasmon modes. We stress that in the high-frequency limit  $I_1(\mathbf{q}, i\nu_m \rightarrow \infty) = U_{\mathbf{q}}$  is simply the intralayer bare Coulomb repulsion and is therefore unaffected by the neighbouring layer. We therefore conclude that dynamical interlayer screening allows us to tune only the attractive low-energy part of the interaction, without altering the high-energy repulsive part.

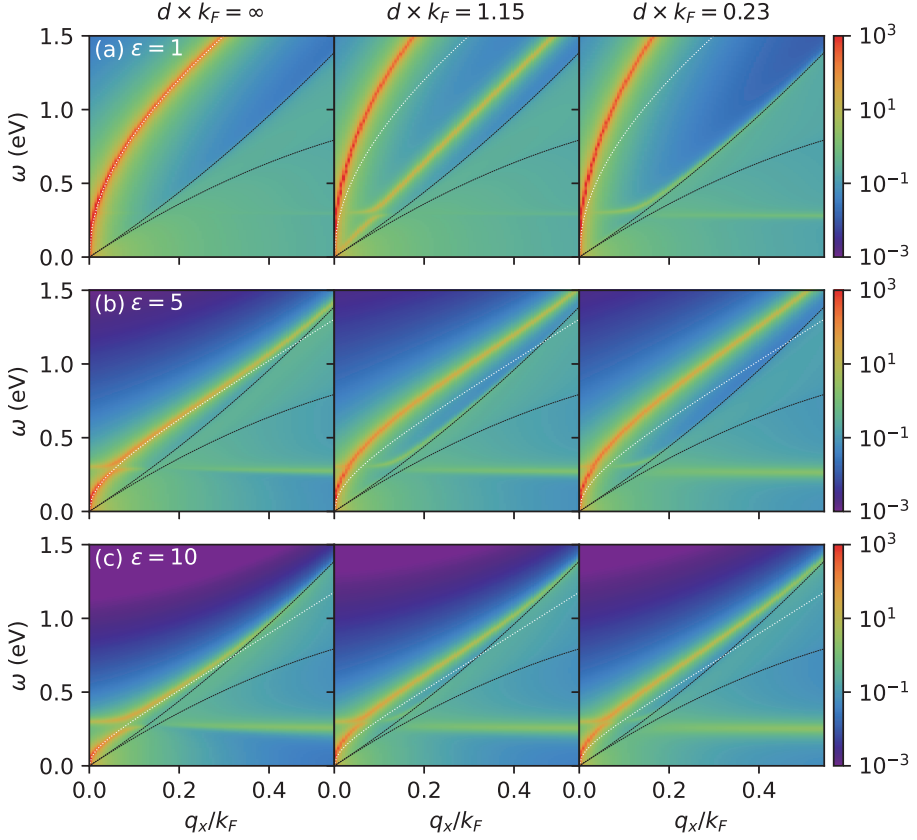


Figure 6.2: The longitudinal electron-electron coupling  $\lambda_{\mathbf{q}}^L(\omega)$  within layer 1, for different interlayer distances  $d$  at  $\varepsilon = 1$  (a),  $\varepsilon = 5$  (b) and  $\varepsilon = 10$  (c). The dashed black lines denote the edges of the electron-hole continua and the dotted white lines denote the plasmon dispersion of an isolated layer (i.e., at  $d \times k_F = \infty$ ). These results were obtained for equivalent monolayers, with  $m_1^* = m_2^* = 0.2m_e$  and  $E_{F1} = E_{F2} = 1$  eV. The temperature is set to  $T = 100$  K.

We show  $\lambda_{\mathbf{q}}^L(\omega)$  in Fig. 6.2, for various interlayer distances  $d$  and environmental dielectric constants  $\varepsilon$ . For infinite layer distance (left-most panels) we reproduce the hybridized phonon-plasmon mode of a monolayer in a static dielectric environment. [62] In this case, at large  $\varepsilon$  there is clear hybridization between the dispersionless phonon mode and the  $\sqrt{q}$ -like two-dimensional plasmon mode, whereas at smaller  $\varepsilon$  the Coulomb interaction screens out the phonon-mode, such that the phonon-plasmon hybridization is negligible. As the interlayer distance is decreased to a



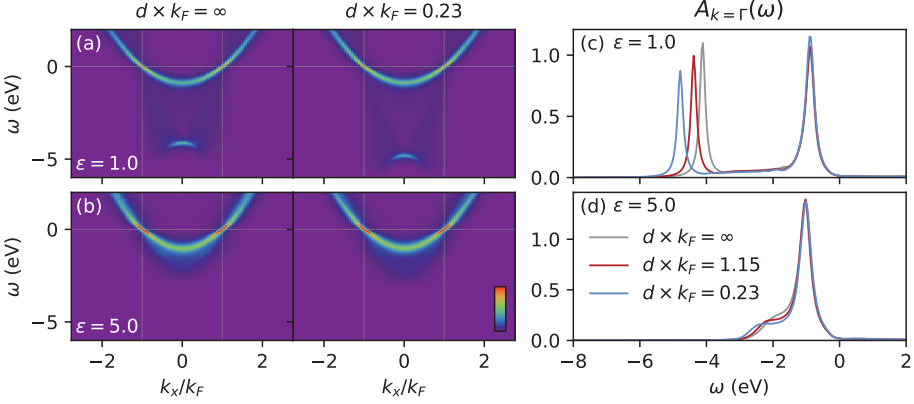


Figure 6.3: (a,b) Momentum-resolved  $G_0W_0$  spectral function  $A_{\mathbf{k}}(\omega)$ , for different interlayer distances at  $\varepsilon = 1$  (a) and  $\varepsilon = 5$  (b). (c,d) Linecut of the spectral function  $A_{\mathbf{k}}(\omega)$  at  $\mathbf{k} = \Gamma$  at  $\varepsilon = 1$  and  $\varepsilon = 5$ , respectively. These results were obtained for equivalent monolayers, with  $m_1^* = m_2^* = 0.2m_e$  and  $E_{F1} = E_{F2} = 1$  eV. The temperature is set to  $T = 100$  K.

finite number at  $\varepsilon = 1$ , two distinct inter-layer plasmon modes appear, as is typical of coupled two-dimensional plasmon modes. [287–290] The high-energy mode is a charged mode, because the corresponding electron density oscillations are in-phase between the layers. It still follows a  $\sqrt{q}$ -like dispersion in the long-wavelength limit, but is shifted to higher energies compared to the plasmon mode at  $d = \infty$  (indicated by the dotted white line) as the interlayer distance decreases. The low-energy mode is a charge neutral mode, since its oscillations of the electron-density are out of phase between the layers. It has a linear dispersion and lies below the energy of the isolated layer plasmon mode. As the interlayer distance decreases, this mode shifts into the electron-hole continuum (indicated by the dashed black lines), such that it is Landau damped if the layers are close enough. Similar trends can be observed for  $\varepsilon > 1$  as well, but in this case the distance at which the charge neutral mode starts to be Landau damped is larger. As for the longitudinal phonon mode, its coupling strength to the electrons (reflected by its intensity in Fig. 6.2) is not significantly affected by the dynamical interlayer screening. This is a consequence of the different energy scales of the phonon and plasmon modes. It does, however, hybridize more strongly with the charge neutral plasmon mode than with the charged plasmon mode.

## 6.5 NORMAL-STATE

In the left panels of Fig. 6.3 we show the dressed electronic spectral function  $A_{\mathbf{k}}(\omega) = -\text{Im}(G(\mathbf{k}, \omega))/\pi$  in the  $G_0W_0$  approximation of a monolayer in a static dielectric environment. These results are reminiscent to those obtained previously in chapter 5 and Ref. [62] for a square lattice. Around the Fermi energy at  $\varepsilon = 5$  we find the typical phononic mass-enhancement, which is strongly reduced for  $\varepsilon = 1$  due to the screening from the Coulomb interaction. Below the band minimum we find additional spectral weight coming from plasmon polaron excitations. For  $\varepsilon = 1$  these excitations induce a relatively coherent shakeoff band, whereas for  $\varepsilon = 5$  they induce an incoherent shoulder. The energy separation between the shakeoff feature and the band minimum is determined by a representative energy scale of the plasmon dispersion, as discussed in chapter 4 and in Ref. [60]. When we introduce the second layer (shown in the right panels of Fig. 6.3(a) and (b)), we find qualitatively the same features. Quantitatively, however, the plasmon polaron shakeoff features shift to lower energies, further away from the band minimum, as seen in the frequency linecuts of  $A_{\mathbf{k}}(\omega)$  at  $\mathbf{k} = \Gamma$  (shown in panels (c) and (d) of Fig. 6.3). This is a consequence of the shift of the plasmonic spectral weight to higher energies, due to the enhanced frequency of the charged interlayer plasmon mode and due to the Landau damping of the neutral interlayer plasmon mode. These results reproduce the conclusion of chapter 4, that interlayer dynamical screening can affect the normal state of a material.

## 6.6 EFFECT OF INTERLAYER COUPLING TO SUPERCONDUCTIVITY

In chapter 5 we have shown that, in the regime of weak (static) environmental screening, plasmons are able to mediate superconductivity in two-dimensional monolayers. [62] However, because of the unfeasible amount of required Matsubara frequencies at low temperatures, our conclusions were based on calculations at temperatures well above the critical temperature  $T_c$ , by observing the behaviour of the leading eigenvalue of the linearized superconducting gap equation. Here, by making use of the recent advances in the compact representation of the Matsubara axis by way of the DLR [140], we are able to do calculations at low enough temperatures to actually resolve  $T_c$  for our chosen parameters. Therefore, we can confirm the conclusions of our previous work directly using  $T_c$ , which we will briefly summarize here.

The gray line in Fig. 6.4 shows the superconducting critical temperature  $T_c$  of a monolayer in a static dielectric environment, as a function of the external dielectric constant  $\varepsilon$ . At  $\varepsilon = \infty$  (the dashed horizontal line) the only interactions contributing to the superconductivity are the LO and TO electron-phonon interactions. Reducing  $\varepsilon$  from there to the regime  $\varepsilon \gtrsim 20$ ,  $T_c$  is reduced by the conventional static Coulomb

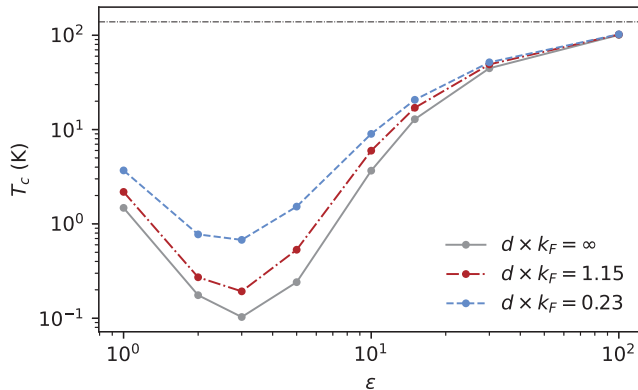


Figure 6.4: The superconducting critical temperature  $T_c$  within layer 1 as a function of external screening  $\epsilon$ , for different interlayer distances  $d$ . The horizontal dashed line denotes the  $T_c$  corresponding to  $\epsilon = \infty$ .

repulsion. Dynamical screening effects do not play a major role here, therefore we denote this regime the phononic regime. As  $\epsilon$  decreases further,  $T_c$  reaches a minimum around  $\epsilon \approx 3$ . Here the electron-phonon coupling is strongly reduced by static Coulomb screening, while at the same time the plasmon-induced attraction is not yet strong enough to overcome the effect of static Coulomb repulsion. The result is a strongly suppressed  $T_c$ . Beyond this minimum, for  $\epsilon \lesssim 2$ , the plasmon mediated electron-electron attraction starts to dominate the interaction, leading again to an enhancement of  $T_c$ . This regime we denote as the plasmonic regime. It is clear that the balance between static repulsion and dynamical attraction plays an important role in the behaviour of  $T_c$  as a function of  $\epsilon$ . In the monolayer limit, the static and dynamic parts of the Coulomb interaction are inherently linked, such that attempts to change one will unavoidably also change the other. The addition of a neighbouring metallic layer can circumvent this limitation, because it can tune the dynamics of the Coulomb interaction without altering the static high-frequency limit. The  $T_c$  obtained when including an additional layer at distance  $d = 1.15/k_F$  and  $d = 0.23/k_F$  are shown in the red and blue lines of Fig. 6.4, respectively. In the phonon-mediated regime ( $\epsilon \gtrsim 20$ ) we find relatively small changes in  $T_c$ . In this regime, phonon mediated attraction and static Coulomb induced repulsion dominate over the plasmonic contributions, such that changes to the plasmonic properties from interlayer coupling are ineffective. However, for  $\epsilon \lesssim 20$  we do find a significant enhancement of  $T_c$  as the interlayer distance  $d$  is reduced. Here the plasmons that contribute to superconductivity are efficiently tuned by dynamical screening from the neighbouring layer.

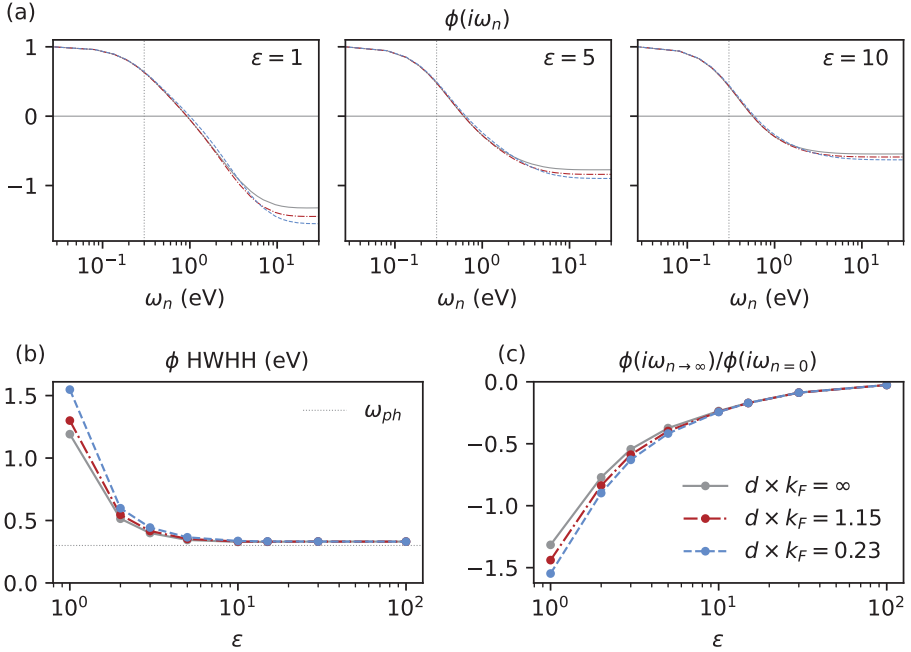


Figure 6.5: (a) The momentum-summed anomalous self-energy  $\phi(i\omega_n)$  at  $T = 100$  K as a function of Matsubara frequency  $\omega_n$ . The left, middle and right panels have  $\epsilon = 1, 5$  and  $10$ , respectively. The vertical dotted line indicates the bare phonon frequency  $\omega_{ph}$ . In all cases  $\phi$  is normalized such that  $\phi(i\omega_{n=0}) = 1$ . (b) The half-width at half-height (HWHH) of  $\phi(i\omega_n)$ . (c) The high-frequency tail of  $\phi(i\omega_n)$ . These results were obtained for equivalent monolayers, with  $m_1^* = m_2^* = 0.2m_e$  and  $E_{F1} = E_{F2} = 1$  eV.

**ANOMALOUS SELF-ENERGY** In Fig. 6.5(a) we show the local (momentum-summed) anomalous self-energy  $\phi(i\omega_n) = \sum_{\mathbf{k}} \phi(\mathbf{k}, i\omega_n)$ . Since  $\phi(\mathbf{k}, i\omega_n)$  is obtained from the linearized gap equation, it has an arbitrary normalization factor. Here, the normalization factor was fixed such that  $\phi(i\omega_{n=0}) = 1$ . For all  $d$  we find the characteristic features of the crossover from phonon to plasmon mediated superconductivity as  $\epsilon$  is reduced, as discussed in chapter 5 and Ref. [62]. In short, the increased half-width at half-height (HWHH) of  $\phi(i\omega_n)$  (shown in panel (b)) as  $\epsilon$  reduces reflects that the dominating mediating boson switches from the lower-energy phonon mode to the higher-energy plasmon mode. Furthermore, the high-frequency tail (shown in panel (c)) is reduced as  $\epsilon$  reduces due to the enhanced static Coulomb repulsion at low  $\epsilon$ .

Introducing the neighbouring metallic layer does not qualitatively change the trends of  $\phi(i\omega_n)$  as a function of  $\epsilon$ , indicating that there is still a crossover from phonon

to plasmon mediated superconductivity. Quantitatively there are some differences however. Firstly, the half-width at half-height of  $\phi(i\omega_n)$  is enhanced by interlayer dynamical screening. Similarly to the changes in the normal state spectral function, this reflects that the spectral weight of the interaction is shifted to higher energies. Secondly, the high-frequency tail of  $\phi(i\omega_n)$  is reduced upon reducing  $d$ . This can be analyzed in an approximate BCS picture, in which the high-frequency tail of  $\phi(i\omega_n)$  behaves as  $-\mu^*/(\lambda_{\text{eff}} - \mu^*)$ , with  $\mu^*$  the TMA Coulomb pseudopotential and  $\lambda_{\text{eff}}$  being an effective parameter describing the electron-electron attraction. [36, 109] We expect the value of  $\lambda_{\text{eff}}$  to increase as the layers are brought closer together, because of the enhanced  $T_c$ . The reduced high-frequency tail therefore indicates that the pseudopotential  $\mu^*$  is also enhanced upon reduced  $d$ . These results again hint towards a delicate balance between dynamical attraction, and (renormalized) static repulsion.

## 6.7 QUALITATIVE MODELLING OF PLASMON MEDIATED SUPERCONDUCTIVITY

In order to disentangle the different contributions to the superconducting state, we define a set of model parameters. Using these parameters we aim to explain the qualitative behaviour of  $T_c$  using a McMillan-Allen-Dynes-like expression for the critical temperature [108, 131–133]

$$k_B T_c^{\text{eff}} = 1.13 \omega_{\text{eff}} \exp\left(-\frac{Z_{\text{eff}}}{\lambda_{\text{eff}} - \mu^*}\right). \quad (6.10)$$

Here the effective dimensionless electron-electron pairing strength  $\lambda_{\text{eff}}$  is defined as the total momentum and frequency integral of the electron-electron coupling

$$\lambda_{\text{eff}} = \int_0^\infty d\omega \left( \sum_{\mathbf{q}} \lambda_{\mathbf{q}}^L(\omega) + \lambda^T(\omega) \right). \quad (6.11)$$

This effective coupling is counteracted by the static Coulomb repulsion. Similar to the coupling, we will define a corresponding dimensionless parameter  $\mu^C$ . A common definition of  $\mu^C$  is a double Fermi surface average of  $U_{\mathbf{q}}$ . [109, 111, 129] Here, we instead define it by the momentum sum  $\mu^C = N_0 \sum_{\mathbf{q}} U_{\mathbf{q}}$  for consistency with  $\lambda_{\text{eff}}$ . From Eliashberg theory we understand, however, that it is not the bare potential  $\mu^C$  that enters the effective low-energy gap-equation, but the renormalized Tolmachev-Morel-Anderson pseudopotential  $\mu^*$  [109, 134], given by

$$\mu^* = \frac{\mu^C}{1 + \mu^C \log(E_B/\omega_{\text{eff}})}, \quad (6.12)$$

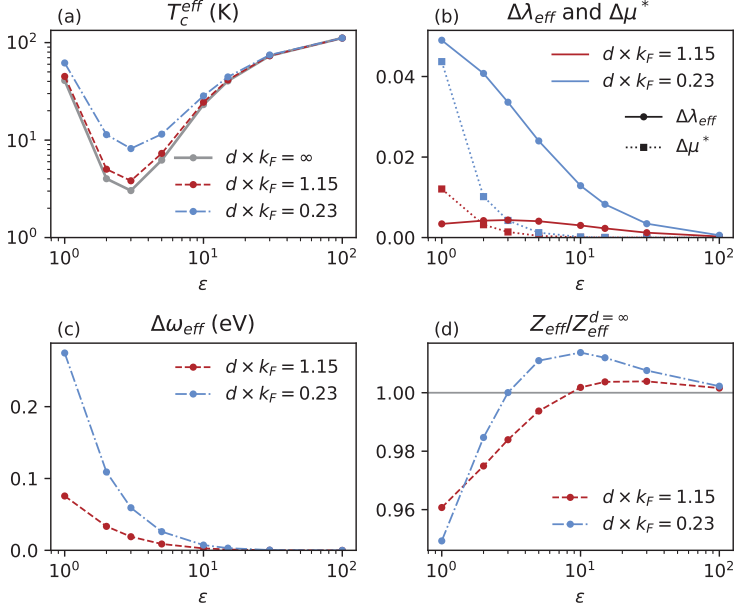


Figure 6.6: Qualitative modelling of plasmon mediated superconductivity. (a) The modelled critical temperature  $T_c^{\text{eff}}$  as a function of  $\epsilon$  for different interlayer distances  $d$ . (b) The change of the effective pairing strength  $\Delta\lambda_{\text{eff}} = \lambda_{\text{eff}} - \lambda_{\text{eff}}^{d=\infty}$  (solid lines) and TMA pseudo-potential  $\Delta\mu^* = \mu^* - \mu_{d=\infty}^*$  (dotted lines) upon introducing a neighbouring metallic layer. (c) The change of the effective boson frequency  $\Delta\omega_{\text{eff}} = \omega_{\text{eff}} - \omega_{\text{eff}}^{d=\infty}$ . (d) The relative change of the effective mass-renormalization factor  $Z_{\text{eff}}/Z_{\text{eff}}^{d=\infty}$ . All results were obtained for  $m_1^* = m_2^* = 0.2m_e$  and  $E_{F1} = E_{F2} = 1$  eV, at  $T = 100$  K.

where  $E_B$  is the bandwidth (set here to  $E_B = 4E_{F1}$  for simplicity). The effective boson frequency  $\omega_{\text{eff}}$  we define using the logarithmic average

$$\omega_{\text{eff}} = \exp \left[ \frac{1}{\lambda_{\text{eff}}} \int_0^\infty d\omega \left( \sum_{\mathbf{q}} \lambda_{\mathbf{q}}^L(\omega) + \lambda^T(\omega) \right) \log(\omega) \right]. \quad (6.13)$$

The final contribution to the critical temperature is the mass-renormalization factor  $Z_{\text{eff}}$ . Similar to Eliashberg theory, we define it using the frequency derivative of the  $G_0W_0$  self-energy evaluated at  $k_F$

$$Z_{\text{eff}} = 1 - \left. \frac{\partial \Sigma(k_F, i\omega_n)}{\partial (i\omega_n)} \right|_{i\omega_n=0}. \quad (6.14)$$

In Fig. 6.6(a) we show  $T_c^{\text{eff}}$  as a function of  $\epsilon$  for different interlayer distances  $d$ . As expected, the quantitative values of  $T_c^{\text{eff}}$  are incorrect due to the simplifications

made by averaging over momentum and frequency. This is especially true for low  $\varepsilon$ , where the non-local nature of the Coulomb interaction becomes more important. Nonetheless,  $T_c^{\text{eff}}$  qualitatively follows the same trends as the numerical  $T_c$  shown in Fig. 6.4, with a clear phononic regime at large  $\varepsilon$  and a plasmonic regime at small  $\varepsilon$ . It also correctly captures the enhancement of superconductivity due to dynamical interlayer screening upon reducing  $d$ . Therefore, we will use this model to analyze the response of each of the effective parameters in  $T_c^{\text{eff}}$  to dynamical interlayer screening. In this way, we aim to find the features a bilayer heterostructure should have for an optimal  $T_c$ .

In the solid lines of Fig. 6.6(b) we show the change of  $\lambda_{\text{eff}}$  upon introducing the neighbouring metallic layer at distance  $d$ , as a function of  $\varepsilon$ . In all cases we find an enhancement of  $\lambda_{\text{eff}}$ . The enhancement is larger if the layers are closer, as a consequence of the enhanced interlayer coupling. Furthermore, the enhancement is larger at small  $\varepsilon$ , reflecting the plasmonic nature of the additional coupling.

The dotted lines in Fig. 6.6(b) show the change of  $\mu^*$  upon introducing the neighbouring metallic layer. As argued before,  $\mu$  is not affected by the interlayer coupling. However, the pseudo-potential  $\mu^*$  can be altered by interlayer coupling via changes in the effective boson frequency  $\omega_{\text{eff}}$ . This effect is mostly negligible in the phononic regime, but in the plasmonic regime  $\varepsilon \lesssim 3$  it causes a significant enhancement of  $\mu^*$ , as a consequence of the enhanced  $\omega_{\text{eff}}$  depicted in Fig. 6.6(c). For most values of  $\varepsilon$ ,  $\lambda_{\text{eff}}$  is enhanced significantly more than  $\mu^*$ , which is the driving force behind the  $T_c$  enhancement from dynamic interlayer screening in Fig. 6.4(a). However, around  $\varepsilon \approx 1$  we find that  $\Delta\lambda_{\text{eff}}$  and  $\Delta\mu^*$  have similar values, with for  $d \times k_F = 1.15$  even  $\Delta\mu^* > \Delta\lambda_{\text{eff}}$ . This explains the relatively weak  $T_c$  enhancement for  $\varepsilon = 1$  compared to  $\varepsilon \approx 3$ .

In Fig. 6.6(d) we show the relative change of  $Z_{\text{eff}}$  due to dynamical interlayer screening. Interestingly, the mass-renormalization is enhanced in the phononic regime, whereas it is reduced in the plasmonic regime. The actual changes are, however, only on the order of a few percent, such that mass-renormalization from dynamical interlayer screening alone cannot qualitatively explain the  $T_c$  enhancement. We therefore conclude that the driving force behind the enhancement of  $T_c$  due to dynamical interlayer screening is the enhancement of the effective electron-electron attraction  $\lambda_{\text{eff}}$ . This enhancement is however weakened by the enhancement of  $\mu^*$  in the low  $\varepsilon$  regime as a consequence of the enhanced  $\omega_{\text{eff}}$ .

## 6.8 OPTIMIZING SUPERCONDUCTIVITY

From the modelling in the previous section we understand that in order to obtain a large  $T_c$  enhancement, the neighbouring layer should induce a low-energy plasmon mode which couples strongly to the electrons. With this in mind, we explore two different avenues for creating heterostructures with optimal  $T_c$ : the choice of

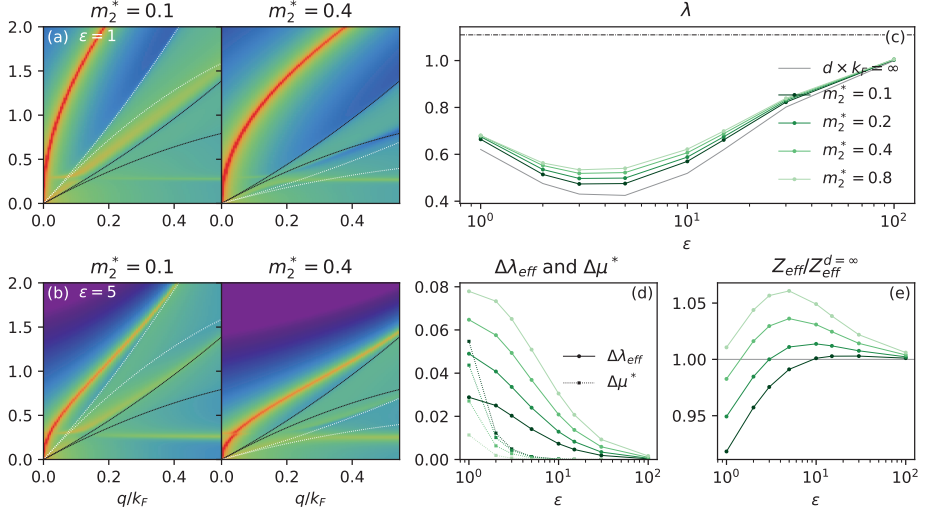


Figure 6.7: Variations in the effective mass of the neighbouring layer  $m_2^*$  at fixed density. The interlayer distance is set to  $d \times k_F = 0.23$  and  $T = 100$  K. (a,b)  $\lambda_{\mathbf{q}}^L(\omega)$  for  $\varepsilon = 1$  and  $\varepsilon = 5$ , respectively, for two effective masses. The black and white dotted lines are the edges of the electron-hole continua of the target layer and the neighbouring layer, respectively. (c) The superconducting leading eigenvalue as a function of  $\varepsilon$ , for various  $m_2^*$ . (d) The change of the effective pairing strength (solid lines) and effective TMA pseudopotential (dotted lines) with respect to the isolated monolayer. (e) The relative change of the mass-renormalization factor with respect to the isolated monolayer.

neighbouring material (captured by the effective mass  $m_2^*$ ) and the doping of the neighbouring material (captured by the Fermi energy  $E_{F2}$ ).

**VARYING THE EFFECTIVE MASS** In Fig. 6.7 we summarize the results when tuning the effective mass of the neighbouring layer  $m_2^*$  at fixed interlayer distance  $d \times k_F = 0.23$ . In these calculations the electron density in layer 2 was kept fixed by changing the Fermi energy  $E_{F2}$  correspondingly. In panels (a) and (b) we show the longitudinal interaction  $\lambda_{\mathbf{q}}^L(\omega)$  in the superconducting layer (layer 1), for two different layer 2 effective masses. We find that the interaction in layer 1 is significantly affected by the effective mass of the neighbouring metallic layer. Enhancing  $m_2^*$  shifts both the charged and neutral plasmon modes to lower energies. For  $m_2^* = 0.1$  the linear neutral mode is still above the continuum of layer 1 (indicated by the black lines), but is broadened by the continuum of layer 2 (indicated by white lines). As  $m_2^*$  is increased to 0.4 it gets damped further, such that it has negligible spectral weight. The charged plasmon mode, on the other



hand, has large regions in the  $(\mathbf{q}, \omega)$  space where it is undamped. Notably, for  $m_2^* = 0.1$  this region is limited by the continuum of layer 2 (white lines), whereas for  $m_2^* = 0.4$  it is limited by the continuum of layer 1 (black lines). Therefore, besides shifting down the plasmon dispersions, enhancing  $m_2^*$  also increases the spectral weight of the charged plasmon mode by shifting away the layer 2 electron-hole continuum. This effect is reflected in the enhancement of  $\lambda_{\text{eff}}$  shown in the solid lines of panel (d).

The dotted lines of panel (d) show that the Coulomb pseudopotential  $\mu^*$  is reduced for enhanced  $m_2^*$ . This is a consequence of the reduced energy of the charged plasmon mode. Both the enhancement of  $\lambda_{\text{eff}}$  and the reduction of  $\mu^*$  contribute to an enhanced critical temperature  $T_c$ , as reflected by the enhancement of the leading eigenvalue  $\lambda$  in panel (c). We note, however, that the enhancement of  $\lambda$  is not the same for all  $\varepsilon$ , with at  $\varepsilon = 1$  even negligible changes of  $\lambda$ . This can be explained by the larger mass-renormalization  $Z_{\text{eff}}$  shown in panel (e), which counteracts the enhancement induced by the changes in  $\lambda_{\text{eff}}$  and  $\mu^*$ .

Overall we conclude that a neighbouring layer with a large effective mass is generally favourable for interlayer plasmon mediated superconductivity.

**VARYING THE FERMI ENERGY** In Fig. 6.8 we summarize the effect of tuning the Fermi energy of the neighbouring layer  $E_{F2}$  at fixed effective mass  $m_2^*$ , thereby changing the electron density in layer 2. Opposite to the effective mass, enhancing  $E_{F2}$  causes the charged plasmon mode to shift to higher energies, as shown on panels (a) and (b). This leads to the enhancement of  $\mu^*$  shown in panel (d). Interestingly, the effect of  $E_{F2}$  on  $\lambda_{\text{eff}}$  is relatively weak, such that the combined  $\Delta\lambda_{\text{eff}} - \Delta\mu^*$  suggests a reduction of the leading eigenvalue  $\lambda$  with increased  $E_{F2}$ . The reason that this reduction is not visible in the numerical evaluation of  $\lambda$  in panel (c) is the mass-renormalization  $Z_{\text{eff}}$ , which is significantly reduced. As a consequence, the different contributions to  $T_c$  cancel each other, such that the total effect of enhancing  $E_{F2}$  is only a relatively small enhancement of the critical temperature.

## 6.9 CONCLUSIONS

We have shown that dynamic screening from a metallic environment can significantly affect the superconducting state of a two-dimensional material. Especially in the regime of intermediate screening, where in the monolayer limit  $T_c$  has a minimum due to the strong static Coulomb repulsion,  $T_c$  can be enhanced by an order of magnitude from dynamic interlayer screening. The driving mechanism behind this enhancement is the hybridization of the two single layer plasmon modes, yielding a charged and a charge neutral interlayer plasmon mode. The linear neutral mode is usually Landau damped, such that it has a negligible effect on

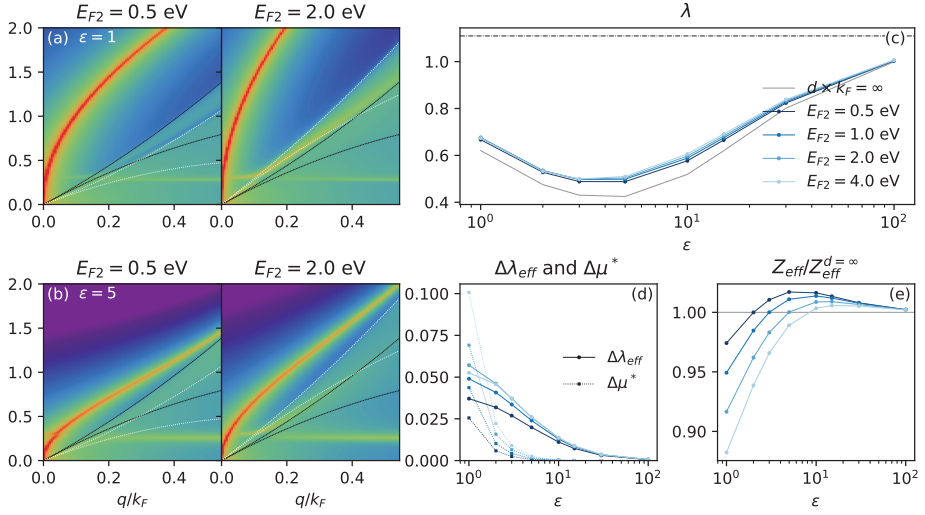


Figure 6.8: Variations in the Fermi energy of the neighbouring layer  $E_{F2}$ . The interlayer distance is set to  $d \times k_F = 0.23$  and  $T = 100$  K. (a,b)  $\lambda_q^L(\omega)$  for  $\varepsilon = 1$  and  $\varepsilon = 5$ , respectively, for two Fermi energies. The black and white dotted lines are the edges of the electron-hole continua of the target layer and the neighbouring layer, respectively. (c) The superconducting leading eigenvalue as a function of  $\varepsilon$ , for various  $E_{F2}$ . (d) The change of the effective pairing strength (solid lines) and effective TMA pseudopotential (dotted lines) with respect to the isolated monolayer. (e) The relative change of the mass-renormalization factor with respect to the isolated monolayer.

the superconducting state. The  $\sqrt{q}$ -like charged mode, however, does couple to electrons, with a coupling strength that is stronger than the coupling of the inherent monolayer plasmon mode, thus giving rise to the enhancement of  $T_c$ . The enhanced coupling strength is however counteracted by the Coulomb pseudopotential  $\mu^*$  and the mass-renormalization  $Z$ , which are also affected by interlayer coupling. Our results show that, in order to get the most favourable combination of all these competing effects for high  $T_c$ , the metallic layer neighbouring the superconducting layer should have large effective mass. The electron density of the neighbouring layer should furthermore be large for optimal  $T_c$ , although we find this effect to be significantly less relevant than the effective mass.

For experimental verification of our results, electron doped semiconducting transition metal dichalcogenides are especially promising. Some of the TMDCs, such as  $\text{MoS}_2$  [173] and  $\text{WS}_2$  [291], have been shown to be superconducting in the monolayer limit upon electron doping. Even more, the normal state of TMDCs has been shown to be sensitive to (dynamical) environmental screening [60, 186] and the conduction band minimum is well described by an effective mass approxi-

mation [177, 178]. A heterostructure of such a superconducting TMDC monolayer and another metallic monolayer with larger effective mass, such as electron-doped doped MoSe<sub>2</sub> [177, 178, 292], might therefore be an experimental realization of the model discussed here. However, electronic hybridization between the layers can induce additional effects which are not discussed here. To suppress such effects, a spacer layer of hBN might be placed in between the metallic monolayers, which is a method often used in the investigation of excitonic bound states. [292, 293] Our results might furthermore be relevant in the observed enhancement of  $T_c$  in electron-doped semi-conducting TMDC heterostructures as the number of material layers is increased. [15–17] Previous work has shown that effects from static screening alone cannot explain this behaviour [101], but additional coupling from interlayer plasmon modes could explain the  $T_c$  enhancement.



---

 BEYOND ONE-LOOP SUPERCONDUCTIVITY THEORY
 

---

This chapter is based on unpublished work that was done in collaboration with M.I. Katsnelson, M. Rösner and A.J. Millis. All calculations and derivations were performed by me, with frequent discussions on the interpretation and further steps from all collaborators. The text in this chapter has been written by me, with input from M. Rösner.

## 7.1 INTRODUCTION

Eliashberg theory is one of the most common theories used for the evaluation of (ab-initio) superconducting critical temperatures  $T_c$ . [27, 28, 125] As discussed in chapter 2, the theory is based on a one-loop approximation of the self-energy in which vertex corrections are neglected. This approximation is justified by Migdal's theorem, which states that vertex corrections are small with a factor  $\omega_e/E_F$  in 3D systems, with  $\omega_e$  the effective phonon frequency and  $E_F$  the Fermi energy. [26]

There have been several works devoted to studying the limits of Migdal's theorem. For example, the validity of Migdal's theorem has been debated in the regime of large electron-phonon coupling  $\lambda_{\text{BCS}}$ . [294–296] Closely related works have developed theories that go beyond Eliashberg theory, for example by systematically including higher-order self-energy diagrams [297–301] or by deriving algorithms that find the exact self-energy in certain limits [302, 303]. Other works have instead focused on corrections to the interaction, for instance by including vertex corrections in the form of the Kukkonen–Overhauser ansatz [71, 252] or by incorporating the renormalization of phononic properties by the electrons [304].

So far in this thesis, we have used the one-loop approximation to describe combined phonon- and plasmon-mediated superconductivity in layered 2D materials. However, the applicability of this approximation is formally not ensured in this case, since Migdal's theorem is only valid for electron-phonon mediated superconducting systems in 3D. [26, 296, 305] It is therefore important to understand to what extent the results in the previous chapters are affected by vertex corrections. A number of works have investigated Migdal's theorem in systems with dimension other than 3. [294, 295, 306] Schrodri et al. furthermore systematically studied the effect of vertex corrections in 1, 2 and 3D systems, without resorting to the common Fermi surface averaging approximation. [296]

A further complication in 2D systems is the relatively weak screening of the Coulomb interaction compared to 3D bulk materials. As a consequence, the 2D

Coulomb interaction is relatively strong and non-local. The effect of such non-local interactions on vertex corrections to the superconducting state has, to the best of our knowledge, not been studied yet. Moreover, it is unknown if Migdal's theorem holds for other bosons, such as the 2D plasmon mode, which do not have a well-defined characteristic energy scale  $\omega_e$ .

In order to address these questions, we propose here a formalism for quantifying the importance of vertex corrections in the presence of (non-local) Coulomb interactions. The formalism is based on a perturbation theory around the leading eigenvalue of the linearized superconducting gap equation. In this way, it avoids the computationally expensive diagonalization of the full beyond one-loop superconducting kernel. The formalism furthermore allows to disentangle the contributions of different diagrams to the vertex corrections, yielding a better understanding of the origin of the breakdown of one-loop theories.

After deriving the formalism, we will present preliminary results for a 2D phonon-mediated superconductor with and without a local Coulomb repulsion term, which will serve as a proof of concept for the formalism.

## 7.2 SECOND-ORDER DIAGRAMS

In order to systematically investigate second-order corrections beyond the one-loop approximation, we define a Dyson perturbation series that starts from the solution of the one-loop gap equation. To avoid double counting diagrams, the one-loop calculation is performed without normal state renormalization, such that we define the one-loop self-energy in Nambu-Gor'kov space as

$$\Sigma^{(\text{OL})}(\mathbf{k}, i\omega_n) = \begin{pmatrix} 0 & \phi^{(1)}(\mathbf{k}, i\omega_n) \\ \phi^{(1),*}(\mathbf{k}, i\omega_n) & 0 \end{pmatrix}, \quad (7.1)$$

where  $\phi^{(1)}(\mathbf{k}, i\omega_n)$  is the anomalous self-energy in the one-loop approximation defined in Eq. 2.92. The one-loop Green's function  $\mathbf{G}^{(\text{OL})}(\mathbf{k}, i\omega_n)$  is given by the usual Dyson equation

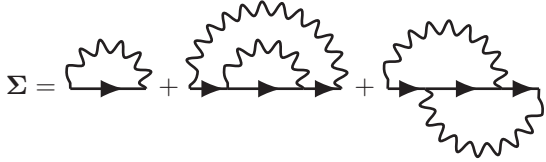
$$\begin{aligned} \mathbf{G}^{(\text{OL})}(\mathbf{k}, i\omega_n) &= \mathbf{G}^{(0)}(\mathbf{k}, i\omega_n) + \mathbf{G}^{(0)}(\mathbf{k}, i\omega_n) \Sigma^{(\text{OL})}(\mathbf{k}, i\omega_n) \mathbf{G}^{(\text{OL})}(\mathbf{k}, i\omega_n) \\ &= \begin{pmatrix} G^{(0)}(\mathbf{k}, i\omega_n) & F^{(1)}(\mathbf{k}, i\omega_n) \\ F^{(1),\dagger}(\mathbf{k}, i\omega_n) & -G^{(0)}(-\mathbf{k}, -i\omega_n) \end{pmatrix}, \end{aligned} \quad (7.2)$$

with  $F^{(1)}(\mathbf{k}, i\omega_n)$  the anomalous propagator in the one-loop approximation, defined in Eq. 2.88 by setting  $G^{(e)} = G^{(0)}$ .

Corrections beyond the one-loop self-energy are treated in a procedure reminiscent of screening in the constrained random phase approximation. [30] We find for the dressed Green's function

$$\mathbf{G}(\mathbf{k}, i\omega_n) = \mathbf{G}^{(\text{OL})}(\mathbf{k}, i\omega_n) + \mathbf{G}^{(\text{OL})}(\mathbf{k}, i\omega_n) \left( \boldsymbol{\Sigma}(\mathbf{k}, i\omega_n) - \boldsymbol{\Sigma}^{(\text{OL})}(\mathbf{k}, i\omega_n) \right) \mathbf{G}(\mathbf{k}, i\omega_n), \quad (7.3)$$

where  $\boldsymbol{\Sigma}(\mathbf{k}, i\omega_n)$  is the exact self-energy. We are interested here in the lowest order vertex corrections, such that we truncate the Dyson series after second order in  $W$ . This corresponds to the following self-energy diagrams (omitting all indices for clarity)



$$\Sigma = \text{[Diagram 1]} + \text{[Diagram 2]} + \text{[Diagram 3]} - \text{d.c.} + \mathcal{O}(W^3), \quad (7.4)$$

where d.c. stands for double counted diagrams. Note that the bare Green's function lines in these diagrams are given by the one-loop solution  $\mathbf{G}^{(\text{OL})}$ , instead of the bare Green's function  $\mathbf{G}^{(0)}$ . The first diagram in Eq. 7.4 simply yields a one-loop self-energy which additionally includes the  $G_0W_0$  normal-state renormalization terms that we neglected in  $\boldsymbol{\Sigma}^{(\text{OL})}$ . The second diagram is second order in  $W$ , but it is not a vertex correction term. For the normal part, it generates diagrams which are part of the self-consistent GWA, but not of the  $G_0W_0$  approximation. For the anomalous part, it partially captures the effect of  $G_0W_0$  normal state renormalization on the superconducting state. The third diagram is a vertex correction term of second order in  $W$ , which is not captured in any one-loop theory.

In order to shorten the mathematical expressions in this chapter, we introduce respective fermionic and bosonic four-vectors as

$$\vec{k}_n = (\mathbf{k}, i\omega_n) \quad \text{and} \quad \vec{q}_m = (\mathbf{q}, i\nu_m), \quad (7.5)$$

as well as the corresponding sum  $\sum_{\vec{k}_n} = \sum_{\mathbf{k}, n}$  and analogously for the bosonic vector. Using this shorthand, we show in Fig. 7.1 the two beyond one-loop self-energy diagrams in more detail. As in Eliashberg theory, each bare vertex (indicated

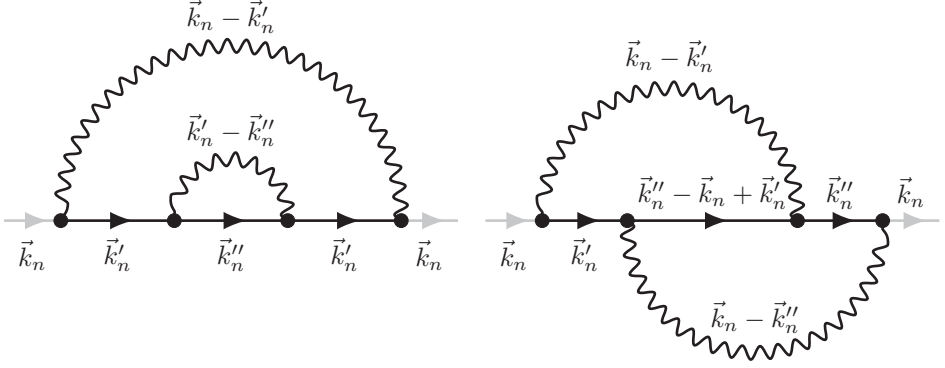


Figure 7.1: Second-order self-energy diagrams. The solid lines are one-loop electron propagators in the Nambu Gor'kov space  $\mathbf{G}^{(\text{OL})}$ , the wavy lines are the electron-electron interactions  $W$  and the dots are vertices given by  $\tau_3$  matrices. For all indices we use the four-vector notation defined in Eq. 7.5 and the gray Green's function lines are considered amputated.

by black dots in Fig. 7.1) is accompanied by a  $\tau_3$  Pauli matrix, such that the mathematical expression of the second-order self-energy correction is

$$\begin{aligned}
 \Sigma^{(2)}(\vec{k}_n) &= \frac{1}{\beta^2} \sum_{\vec{k}'_n, \vec{k}''_n} \tau_3 \mathbf{G}^{(\text{OL})}(\vec{k}'_n) \tau_3 \mathbf{G}^{(\text{OL})}(\vec{k}''_n) \tau_3 \mathbf{G}^{(\text{OL})}(\vec{k}'_n) \tau_3 \\
 &\quad \times \left[ -W(\vec{k}_n - \vec{k}'_n) \right] \left[ -W(\vec{k}'_n - \vec{k}''_n) \right] \\
 &+ \frac{1}{\beta^2} \sum_{\vec{k}'_n, \vec{k}''_n} \tau_3 \mathbf{G}^{(\text{OL})}(\vec{k}'_n) \tau_3 \mathbf{G}^{(\text{OL})}(\vec{k}''_n - \vec{k}_n + \vec{k}'_n) \tau_3 \mathbf{G}^{(\text{OL})}(\vec{k}''_n) \tau_3 \\
 &\quad \times \left[ -W(\vec{k}_n - \vec{k}'_n) \right] \left[ -W(\vec{k}_n - \vec{k}''_n) \right]. \tag{7.6}
 \end{aligned}$$

The first and second term correspond to the left and right diagram of Fig. 7.1, respectively. By performing the matrix products in Nambu-Gor'kov space we find expressions for the normal and anomalous elements of the self-energy, defined by

$$\Sigma^{(2)}(\vec{k}_n) = \begin{pmatrix} \Sigma^{(2)}(\vec{k}_n) & \phi^{(2)}(\vec{k}_n) \\ \phi^{(2),*}(\vec{k}_n) & -\Sigma^{(2)}(-\vec{k}_n) \end{pmatrix}. \tag{7.7}$$



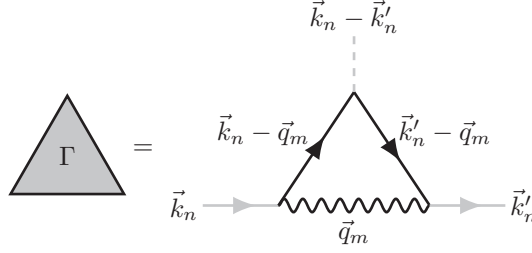


Figure 7.2: The lowest-order three point vertex  $\Gamma(\vec{k}_n, \vec{k}'_n)$ . The solid lines are bare normal-state propagators  $G^{(0)}$  and the wavy lines are the electron-electron interactions  $W$ . For all indices we use the four-vector notation defined in Eq. 7.5 and gray lines are considered amputated.

Since we are mainly interested in corrections to the critical temperature, we furthermore linearize all expressions in the anomalous propagator (i.e., neglect terms of  $\mathcal{O}(F^2)$ ). This yields for the normal-state self-energy corrections

$$\begin{aligned}
 \Sigma^{(2)}(\vec{k}_n) &= \text{diagram with } \Sigma^{(1)} \text{ in a circle} + \text{diagram with } \Gamma \text{ in a triangle} \\
 &= -\frac{1}{\beta} \sum_{\vec{k}'_n} G^{(0)}(\vec{k}'_n) \Sigma^{(1)}(\vec{k}'_n) G^{(0)}(\vec{k}'_n) W(\vec{k}_n - \vec{k}'_n) \\
 &\quad - \frac{1}{\beta} \sum_{\vec{k}'_n} G^{(0)}(\vec{k}'_n) \Gamma(\vec{k}_n, \vec{k}'_n) W(\vec{k}_n - \vec{k}'_n), \tag{7.8}
 \end{aligned}$$

where the gray Green's function lines are considered amputated. The first term corresponds to the self-energy of the second self-consistency cycle in the GWA, with  $\Sigma^{(1)}(\vec{k}_n)$  the  $G_0W_0$  self-energy defined in Eq. 2.36. The second term is a second-order vertex correction term, with the lowest-order three-point vertex  $\Gamma(\vec{k}_n, \vec{k}'_n)$  defined diagrammatically in Fig. 7.2 and given mathematically by

$$\Gamma(\vec{k}_n, \vec{k}'_n) = -\frac{1}{\beta} \sum_{\vec{q}_m} W(\vec{q}_m) G^{(0)}(\vec{k}_n - \vec{q}_m) G^{(0)}(\vec{k}'_n - \vec{q}_m). \tag{7.9}$$

In a similar way, we obtain for the anomalous self-energy corrections

$$\phi^{(2)}(\vec{k}_n) = \text{[diagrams]} \tag{7.10}$$

where we defined the one-loop anomalous propagator diagram as

$$F^{(1)}(\vec{k}_n) = \text{[diagram]} \tag{7.11}$$

The corresponding mathematical expression is

$$\begin{aligned} \phi^{(2)}(\vec{k}_n) &= \frac{1}{\beta} \sum_{\vec{k}'_n} W(\vec{k}_n - \vec{k}'_n) F^{(1)}(\vec{k}'_n) \left( G^{(0)}(\vec{k}'_n) \Sigma^{(1)}(\vec{k}'_n) + \Sigma^{(1)}(-\vec{k}'_n) G^{(0)}(-\vec{k}'_n) \right) \\ &+ \frac{1}{\beta} \sum_{\vec{k}'_n} W(\vec{k}_n - \vec{k}'_n) F^{(1)}(\vec{k}'_n) \left( \Gamma(\vec{k}_n, \vec{k}'_n) + \Gamma(-\vec{k}_n, -\vec{k}'_n) \right) \\ &- \frac{1}{\beta} \sum_{\vec{k}'_n} F^{(1)}(\vec{k}'_n) \chi(\vec{k}_n, \vec{k}'_n). \end{aligned} \tag{7.12}$$

The first two terms capture the effect of normal-state renormalization from the first non-trivial term in the  $G_0W_0$  Dyson series to the superconducting state. The second and third diagrams are typical three-point vertex corrections diagrams, similar to the normal-state vertex corrections in Eq. 7.8. The final diagram is a four-point vertex correction, where the four-point vertex  $\chi(\vec{k}_n, \vec{k}'_n)$  is shown diagrammatically in Fig. 7.3 and given by

$$\chi(\vec{k}_n, \vec{k}'_n) = \frac{1}{\beta} \sum_{\vec{k}''_n} W(\vec{k}'_n - \vec{k}''_n) W(\vec{k}_n - \vec{k}''_n) G^{(0)}(\vec{k}'_n + \vec{k}_n - \vec{k}''_n) G^{(0)}(-\vec{k}''_n). \tag{7.13}$$

In principle, the following anomalous self-energy contribution is also contained in the diagrams of Fig. 7.1



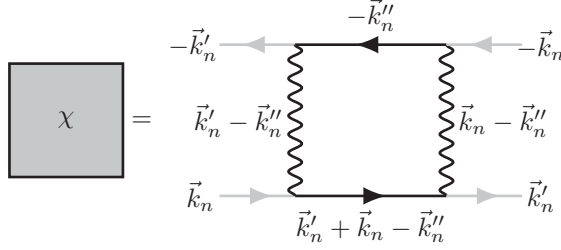


Figure 7.3: The four-point vertex  $\chi(\vec{k}_n, \vec{k}'_n)$ . The solid lines are bare normal-state propagators  $G^{(0)}$  and the wavy lines are the electron-electron interactions  $W$ . For all indices we use the four-vector notation defined in Eq. 7.5 and the gray Green's function lines are considered amputated.

However, since the anomalous self-energy  $\phi^{(1)}$  is solved self-consistently in one-loop superconductivity theory, this diagram is already contained in the one-loop anomalous propagator  $F^{(1)}$ , such that it is removed to avoid double counting.

### 7.3 THE PERTURBATIVE FORMALISM

As discussed in chapter 2, the linearized gap-equation can be written as an eigenproblem

$$\lambda_i \vec{\phi}_i = \hat{K} \vec{\phi}_i, \quad (7.14)$$

where  $\lambda_i$  are eigenvalues defined such that at  $T = T_c$  the leading eigenvalue (from here on denoted by  $\lambda$ ) is unity. We define a matrix-vector product in this basis as

$$\left( \hat{K} \vec{\phi} \right)_{\vec{k}_n} = \frac{1}{\beta} \sum_{\vec{k}'_n} \hat{K}_{\vec{k}_n, \vec{k}'_n} \phi(\vec{k}'_n). \quad (7.15)$$

In order to quantify the beyond one-loop corrections, we aim to find the change of the leading eigenvalue  $\lambda$  as a consequence of second-order self-energy correction terms defined in Eq. 7.12. To this end, we start from a given one-loop kernel obtained from Eq. 2.95

$$\hat{K}_{\vec{k}_n, \vec{k}'_n}^{(1)} = -W(\vec{k}_n - \vec{k}'_n) G^{(0)}(\vec{k}'_n) G^{(0)}(-\vec{k}'_n), \quad (7.16)$$

with eigenvalues  $\lambda_i^{(1)}$  and (right) eigenvectors  $\vec{\phi}_i^{(1)}$ , such that

$$\lambda_i^{(1)} \vec{\phi}_i^{(1)} = \hat{K}^{(1)} \vec{\phi}_i^{(1)}. \quad (7.17)$$

The matrix  $\hat{K}^{(1)}$  is in general not symmetric, which means its (right) eigenvectors are not orthogonal. As a consequence, we cannot use the conventional eigenvalue perturbation theory. Therefore, we use an extension of the perturbative formalism which makes use of the left eigenvectors  $\vec{\phi}_i^{(1L)}$  defined by

$$\vec{\phi}_i^{(1L),T} \lambda_i^{(1)} = \vec{\phi}_i^{(1L),T} \hat{K}^{(1)}. \quad (7.18)$$

Here the left and right one-loop eigenvalues  $\lambda^{(1)}$  are equivalent, because  $\hat{K}^{(1)}$  is a square matrix. Applying the perturbative formalism, we find that a beyond one-loop correction kernel  $\hat{K}^{(2)}$  causes the following change in the eigenvalues

$$\lambda_i \approx \lambda_i^{(1)} + \vec{\phi}_i^{(1L),T} \hat{K}^{(2)} \vec{\phi}_i^{(1)} + \mathcal{O} \left( \left( \hat{K}^{(2)} \right)^2 \right), \quad (7.19)$$

where we normalized the one-loop eigenvectors such that  $\vec{\phi}_i^{(1L),T} \vec{\phi}_i^{(1)} = 1$ . Therefore, the change in the leading eigenvalue  $\Delta\lambda^{(2)}$  due to perturbation  $\hat{K}^{(2)}$  is given by

$$\Delta\lambda^{(2)} = \lambda - \lambda^{(1)} \approx \frac{1}{\beta^2} \sum_{\vec{k}_n, \vec{k}'_n} \phi^{(1L)}(\vec{k}_n) \hat{K}_{\vec{k}_n, \vec{k}'_n}^{(2)} \phi^{(1)}(\vec{k}'_n). \quad (7.20)$$

We note that the left eigenvectors  $\phi^{(1L)}$  are a mathematical construct, without physical relevance on their own. They can be obtained by evaluating the (right) eigenvectors of the transposed one-loop kernel  $\hat{K}^{(1),T}$ .

Expressions for the kernels  $\hat{K}^{(2)}$  can be found by substituting the linearized expression of  $F^{(1)}$  (Eq. 2.94) into the expression for the anomalous self-energy correction  $\phi^{(2)}$  (Eq. 7.12). The resulting eigenvalue corrections we split into three contributions  $\Delta\lambda^{(2)} = \Delta\lambda^{(2\Sigma)} + \Delta\lambda^{(2\Gamma)} + \Delta\lambda^{(2\chi)}$ , by also splitting the kernel  $\hat{K}^{(2)} = \hat{K}^{(2\Sigma)} + \hat{K}^{(2\Gamma)} + \hat{K}^{(2\chi)}$ . In this way, we can disentangle the corrections from the various diagrams discussed in the previous section. The  $(2\Sigma)$  term is the GW-like correction from the first two terms in Eq. 7.12, such that its kernel is given by

$$\begin{aligned} \hat{K}_{\vec{k}_n, \vec{k}'_n}^{(2\Sigma)} &= -W(\vec{k}_n - \vec{k}'_n) G^{(0)}(\vec{k}'_n) G^{(0)}(-\vec{k}'_n) \\ &\times \left( G^{(0)}(-\vec{k}'_n) \Sigma^{(1)}(-\vec{k}'_n) + \Sigma^{(1)}(\vec{k}'_n) G^{(0)}(\vec{k}'_n) \right). \end{aligned} \quad (7.21)$$

The  $(2\Gamma)$  kernel contains the three-point vertex corrections and is given by

$$\hat{K}_{\vec{k}_n, \vec{k}'_n}^{(2\Gamma)} = -W(\vec{k}_n - \vec{k}'_n) G^{(0)}(\vec{k}'_n) G^{(0)}(-\vec{k}'_n) \left( \Gamma(-\vec{k}_n, -\vec{k}'_n) + \Gamma(\vec{k}_n, \vec{k}'_n) \right). \quad (7.22)$$

And finally, the four-point vertex correction kernel  $(2\chi)$  is defined as

$$\hat{K}_{\vec{k}_n, \vec{k}'_n}^{(2\chi)} = G^{(0)}(\vec{k}'_n) G^{(0)}(-\vec{k}'_n) \chi(\vec{k}_n, \vec{k}'_n). \quad (7.23)$$

## 7.4 THE MODEL

We will apply the formalism to the same system as described in chapter 5, i.e., a square-lattice model with only nearest-neighbour hopping  $t = 1.5\text{eV}$ . As a proof of concept, we will assume that the interaction has the form of an effective electron-electron interaction mediated by a local Einstein phonon mode, given by

$$W(\mathbf{q}, i\nu_m) \approx W(i\nu_m) = U + g^2 \frac{2\omega_e}{(i\nu_m)^2 - \omega_e^2}, \quad (7.24)$$

here  $g^2$  and  $\omega_e$  are the electron-phonon coupling and the Einstein frequency, respectively, and we additionally include a local Coulomb repulsion term  $U$ . In order to quantify the strength of the phonon induced electron-electron interaction, we define the usual BCS pairing strength  $\lambda_{\text{BCS}} = 2g^2 N_0 / \omega_e$ , with  $N_0$  the density of states (DOS) at the Fermi energy.

Even with a local interaction, the momentum dependence of the Green's function causes the numerical complexity of solving for beyond one-loop corrections to be significantly larger than the one-loop theory. For simplicity, we therefore make an approximation reminiscent of dynamical mean field theory (DMFT) by integrating all vertices over their momentum arguments. In this way we eliminate the momentum dependencies of the self-energies and vertices. We find the following expressions for the vertices

$$\Gamma(i\omega_n, i\omega_{n'}) \approx -\frac{1}{\beta} \sum_{n''} W(i\omega_n - i\omega_{n''}) G^{(0)}(i\omega_{n''}) G^{(0)}(i\omega_{n'} - i\omega_n + i\omega_{n''}) \quad (7.25)$$

$$\begin{aligned} \chi(i\omega_n, i\omega_{n'}) &\approx \frac{1}{\beta} \sum_{n''} W(i\omega_{n'} - i\omega_{n''}) W(i\omega_n - i\omega_{n''}) \\ &\times G^{(0)}(i\omega_{n'} + i\omega_n - i\omega_{n''}) G^{(0)}(-i\omega_{n''}). \end{aligned} \quad (7.26)$$

where we defined the local Green's function  $G^{(0)}(i\omega_n) = \sum_{\mathbf{k}} G^{(0)}(\mathbf{k}, i\omega_n)$ . All eigenvectors and kernels are also local in this approximation, such that

$$\begin{aligned} \hat{K}_{i\omega_n, i\omega_{n'}}^{(2\Sigma)} &\approx -W(i\omega_n - i\omega_{n'}) \sum_{\mathbf{k}} G^{(0)}(\mathbf{k}, i\omega_{n'}) G^{(0)}(-\mathbf{k}, -i\omega_{n'}) \\ &\times \left( G^{(0)}(-\mathbf{k}, -i\omega_{n'}) \Sigma^{(1)}(-i\omega_{n'}) + \Sigma^{(1)}(i\omega_{n'}) G^{(0)}(\mathbf{k}, i\omega_{n'}) \right) \end{aligned} \quad (7.27)$$

$$\begin{aligned} \hat{K}_{i\omega_n, i\omega_{n'}}^{(2\Gamma)} &\approx -W(i\omega_n - i\omega_{n'}) \sum_{\mathbf{k}} G^{(0)}(\mathbf{k}, i\omega_{n'}) G^{(0)}(-\mathbf{k}, -i\omega_{n'}) \\ &\times (\Gamma(-i\omega_n, -i\omega_{n'}) + \Gamma(i\omega_n, i\omega_{n'})) \end{aligned} \quad (7.28)$$

$$\hat{K}_{i\omega_n, i\omega_{n'}}^{(2\chi)} \approx \chi(i\omega_n, i\omega_{n'}) \sum_{\mathbf{k}} G^{(0)}(\mathbf{k}, i\omega_{n'}) G^{(0)}(-\mathbf{k}, -i\omega_{n'}). \quad (7.29)$$

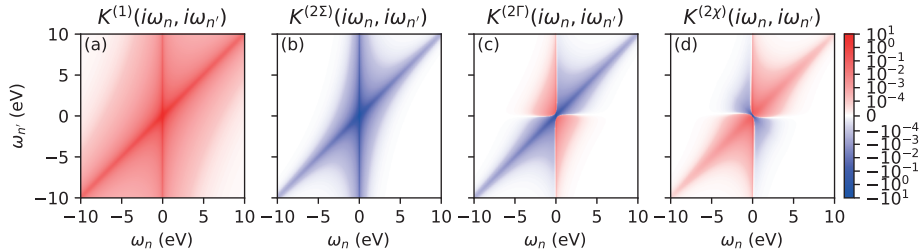


Figure 7.4: One-loop (a) and second-order (b-d) contributions to the kernel of the linearized superconducting gap equation. Here  $g^2 = 0.5 \text{ eV}^2$ ,  $\omega_e = 0.3 \text{ eV}$ ,  $E_F = 4 \text{ eV}$  and  $U = 0$ . The temperature was set to the critical temperature in the corresponding one-loop approximation. Note that the color scale is linear in between  $\pm 10^{-4}$  and logarithmic elsewhere.

The corrections to the leading eigenvalues are now given by

$$\Delta\lambda_i = \frac{1}{\beta^2} \sum_{n,n'} \phi_i^{(1L)}(i\omega_n) \hat{K}_{i\omega_n, i\omega_{n'}}^{(2)} \phi_i^{(1)}(i\omega_{n'}). \quad (7.30)$$

For later reference, the one-loop kernel in this local approximation is given by

$$\hat{K}_{i\omega_n, i\omega_{n'}}^{(1)} = -W(i\omega_n - i\omega_{n'}) \sum_{\mathbf{k}} G^{(0)}(\mathbf{k}, i\omega_{n'}) G^{(0)}(-\mathbf{k}, -i\omega_{n'}). \quad (7.31)$$

**COMPUTATIONAL DETAILS** The model described in this section was implemented in the TRIQS [155] and TPRF [257] codebase. All momentum sums were performed on linearly discretized meshes with 600x600 points. The one-loop gap equation was first solved using a discrete Lehman representation (DLR) [140, 154] of the Matsubara axis, using a real-frequency cutoff of  $\omega_c = 30 \text{ eV}$  and a DLR tolerance of  $\epsilon = 10^{-10}$ . The beyond one-loop kernels were then evaluated on full linearly discretized Matsubara meshes, with a high-frequency cutoff at  $\omega_c = 30 \text{ eV}$ .

## 7.5 PRELIMINARY RESULTS: ELECTRON-PHONON COUPLING

To start, we will neglect the Coulomb contributions and consider the importance of vertex corrections for superconductivity mediated by a local phonon mode only (i.e.,  $U = 0$ ). In Fig. 7.4(a) we show the corresponding one-loop kernel defined by Eq. 7.31. It is positive for all frequencies, reflecting the attractive nature of the phonon mediated electron-electron interaction. Analyzing its structure, we note that the peak along  $i\omega_n = i\omega_{n'}$  corresponds to the phononic pole of the interaction  $W(i\omega_n - i\omega_{n'})$ . The peak along  $i\omega_{n'}$  at  $i\omega_n = 0$  instead originates from the product

of Green's functions. Together, these features render the region of  $\pm\omega_e$  around the Fermi energy the dominant region for conventional phonon-mediated pairing. The GW-like correction  $K^{(2\Sigma)}$ , shown in panel (b), has a negative sign for all frequencies. This reflects the well-known reduction of the critical temperature due to normal-state renormalization. [126] The frequency structure of  $K^{(2\Sigma)}$  is furthermore qualitatively similar to that of  $K^{(1)}$ , such that one can approximately interpret the GW-like correction as a scalar renormalization of the one-loop kernel. A similar approximation can be derived from the low-energy limit of Eliashberg theory, in which the scalar mass-renormalization factor  $Z$  effectively rescales the phonon-induced electron-electron attraction (as discussed in chapter 2). [108, 133] The corrections to the kernel from second-order vertex corrections, shown in panels (c) and (d), have a more complicated structure. Both have sign changes at  $i\omega_n = 0$  and at  $i\omega_{n'} = 0$ , indicating that there are both repulsive and attractive corrections in different regions of the frequency space. To make an educated guess about the changes to the critical temperature, we may consider only the diagonal  $i\omega_n = i\omega_{n'}$ . As mentioned before, in the one-loop kernel this diagonal originates from the phononic pole, such that corrections to it can be understood as renormalizations of the interaction strength. We find that corrections from the three-point vertex  $K^{(2\Gamma)}$  (shown in panel (c)) are negative along  $i\omega_n = i\omega_{n'}$ , such that we predict it to effectively reduce the one-loop coupling strength and thus reduce the critical temperature. These findings are consistent with previous works. [297–299, 301] Corrections from the four-point vertex  $K^{(2\chi)}$  (shown in panel(d)) are however not as clear to interpret, because of the sign change along  $i\omega_n = i\omega_{n'}$ . For the current parameters, the region of negative sign is relatively small compared to the region of positive sign, such that we expect the four-point vertex to enhance the critical temperature. We do not expect that tuning the electron-phonon coupling  $g^2$  changes this interpretation, since it enters as a scalar prefactor in the expression for  $K^{(2\chi)}$ . However, tuning the phonon frequency  $\omega_e$  or the Fermi energy  $E_F$  has a less trivial effect on the kernel, such that this could affect the sign of the corrections to  $T_c$  from the four-point vertex.

In Fig. 7.5 we show the various second-order corrections  $\Delta\lambda^{(2)}$  to the leading eigenvalue of the linearized one-loop gap-equation  $\lambda^{(1)}$ . In all cases, the temperature was tuned such that  $\lambda^{(1)} = 1$ . In panel (a) we tune the effective coupling strength  $\lambda_{\text{BCS}}$  by varying  $g^2$ , while fixing  $\omega_e = 0.3\text{eV}$  and  $E_F = 4\text{eV}$ . The GW-like correction  $\lambda^{(2\Sigma)}$  is negative, again reflecting the reduction of  $T_c$  due to normal-state renormalization. The signs of the vertex corrections  $\Delta\lambda^{(2\Gamma)}$  and  $\Delta\lambda^{(2\chi)}$  are opposite, as predicted from the analysis of the kernels. Interestingly, however, they also have similar magnitude, such that the total vertex corrections  $\Delta\lambda^{(2\Gamma)} + \Delta\lambda^{(2\chi)}$  (black dashed line) has a magnitude less than 0.05 up to  $g^2 \approx 1.7\text{eV}^2$ . Since in all cases  $\omega_e/E_F \ll 1$ , these findings are in agreement with Migdal's theorem.

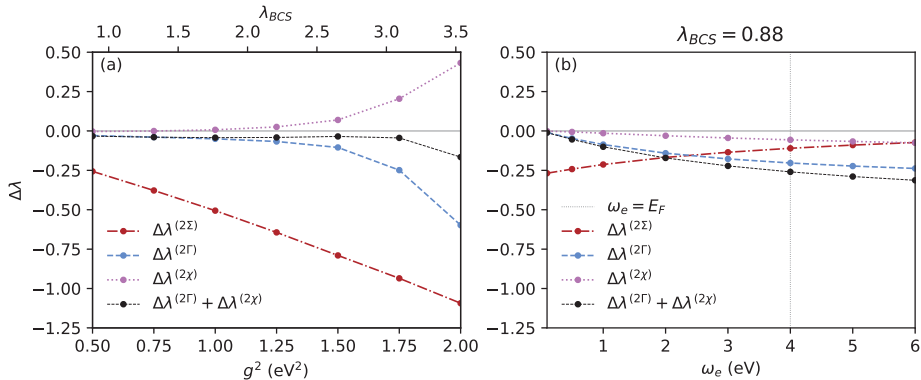


Figure 7.5: Second-order corrections to the leading eigenvalue of the linearized one-loop gap-equation. In all cases, the temperature was fixed to the critical temperature in the corresponding one-loop approximation, such that  $\lambda^{(1)} = 1$  for all parameters. Here we start from the parameters  $g^2 = 0.5 \text{ eV}^2$ ,  $\omega_e = 0.3 \text{ eV}$ ,  $E_F = 4 \text{ eV}$  and  $U = 0$ , and from there vary  $g^2$  in panel (a) and vary  $\omega_e$  and  $g^2$  such that  $\lambda_{BCS}$  is fixed in panel (b). The dotted vertical line in panel (b) indicates where  $\omega_e = E_F$ .

To further test the validity of Migdal's theorem in 2D, we vary in panel (b) the phonon frequency  $\omega_e$  at fixed  $\lambda_{BCS}$ . We find that  $\Delta\lambda^{(2\Gamma)}$  is negative for all  $\omega_e$ . Its magnitude furthermore increases as  $\omega_e$  increases, up until  $\omega_e = E_F$ , after which it saturates to  $\Delta\lambda^{(2\Gamma)} \approx -0.25$ . The corrections from the four-point vertex term  $\Delta\lambda^{(2\chi)}$  now also become negative as  $\omega_e$  is increased and saturate to  $\Delta\lambda^{(2\chi)} \approx -0.07$  for  $\omega_e > E_F$ . Since both vertex corrections are negative, we do not get the cancellation effect we observed when varying  $\lambda_{BCS}$ . The total magnitude of vertex corrections therefore increases as  $\omega_e$  is tuned closer to  $E_F$ , as predicted by Migdal's theorem.

## 7.6 PRELIMINARY RESULTS: LOCAL COULOMB INTERACTIONS

In Fig. 7.6 we show the one-loop and beyond one-loop kernels when including a local Coulomb interaction  $U = 0.3 \text{ eV}$ . The one-loop kernel, shown in panel (a), depends linearly on the interaction  $W$ . Inclusion of a local Coulomb interaction therefore simply reduces the intensity of the kernel by the  $i\omega_n$ -independent term  $-U \sum_{\mathbf{k}} G^{(0)}(\mathbf{k}, i\omega_{n'}) G^{(0)}(-\mathbf{k}, -i\omega_{n'})$ . As a consequence, the kernel has an attractive low-frequency region along the diagonal, and a repulsive high-frequency tail for  $\omega_n \rightarrow \infty$ . This structure yields the typical sign-change in the anomalous self-energy when the Coulomb interaction is treated as a scalar pseudo-potential in Eliashberg theory. [36, 109]



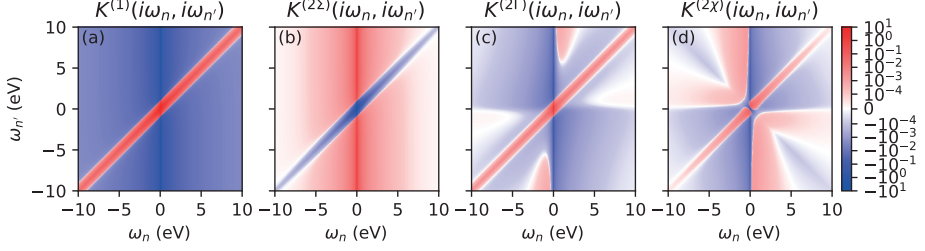


Figure 7.6: One-loop and second-order contributions to the kernel of the linearized superconducting gap equation, when including both electron-phonon coupling and a local Coulomb repulsion term. Here  $g^2 = 0.5 \text{ eV}^2$ ,  $\omega_e = 0.3 \text{ eV}$ ,  $E_F = 4 \text{ eV}$  and  $U = 0.3 \text{ eV}$ . The temperature was fixed to  $T = 51 \text{ K}$ , which is the critical temperature at  $U = 0$  in the one-loop approximation. Note that the color scale is linear in between  $\pm 10^{-4}$  and logarithmic elsewhere.

Similar to the  $U = 0$  case, the GW-like kernel  $K^{(2\Sigma)}$  has a similar structure to the one-loop kernel, but with opposite sign. Therefore, it still effectively reduces the phonon induced attraction along the diagonal. Interestingly, however, it now has an attractive high-frequency limit, which may counteract the  $T_c$  reduction from mass-renormalization observed at  $U = 0$ .

The structure of the vertex-corrections kernels  $K^{(2\Gamma)}$  and  $K^{(2\chi)}$  is significantly altered by the including of Coulomb repulsion. For  $K^{(2\Gamma)}$ , the diagonal is positive, whereas it was negative at  $U = 0$ . This indicates that vertex corrections from the three-point vertex might switch from repulsive to attractive as the value of  $U$  is increased. On the other hand, the diagonal of the kernel  $K^{(2\chi)}$  has a qualitatively similar structure as the corresponding kernel at  $U = 0$ , such that we hypothesize it to still reduce the critical temperature upon the inclusion of non-zero  $U$ . However, in both cases, the high-frequency limit is drastically altered upon the inclusion of Coulomb repulsion. It has alternating attractive and repulsive regions, which might have hard-to-predict consequences for the critical temperature.

In Fig. 7.7(a) we show  $\lambda^{(1)}$  as well as the various contributions to  $\Delta\lambda^{(2)}$  when including Coulomb repulsion  $U$ . To limit computational cost, these calculations have been done at fixed temperature  $T = 51 \text{ K}$ , such that  $\lambda^{(1)}$  changes as we vary  $U$ .

Let us first focus on the regime  $U < \lambda_{\text{BCS}}/N_0$  (i.e., left of the gray dotted line). Here,  $\lambda^{(1)}$  (green line) is suppressed by enhanced Coulomb repulsion  $U$ , as predicted by conventional Eliashberg theory. [109, 131–134] Interestingly, the magnitude of the  $T_c$ -suppression from GW-like normal state renormalization (red line) is also reduced

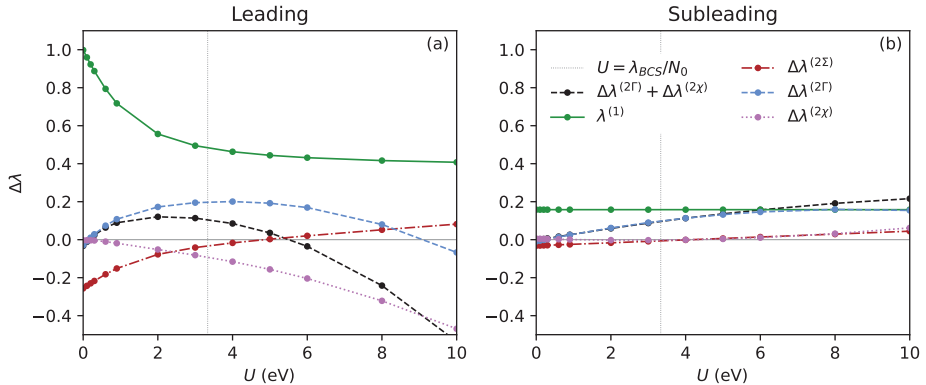


Figure 7.7: Second-order corrections to the one-loop leading (a) and subleading (b) eigenvalues, upon varying the local Coulomb repulsion  $U$ . Here  $g^2 = 0.5 \text{ eV}^2$ ,  $\omega_e = 0.3 \text{ eV}$  and  $E_F = 4 \text{ eV}$ . The temperature was fixed to  $T = 51 \text{ K}$ , which is the critical temperature at  $U = 0$  in the one-loop approximation.

for larger  $U$ , thus counteracting the suppression of  $\lambda^{(1)}$ . This is a consequence of the attractive high-frequency limit of the corresponding kernel  $K^{(2\Sigma)}$ .

The correction from the three-point vertex  $\Delta\lambda^{(2\Gamma)}$  is negative at  $U = 0$ , but changes to positive as soon as the Coulomb interaction is increased to  $U \approx 0.2 \text{ eV}$ . The four-point vertex correction  $\Delta\lambda^{(2\chi)}$  is negative for all frequencies, however, thus counteracting the corrections from  $\Delta\lambda^{(2\Gamma)}$ . As a consequence, the total second-order vertex corrections (black dashed line) are smaller than 5% for  $U < 0.5 \text{ eV}$ . When  $U$  increases further, the vertex corrections significantly enhance the critical temperature due to the increasing size of  $\Delta\lambda^{(2\Gamma)}$ , which reaches its maximum around  $U \approx \lambda_{\text{BCS}}/N_0$ .

In the regime  $U > \lambda_{\text{BCS}}/N_0$  (i.e., right of the gray dotted line) the strength of the Coulomb repulsion is stronger than the phonon induced electron-electron interaction for all frequencies. As a consequence, the one-loop kernel  $K^{(1)}(i\omega_n, i\omega_{n'}) < 0$  for all  $i\omega_n$  and  $i\omega_{n'}$ . Unintuitively, we find that the one-loop leading eigenvalue  $\lambda^{(1)}$  saturates as  $U$  is increased in this regime. The GW-like normal-state renormalization furthermore becomes positive for  $U \gtrsim 5 \text{ eV}$ , suggesting that it enhances the critical temperature. Around the same value of  $U$  we find that the sign of the total second-order vertex corrections changes sign, due to strong cancellation of the  $\Delta\lambda^{(2\Gamma)}$  and  $\Delta\lambda^{(2\chi)}$  corrections. We hypothesize that these unusual findings are a consequence of the relative strength of vertex corrections, such that our perturbative formalism breaks down. This hypothesis is further corroborated by the fact that  $U$  is on a similar order of magnitude as the bandwidth  $W = 4t = 6 \text{ eV}$  in this regime, such that strong correlation effects on the DMFT level are expected to play a role.

In Fig. 7.7(b) we furthermore show the corrections to the subleading eigenvalue of the one-loop gap-equation. As expected, we find for all  $U$  that the one-loop subleading eigenvalue (green line) is smaller than the corresponding leading eigenvalue shown in panel (a). However, when including all second-order vertex corrections (obtained from adding the green solid and black dashed lines), we find that the corrected subleading eigenvalue becomes larger than the corrected leading eigenvalue for  $U \gtrsim 7$  eV. This suggests a phase transition to another superconducting state, which cannot be described using our formalism. These data therefore again indicate that our perturbative formalism breaks down in the regime of large  $U$ , such that higher-order vertex corrections are relevant.

## 7.7 CONCLUSIONS & OUTLOOK

In conclusion, we have proposed a formalism for quantifying the importance of vertex corrections beyond one-loop theories in superconducting systems. The formalism is based on a perturbative expansion of the leading eigenvalue of the linearized superconducting gap-equation. For a 2D nearest-neighbour tight-binding model on a square lattice, we have shown that vertex corrections are small for 2D phonon-mediated superconductivity, as long as  $\omega_e/E_F \ll 1$  and the coupling strength  $\lambda_{\text{BCS}}$  is small enough, in agreement with Refs. [295, 296]. At larger coupling strengths of  $\lambda_{\text{BCS}} \gtrsim 2.5$ , the corrections from the three-point and four-point vertices both become significant, but opposite in sign, such that the total vertex corrections to the one-loop leading eigenvalue are less than 5 percent up to  $\lambda_{\text{BCS}} \approx 3$ . The inclusion of a local Coulomb term  $U$  in the interaction introduces additional structure in the beyond one-loop kernels, which causes the sign of vertex corrections to change from repulsive to attractive as  $U$  is increased. The magnitude of the corrections to the leading eigenvalue are, however, less than 5% for  $U \lesssim 0.5$  eV.

We need to stress, however, that the results in this chapter are preliminary. Additional checks for convergence and further comparisons to literature still have to be done. We should furthermore investigate the magnitude of higher order perturbations to the leading eigenvalue, which may serve as a signature of the breakdown of our formalism. Nonetheless, the results in this chapter suggest that the one-loop theory for superconductivity is justified for conventional 2D electron-phonon mediated superconductors as long as  $\omega_e/E_F \ll 1$ , coupling strengths  $\lambda_{\text{BCS}} \lesssim 3$  and local Coulomb interactions  $U \lesssim 0.5$  eV. To connect to conventional approaches, the latter corresponds to a dimensionless Coulomb potential  $\mu^C = N_0 U \lesssim 0.13$ .

The formalism we proposed is not limited to local interactions, such that a natural extension of this work is to investigate the effect of non-locality in the interaction  $W$  on vertex corrections in 2D. However, the  $\mathcal{O}(N_k^3)$  scaling of the vertex functions with the momentum mesh size  $N_k$  quickly makes computations unfeasibly expensive when using the simple linearly discretized meshes employed here. More sophisticated

methods for evaluating momentum sums, including methods based on tensor networks [307] or adaptive Brillouin zone integration methods [308, 309], could be used instead. Our formalism can furthermore be used to explore the effect of a boson with a momentum dependent dispersion on vertex corrections. This is especially relevant for the weak screening limit of layered materials, as discussed in chapters 5 and 6, where the 2D plasmon modes with a  $\sqrt{q}$  dispersion play a significant role in the superconducting pairing mechanism. [62, 68, 69, 72] Finally, a non-local extension of our formalism may be used to study vertex corrections in superconductors whose gap-function has unconventional symmetry, such as p-wave or d-wave symmetry.

## CONCLUSIONS & OUTLOOK

---

In this thesis we have implemented and applied methods that go beyond the state of the art to evaluate normal and superconducting state properties, in order to gain a deeper understanding of the role of screening to the Coulomb interaction in layered 2D materials.

For the normal state, we have shown in chapter 4 that interlayer dynamical screening can induce novel interlayer plasmon polaron excitations. These excitations create so far unseen shakeoff features in the spectral function of a WS<sub>2</sub>/graphene heterostructure, and lead to electronic spectral weight transfer away from the Fermi energy.

For the superconducting state, we have shown in chapter 5 that, already in a 2D monolayer, internal dynamical screening from conduction electrons can give rise to an unconventional plasmon-mediated pairing mechanism. We have furthermore shown in chapter 6 that plasmon modes in a neighbouring layer can similarly contribute to the pairing via dynamical interlayer screening, with the potential of yielding more than an order of magnitude enhancement of the superconducting critical temperature in some cases.

Moreover, for both the normal and superconducting states we have shown that the applicability of commonly used one-loop theories, such as the GWA or Eliashberg theory, requires special attention in 2D systems. Therefore, in chapter 7, we introduced a formalism for evaluating the necessity of vertex corrections that go beyond the one-loop approximation.

The results of this thesis show that a careful consideration of all screening channels is crucial for the understanding of superconductivity in layered materials. Based on our findings, we expect plasmons to play a role in the Cooper pairing in most 2D superconductors, especially for materials mounted on substrates with low dielectric constants. We furthermore anticipate that stacking such layered materials into superconducting heterostructures can significantly enhance the superconducting critical temperature due to additional pairing strength from interlayer plasmon modes. Such effects could be especially relevant in heterostructures of TMDCs, in which such an enhancement of  $T_c$  upon stacking multiple monolayers was experimentally already observed. [15–17]

To make material-specific quantitative theoretical predictions, the methods used throughout this thesis have to be connected to first principle methods. To this end, we could make use of a downfolded three-band model, which is known to

correctly describe the low-energy physics of the semi-conducting TMDCs. [101,181] Coulomb interaction matrix elements as well as phonon properties can furthermore be obtained using the constrained random phase approximation (cRPA) [30,98] and constrained density functional perturbation theory (cDFPT) [310], respectively. Therefore, all tools for investigating the existence of a plasmon mediated superconducting state in TMDCs from first principles are in principle already available.

Experimentally proving the existence of plasmonic contributions to the superconducting state is, however, not trivial. Most signatures we discussed in chapters 5 and 6 are inconclusive on their own. Therefore, to aid the experimental classification, footprints of plasmonic pairing on additional physical observables should be studied theoretically. For example, plasmonic signatures to the superconducting coherence length and penetration depth might be identified using the formalism recently proposed by Witt *et al.* [311] Moreover, the effect of plasmonic superconductivity on spectral features, such as superconducting gap sizes or coherence peaks, should be investigated. Such information is unavailable in the current imaginary-time based formalism due to the low accuracy of common analytical continuation schemes, but using novel continuation methods, such as the minimal pole method [312,313] or Nevanlinna [314,315], we may be able to gain access to this information.

Finally, it is clear that the applicability of common theoretical methods should be re-evaluated for layered systems. To this end, the formalism described in chapter 7 should be extended and applied to 2D models with non-local Coulomb interactions and dispersive boson modes, for example using the plasmon-pole approximation. This is, however, involving due to the computational complexity of the formalism, which becomes prohibitively large when taking momentum dependencies into account. To remedy this, we may employ recent numerical advances, such as the extension of the DLR to three-point functions [141], which can be used to treat the frequency dependence of the kernels, or tensor network methods [307], which may be used to find compressed representations of the quantities defined on momentum meshes.

## POPULAR SUMMARY

---

Scientific understanding of the world around us is always gained by a combination of theory and experiment. Either something is first measured experimentally and afterwards explained by a theoretical model, or a theoretical model makes a prediction which is then verified (or not) by an experiment. Nowadays, most of our theoretical models are written in the language of mathematics, which means we need to solve equations in order to compare our theories to experiments. In many cases this is unfeasible to do by hand, but fortunately a computer is perfectly suited for such tasks. In this thesis we therefore focus on developing and applying theoretical models which we can solve using computers.

The subject of this thesis are the electronic properties of so-called *layered materials*. These are materials that consist of stacks of weakly-bound, atomically thin layers. An everyday example of a layered material is graphite, which is made out of stacks of flat sheets of carbon atoms called graphene. Because of the weak interlayer bonds, the graphene sheets can easily detach, which makes it possible to write with a stick of graphite. In this thesis, we are specifically interested in layered materials which consist of only a few atomically thin layers. These are particularly promising for future applications, since their small thickness might allow for the creation of extremely thin (around one millionth of a millimeter) and flexible electronic devices. However, to aid the design of such devices, we need a theoretical understanding of what gives rise to the electronic properties of layered materials and how we can influence them.

The electronic properties of a material are mostly determined by the behaviour of tiny particles called *electrons*. An electron is never alone, because it is always being repelled by all other electrons due to its negative charge. As a consequence, all electrons ‘feel’ each other at all times; they are *correlated* with each other. The aim of this thesis is to construct theoretical models of these electron correlations, such that we can gain a deeper understanding of their effect on the electronic properties of layered materials.

After the introductory chapters, we start in Ch. 4 by investigating the behaviour of electrons in a two-layer material, consisting of an atomically thin layer of WS<sub>2</sub> (tungsten disulfide) and a layer of graphene on top. In this material our experimental colleagues from Denmark and the United States found signatures of a new kind of movement of the electrons in the WS<sub>2</sub> layer, which was not present without the graphene layer. It is already well known that electrons can oscillate collectively, which forms waves that are called *plasmons*, similar to how water particles form

waves in the ocean. From our theoretical modelling we now understand that the experimental signature in  $\text{WS}_2$  was likely created by electrons in the  $\text{WS}_2$  layer ‘feeling’ these plasmon waves in the graphene layer. This creates a new state where the electron and plasmon move together, like a boat floating up and down on the ocean waves.

In the chapters that follow we focus on *superconductivity* in layered materials. A superconductor is a material in which electrical current can flow without resistance, which means that it does not produce heat and therefore does not waste energy. An important property of superconductors is the *critical temperature*, denoted by  $T_c$ , which indicates below which temperature a material becomes superconducting. Unfortunately, for most materials this critical temperature is extremely low, around  $-270^\circ\text{C}$ , such that everyday applications seem out of reach. There is a class of materials, however, for which  $T_c$  lies much closer to room-temperature. These are the so-called ‘high- $T_c$ ’ superconductors, of which the highest critical temperature currently is  $T_c \approx -140^\circ\text{C}$ . Intriguingly, these materials have a layered structure, which is believed to be crucial for their high critical temperatures. Therefore, if we want to eventually find a superconductor at room temperature, it is promising to study which mechanisms play a role for superconductivity in layered materials.

To this end, we study in Chs. 5 and 6 if plasmons, the collective electron waves we mentioned before, also play a role in layered superconductors. We did this by extending existing theories to include the effect of plasmons. Based on this, we show that neglecting plasmons in a theory will often lead to an underestimation of the critical temperature. We furthermore describe experimental signatures of the effect of plasmons on superconductors, such that future experiments may be able to verify our predictions.

Ch. 7 describes a more abstract work in which we introduce a new method for determining the validity of theories for superconductivity. Using this method we study in which regimes one can apply state-of-the-art methods and in which regimes we will need to develop new theories.

All in all, we show in this thesis that one needs to carefully consider the effect of the repulsive force between electrons to theoretically describe layered materials. We have both explained experimental data based on our current theoretical models, as well as proposed new theories and mechanisms that may be verified in the future. Therefore, the results of this thesis contribute to a deeper theoretical understanding of the electronic properties of layered materials.



## POPULAIRE SAMENVATTING

---

Het verkrijgen van wetenschappelijke kennis over de wereld om ons heen gebeurt altijd door een combinatie van theorie en experiment. Ofwel iets wordt experimenteel gemeten en daarna verklaard door een theoretisch model, of een theoretisch model doet een voorspelling die vervolgens wordt geverifieerd (of niet) door een experiment. Tegenwoordig zijn de meeste van onze theorieën geschreven in de taal van de wiskunde, wat betekent dat we formules zullen moeten oplossen om een theorie te kunnen vergelijken met experimenten. Dit is meestal onbegonnen werk met de hand, maar gelukkig zijn computers perfect geschikt voor dit soort taken. In dit proefschrift richten we ons daarom op het ontwikkelen en toepassen van theoretische modellen die we kunnen oplossen met computers.

Het onderwerp van dit proefschrift zijn de elektronische eigenschappen van zogenaamde *gelaagde materialen*. Dit zijn materialen die bestaan uit stapels van zwak gebonden lagen die een enkel atoom dik zijn. Een alledaags voorbeeld van een gelaagd materiaal is grafiet, wat bestaat uit stapels van platte vellen koolstofatomen die we grafeen noemen. Vanwege de zwakke bindingen tussen de lagen, kunnen de grafeenvellen elkaar gemakkelijk loslaten. Dit maakt het mogelijk om met een staafje grafiet te kunnen schrijven. In dit proefschrift kijken we specifiek naar gelaagde materialen die uit slechts een paar atomair dunne lagen bestaan. Deze zijn veelbelovend voor toekomstige toepassingen, omdat hun kleine dikte de constructie van extreem dunne (rond een miljoenste van een millimeter) en flexibele elektronische apparaten mogelijk kan maken. Om het ontwerp van dergelijke apparaten te helpen moeten we echter begrijpen wat de eigenschappen van gelaagde materialen zijn en hoe we deze kunnen beïnvloeden.

De elektronische eigenschappen van een materiaal worden grotendeels bepaald door het gedrag van kleine deeltjes die we *elektronen* noemen. Een elektron is nooit alleen, omdat zijn negatieve lading ervoor zorgt dat het afgestoten zal worden van alle andere elektronen. Als gevolg hiervan ‘voelen’ alle elektronen elkaar altijd; ze zijn *gecorrleerd* met elkaar. Het doel van dit proefschrift is om theoretische modellen van deze elektron correlaties te maken, om beter te kunnen begrijpen wat hun effect is op de elektronische eigenschappen van gelaagde materialen.

Na de inleidende hoofdstukken beginnen we in hoofdstuk 4 met het onderzoeken van het gedrag van elektronen in een materiaal wat bestaat uit twee lagen, een atomair dunne laag  $WS_2$  (wolfraam disulfide) en een laag grafeen. In dit materiaal hebben onze experimentele collega's in Denemarken en de Verenigde Staten kenmerken gezien van een nieuwe soort beweging van de elektronen in de  $WS_2$  laag, die niet

zichtbaar is zonder de grafeen laag. Het is bekend dat elektronen collectief kunnen trillen en dat dit golven vormt die we *plasmonen* noemen, vergelijkbaar met hoe waterdeeltjes golven vormen in de oceaan. Aan de hand van onze theoretische modellen begrijpen we nu dat de kenmerken in de  $WS_2$  laag waarschijnlijk gevormd worden doordat de elektronen in de  $WS_2$  laag deze plasmonen in de grafeen laag kunnen ‘voelen’. Dit creëert een nieuwe toestand waarin een elektron en de plasmon samen bewegen, vergelijkbaar met een boot die op en neer deint op de golven. In de volgende hoofdstukken richten we ons op *supergeleiding* in gelaagde materialen. Een supergeleider is een materiaal waarin elektriciteit kan stromen zonder weerstand, waardoor het geen hitte produceert en dus geen energie verspilt. Een belangrijke eigenschap van supergeleiders is de *kritische temperatuur*, aangegeven met  $T_c$ , wat de temperatuur is waaronder een materiaal supergeleidend wordt. Helaas is de kritische temperatuur van de meeste materialen extreem laag, rond  $-270^\circ\text{C}$ , waardoor alledaagse toepassingen onmogelijk zijn. Er is echter een klasse materialen waarvan  $T_c$  een stuk dichterbij kamertemperatuur ligt. Deze worden de ‘high- $T_c$ ’ supergeleiders genoemd, waarvan op dit moment de hoogste kritische temperatuur  $T_c \approx -140^\circ\text{C}$  is. Interessant genoeg hebben deze materialen een gelaagde structuur, die ook belangrijk lijkt te zijn voor hun hoge kritische temperaturen. Om dus uiteindelijk een supergeleider op kamertemperatuur te vinden, is het veelbelovend te bestuderen welke mechanismen een rol spelen voor supergeleiding in gelaagde materialen.

Met dit als doel bestuderen we in hoofdstukken 5 en 6 of plasmonen, de eerder genoemde collectieve elektron golven, ook een rol spelen in gelaagde supergeleiders. We hebben dit gedaan door bestaande theorieën uit te breiden door het effect van plasmonen mee te nemen. Hiermee laten we zien dat het negeren van plasmonen in een theorie er in veel gevallen voor zorgt dat de kritische temperatuur van een materiaal onderschat zal worden. Daarnaast beschrijven we ook een aantal experimentele kenmerken van het effect van plasmonen op supergeleiders, zodat toekomstige experimenten onze resultaten kunnen verifiëren.

Hoofdstuk 7 beschrijft een meer abstract werk, waarin we een nieuwe methode introduceren die de betrouwbaarheid van theorieën voor supergeleiding kan bepalen. Met deze methode bestuderen we in welke regimes we gebruikelijke theorieën kunnen toepassen en voor welke regimes we nieuwe theorieën zullen moeten ontwikkelen.

Al met al laten we in dit proefschrift zien dat de afstotende kracht tussen elektronen zorgvuldig meegenomen moet worden om gelaagde materialen theoretisch te kunnen beschrijven. We hebben zowel experimentele resultaten verklaard aan de hand van onze huidige theoretische modellen, als nieuwe theorieën en mechanismen voorgesteld die in de toekomst geverifieerd kunnen worden. De resultaten van dit proefschrift dragen dus bij aan een dieper theoretisch begrip van de elektronische eigenschappen van gelaagde materialen.

## BIBLIOGRAPHY

---

- [1] K.S. Novoselov, A.K. Geim, S.V. Morozov, D. Jiang, Y. Zhang, S.V. Dubonos et al., *Electric Field Effect in Atomically Thin Carbon Films*, *Science* **306** (2004) 666.
- [2] K.S. Novoselov, A.K. Geim, S.V. Morozov, D. Jiang, M.I. Katsnelson, I.V. Grigorieva et al., *Two-dimensional gas of massless Dirac fermions in graphene*, *Nature* **438** (2005) 197.
- [3] K.S. Novoselov, D. Jiang, F. Schedin, T.J. Booth, V.V. Khotkevich, S.V. Morozov et al., *Two-dimensional atomic crystals*, *Proceedings of the National Academy of Sciences* **102** (2005) 10451.
- [4] A. Reina, X. Jia, J. Ho, D. Nezich, H. Son, V. Bulovic et al., *Large Area, Few-Layer Graphene Films on Arbitrary Substrates by Chemical Vapor Deposition*, *Nano Letters* **9** (2009) 30.
- [5] M.I. Katsnelson, *Graphene: Carbon in Two Dimensions*, Cambridge University Press, 1 ed. (Apr., 2012), 10.1017/CBO9781139031080.
- [6] D.Y. Qiu, F.H. Da Jornada and S.G. Louie, *Optical Spectrum of MoS<sub>2</sub>: Many-Body Effects and Diversity of Exciton States*, *Physical Review Letters* **111** (2013) 216805.
- [7] F. Hüser, T. Olsen and K.S. Thygesen, *How dielectric screening in two-dimensional crystals affects the convergence of excited-state calculations: Monolayer MoS<sub>2</sub>*, *Physical Review B* **88** (2013) 245309.
- [8] D. Vaquero, V. Clericò, J. Salvador-Sánchez, A. Martín-Ramos, E. Díaz, F. Domínguez-Adame et al., *Excitons, trions and Rydberg states in monolayer MoS<sub>2</sub> revealed by low-temperature photocurrent spectroscopy*, *Communications Physics* **3** (2020) 194.
- [9] G. Giuliani and G. Vignale, *Quantum Theory of the Electron Liquid*, Cambridge University Press, Cambridge (2005), 10.1017/CBO9780511619915.
- [10] A.K. Geim and I.V. Grigorieva, *Van der Waals heterostructures*, *Nature* **499** (2013) 419.
- [11] K.S. Novoselov, A. Mishchenko, A. Carvalho and A.H. Castro Neto, *2D materials and van der Waals heterostructures*, *Science* **353** (2016) aac9439.

- [12] Y. Liu, N.O. Weiss, X. Duan, H.-C. Cheng, Y. Huang and X. Duan, *Van der Waals heterostructures and devices*, *Nature Reviews Materials* **1** (2016) 16042.
- [13] Y. Lei, T. Zhang, Y.-C. Lin, T. Granzier-Nakajima, G. Bepete, D.A. Kowalczyk et al., *Graphene and Beyond: Recent Advances in Two-Dimensional Materials Synthesis, Properties, and Devices*, *ACS Nanoscience Au* **2** (2022) 450.
- [14] F. Giustino, J.H. Lee, F. Trier, M. Bibes, S.M. Winter, R. Valentí et al., *The 2021 quantum materials roadmap*, *Journal of Physics: Materials* **3** (2020) 042006.
- [15] D. Costanzo, S. Jo, H. Berger and A.F. Morpurgo, *Gate-induced superconductivity in atomically thin  $\text{MoS}_2$  crystals*, *Nature Nanotechnology* **11** (2016) 339.
- [16] E. Khestanova, J. Birkbeck, M. Zhu, Y. Cao, G.L. Yu, D. Ghazaryan et al., *Unusual Suppression of the Superconducting Energy Gap and Critical Temperature in Atomically Thin  $\text{NbSe}_2$* , *Nano Letters* **18** (2018) 2623.
- [17] A. Benyamini, E.J. Telford, D.M. Kennes, D. Wang, A. Williams, K. Watanabe et al., *Fragility of the dissipationless state in clean two-dimensional superconductors*, *Nature Physics* **15** (2019) 947.
- [18] W.H. Zhang, X. Liu, C.H.P. Wen, R. Peng, S.Y. Tan, B.P. Xie et al., *Effects of Surface Electron Doping and Substrate on the Superconductivity of Epitaxial  $\text{FeSe}$  Films*, *Nano Letters* **16** (2016) 1969.
- [19] Q.-Y. Wang, Z. Li, W.-H. Zhang, Z.-C. Zhang, J.-S. Zhang, W. Li et al., *Interface-Induced High-Temperature Superconductivity in Single Unit-Cell  $\text{FeSe}$  Films on  $\text{SrTiO}_3$* , *Chinese Physics Letters* **29** (2012) 037402.
- [20] Y. Cao, V. Fatemi, S. Fang, K. Watanabe, T. Taniguchi, E. Kaxiras et al., *Unconventional superconductivity in magic-angle graphene superlattices*, *Nature* **556** (2018) 43.
- [21] Y. Xia, Z. Han, K. Watanabe, T. Taniguchi, J. Shan and K.F. Mak, *Superconductivity in twisted bilayer  $\text{WSe}_2$* , *Nature* (2024) .
- [22] Y. Guo, J. Pack, J. Swann, L. Holtzman, M. Cothrine, K. Watanabe et al., *Superconductivity in  $5.0^\circ$  twisted bilayer  $\text{WSe}_2$* , *Nature* **637** (2025) 839.
- [23] B. Keimer, S.A. Kivelson, M.R. Norman, S. Uchida and J. Zaanen, *From quantum matter to high-temperature superconductivity in copper oxides*, *Nature* **518** (2015) 179.

- [24] L. Hedin, *New Method for Calculating the One-Particle Green's Function with Application to the Electron-Gas Problem*, *Physical Review* **139** (1965) A796.
- [25] F. Aryasetiawan and O. Gunnarsson, *The GW method*, *Reports on Progress in Physics* **61** (1998) 237.
- [26] A.B. Migdal, *Interaction between electrons and lattice vibrations in a normal metal*, *Sov. Phys. JETP* **7** (1958) 996.
- [27] G. Eliashberg, *Interactions between electrons and lattice vibrations in a superconductor*, *Zh. Eksperim. i Teor. Fiz.* **38** (1960) 966.
- [28] G. Eliashberg, *Temperature Green's Function for Electrons in a Superconductor*, *Zh. Eksperim. i Teor. Fiz.* **38** (1960) 1437.
- [29] N. Marzari, A.A. Mostofi, J.R. Yates, I. Souza and D. Vanderbilt, *Maximally localized Wannier functions: Theory and applications*, *Reviews of Modern Physics* **84** (2012) 1419.
- [30] F. Aryasetiawan, M. Imada, A. Georges, G. Kotliar, S. Biermann and A.I. Lichtenstein, *Frequency-dependent local interactions and low-energy effective models from electronic structure calculations*, *Physical Review B* **70** (2004) 195104.
- [31] E. Pavarini, E. Koch, D. Vollhardt, A.I. Lichtenstein, I. for Advanced Simulation, G.R.S. for Simulation Sciences et al., eds., *The LDA+DMFT approach to strongly correlated materials: lecture notes of the Autumn School 2011 Hands-on LDA+DMFT: at Forschungszentrum Jülich, 4-7 October 2011*, no. Band 1 in Schriften des Forschungszentrums Jülich. Reihe Modeling and Simulation, Forschungszentrum Jülich, Zentralbibliothek, Verl, Jülich (2011).
- [32] E. Pavarini, E. Koch, U. Schollwöck, I. for Advanced Simulation and G.R.S. for Simulation Sciences, eds., *Emergent phenomena in correlated matter: lecture notes of the Autumn School Correlated Electrons 2013: at Forschungszentrum Jülich, 23-27 September 2013*, no. Band 3 in Schriften des Forschungszentrums Jülich. Reihe Modeling and Simulation, Forschungszentrum, Zentralbibliothek, Jülich (2013).
- [33] E. Pavarini, E. Koch, R. Scalettar, R. Martin, Institute for Advanced Simulation and German Research School for Simulation Sciences, eds., *The Physics of Correlated Insulators, Metals, and Superconductors: lecture notes of the Autumn School on Correlated Electrons 2017: at Forschungszentrum Jülich, 25-29 September 2017*, no. Band 7 in Schriften des

- Forschungszentrums Jülich. Reihe Modeling and Simulation, Forschungszentrum, Zentralbibliothek, Jülich (2017).
- [34] G.D. Mahan, *Many-Particle Physics*, Springer US, Boston, MA (2000), 10.1007/978-1-4757-5714-9.
- [35] H. Bruus and K. Flensberg, *Many-body quantum theory in condensed matter physics: an introduction*, Oxford University Press, Oxford New York, corrected version ed. (Nov., 2004).
- [36] P. Coleman, *Introduction to many-body physics*, Cambridge University Press, Cambridge (2015), 10.1017/CBO9781139020916.
- [37] H. Zhang, T. Pincelli, C. Jozwiak, T. Kondo, R. Ernstorfer, T. Sato et al., *Angle-resolved photoemission spectroscopy*, *Nature Reviews Methods Primers* **2** (2022) 54.
- [38] L. Hedin, *On correlation effects in electron spectroscopies and the GW approximation*, *Journal of Physics: Condensed Matter* **11** (1999) R489.
- [39] K. Delaney, P. García-González, A. Rubio, P. Rinke and R.W. Godby, *Comment on “Band-Gap Problem in Semiconductors Revisited: Effects of Core States and Many-Body Self-Consistency”*, *Physical Review Letters* **93** (2004) 249701.
- [40] A.L. Kutepov, *Electronic structure of Na, K, Si, and LiF from self-consistent solution of Hedin’s equations including vertex corrections*, *Physical Review B* **94** (2016) 155101.
- [41] Y. Takada, *Role of the ward identity and relevance of the G0W0 approximation in normal and superconducting states*, *Molecular Physics* **114** (2016) 1041.
- [42] A. Tal, W. Chen and A. Pasquarello, *Vertex function compliant with the Ward identity for quasiparticle self-consistent calculations beyond GW*, *Physical Review B* **103** (2021) L161104.
- [43] E.G.C.P. Van Loon, M. Rösner, M.I. Katsnelson and T.O. Wehling, *Random phase approximation for gapped systems: Role of vertex corrections and applicability of the constrained random phase approximation*, *Physical Review B* **104** (2021) 045134.
- [44] A. Schindlmayr, P. García-González and R.W. Godby, *Diagrammatic self-energy approximations and the total particle number*, *Physical Review B* **64** (2001) 235106.

- [45] G. Onida, L. Reining and A. Rubio, *Electronic excitations: density-functional versus many-body Green's-function approaches*, *Reviews of Modern Physics* **74** (2002) 601.
- [46] A. Kutepov, S.Y. Savrasov and G. Kotliar, *Ground-state properties of simple elements from GW calculations*, *Physical Review B* **80** (2009) 041103.
- [47] A.L. Kutepov, *Self-consistent solution of Hedin's equations: Semiconductors and insulators*, *Physical Review B* **95** (2017) 195120.
- [48] A. Georges and G. Kotliar, *Hubbard model in infinite dimensions*, *Physical Review B* **45** (1992) 6479.
- [49] A. Georges, G. Kotliar, W. Krauth and M.J. Rozenberg, *Dynamical mean-field theory of strongly correlated fermion systems and the limit of infinite dimensions*, *Reviews of Modern Physics* **68** (1996) 13.
- [50] Y. Takada, *Electron correlations in a multivalley electron gas and Fermion-boson conversion*, *Physical Review B* **43** (1991) 5962.
- [51] K. Chen and K. Haule, *A combined variational and diagrammatic quantum Monte Carlo approach to the many-electron problem*, *Nature Communications* **10** (2019) 3725.
- [52] F. Aryasetiawan, L. Hedin and K. Karlsson, *Multiple Plasmon Satellites in Na and Al Spectral Functions from Ab Initio Cumulant Expansion*, *Physical Review Letters* **77** (1996) 2268.
- [53] F. Caruso and F. Giustino, *The GW plus cumulant method and plasmonic polarons: application to the homogeneous electron gas\**, *The European Physical Journal B* **89** (2016) 238.
- [54] J. Lindhard, *On the properties of a gas of charged particles*, *Kgl. Danske Videnskab. Selskab Mat.-fys. Medd.* **28 - 8** (1954) .
- [55] H. Ehrenreich and M.H. Cohen, *Self-Consistent Field Approach to the Many-Electron Problem*, *Physical Review* **115** (1959) 786.
- [56] D. Bohm and D. Pines, *A Collective Description of Electron Interactions. I. Magnetic Interactions*, *Physical Review* **82** (1951) 625.
- [57] D. Pines and D. Bohm, *A Collective Description of Electron Interactions: II. Collective vs Individual Particle Aspects of the Interactions*, *Physical Review* **85** (1952) 338.

- [58] D. Bohm and D. Pines, *A Collective Description of Electron Interactions: III. Coulomb Interactions in a Degenerate Electron Gas*, *Physical Review* **92** (1953) 609.
- [59] J.M. Riley, F. Caruso, C. Verdi, L.B. Duffy, M.D. Watson, L. Bawden et al., *Crossover from lattice to plasmonic polarons of a spin-polarised electron gas in ferromagnetic EuO*, *Nature Communications* **9** (2018) 2305.
- [60] S. Ulstrup, Y. in 't Veld, J.A. Miwa, A.J.H. Jones, K.M. McCreary, J.T. Robinson et al., *Observation of interlayer plasmon polaron in graphene/WS<sub>2</sub> heterostructures*, *Nature Communications* **15** (2024) 3845.
- [61] F. Caruso, P. Amsalem, J. Ma, A. Aljarb, T. Schultz, M. Zacharias et al., *Two-dimensional plasmonic polarons in n-doped monolayer MoS<sub>2</sub>*, *Physical Review B* **103** (2021) 205152.
- [62] Y. In 't Veld, M.I. Katsnelson, A.J. Millis and M. Rösner, *Screening induced crossover between phonon- and plasmon-mediated pairing in layered superconductors*, *2D Materials* **10** (2023) 045031.
- [63] Y. Takada, *Plasmon Mechanism of Superconductivity in Two- and Three-Dimensional Electron Systems*, *Journal of the Physical Society of Japan* **45** (1978) 786.
- [64] Y. Takada, *Plasmon Mechanism of Superconductivity in the Multivalley Electron Gas*, *Journal of the Physical Society of Japan* **61** (1992) 238.
- [65] R. Akashi and R. Arita, *Development of Density-Functional Theory for a Plasmon-Assisted Superconducting State: Application to Lithium Under High Pressures*, *Physical Review Letters* **111** (2013) 057006.
- [66] R. Akashi and R. Arita, *Density Functional Theory for Plasmon-Assisted Superconductivity*, *Journal of the Physical Society of Japan* **83** (2014) 061016.
- [67] S. Zhang, T. Wei, J. Guan, Q. Zhu, W. Qin, W. Wang et al., *Enhanced Superconducting State in FeSe / SrTiO<sub>3</sub> by a Dynamic Interfacial Polaron Mechanism*, *Physical Review Letters* **122** (2019) 066802.
- [68] A. Bill, H. Morawitz and V.Z. Kresin, *Electronic collective modes and superconductivity in layered conductors*, *Physical Review B* **68** (2003) 144519.
- [69] E.A. Pashitskii and V.I. Pentegov, *On the plasmon mechanism of high-T<sub>c</sub> superconductivity in layered crystals and two-dimensional systems*, *Low Temperature Physics* **34** (2008) 113.



- [70] A. Davydov, A. Sanna, C. Pellegrini, J.K. Dewhurst, S. Sharma and E.K.U. Gross, *Ab initio theory of plasmonic superconductivity within the Eliashberg and density-functional formalisms*, *Physical Review B* **102** (2020) 214508.
- [71] X. Cai, T. Wang, N.V. Prokof'ev, B.V. Svistunov and K. Chen, *Superconductivity in the uniform electron gas: Irrelevance of the Kohn-Luttinger mechanism*, *Physical Review B* **106** (2022) L220502.
- [72] A. Grankin and V. Galitski, *Interplay of hyperbolic plasmons and superconductivity*, *Physical Review B* **108** (2023) 094506.
- [73] A.W. Blackstock, R.H. Ritchie and R.D. Birkhoff, *Mean Free Path for Discrete Electron Energy Losses in Metallic Foils*, *Physical Review* **100** (1955) 1078.
- [74] M.S. Hybertsen and S.G. Louie, *Electron correlation in semiconductors and insulators: Band gaps and quasiparticle energies*, *Physical Review B* **34** (1986) 5390.
- [75] H. Morawitz, I. Bozovic, V.Z. Kresin, G. Rietveld and D. Van Der Marel, *The plasmon density of states of a layered electron gas*, *Zeitschrift für Physik B Condensed Matter* **90** (1993) 277.
- [76] A. Bostwick, F. Speck, T. Seyller, K. Horn, M. Polini, R. Asgari et al., *Observation of Plasmarons in Quasi-Freestanding Doped Graphene*, *Science* **328** (2010) 999.
- [77] A.L. Walter, A. Bostwick, K.-J. Jeon, F. Speck, M. Ostler, T. Seyller et al., *Effective screening and the plasmaron bands in graphene*, *Physical Review B* **84** (2011) 085410.
- [78] M. Guzzo, G. Lani, F. Sottile, P. Romaniello, M. Gatti, J.J. Kas et al., *Valence Electron Photoemission Spectrum of Semiconductors: Ab Initio Description of Multiple Satellites*, *Physical Review Letters* **107** (2011) 166401.
- [79] J. Lischner, D. Vigil-Fowler and S.G. Louie, *Physical Origin of Satellites in Photoemission of Doped Graphene: An Ab Initio GW Plus Cumulant Study*, *Physical Review Letters* **110** (2013) 146801.
- [80] A. Bostwick, T. Ohta, T. Seyller, K. Horn and E. Rotenberg, *Quasiparticle dynamics in graphene*, *Nature Physics* **3** (2007) 36.

- [81] S.Y. Zhou, G.-H. Gweon, J. Graf, A.V. Fedorov, C.D. Spataru, R.D. Diehl et al., *First direct observation of Dirac fermions in graphite*, *Nature Physics* **2** (2006) 595.
- [82] M. Polini, R. Asgari, G. Borghi, Y. Barlas, T. Pereg-Barnea and A.H. MacDonald, *Plasmons and the spectral function of graphene*, *Physical Review B* **77** (2008) 081411.
- [83] E.H. Hwang and S. Das Sarma, *Quasiparticle spectral function in doped graphene: Electron-electron interaction effects in ARPES*, *Physical Review B* **77** (2008) 081412.
- [84] J.J. Kas, J.J. Rehr and L. Reining, *Cumulant expansion of the retarded one-electron Green function*, *Physical Review B* **90** (2014) 085112.
- [85] F. Caruso, H. Lambert and F. Giustino, *Band Structures of Plasmonic Polarons*, *Phys. Rev. Lett.* **114** (2015) 146404.
- [86] C.A. Kukkonen and A.W. Overhauser, *Electron-electron interaction in simple metals*, *Physical Review B* **20** (1979) 550.
- [87] C.A. Kukkonen and K. Chen, *Quantitative electron-electron interaction using local field factors from quantum Monte Carlo calculations*, *Physical Review B* **104** (2021) 195142.
- [88] B. Cunningham, M. Grüning, D. Pashov and M. Van Schilfgaarde, *QS GW: Quasiparticle self-consistent GW with ladder diagrams in W*, *Physical Review B* **108** (2023) 165104.
- [89] P.-F. Loos and P. Romaniello, *Static and dynamic Bethe–Salpeter equations in the T-matrix approximation*, *The Journal of Chemical Physics* **156** (2022) 164101.
- [90] M. Guzzo, J.J. Kas, L. Sponza, C. Giorgetti, F. Sottile, D. Pierucci et al., *Multiple satellites in materials with complex plasmon spectra: From graphite to graphene*, *Physical Review B* **89** (2014) 085425.
- [91] B. Gumhalter, V. Kovač, F. Caruso, H. Lambert and F. Giustino, *On the combined use of GW approximation and cumulant expansion in the calculations of quasiparticle spectra: The paradigm of Si valence bands*, *Physical Review B* **94** (2016) 035103.
- [92] D.C. Langreth, *Singularities in the X-Ray Spectra of Metals*, *Physical Review B* **1** (1970) 471.

- [93] H. Ness, L.K. Dash, M. Stankovski and R.W. Godby, *GW approximations and vertex corrections on the Keldysh time-loop contour: Application for model systems at equilibrium*, *Physical Review B* **84** (2011) 195114.
- [94] J.P. Nery, P.B. Allen, G. Antonius, L. Reining, A. Miglio and X. Gonze, *Quasiparticles and phonon satellites in spectral functions of semiconductors and insulators: Cumulants applied to the full first-principles theory and the Fröhlich polaron*, *Physical Review B* **97** (2018) 115145.
- [95] N. Marzari and D. Vanderbilt, *Maximally localized generalized Wannier functions for composite energy bands*, *Physical Review B* **56** (1997) 12847.
- [96] I. Souza, N. Marzari and D. Vanderbilt, *Maximally localized Wannier functions for entangled energy bands*, *Physical Review B* **65** (2001) 035109.
- [97] F. Aryasetiawan and F. Nilsson, *Downfolding Methods in Many-Electron Theory*, AIP Publishing LLC Melville, New York (Aug., 2022), 10.1063/9780735422490.
- [98] M. Rösner, E. Şaşıoğlu, C. Friedrich, S. Blügel and T.O. Wehling, *Wannier function approach to realistic Coulomb interactions in layered materials and heterostructures*, *Physical Review B* **92** (2015) 085102.
- [99] L.V. Keldysh, *Coulomb interaction in thin semiconductor and semimetal films*, *Soviet Journal of Experimental and Theoretical Physics Letters* **29** (1979) 658.
- [100] A. Steinhoff, M. Rösner, F. Jahnke, T.O. Wehling and C. Gies, *Influence of Excited Carriers on the Optical and Electronic Properties of MoS<sub>2</sub>*, *Nano Letters* **14** (2014) 3743.
- [101] G. Schönhoff, M. Rösner, R.E. Groenewald, S. Haas and T.O. Wehling, *Interplay of screening and superconductivity in low-dimensional materials*, *Physical Review B* **94** (2016) 134504.
- [102] C. Steinke, T.O. Wehling and M. Rösner, *Coulomb-engineered heterojunctions and dynamical screening in transition metal dichalcogenide monolayers*, *Physical Review B* **102** (2020) 115111.
- [103] D. Soriano, A.N. Rudenko, M.I. Katsnelson and M. Rösner, *Environmental screening and ligand-field effects to magnetism in CrI<sub>3</sub> monolayer*, *npj Computational Materials* **7** (2021) 1.
- [104] E.A. Stepanov, V. Harkov, M. Rösner, A.I. Lichtenstein, M.I. Katsnelson and A.N. Rudenko, *Coexisting charge density wave and ferromagnetic instabilities in monolayer InSe*, *npj Computational Materials* **8** (2022) 1.

- [105] H. Fröhlich, *Theory of the Superconducting State. I. The Ground State at the Absolute Zero of Temperature*, *Physical Review* **79** (1950) 845.
- [106] H. Fröhlich, *Superconductivity in metals with incomplete inner shells*, *Journal of Physics C: Solid State Physics* **1** (1968) 544.
- [107] J. Bardeen, L.N. Cooper and J.R. Schrieffer, *Theory of Superconductivity*, *Physical Review* **108** (1957) 1175.
- [108] J.P. Carbotte, *Properties of boson-exchange superconductors*, *Reviews of Modern Physics* **62** (1990) 1027.
- [109] P. Morel and P.W. Anderson, *Calculation of the Superconducting State Parameters with Retarded Electron-Phonon Interaction*, *Physical Review* **125** (1962) 1263.
- [110] J. Bauer, J.E. Han and O. Gunnarsson, *Retardation effects and the Coulomb pseudopotential in the theory of superconductivity*, *Physical Review B* **87** (2013) 054507.
- [111] N.N. Bogoljubov, V.V. Tolmachov and D.V. Širkov, *A New Method in the Theory of Superconductivity*, *Fortschritte der Physik* **6** (1958) 605.
- [112] E.R. Margine and F. Giustino, *Anisotropic Migdal-Eliashberg theory using Wannier functions*, *Physical Review B* **87** (2013) 024505.
- [113] G. Profeta, M. Calandra and F. Mauri, *Phonon-mediated superconductivity in graphene by lithium deposition*, *Nature Physics* **8** (2012) 131.
- [114] C. Tresca, G. Profeta, G. Marini, G.B. Bachelet, A. Sanna, M. Calandra et al., *Why mercury is a superconductor*, *Physical Review B* **106** (2022) L180501.
- [115] M. Grabowski and L.J. Sham, *Superconductivity from nonphonon interactions*, *Physical Review B* **29** (1984) 6132.
- [116] I.I. Mazin, D.J. Singh, M.D. Johannes and M.H. Du, *Unconventional Superconductivity with a Sign Reversal in the Order Parameter of  $\text{LaFeAsO}_{1-x}\text{F}_x$* , *Physical Review Letters* **101** (2008) 057003.
- [117] Z.P. Yin, K. Haule and G. Kotliar, *Spin dynamics and orbital-antiphase pairing symmetry in iron-based superconductors*, *Nature Physics* **10** (2014) 845.
- [118] S. Acharya, D. Pashov, F. Jamet and M. van Schilfhaarde, *Electronic Origin of  $T_c$  in Bulk and Monolayer  $\text{FeSe}$* , *Symmetry* **13** (2021) 169.

- [119] T. Wei and Z. Zhang, *High-temperature superconductivity in monolayer FeSe on SrTiO<sub>3</sub> and related systems mediated by low energy plasmons*, *Physical Review B* **104** (2021) 184503.
- [120] K. Sano, M. Seo and K. Nakamura, *Plasmon Effect on the Coulomb Pseudopotential  $\mu^*$  in the McMillan Equation*, *Journal of the Physical Society of Japan* **88** (2019) 093703.
- [121] A. Sanna, C. Pellegrini and E.K.U. Gross, *Combining Eliashberg Theory with Density Functional Theory for the Accurate Prediction of Superconducting Transition Temperatures and Gap Functions*, *Physical Review Letters* **125** (2020) 057001.
- [122] Y. Nambu, *Quasi-Particles and Gauge Invariance in the Theory of Superconductivity*, *Physical Review* **117** (1960) 648.
- [123] L.P. Gor'Kov, *On the energy spectrum of superconductors*, *Sov. Phys. JETP* **34(7)** (1958) 505.
- [124] F. Marsiglio, *Eliashberg theory in the weak-coupling limit*, *Physical Review B* **98** (2018) 024523.
- [125] F. Marsiglio, *Eliashberg theory of the critical temperature and isotope effect. Dependence on bandwidth, band-filling, and direct Coulomb repulsion*, *Journal of Low Temperature Physics* **87** (1992) 659.
- [126] F. Giustino, *Electron-phonon interactions from first principles*, *Reviews of Modern Physics* **89** (2017) 015003.
- [127] F. Marsiglio, *Eliashberg theory: A short review*, *Annals of Physics* **417** (2020) 168102.
- [128] J. Berges, *On the scope of McMillan's formula*, Master's thesis, Universität Bremen, Bremen, Nov., 2016.
- [129] M. Simonato, M.I. Katsnelson and M. Rösner, *Revised Tolmachev-Morel-Anderson pseudopotential for layered conventional superconductors with nonlocal Coulomb interaction*, *Physical Review B* **108** (2023) 064513.
- [130] S. Poncé, E. Margine, C. Verdi and F. Giustino, *EPW: Electron-phonon coupling, transport and superconducting properties using maximally localized Wannier functions*, *Computer Physics Communications* **209** (2016) 116.
- [131] W.L. McMillan, *Transition Temperature of Strong-Coupled Superconductors*, *Physical Review* **167** (1968) 331.

- [132] R.C. Dynes, *McMillan's equation and the  $T_c$  of superconductors*, *Solid State Communications* **10** (1972) 615.
- [133] P.B. Allen and R.C. Dynes, *Transition temperature of strong-coupled superconductors reanalyzed*, *Physical Review B* **12** (1975) 905.
- [134] V.V. Tolmachev, *Logarithmic criterion for superconductivity*, *Dokl. Akad. Nauk SSSR* **140** (1961) 563.
- [135] E. Gull, S. Iskakov, I. Krivenko, A.A. Rusakov and D. Zgid, *Chebyshev polynomial representation of imaginary-time response functions*, *Physical Review B* **98** (2018) 075127.
- [136] L. Boehnke, H. Hafermann, M. Ferrero, F. Lechermann and O. Parcollet, *Orthogonal polynomial representation of imaginary-time Green's functions*, *Physical Review B* **84** (2011) 075145.
- [137] X. Dong, D. Zgid, E. Gull and H.U.R. Strand, *Legendre-spectral Dyson equation solver with super-exponential convergence*, *The Journal of Chemical Physics* **152** (2020) 134107.
- [138] W. Ku and A.G. Eguiluz, *Band-Gap Problem in Semiconductors Revisited: Effects of Core States and Many-Body Self-Consistency*, *Physical Review Letters* **89** (2002) 126401.
- [139] A.A. Kananenka, A.R. Welden, T.N. Lan, E. Gull and D. Zgid, *Efficient Temperature-Dependent Green's Function Methods for Realistic Systems: Using Cubic Spline Interpolation to Approximate Matsubara Green's Functions*, *Journal of Chemical Theory and Computation* **12** (2016) 2250.
- [140] J. Kaye, K. Chen and O. Parcollet, *Discrete Lehmann representation of imaginary time Green's functions*, *Physical Review B* **105** (2022) 235115.
- [141] D. Kiese, H.U.R. Strand, K. Chen, N. Wentzell, O. Parcollet and J. Kaye, *Discrete Lehmann representation of three-point functions*, *Physical Review B* **111** (2025) 035135.
- [142] H. Shinaoka, J. Otsuki, M. Ohzeki and K. Yoshimi, *Compressing Green's function using intermediate representation between imaginary-time and real-frequency domains*, *Physical Review B* **96** (2017) 035147.
- [143] N. Chikano, J. Otsuki and H. Shinaoka, *Performance analysis of a physically constructed orthogonal representation of imaginary-time Green's function*, *Physical Review B* **98** (2018) 035104.

- [144] H. Shinaoka, N. Chikano, E. Gull, J. Li, T. Nomoto, J. Otsuki et al., *Efficient ab initio many-body calculations based on sparse modeling of Matsubara Green's function*, *SciPost Physics Lecture Notes* (2022) 63.
- [145] M. Wallerberger, S. Badr, S. Hoshino, S. Huber, F. Kakizawa, T. Koretsune et al., *sparse-ir: Optimal compression and sparse sampling of many-body propagators*, *SoftwareX* **21** (2023) 101266.
- [146] M. Kaltak and G. Kresse, *Minimax isometry method: A compressive sensing approach for Matsubara summation in many-body perturbation theory*, *Physical Review B* **101** (2020) 205145.
- [147] Y. Nagai and H. Shinaoka, *Smooth Self-energy in the Exact-diagonalization-based Dynamical Mean-field Theory: Intermediate-representation Filtering Approach*, *Journal of the Physical Society of Japan* **88** (2019) 064004.
- [148] M. Wallerberger, H. Shinaoka and A. Kauch, *Solving the Bethe-Salpeter equation with exponential convergence*, *Physical Review Research* **3** (2021) 033168.
- [149] T. Wang, T. Nomoto, Y. Nomura, H. Shinaoka, J. Otsuki, T. Koretsune et al., *Efficient ab initio Migdal-Eliashberg calculation considering the retardation effect in phonon-mediated superconductors*, *Physical Review B* **102** (2020) 134503.
- [150] H. Shinaoka and Y. Nagai, *Sparse modeling of large-scale quantum impurity models with low symmetries*, *Physical Review B* **103** (2021) 045120.
- [151] N. Witt, E.G.C.P. Van Loon, T. Nomoto, R. Arita and T.O. Wehling, *Efficient fluctuation-exchange approach to low-temperature spin fluctuations and superconductivity: From the Hubbard model to  $\text{Na}_x\text{CoO}_2 \cdot y\text{H}_2\text{O}$* , *Physical Review B* **103** (2021) 205148.
- [152] J. Kaye, K. Chen and H.U. Strand, *libdlr: Efficient imaginary time calculations using the discrete Lehmann representation*, *Computer Physics Communications* **280** (2022) 108458.
- [153] *NumericalEFT*, Oct., 2020,  
<https://numericaleft.github.io/NumericalEFT.jl/stable/>.
- [154] J. Kaye, H.U.R. Strand and N. Wentzell, *cppdlr: Imaginary time calculations using the discrete Lehmann representation*, *Journal of Open Source Software* **9** (2024) 6297.

- [155] O. Parcollet, M. Ferrero, T. Ayrat, H. Hafermann, I. Krivenko, L. Messio et al., *TRIQS: A toolbox for research on interacting quantum systems*, *Computer Physics Communications* **196** (2015) 398.
- [156] M.I. Katsnelson, K.S. Novoselov and A.K. Geim, *Chiral tunnelling and the Klein paradox in graphene*, *Nature Physics* **2** (2006) 620.
- [157] T. Tudorovskiy, K.J.A. Reijnders and M.I. Katsnelson, *Chiral tunneling in single-layer and bilayer graphene*, *Physica Scripta* **T146** (2012) 014010.
- [158] Y. Zhang, Y.-W. Tan, H.L. Stormer and P. Kim, *Experimental observation of the quantum Hall effect and Berry's phase in graphene*, *Nature* **438** (2005) 201.
- [159] K.S. Novoselov, Z. Jiang, Y. Zhang, S.V. Morozov, H.L. Stormer, U. Zeitler et al., *Room-Temperature Quantum Hall Effect in Graphene*, *Science* **315** (2007) 1379.
- [160] S. Reich, J. Maultzsch, C. Thomsen and P. Ordejón, *Tight-binding description of graphene*, *Physical Review B* **66** (2002) 035412.
- [161] M. Rösner, *Electronic structure of novel two-dimensional materials and graphene heterostructures*, Ph.D. thesis, Universität Bremen, Bremen, Oct., 2016.
- [162] B. Wunsch, T. Stauber, F. Sols and F. Guinea, *Dynamical polarization of graphene at finite doping*, *New Journal of Physics* **8** (2006) 318.
- [163] E.H. Hwang and S. Das Sarma, *Dielectric function, screening, and plasmons in two-dimensional graphene*, *Physical Review B* **75** (2007) 205418.
- [164] P.K. Pyatkovskiy, *Dynamical polarization, screening, and plasmons in gapped graphene*, *Journal of Physics: Condensed Matter* **21** (2009) 025506.
- [165] Q.H. Wang, K. Kalantar-Zadeh, A. Kis, J.N. Coleman and M.S. Strano, *Electronics and optoelectronics of two-dimensional transition metal dichalcogenides*, *Nature Nanotechnology* **7** (2012) 699.
- [166] L. Liao, J. Bai, Y. Qu, Y.-c. Lin, Y. Li, Y. Huang et al., *High- $\kappa$  oxide nanoribbons as gate dielectrics for high mobility top-gated graphene transistors*, *Proceedings of the National Academy of Sciences* **107** (2010) 6711.
- [167] L. Liao, Y.-C. Lin, M. Bao, R. Cheng, J. Bai, Y. Liu et al., *High-speed graphene transistors with a self-aligned nanowire gate*, *Nature* **467** (2010) 305.



- [168] B. Radisavljevic, A. Radenovic, J. Brivio, V. Giacometti and A. Kis, *Single-layer MoS<sub>2</sub> transistors*, *Nature Nanotechnology* **6** (2011) 147.
- [169] G. Konstantatos, M. Badioli, L. Gaudreau, J. Osmond, M. Bernechea, F.P.G. De Arquer et al., *Hybrid graphene–quantum dot phototransistors with ultrahigh gain*, *Nature Nanotechnology* **7** (2012) 363.
- [170] J. Yan, M.-H. Kim, J.A. Elle, A.B. Sushkov, G.S. Jenkins, H.M. Milchberg et al., *Dual-gated bilayer graphene hot-electron bolometer*, *Nature Nanotechnology* **7** (2012) 472.
- [171] G. Wang, Y. Zhang, C. You, B. Liu, Y. Yang, H. Li et al., *Two dimensional materials based photodetectors*, *Infrared Physics & Technology* **88** (2018) 149.
- [172] K. Zhang, L. Zhang, L. Han, L. Wang, Z. Chen, H. Xing et al., *Recent progress and challenges based on two-dimensional material photodetectors*, *Nano Express* **2** (2021) 012001.
- [173] J.M. Lu, O. Zheliuk, I. Leermakers, N.F.Q. Yuan, U. Zeitler, K.T. Law et al., *Evidence for two-dimensional Ising superconductivity in gated MoS<sub>2</sub>*, *Science* **350** (2015) 1353.
- [174] J. Lu, O. Zheliuk, Q. Chen, I. Leermakers, N.E. Hussey, U. Zeitler et al., *Full superconducting dome of strong Ising protection in gated monolayer WS<sub>2</sub>*, *Proceedings of the National Academy of Sciences* **115** (2018) 3551.
- [175] W.S. Yun, S.W. Han, S.C. Hong, I.G. Kim and J.D. Lee, *Thickness and strain effects on electronic structures of transition metal dichalcogenides: 2H-MX<sub>2</sub> semiconductors (M = Mo, W; X = S, Se, Te)*, *Physical Review B* **85** (2012) 033305.
- [176] A. Kuc, N. Zibouche and T. Heine, *Influence of quantum confinement on the electronic structure of the transition metal sulfide TS<sub>2</sub>*, *Physical Review B* **83** (2011) 245213.
- [177] S. Hastrup, M. Strange, M. Pandey, T. Deilmann, P.S. Schmidt, N.F. Hinsche et al., *The Computational 2D Materials Database: high-throughput modeling and discovery of atomically thin crystals*, *2D Materials* **5** (2018) 042002.
- [178] M.N. Gjerding, A. Taghizadeh, A. Rasmussen, S. Ali, F. Bertoldo, T. Deilmann et al., *Recent progress of the Computational 2D Materials Database (C2DB)*, *2D Materials* **8** (2021) 044002.

- [179] A. Chaves, J.G. Azadani, H. Alsalman, D.R. da Costa, R. Frisenda, A.J. Chaves et al., *Bandgap engineering of two-dimensional semiconductor materials*, *npj 2D Materials and Applications* **4** (2020) 1.
- [180] J. Gusakova, X. Wang, L.L. Shiau, A. Krivosheeva, V. Shaposhnikov, V. Borisenko et al., *Electronic Properties of Bulk and Monolayer TMDs: Theoretical Study Within DFT Framework (GVJ-2e Method)*, *physica status solidi (a)* **214** (2017) 1700218.
- [181] R.E. Groenewald, M. Rösner, G. Schönhoff, S. Haas and T.O. Wehling, *Valley plasmonics in transition metal dichalcogenides*, *Physical Review B* **93** (2016) 205145.
- [182] Y. Tang, L. Li, T. Li, Y. Xu, S. Liu, K. Barmak et al., *Simulation of Hubbard model physics in  $WSe_2/WS_2$  moiré superlattices*, *Nature* **579** (2020) 353.
- [183] E.C. Regan, D. Wang, C. Jin, M.I. Bakti Utama, B. Gao, X. Wei et al., *Mott and generalized Wigner crystal states in  $WSe_2/WS_2$  moiré superlattices*, *Nature* **579** (2020) 359.
- [184] D.M. Kennes, M. Claassen, L. Xian, A. Georges, A.J. Millis, J. Hone et al., *Moiré heterostructures as a condensed-matter quantum simulator*, *Nature Physics* **17** (2021) 155.
- [185] S. Ulstrup, C.E. Giusca, J.A. Miwa, C.E. Sanders, A. Browning, P. Dudin et al., *Nanoscale mapping of quasiparticle band alignment*, *Nature Communications* **10** (2019) 3283.
- [186] L. Waldecker, A. Raja, M. Rösner, C. Steinke, A. Bostwick, R.J. Koch et al., *Rigid Band Shifts in Two-Dimensional Semiconductors through External Dielectric Screening*, *Phys. Rev. Lett.* **123** (2019) 206403.
- [187] S. Ulstrup, R.J. Koch, S. Singh, K.M. McCreary, B.T. Jonker, J.T. Robinson et al., *Direct observation of minibands in a twisted graphene/ $WS_2$  bilayer*, *Science Advances* **6** (2020) eaay6104.
- [188] S. Xie, B.D. Faeth, Y. Tang, L. Li, E. Gerber, C.T. Parzyck et al., *Strong interlayer interactions in bilayer and trilayer moiré superlattices*, *Science Advances* **8** (2022) eabk1911.
- [189] H.S. Arora, R. Polski, Y. Zhang, A. Thomson, Y. Choi, H. Kim et al., *Superconductivity in metallic twisted bilayer graphene stabilized by  $WSe_2$* , *Nature* **583** (2020) 379.

- [190] Z. Hennighausen, J. Moon, K.M. McCreary, C.H. Li, O.M.J. van 't Erve and B.T. Jonker, *Interlayer Exciton–Phonon Bound State in  $\text{Bi}_2\text{Se}_3/\text{Monolayer WS}_2$  van der Waals Heterostructures*, *ACS Nano* **17** (2023) 2529.
- [191] S. Moser, L. Moreschini, J. Jaćimović, O.S. Barišić, H. Berger, A. Magrez et al., *Tunable Polaronic Conduction in Anatase  $\text{TiO}_2$* , *Physical Review Letters* **110** (2013) 196403.
- [192] Z. Wang, S. McKeown Walker, A. Tamai, Y. Wang, Z. Ristic, F.Y. Bruno et al., *Tailoring the nature and strength of electron–phonon interactions in the  $\text{SrTiO}_3(001)$  2D electron liquid*, *Nature Materials* **15** (2016) 835.
- [193] M. Kang, S.W. Jung, W.J. Shin, Y. Sohn, S.H. Ryu, T.K. Kim et al., *Holstein polaron in a valley-degenerate two-dimensional semiconductor*, *Nature Materials* **17** (2018) 676.
- [194] C. Chen, J. Avila, S. Wang, Y. Wang, M. Mucha-Kruczyński, C. Shen et al., *Emergence of Interfacial Polarons from Electron–Phonon Coupling in Graphene/ $h$ -BN van der Waals Heterostructures*, *Nano Letters* **18** (2018) 1082.
- [195] M. Xiang, X. Ma, C. Gao, Z. Guo, C. Huang, Y. Xing et al., *Revealing the Polaron State at the  $\text{MoS}_2/\text{TiO}_2$  Interface*, *The Journal of Physical Chemistry Letters* **14** (2023) 3360.
- [196] X. Ma, Z. Cheng, M. Tian, X. Liu, X. Cui, Y. Huang et al., *Formation of Plasmonic Polarons in Highly Electron-Doped Anatase  $\text{TiO}_2$* , *Nano Letters* **21** (2021) 430.
- [197] P.V. Nguyen, N.C. Teutsch, N.P. Wilson, J. Kahn, X. Xia, A.J. Graham et al., *Visualizing electrostatic gating effects in two-dimensional heterostructures*, *Nature* **572** (2019) 220.
- [198] H.-J. Chuang, X. Tan, N.J. Ghimire, M.M. Perera, B. Chamlagain, M.M.-C. Cheng et al., *High Mobility  $\text{WSe}_2$  p- and n-Type Field-Effect Transistors Contacted by Highly Doped Graphene for Low-Resistance Contacts*, *Nano Letters* **14** (2014) 3594.
- [199] X. Cui, G.-H. Lee, Y.D. Kim, G. Arefe, P.Y. Huang, C.-H. Lee et al., *Multi-terminal transport measurements of  $\text{MoS}_2$  using a van der Waals heterostructure device platform*, *Nature Nanotechnology* **10** (2015) 534.
- [200] Y. Liu, H. Wu, H.-C. Cheng, S. Yang, E. Zhu, Q. He et al., *Toward Barrier Free Contact to Molybdenum Disulfide Using Graphene Electrodes*, *Nano Letters* **15** (2015) 3030.

- [201] R. Pisoni, Y. Lee, H. Overweg, M. Eich, P. Simonet, K. Watanabe et al., *Gate-Defined One-Dimensional Channel and Broken Symmetry States in MoS<sub>2</sub> van der Waals Heterostructures*, *Nano Letters* **17** (2017) 5008.
- [202] S.-S. Chee, D. Seo, H. Kim, H. Jang, S. Lee, S.P. Moon et al., *Lowering the Schottky Barrier Height by Graphene/Ag Electrodes for High-Mobility MoS<sub>2</sub> Field-Effect Transistors*, *Advanced Materials* **31** (2019) 1804422.
- [203] J. Katoch, S. Ulstrup, R.J. Koch, S. Moser, K.M. McCreary, S. Singh et al., *Giant spin-splitting and gap renormalization driven by trions in single-layer WS<sub>2</sub>/h-BN heterostructures*, *Nature Physics* **14** (2018) 355.
- [204] N.F. Hinsche, A.S. Ngankeu, K. Guilloy, S.K. Mahatha, A. Grubišić Čabo, M. Bianchi et al., *Spin-dependent electron-phonon coupling in the valence band of single-layer WS<sub>2</sub>*, *Physical Review B* **96** (2017) 121402.
- [205] Z.Y. Zhu, Y.C. Cheng and U. Schwingenschlögl, *Giant spin-orbit-induced spin splitting in two-dimensional transition-metal dichalcogenide semiconductors*, *Phys. Rev. B* **84** (2011) 153402.
- [206] W.H. Sio and F. Giustino, *Polarons in two-dimensional atomic crystals*, *Nature Physics* **19** (2023) 629.
- [207] R. Krause, S. Aeschlimann, M. Chávez-Cervantes, R. Perea-Causin, S. Brem, E. Malic et al., *Microscopic Understanding of Ultrafast Charge Transfer in van der Waals Heterostructures*, *Phys. Rev. Lett.* **127** (2021) 276401.
- [208] N. Hofmann, L. Weigl, J. Gradl, N. Mishra, G. Orlandini, S. Forti et al., *Link between interlayer hybridization and ultrafast charge transfer in WS<sub>2</sub>-graphene heterostructures*, *2D Materials* **10** (2023) 035025.
- [209] I. Gierz, J. Henk, H. Höchst, C.R. Ast and K. Kern, *Illuminating the dark corridor in graphene: Polarization dependence of angle-resolved photoemission spectroscopy on graphene*, *Physical Review B* **83** (2011) 121408.
- [210] A. Berkdemir, H.R. Gutiérrez, A.R. Botello-Méndez, N. Perea-López, A.L. Elías, C.-I. Chia et al., *Identification of individual and few layers of WS<sub>2</sub> using Raman Spectroscopy*, *Scientific Reports* **3** (2013) 1755.
- [211] D. Novko, *Dopant-Induced Plasmon Decay in Graphene*, *Nano Letters* **17** (2017) 6991.
- [212] E.R. Margine, H. Lambert and F. Giustino, *Electron-phonon interaction and pairing mechanism in superconducting Ca-intercalated bilayer graphene*, *Scientific Reports* **6** (2016) 21414.

- [213] D. Vigil-Fowler, S.G. Louie and J. Lischner, *Dispersion and line shape of plasmon satellites in one, two, and three dimensions*, *Physical Review B* **93** (2016) 235446.
- [214] S. Zihlmann, A.W. Cummings, J.H. Garcia, M. Kedves, K. Watanabe, T. Taniguchi et al., *Large spin relaxation anisotropy and valley-Zeeman spin-orbit coupling in WSe<sub>2</sub>/graphene/h-BN heterostructures*, *Phys. Rev. B* **97** (2018) 075434.
- [215] D. Hernangómez-Pérez, A. Donarini and S. Refaely-Abramson, *Charge quenching at defect states in transition metal dichalcogenide-graphene van der Waals heterobilayers*, *Physical Review B* **107** (2023) 075419.
- [216] G. Kresse and J. Hafner, *Ab initio molecular dynamics for liquid metals*, *Physical Review B* **47** (1993) 558.
- [217] G. Kresse and J. Furthmüller, *Efficient iterative schemes for ab initio total-energy calculations using a plane-wave basis set*, *Physical Review B* **54** (1996) 11169.
- [218] G. Kresse and D. Joubert, *From ultrasoft pseudopotentials to the projector augmented-wave method*, *Physical Review B* **59** (1999) 1758.
- [219] P.E. Blöchl, *Projector augmented-wave method*, *Physical Review B* **50** (1994) 17953.
- [220] J.P. Perdew, K. Burke and M. Ernzerhof, *Generalized Gradient Approximation Made Simple*, *Phys. Rev. Lett.* **77** (1996) 3865.
- [221] V. Popescu and A. Zunger, *Extracting  $E$  vs  $k$  effective band structure from supercell calculations on alloys and impurities*, *Physical Review B* **85** (2012) 085201.
- [222] Q. Zheng, *QijingZheng/VaspBandUnfolding*, 2023, <https://github.com/QijingZheng/VaspBandUnfolding>.
- [223] S. Qin, J. Kim, Q. Niu and C.-K. Shih, *Superconductivity at the Two-Dimensional Limit*, *Science* **324** (2009) 1314.
- [224] T. Zhang, P. Cheng, W.-J. Li, Y.-J. Sun, G. Wang, X.-G. Zhu et al., *Superconductivity in one-atomic-layer metal films grown on Si(111)*, *Nature Physics* **6** (2010) 104.
- [225] W.M.J. Van Weerdenburg, A. Kamlapure, E.H. Fyhn, X. Huang, N.P.E. Van Mullekom, M. Steinbrecher et al., *Extreme enhancement of superconductivity in epitaxial aluminum near the monolayer limit*, *Science Advances* **9** (2023) eadf5500.

- [226] A. Ohtomo and H.Y. Hwang, *A high-mobility electron gas at the  $\text{LaAlO}_3/\text{SrTiO}_3$  heterointerface*, *Nature* **427** (2004) 423.
- [227] N. Reyren, S. Thiel, A.D. Caviglia, L.F. Kourkoutis, G. Hammerl, C. Richter et al., *Superconducting Interfaces Between Insulating Oxides*, *Science* **317** (2007) 1196.
- [228] R.F. Frindt, *Superconductivity in Ultrathin  $\text{NbSe}_2$  Layers*, *Physical Review Letters* **28** (1972) 299.
- [229] J.T. Ye, Y.J. Zhang, R. Akashi, M.S. Bahramy, R. Arita and Y. Iwasa, *Superconducting Dome in a Gate-Tuned Band Insulator*, *Science* **338** (2012) 1193.
- [230] Y. Cao, A. Mishchenko, G.L. Yu, E. Khestanova, A.P. Rooney, E. Prestat et al., *Quality Heterostructures from Two-Dimensional Crystals Unstable in Air by Their Assembly in Inert Atmosphere*, *Nano Letters* **15** (2015) 4914.
- [231] X. Xi, Z. Wang, W. Zhao, J.-H. Park, K.T. Law, H. Berger et al., *Ising pairing in superconducting  $\text{NbSe}_2$  atomic layers*, *Nature Physics* **12** (2016) 139.
- [232] H. Wang, X. Huang, J. Lin, J. Cui, Y. Chen, C. Zhu et al., *High-quality monolayer superconductor  $\text{NbSe}_2$  grown by chemical vapour deposition*, *Nature Communications* **8** (2017) 394.
- [233] Y. Zhou and A.J. Millis, *Dipolar phonons and electronic screening in monolayer  $\text{FeSe}$  on  $\text{SrTiO}_3$* , *Physical Review B* **96** (2017) 054516.
- [234] K. Kanetani, K. Sugawara, T. Sato, R. Shimizu, K. Iwaya, T. Hitosugi et al., *Ca intercalated bilayer graphene as a thinnest limit of superconducting  $\text{C}_6\text{Ca}$* , *Proceedings of the National Academy of Sciences* **109** (2012) 19610.
- [235] J. Chapman, Y. Su, C.A. Howard, D. Kundys, A.N. Grigorenko, F. Guinea et al., *Superconductivity in Ca-doped graphene laminates*, *Scientific Reports* **6** (2016) 23254.
- [236] X. Wang, N. Liu, Y. Wu, Y. Qu, W. Zhang, J. Wang et al., *Strong Coupling Superconductivity in Ca-Intercalated Bilayer Graphene on  $\text{SiC}$* , *Nano Letters* **22** (2022) 7651.
- [237] K. Andersen, S. Latini and K.S. Thygesen, *Dielectric Genome of van der Waals Heterostructures*, *Nano Letters* **15** (2015) 4616.
- [238] J. Hall, N. Ehlen, J. Berges, E. van Loon, C. van Efferen, C. Murray et al., *Environmental Control of Charge Density Wave Order in Monolayer  $2\text{H-TaS}_2$* , *ACS Nano* **13** (2019) 10210.

- [239] *Universal slow plasmons and giant field enhancement in atomically thin quasi-two-dimensional metals*, .
- [240] Z. Jiang, S. Haas and M. Rösner, *Plasmonic waveguides from Coulomb-engineered two-dimensional metals*, *2D Materials* **8** (2021) 035037.
- [241] R. Akashi, *Revisiting homogeneous electron gas in pursuit of properly normed ab initio Eliashberg theory*, *Physical Review B* **105** (2022) 104510.
- [242] E.A. Pashitskii, V. Pentegov, D. Manske and I. Eremin, *Influence of Long-Range Coulomb Interaction and On-Site Hubbard Repulsion on the Formation of d-Wave Copper-Pairing in High- $T_c$  Cuprates*, *Journal of Superconductivity* **17** (2004) 421.
- [243] M. Calandra, I.I. Mazin and F. Mauri, *Effect of dimensionality on the charge-density wave in few-layer 2H-NbSe<sub>2</sub>*, *Physical Review B* **80** (2009) 241108.
- [244] Y. Ge and A.Y. Liu, *Phonon-mediated superconductivity in electron-doped single-layer MoS<sub>2</sub>: A first-principles prediction*, *Physical Review B* **87** (2013) 241408.
- [245] B. Li, Z.W. Xing, G.Q. Huang and D.Y. Xing, *Electron-phonon coupling enhanced by the FeSe/SrTiO<sub>3</sub> interface*, *Journal of Applied Physics* **115** (2014) 193907.
- [246] M. Rosner, S. Haas and T.O. Wehling, *Phase diagram of electron-doped dichalcogenides*, *Physical Review B* (2014) 6.
- [247] S. Coh, M.L. Cohen and S.G. Louie, *Large electron-phonon interactions from FeSe phonons in a monolayer*, *New Journal of Physics* **17** (2015) 073027.
- [248] C. Zhang, Z. Liu, Z. Chen, Y. Xie, R. He, S. Tang et al., *Ubiquitous strong electron-phonon coupling at the interface of FeSe/SrTiO<sub>3</sub>*, *Nature Communications* **8** (2017) 14468.
- [249] D. Pines and J.R. Schrieffer, *Approach to Equilibrium of Electrons, Plasmons, and Phonons in Quantum and Classical Plasmas*, *Physical Review* **125** (1962) 804.
- [250] P. Hou, X. Cai, T. Wang, Y. Deng, N.V. Prokof'ev, B.V. Svistunov et al., *Probing Superconductivity in Two-dimensional Uniform Electron Gas by Precursory Cooper Flow*, Mar., 2023.
- [251] H.M. Dong, Z.H. Tao, Y.F. Duan, F. Huang and C.X. Zhao, *Coupled plasmon-phonon modes in monolayer MoS<sub>2</sub>*, *Journal of Physics: Condensed Matter* **32** (2020) 125703.

- [252] T. Wang, X. Cai, K. Chen, B.V. Svistunov and N.V. Prokof'ev, *Origin of the Coulomb pseudopotential*, *Physical Review B* **107** (2023) L140507.
- [253] M. Royo and M. Stengel, *Exact Long-Range Dielectric Screening and Interatomic Force Constants in Quasi-Two-Dimensional Crystals*, *Physical Review X* **11** (2021) 041027.
- [254] S. Poncé, M. Royo, M. Stengel, N. Marzari and M. Gibertini, *Long-range electrostatic contribution to electron-phonon couplings and mobilities of two-dimensional and bulk materials*, *Physical Review B* **107** (2023) 155424.
- [255] J. Berges, N. Girotto, T. Wehling, N. Marzari and S. Poncé, *Phonon Self-Energy Corrections: To Screen, or Not to Screen*, *Physical Review X* **13** (2023) 041009.
- [256] N. Girotto and D. Novko, *Dynamical renormalization of electron-phonon coupling in conventional superconductors*, *Physical Review B* **107** (2023) 064310.
- [257] N. Wentzell, H.U.R. Strand, S. Dienst, Y. in 't Veld, D. Simon, A. Hampel et al., *TRIQS/tprf: Version 3.3.1*, Sept., 2024, 10.5281/ZENODO.13652322.
- [258] C. Pellegrini, R. Heid and A. Sanna, *Eliashberg theory with ab-initio Coulomb interactions: a minimal numerical scheme applied to layered superconductors*, *Journal of Physics: Materials* **5** (2022) 024007.
- [259] J. Robertson, *High dielectric constant oxides*, *The European Physical Journal Applied Physics* **28** (2004) 265.
- [260] L. Wang, Y. Pu, A.K. Soh, Y. Shi and S. Liu, *Layers dependent dielectric properties of two dimensional hexagonal boron nitridenanosheets*, *AIP Advances* **6** (2016) 125126.
- [261] A. Laturia, M.L. Van de Put and W.G. Vandenberghe, *Dielectric properties of hexagonal boron nitride and transition metal dichalcogenides: from monolayer to bulk*, *npj 2D Materials and Applications* **2** (2018) 1.
- [262] K.A. Müller and H. Burkard, *SrTiO<sub>3</sub>: An intrinsic quantum paraelectric below 4 K*, *Physical Review B* **19** (1979) 3593.
- [263] M. Rösner, C. Steinke, M. Lorke, C. Gies, F. Jahnke and T.O. Wehling, *Two-Dimensional Heterojunctions from Nonlocal Manipulations of the Interactions*, *Nano Letters* **16** (2016) 2322.
- [264] A. Raja, A. Chaves, J. Yu, G. Arefe, H.M. Hill, A.F. Rigosi et al., *Coulomb engineering of the bandgap and excitons in two-dimensional materials*, *Nature Communications* **8** (2017) 15251.



- [265] E. Maxwell, *Isotope Effect in the Superconductivity of Mercury*, *Physical Review* **78** (1950) 477.
- [266] C.A. Reynolds, B. Serin, W.H. Wright and L.B. Nesbitt, *Superconductivity of Isotopes of Mercury*, *Physical Review* **78** (1950) 487.
- [267] J. De Launay, *The Isotope Effect in Superconductivity*, *Physical Review* **93** (1954) 661.
- [268] A. Bill, V.Z. Kresin and S.A. Wolf, *The Isotope Effect in Superconductors*, in *Pair Correlations in Many-Fermion Systems*, V.Z. Kresin, ed., (Boston, MA), pp. 25–55, Springer US (1998), 10.1007/978-1-4899-1555-9\_2.
- [269] K. Kaasbjerg, K.S. Thygesen and K.W. Jacobsen, *Phonon-limited mobility in n-type single-layer MoS<sub>2</sub> from first principles*, *Physical Review B* **85** (2012) 115317.
- [270] D. Tebbe, M. Schütte, K. Watanabe, T. Taniguchi, C. Stampfer, B. Beschoten et al., *Tailoring the dielectric screening in WS<sub>2</sub>-graphene heterostructures*, *npj 2D Materials and Applications* **7** (2023) 29.
- [271] D.Y. Qiu, F.H. Da Jornada and S.G. Louie, *Environmental Screening Effects in 2D Materials: Renormalization of the Bandgap, Electronic Structure, and Optical Spectra of Few-Layer Black Phosphorus*, *Nano Letters* **17** (2017) 4706.
- [272] E.G.C.P. Van Loon, M. Schüler, D. Springer, G. Sangiovanni, J.M. Tomczak and T.O. Wehling, *Coulomb engineering of two-dimensional Mott materials*, *npj 2D Materials and Applications* **7** (2023) 47.
- [273] A. Steinhoff, M. Florian and F. Jahnke, *Dynamical screening effects of substrate phonons on two-dimensional excitons*, *Physical Review B* **101** (2020) 045411.
- [274] A. Steinhoff, T.O. Wehling and M. Rösner, *Frequency-dependent substrate screening of excitons in atomically thin transition metal dichalcogenide semiconductors*, *Physical Review B* **98** (2018) 045304.
- [275] J.J. Lee, F.T. Schmitt, R.G. Moore, S. Johnston, Y.-T. Cui, W. Li et al., *Interfacial mode coupling as the origin of the enhancement of T<sub>2</sub> in FeSe films on SrTiO<sub>3</sub>*, *Nature* **515** (2014) 245.
- [276] Y. Wang, L. Rademaker, E. Dagotto and S. Johnston, *Phonon linewidth due to electron-phonon interactions with strong forward scattering in FeSe thin films on oxide substrates*, *Physical Review B* **96** (2017) 054515.

- [277] S. Zhang, J. Guan, X. Jia, B. Liu, W. Wang, F. Li et al., *Role of SrTiO<sub>3</sub> phonon penetrating into thin FeSe films in the enhancement of superconductivity*, *Physical Review B* **94** (2016) 081116.
- [278] A. Aperis and P.M. Oppeneer, *Multiband full-bandwidth anisotropic Eliashberg theory of interfacial electron-phonon coupling and high- $T_c$  superconductivity in FeSe / SrTiO<sub>3</sub>*, *Physical Review B* **97** (2018) 060501.
- [279] B. Rosenstein and B.Y. Shapiro, *High-temperature superconductivity in single unit cell layer FeSe due to soft phonons in the interface layer of the SrTiO<sub>3</sub> substrate*, *Physical Review B* **100** (2019) 054514.
- [280] V.Z. Kresin and H. Morawitz, *Layer plasmons and high- $T_c$  superconductivity*, *Physical Review B* **37** (1988) 7854.
- [281] D. Guerci, D. Kaplan, J. Ingham, J.H. Pixley and A.J. Millis, *Topological superconductivity from repulsive interactions in twisted WSe<sub>2</sub>*, Aug., 2024. 10.48550/arXiv.2408.16075.
- [282] T. Cea and F. Guinea, *Coulomb interaction, phonons, and superconductivity in twisted bilayer graphene*, *Proceedings of the National Academy of Sciences* **118** (2021) e2107874118.
- [283] L. Peng, I. Yudhistira, G. Vignale and S. Adam, *Theoretical determination of the effect of a screening gate on plasmon-induced superconductivity in twisted bilayer graphene*, *Physical Review B* **109** (2024) 045404.
- [284] V. Fatemi and J. Ruhman, *Synthesizing Coulombic superconductivity in van der Waals bilayers*, *Physical Review B* **98** (2018) 094517.
- [285] F. Jin, R. Roldán, M.I. Katsnelson and S. Yuan, *Screening and plasmons in pure and disordered single- and bilayer black phosphorus*, *Physical Review B* **92** (2015) 115440.
- [286] A. Principi, E. van Loon, M. Polini and M.I. Katsnelson, *Confining graphene plasmons to the ultimate limit*, *Physical Review B* **98** (2018) 035427.
- [287] S. Das Sarma and A. Madhukar, *Collective modes of spatially separated, two-component, two-dimensional plasma in solids*, *Physical Review B* **23** (1981) 805.
- [288] G.E. Santoro and G.F. Giuliani, *Acoustic plasmons in a conducting double layer*, *Physical Review B* **37** (1988) 937.
- [289] E.H. Hwang and S. Das Sarma, *Plasmon modes of spatially separated double-layer graphene*, *Physical Review B* **80** (2009) 205405.

- [290] R. Sensarma, E.H. Hwang and S. Das Sarma, *Dynamic screening and low-energy collective modes in bilayer graphene*, *Physical Review B* **82** (2010) 195428.
- [291] O. Zheliuk, J. Lu, J. Yang and J. Ye, *Monolayer Superconductivity in  $WS_2$ , physica status solidi (RRL) - Rapid Research Letters* **11** (2017) 1700245.
- [292] S. Conti, D. Neilson, F.M. Peeters and A. Perali, *Transition Metal Dichalcogenides as Strategy for High Temperature Electron-Hole Superfluidity*, *Condensed Matter* **5** (2020) 22.
- [293] Y. Yoon, Z. Zhang, R. Qi, A.Y. Joe, R. Sailus, K. Watanabe et al., *Charge Transfer Dynamics in  $MoSe_2$  / $hBN$ / $WSe_2$  Heterostructures*, *Nano Letters* **22** (2022) 10140.
- [294] J. Bauer, J.E. Han and O. Gunnarsson, *Quantitative reliability study of the Migdal-Eliashberg theory for strong electron-phonon coupling in superconductors*, *Physical Review B* **84** (2011) 184531.
- [295] I. Esterlis, B. Nosarzewski, E.W. Huang, B. Moritz, T.P. Devereaux, D.J. Scalapino et al., *Breakdown of the Migdal-Eliashberg theory: A determinant quantum Monte Carlo study*, *Physical Review B* **97** (2018) 140501.
- [296] F. Schrodi, P.M. Oppeneer and A. Aperis, *Full-bandwidth Eliashberg theory of superconductivity beyond Migdal's approximation*, *Physical Review B* **102** (2020) 024503.
- [297] C. Grimaldi, L. Pietronero and S. Strässler, *Nonadiabatic Superconductivity: Electron-Phonon Interaction Beyond Migdal's Theorem*, *Physical Review Letters* **75** (1995) 1158.
- [298] L. Pietronero, S. Strässler and C. Grimaldi, *Nonadiabatic superconductivity. I. Vertex corrections for the electron-phonon interactions*, *Physical Review B* **52** (1995) 10516.
- [299] C. Grimaldi, L. Pietronero and S. Strässler, *Nonadiabatic superconductivity. II. Generalized Eliashberg equations beyond Migdal's theorem*, *Physical Review B* **52** (1995) 10530.
- [300] E. Cappelluti and L. Pietronero, *Nonadiabatic superconductivity: The role of van Hove singularities*, *Physical Review B* **53** (1996) 932.
- [301] W. Sano, T. Koretsune, T. Tadano, R. Akashi and R. Arita, *Effect of Van Hove singularities on high- $T_c$  superconductivity in  $H_3S$* , *Physical Review B* **93** (2016) 094525.

- [302] Y. Takada, *Exact self-energy of the many-body problem from conserving approximations*, *Physical Review B* **52** (1995) 12708.
- [303] Y. Takada and T. Higuchi, *Vertex function for the coupling of an electron with intramolecular phonons: Exact results in the antiadiabatic limit*, *Physical Review B* **52** (1995) 12720.
- [304] F. Schrodi, A. Aperis and P.M. Oppeneer, *Influence of phonon renormalization in Eliashberg theory for superconductivity in two- and three-dimensional systems*, *Physical Review B* **103** (2021) 064511.
- [305] A. Madhukar, *Coupled electron-phonon system in two dimensions and its implications for inversion layers*, *Solid State Communications* **24** (1977) 11.
- [306] E.J. Nicol and J.K. Freericks, *Vertex corrections to the theory of superconductivity*, *Physica C: Superconductivity* **235-240** (1994) 2379.
- [307] Y. Núñez Fernández, M. Jeannin, P.T. Dumitrescu, T. Kloss, J. Kaye, O. Parcollet et al., *Learning Feynman Diagrams with Tensor Trains*, *Physical Review X* **12** (2022) 041018.
- [308] J. Kaye, S. Beck, A. Barnett, L. Van Muñoz and O. Parcollet, *Automatic, high-order, and adaptive algorithms for Brillouin zone integration*, *SciPost Physics* **15** (2023) 062.
- [309] L. Van Munoz, S. Beck and J. Kaye, *AutoBZ.jl: Automatic, adaptive Brillouin zone integration using Wannier interpolation*, *Journal of Open Source Software* **9** (2024) 7080.
- [310] Y. Nomura and R. Arita, *Ab initio downfolding for electron-phonon-coupled systems: Constrained density-functional perturbation theory*, *Physical Review B* **92** (2015) 245108.
- [311] N. Witt, Y. Nomura, S. Brener, R. Arita, A.I. Lichtenstein and T.O. Wehling, *Bypassing the lattice BCS-BEC crossover in strongly correlated superconductors through multiorbital physics*, *npj Quantum Materials* **9** (2024) 100.
- [312] L. Zhang and E. Gull, *Minimal pole representation and controlled analytic continuation of Matsubara response functions*, *Physical Review B* **110** (2024) 035154.
- [313] L. Zhang, Y. Yu and E. Gull, *Minimal pole representation and analytic continuation of matrix-valued correlation functions*, *Physical Review B* **110** (2024) 235131.

- [314] J. Fei, C.-N. Yeh and E. Gull, *Nevanlinna Analytical Continuation*, *Physical Review Letters* **126** (2021) 056402.
- [315] J. Fei, C.-N. Yeh, D. Zgid and E. Gull, *Analytical continuation of matrix-valued functions: Carathéodory formalism*, *Physical Review B* **104** (2021) 165111.



## RESEARCH DATA MANAGEMENT

---

This thesis research has been carried out in accordance with the research data management policy of the Institute for Molecules and Materials of Radboud University, the Netherlands.\*

With the exception of the experimental data discussed in chapter 4, all the raw data, scripts and software needed to reproduce the figures in this thesis have been stored on the Radboud Data Repository (RDR). The experimental data discussed in chapter 4 are available from the corresponding authors of the original work [60] upon request.

All datasets stored in the RDR are publicly available via the following digital object identifiers (DOIs)

- Chapter 4: 10.34973/n64d-0s91
- Chapter 5: 10.34973/8kse-4927
- Chapter 6: 10.34973/p73y-tt10
- Chapter 7: 10.34973/hdg1-bf52

Most of the libraries implemented and used for this thesis are furthermore publicly available in the TRIQS [155] and TPRF [257] codebases.

---

\* <https://www.ru.nl/rdm/vm/policy-documents/policy-imm/>





## PUBLICATIONS

---

Publications on which this thesis is based

- **Y. in 't Veld**, M. I. Katsnelson, A. J. Millis and M. Rösner, *Enhanced Superconductivity from Dynamical Environmental Screening*, in preparation (2025)
- **Y. in 't Veld**, M. I. Katsnelson, M. Rösner and A. J. Millis, *Quantifying the Relevance of Vertex Corrections for the Description of Layered Superconductors*, in preparation (2025)
- S. Ulstrup, **Y. in 't Veld**, J. A. Miwa, A. J. H. Jones, K. M. McCreary, J. T. Robinson, B. T. Jonker, S. Singh, R. J. Koch, E. Rotenberg, A. Bostwick, C. Jozwiak, M. Rösner and J. Katoch, *Observation of Interlayer Plasmon Polaron in Graphene/WS<sub>2</sub> Heterostructures*, Nature Comm. **15**, 3845 (2024)
- **Y. in 't Veld**, M. I. Katsnelson, A. J. Millis and M. Rösner, *Screening Induced Crossover between Phonon- and Plasmon-Mediated Pairing in Layered Superconductors*, 2D Materials **10**, 045031 (2023)

Contributions to open source software

- N. Wentzell, H. U. R. Strand, S. Dienst, **Y. in 't Veld**, D. Simon, A. Hampel, T. Hahn, M. Rösner, E. G. C. P. van Loon, H. Menke, O. Gingras, O. Parcollet, Phillip D., M. Zingl, *TRIQS/tprf: Version 3.3.1*, 10.5281/zenodo.13652322 (2024)

Other publications

- C. Sahoo, **Y. in 't Veld**, A. J. H. Jones, Z. Jiang, G. Lupi, P. E. Majchrzak, K. Hsieh, K. Watanabe, T. Taniguchi, P. Hofmann, J. A. Miwa, Y. P. Chen, M. Rösner and S. Ulstrup, *Quasiparticle Gap Renormalization Driven by Internal and External Screening in WS<sub>2</sub> Device*, submitted, preprint arXiv:2503.16234 (2025)
- X. Peng, **Y. in 't Veld**, G. Lupi, M. Rösner, J. Ye, *et al.*, *Doping Asymmetry-Dependent K/K' Valley Populations Across Different Layers in Four-Layer Transition Metal Dichalcogenides*, in preparation (2025)
- A. M. H. Krieg, A. Reinhold, **Y. in 't Veld**, M. Rösner, D. Wegner, A. A. Khajetoorians, *et al.*, *Cs Structures on InSb(110) as a Correlated Quantum Simulator*, in preparation (2025)
- **Y. in 't Veld**, M. Schüler, T. O. Wehling, M. I. Katsnelson and E. G. C. P. van Loon, *Bandwidth Renormalization due to the Intersite Coulomb Interaction*, J. Phys.: Condens. Matter **31**, 465603 (2019)



## ACKNOWLEDGMENTS

---

My PhD project has been a large undertaking which I could not have done on my own. Here I would like to thank those who have contributed in one way or another to the completion of this thesis.

To start, I could not have done this without my supervisor and co-promotor Malte Rösner. Malte, your generous support and feedback on all aspects of science, be it work ethic, writing, presenting or programming, have made me into the scientist I am now. I really enjoyed our discussions, especially the brainstormy ones, and I am very grateful that you introduced me to your network, which has allowed me to meet and collaborate with outstanding scientists all over the world. I am very much looking forward to our future projects together.

I am also indebted to my promotor, Misha Katsnelson, for giving me the opportunity to work at the TCM department during my PhD. Misha, your ideas and broad knowledge have been an inspiration to me throughout my scientific career, from my bachelor and master projects, to your wonderful master courses, and now my PhD. Thank you very much for your kindness and your input at every step of the way. I am furthermore extremely grateful to Andy Millis, who has been an important collaborator for most of the chapters in this thesis. Andy, every meeting with you I left having learned something new. Thank you for your many suggestions, which often lead to exciting new projects. I am also very grateful that you invited me (twice) to the Flatiron Institute in New York. The connections I made during my time there have been, and will be, invaluable to me.

I am very grateful to Ryotaro Arita, for hosting me at Tokyo University near the end of my PhD and for the pleasant collaborations that followed. I furthermore had the pleasure to collaborate with Søren Ulstrup, Jyoti Katoch and Chakradhar Sahoo on TMDC heterostructures, as well as with Hugo Strand, Nils Wentzell, Jason Kaye and Alex Hampel on the TRIQS and TPRF codebases. Special thanks to Hugo and Nils for teaching me proper scientific programming practices along the way.

The TCM has been an incredible workplace for my PhD. First of all, I would like to thank Belinda Eijgenraam for the secretarial support and for making the department a more pleasant and welcoming place. I also want to thank my officemate Sergii Grytsiuk for the many enjoyable chats about science and about life around science. Thanks to Koen Reijnders and Fabio Salvati for co-organizing the group meetings with me. Thanks to all staff, PhDs, PostDocs and students in TCM for creating the nice and comfortable atmosphere. I will miss our coffee breaks and cake meetings at the blue benches.

Tot slot wil ik graag mijn vrienden Jesse, Marieke, Jacco, Ilona, Daniël, Ilse en Michiel, en mijn familie Anneriet, Mark en Sjors bedanken. Heel erg bedankt voor de (board)game sessies, vakanties, gezelligheid en voor het altijd bereid zijn te luisteren.

- *Yann in 't Veld, January 2025*

I gratefully acknowledge financial support from the Dutch Research Council (NWO) via the 'TOPCORE' consortium.

## CURRICULUM VITAE

---

Yann in 't Veld was born on 21 April 1997 in Nijmegen, the Netherlands. From 2009 he attended high-school at the Nijmeegse Scholengemeenschap Groenewoud (NSG) in Nijmegen, from which he graduated in 2015 (cum laude).

In 2015, Yann started his studies at the Radboud University. There, he obtained a BSc. in Physics and Astronomy (cum laude) and a BSc. in Chemistry in 2018, followed by a MSc. in Physics and Astronomy (cum laude) in 2020. His master thesis, entitled *Plasmonic Superconductivity in Layered Materials*, was done under the supervision of Malte Rösner in the group of Mikhail Katsnelson. The thesis was furthermore done in collaboration with Ryotaro Arita, from the University of Tokyo, whom Yann visited for 8 months in 2020 in Tokyo.

Starting from 2020, Yann was employed as a PhD student at the Theory of Condensed Matter (TCM) department at the Institute for Molecules and Materials (IMM) of the Radboud University, working under the supervision of Malte Rösner and Mikhail Katsnelson. During his PhD, he was teaching assistant for courses on numerical methods and statistical physics. He furthermore supervised 2 bachelor students and 3 master students with the day-to-day work of their thesis. Now, Yann is employed as a postdoctoral researcher at Universität Hamburg, in the group of Tim Wehling.



As a result of their large surface-to-volume ratio, layered materials are generally much more sensitive to external stimuli compared to bulk systems. At the same time, the Coulomb interaction between electrons in layered materials can be particularly strong and is generically long-ranged, due to the reduced screening in atomically thin materials. The combination of these features paves the way for control over correlation effects induced by the Coulomb interaction, which would render microscopic material properties tunable from the outside.

To exploit these possibilities, we require a fundamental understanding of the physics that governs the properties of these systems. To this end, we theoretically study in this thesis the effect of the long-range 2D Coulomb interaction, as well as screening to it, on the electronic structure and the superconducting properties of layered van-der-Waals heterostructures. By developing and applying methods that go beyond state-of-the-art, we show that dynamical screening can induce novel interlayer electronic excitations, as well as introduce additional superconducting pairing mechanisms. Moreover, these effects are found to be highly sensitive to screening from the environment, yielding efficient tuning knobs for spectral functions and superconducting critical temperatures. The results in this thesis show that a careful consideration of all screening channels is crucial for a reliable description of layered materials and simultaneously opens up various avenues towards controllable microscopic material properties.

